

ABSTRACT

DAVIS, JASON MATTHEW. Radar Climatology of Tornadoic and Non-tornadoic Vortices in High Shear, Low CAPE Environments in the Mid-Atlantic and Southeast. (Under the direction of Dr. Matthew D. Parker.)

Tornadoes occurring in environments characterized by strong vertical wind shear (0-6 km bulk shear vector magnitude > 35 kts) but low Convective Available Potential Energy (CAPE < 500 J kg⁻¹), also known as high shear, low CAPE (HSLC) environments, are an important challenge for forecasters, especially in the Mid-Atlantic and Southeast. In this study, 95 tornadoic and 135 non-tornadoic supercell mesocyclones and quasi-linear convective system (QLCS) mesovortices were tracked. Values of azimuthal shear were recorded along the vortex tracks, and operationally relevant radar reflectivity signatures were also manually identified in association with these vortices.

Statistically significant differences in azimuthal shear were found between tornadoic and non-tornadoic QLCS mesovortices (and all tornadoic and non-tornadoic vortices overall) within 60 km of the radar. However, no statistically significant differences were found between tornadoic and non-tornadoic supercell mesocyclones within 60 km of the radar. Beyond 60 km from the radar, no statistically significant differences were found, due to the increasing beam height (causing low-level rotation to be poorly observed) and the increasing beamwidth (causing vortices to be poorly resolved). Hook echoes and bounded weak echo regions/weak echo regions (BWERs/WERs) were observed with almost all tornadoic and non-tornadoic supercell mesocyclones close to the radar. They developed at least 15 min prior to the tornado (implying lead time), but they were observed much less often > 100 km from the radar. Rear inflow notches, bowing segments, gust front cusps, and forward inflow notches were found with most tornadoic and non-tornadoic QLCS mesovortices close to the radar. They typically developed only a few minutes prior to the tornado and also were not detected very well far from the radar. False alarm rates were high for almost all reflectivity signatures. While azimuthal shear and radar reflectivity signatures show the potential for high probability of detection within 100 km of the radar, high false alarm rates and lead time will continue to be a challenge.

© Copyright 2013 by Jason Matthew Davis

All Rights Reserved

Radar Climatology of Tornadic and Non-tornadic Vortices in High Shear, Low CAPE
Environments in the Mid-Atlantic and Southeast

by
Jason Matthew Davis

A thesis submitted to the Graduate Faculty of
North Carolina State University
in partial fulfillment of the
requirements for the degree of
Master of Science

Marine, Earth and Atmospheric Sciences

Raleigh, North Carolina

2013

APPROVED BY:

Matthew D. Parker
Committee Chair

Sandra Yuter

Gary Lackmann

DEDICATION

To the One who has given me more grace and blessings than I could ever deserve.

BIOGRAPHY

Jason Davis grew up in Davenport, Iowa. He was always fascinated by all of the different types of weather that can occur in Iowa, especially severe thunderstorms. He rarely missed the local weather on television, and during every severe weather outbreak he was glued to the local TV coverage of the event and his NOAA Weather radio. All of his science fair projects pertained to weather, and he kept a daily log of high and low temperatures for several years. He graduated Summa Cum Laude from Valparaiso University with a Bachelor of Science in meteorology and minors in mathematics and music in May 2011. During his time at Valpo, he went on three 11 day long storm chase trips in the Great Plains, solidifying his interest in severe weather, though all types of weather still interest him. He served as treasurer and later vice-president of the Northwest Indiana Chapter of the American Meteorological Society/National Weather Association, where he was responsible for planning the Great Lakes Meteorology Conference. His interest in severe weather research stemmed from a summer research internship at the Storm Prediction Center through the NOAA Hollings Scholar program, where he studied verification of “high risk” convective outlooks. In August 2011, he joined the Convective Storms Group at North Carolina State University, working on a master’s degree under Dr. Matthew Parker. In his free time, Jason enjoys biking, hiking, traveling, playing disc golf, watching sports, and playing trombone and piano.

ACKNOWLEDGMENTS

I first want to thank my parents, Larry and Mary Davis, for all they have done for me, always supporting me and encouraging me to do my best. I also want to thank my advisor, Dr. Matthew Parker, for all of his feedback and guidance throughout this project as well as his positive attitude and encouragement. Drs. Sandra Yuter and Gary Lackmann, my committee members, also provided very useful discussions and feedback that improved the quality of this work. All of the National Weather Service collaborators played a vital role in shaping the approach to this project, providing frequent input, and also developing the initial list of cases. I especially want to thank Justin Lane, Patrick Moore, Jonathan Blaes, Hunter Coleman, Larry Lee, and Steve Keighton for their very beneficial feedback and helping me understand the challenges of warning operations during these events. Current and past members of the Convective Storms Group were also extremely helpful, through technical assistance, feedback, and support. These members include Drs. Casey Davenport, Adam French, and Johannes Dahl, as well as Keith Sherburn, Chris MacIntosh, and Brice Coffey. I am also grateful for the support of all the Marine, Earth, and Atmospheric Sciences graduate students. Finally, I want to thank everyone at Summit Church, especially those in my Bible study group, for their prayers and support and helping me to maintain perspective through the difficulties of graduate school. This research was supported by the NOAA Collaborative Science, Training, and Research (CSTAR) program, NOAA grant NA10NWS4680007, as well as an AMS/NASA Earth Science graduate fellowship.

TABLE OF CONTENTS

LIST OF TABLES	vi
LIST OF FIGURES	viii
Chapter 1 Introduction	1
Chapter 2 Background	5
2.1 HSLC Tornado Frequency and Annual/Diurnal Trends	5
2.2 HSLC Tornado Environments	7
2.3 HSLC Convective Modes	8
2.3.1 Mini-supercells	8
2.3.2 QLCSs	11
2.3.3 Climatology of Storm Types.....	14
2.4 Unique HSLC Radar Signatures	15
2.5 Summary	17
Chapter 3 Data and Methods.....	33
3.1 Spatiotemporal Domain	33
3.2 Tornado and Environment Data.....	34
3.3 Azimuthal Shear Climatology.....	35
3.3.1 Method of Calculating Azimuthal Shear	35
3.3.2 Vortex Tracking	37
3.4 Convective Mode Identification	42
3.5 Assessment of Radar Signatures	43
Chapter 4 Results.....	64
4.1 Convective Modes Climatology	64
4.2 Azimuthal Shear.....	66
4.2.1 Results for Vortices Close to the Radar	66
4.2.2 Results for Vortices Farther from the Radar.....	74
4.3.3 Evaluation of Other Rotational Metrics	78
4.3.4 Operational Ramifications	80
4.3 Radar Reflectivity Signatures Climatology	81
4.4 Tornadic and Non-tornadic Vortex Environments	85
Chapter 5 Discussion and Conclusions	135
5.1 Interpretation of Principal Results	135
5.2 Recommendations.....	139
5.3 Future Work	140
5.4 Conclusions.....	142
REFERENCES	144

LIST OF TABLES

Table 3.1 List of cases used in this study (using date in UTC time of first vortex from that case), and number of tornadic and non-tornadic vortices for each case. Vortices were included in the same case if no more than 12 h existed between tornadoes/false alarm warnings. Cases highlighted in red indicate common cases between the tornadic and non-tornadic vortices	46
Table 3.2 List of radar reflectivity signatures documented in association with supercell mesocyclones (left) and QLCS mesovortices (right). Italicized signatures were documented for both. Criteria for the signatures are described in the text	48

LIST OF FIGURES

FIG. 2.1 All tornadoes (red circles) with MLCAPE $\leq 500 \text{ J kg}^{-1}$ between 2003 and 2009, from Guyer and Dean (2010).....	18
FIG. 2.2 Same as FIG 2.1, but for (E)F2 and greater tornadoes.....	19
FIG. 2.3. Number of hours between 2003 and 2007 that a SPC mesoanalysis 40 km grid cell had lightning inside of it, binned by MLCAPE and 0-6 km bulk shear vector magnitude, from Schneider and Dean (2008).....	20
FIG. 2.4. Number of hourly SPC mesoanalysis grid cells that had tornado reports divided by number of grid cells that had lightning, between 2003 and 2007, binned by MLCAPE and 0-6 km bulk shear vector magnitude, from Schneider and Dean (2008). This produces a conditional probability that a tornado will occur given the presence of lightning.....	21
FIG. 2.5. Radar reflectivity (dBZ) using the same spatial scale for (a) a classic Plains supercell (non-tornadic at the time) at 2343 UTC on 7 June 2009 from the Kansas City, MO (KEAX) radar and (b) two mini-supercells (the one on the right was tornadic at this time) at 2238 UTC on 27 March 2009 from the Raleigh, NC (KRAX) radar	22
FIG. 2.6. Similar to FIG. 2.5., but a vertical cross-section of radar reflectivity (dBZ). Horizontal lines are drawn for every 10,000 ft (3.05 km) of altitude.....	22
FIG. 2.7. Observed sounding from Topeka, KS (TOP) at 0000 UTC on 8 June 2009, representing the environment of the high CAPE supercell in the left panels of FIGS. 2.5 and 2.6.....	23
FIG. 2.8. Similar to FIG. 2.7. but from Newport, NC (MHX) at 0000 UTC on 28 March 2009, representing the environment for the mini-supercells in the right panels of FIGS. 2.5 and 2.6.....	24
FIG. 2.9. Horizontal cross-section of simulated vertical velocity contours and horizontal wind vectors at $z = 3 \text{ km}$ in QLCS mesovortex simulation by Trapp and Weisman (2003).....	25
FIG. 2.10. Simulated gust front positions (dashed line) over time (left to right) and mesovortex positions (cyclonic vortices shaded in grey, anticyclonic vortices shaded in black) in mesovortex simulation by Atkins and St. Laurent (2009a)	25

FIG. 2.11. Time evolution of vertical cross-section through bow echo gust front in simulation by Atkins and St. Laurent (2009a). The gust front (299-K θ isotherm) is the solid black line, storm-relative winds are plotted as vectors, grey contours are ground-relative wind speed, and vertical vorticity is contoured in black. The mesovortex is shaded in light grey.....26

FIG. 2.12. (G) Radar reflectivity at 1952 UTC, (H) storm-relative velocity at 1952 UTC (probable tornado location indicated by red triangle), (I) radar reflectivity at 2007 UTC, and (J) radial velocity at 2007 UTC, all at the 0.5 degree elevation scan on 8 May 1995 from the Jackson, MS WSR-88D, showing a bookend vortex (adapted from Pfof and Gerard 1997 with annotations added).....27

FIG. 2.13. Box-and-whiskers plot of MLCAPE by season for all right-moving supercell mesocyclones that produced EF2 or greater tornadoes (grey shading), and all QLCS mesovortices that produced EF1 or greater tornadoes (black outline), from Thompson et al. (2012). The boxes span the 25th-75th percentiles, and the whiskers extend upward to the 90th and downward to the 10th percentiles, with values for these percentiles also reported. Median values are marked within the boxes, and sample sizes for each season are shown in parentheses28

FIG. 2.14. Conceptual model of a broken-S radar signature, courtesy of the NWS Greenville-Spartanburg, SC WFO. The blue line represents radar reflectivity greater than 40 dBZ in a QLCS, plotted every 5 min. The yellow band represents the likely swath of wind damage. The magenta arrow indicates when it is hypothesized that the tornado is likely to occur. At time 7, a second possible location for a broken-S to begin to develop is also shown29

FIG. 2.15. Radar reflectivity of a broken-S radar signature at the 0.5 degree elevation scan from the Greer, SC WSR-88D at 2352 UTC on 13 January 2006, from Lane and Moore (2006). Solid white lines indicate the northern and southern segments of the broken-S signature, and the dashed white line indicates the break in the convective line.....30

FIG. 2.16. Conceptual model of radar reflectivity associated with different broken-S signature evolutions as discussed in the text, from Clark (2011). ‘X’ denotes the location of vortices. Darker shading represents higher radar reflectivity values. ‘RIN’ and large bold arrows denote the location of the primary rear inflow notch. ‘WEC’ and the dashed grey lines denote the location of smaller weak echo channels associated with individual vortices.....31

FIG. 2.17. Radar reflectivity at the 1.5 degree (left panel) and 3.3 degree (right panel) elevation scans at 0455 UTC on 17 April 1995 from the Inola, OK WSR-88D for a HP supercell commahead tornado case (from Wolf 1998).....32

FIG. 3.1. Map of the CWAs that comprised the domain of this study: Huntsville, AL (HUN), Peachtree City, GA (FFC), Charleston, SC (CHS), Columbia, SC (CAE), Greenville-Spartanburg, SC (GSP), Wilmington, NC (ILM), Raleigh, NC (RAH), Newport/Morehead City, NC (MHX), Blacksburg, VA (RNK), Wakefield, VA (AKQ), and Baltimore/Washington (LWX).....49

FIG. 3.2. Changes in beam height and beamwidth with range from the radar, for the elevation scans in the WSR-88D's VCP 212. Dashed lines indicate the center of the beam, with the filled region representing the width of the beam.....50

FIG. 3.3. Vortex diameter at the 0.5 degree elevation scan as a function of range from the radar for tornadic vortices (green circles) and non-tornadic vortices (red circles). Best-fit lines are also plotted using the same color convention, with correlation coefficient values reported in the legend51

FIG. 3.4. Example plot of radial velocity (kts) and azimuthal shear (s^{-1}) for a vortex, using the same spatial scale for both. The azimuthal shear field is originally calculated on a polar grid of same resolution as the velocity data, but then interpolated to a 0.005 degree latitude by 0.005 degree longitude Cartesian grid. The radar is located west-northwest of these images52

FIG. 3.5. Flow chart for the tracking algorithm that is described in the text.....53

FIG. 3.6. Idealized schematic of tracking algorithm (not to scale). The vortex position, initially found by searching for an azimuthal shear maximum near the tornado touchdown/false alarm warning location, and then found iteratively by repeating the tracking process, is indicated by the orange diamond. A first guess prediction of the vortex is determined based on an estimate of vortex motion (see text for details), which is shown as the red diamond. An estimate of the uncertainty of the vortex motion vector is given by the black arrow (see text for details), which sweeps out the search radius indicated by the orange circle. The tracking algorithm searches for any MDA-detected mesocyclones within this search radius. If one is found, a smaller search radius is used centered on the MDA-detected mesocyclone's position, and if none are found it searches for the azimuthal shear maximum within this search radius (orange circle). The green diamond indicates a possible actual location for the vortex54

FIG. 3.7. (a) Radar reflectivity, (b) radial velocity, and (c) azimuthal shear at the 0.5

degree elevation scan of the Hytop, AL (KHTX) radar at 0649 UTC on 10 December 2008 for a gust front before the QLCS mesovortex in FIG. 3.8 formed55

FIG. 3.8. Similar to FIG. 3.7, but at 0659 UTC for an embedded mesovortex along a gust front56

FIG. 3.9. Radar reflectivity at the (a) 0.5 degree, (b) 0.9 degree, (c) 1.3 degree, and (d) 1.8 degree elevation scans from the Robins AFB, GA (KJGX) radar at 2324 UTC on 18 February 2009, showing examples of a hook echo, WER, and BWER.....57

FIG. 3.10. (a) Radar reflectivity and (b) radial velocity at the 0.5 degree elevation scan from the Hytop, AL (KHTX) radar at 0917 UTC on 25 October 2010, showing an example of a gust front cusp and bowing segment58

FIG. 3.11. Similar to FIG. 3.9, but from the Greer, SC (KGSP) radar at 0026 UTC on 11 April 2009, showing an example of a forward inflow notch59

FIG. 3.12. Similar to FIG. 3.9, but from the Sterling, VA (KLWX) radar at 2341 UTC on 16 April 2011, showing an example of a hook-like echo associated with a QLCS mesovortex60

FIG. 3.13. Radar reflectivity at the 0.5 degree elevation scan from the Hytop, AL WSR-88D on 6 May 2009 at (a) 1306, (b) 1310, (c) 1315, (d) 1320, (e) 1324, (f) 1329, (g) 1334, (h) 1338, and (i) 1343 UTC, showing the time evolution of a broken-S signature. The line break at the base scan occurs at 1320 UTC (panel d). Tornadoes occurred at 1325 UTC (after panel e), 1342 UTC (before panel i), and 1359 UTC (not shown). This broken-S signature fell in the 60-100 km range bin61

FIG. 3.14. Similar to FIG. 3.7, but from the Hytop, AL (KHTX) radar at 1116 UTC on 27 April 2011 showing an example of a QLCS mesovortex associated with a comma-shaped echo and a RIN62

FIG. 3.15. Similar to FIG. 3.7, but at the 0.9 degree elevation scan of the Peachtree City, GA (KFFC) radar at 2116 UTC on 30 November 2010 showing an example of an embedded supercell with a comma-shaped echo and RIN.....63

FIG. 4.1. Convective mode distributions for the HSLC tornadoes included in the full 2006-2011 HSLC dataset (top), and for all tornadoes nationwide (2003-2011) that were included in the Smith et al. (2012) convective mode database (bottom). Convective mode classifications are described in section 3.4 and in Smith et al. (2012). Percentages are out of 224 for the HSLC tornadoes and out of 10,724 for all tornadoes88

FIG. 4.2. Convective mode distributions for all tornadoes occurring in the domain during HSLC cases, including non-HSLC tornadoes, stratified by SBCAPE, using convective mode data from Smith et al. (2012).....	89
FIG. 4.3. Similar to FIG. 4.1, but comparing convective modes for the tornadic vortices used in the azimuthal shear climatology for which convective mode data was available from the Smith et al. (2012) database, and the non-tornadic vortices, whose convective modes were classified by the author.....	90
FIG. 4.4. Tracks of the 95 tornadic vortices (green lines) and 135 non-tornadic vortices (red lines) in this study (see section 3.3.2 for tracking methods). Concentric circles indicate range bins for the radars used in this study (vortices more than 150 km from the nearest radar are placed in the > 100 km range bin). The Robins AFB radar (KJGX) was only used in a couple cases when archived super-resolution velocity data was available, and is not included in this figure	91
FIG. 4.5. Azimuthal shear time series at the base scan, plotted relative to the time of first HSLC tornado touchdown for the tornadic vortices (green) and first HSLC tornado warning issuance for the non-tornadic vortices (red), for all vortices ≤ 60 km from nearest radar, at the (a) 0.5 degree, (b) 0.9 degree, (c) 1.3 degree, and (d) 1.8 degree elevation scans. Solid lines indicate median values while filled regions indicate the interquartile range. Solid circles above the time series indicate statistically significant positive differences at the 95% confidence level (p value ≤ 0.05) in median azimuthal shear between the tornadic and non-tornadic vortices at that time using the Wilcoxon rank-sum difference of medians test, and open circles indicate statistically significant differences at the 90% confidence level (p value between 0.05 and 0.1)	92
FIG. 4.6. Number of samples (volume scans where vortices existed) in each 5-min time bin, for all tornadic (green) and non-tornadic (red) vortices within 60 km of a radar (solid lines), only tornadic and non-tornadic supercell mesocyclones within 60 km of a radar (dashed lines), and only tornadic and non-tornadic QLCS mesovortices within 60 km of a radar (dash-dotted lines)	93
FIG. 4.7. Similar to FIG. 4.5, but for only tornadic and non-tornadic supercell mesocyclones within 60 km of the radar, using convective modes from the SPC database for the tornadic vortices, and convective modes assigned by the author for the non-tornadic vortices	94
FIG. 4.8. Similar to FIG. 4.7, but only tornadic and non-tornadic QLCS mesovortices within 60 km of the radar.....	95

FIG. 4.9. Same as FIG. 4.5, but only tornadic vortices whose first HSLC tornado was rated EF1 or greater, and all non-tornadic vortices, within 60 km of a radar96

FIG. 4.10. Time-height cross-sections of median azimuthal shear for vortices within 60 km of the radar, including (a) all tornadic vortices, (b) all non-tornadic vortices, (c) only tornadic supercell mesocyclones, (d) only non-tornadic supercell mesocyclones, (e) only tornadic QLCS mesovortices, and (f) only non-tornadic QLCS mesovortices. Values are plotted relative to the time of the first HSLC tornado touchdown (for tornadic vortices) or the first HSLC false alarm warning (for non-tornadic vortices). Azimuthal shear for each vortex at each time bin was linearly interpolated to a 250 m vertical grid, and then the median azimuthal shear value at each time-height gridpoint was calculated. Beam heights were calculated assuming standard atmospheric refraction, and are affected by spreading of the beam in the vertical. Values were only plotted if at least five vortices were present at each time-height gridpoint98

FIG. 4.11. Histogram of vortex lifetime (trackable time with azimuthal shear $\geq 0.006 \text{ s}^{-1}$ at any elevation scan in the lowest 2 km, using a single radar) for all tornadic (green) and non-tornadic (red) vortices within 60 km of a radar at the time of the tornado/warning. Median lifetimes are indicated by vertical lines99

FIG. 4.12. Similar to FIG. 4.11 but for vortex detection lead time, the length of time the vortex could be tracked with azimuthal shear $\geq 0.006 \text{ s}^{-1}$ prior to first HSLC tornado touchdown (for tornadic vortices) or first HSLC false alarm warning issuance (for non-tornadic vortices), for vortices within 60 km of the radar at the time of the tornado/warning99

FIG. 4.13. (a-c) Median vortex lifetime with azimuthal shear above 0.006 s^{-1} (solid lines; calculated using same method as in FIG. 4.11 caption) and 0.01 s^{-1} (dashed lines; consecutive time including the time of the tornado/warning that the vortex maintained azimuthal shear at or above this threshold, only using the 0.5 degree elevation scan) as a function of range from the radar at time of the tornado/warning, for (a) all vortices, (b) only supercell mesocyclones, and (c) only QLCS mesovortices. (d) Median tornadic vortex detection lead time at the 0.006 s^{-1} azimuthal shear threshold (solid lines; using same method as in FIG. 4.12 caption) and 0.01 s^{-1} azimuthal shear threshold (dashed lines; consecutive time prior to the tornado that the vortex maintained azimuthal shear above this threshold including the 5-min time bin prior to the tornado, only using the 0.5 degree elevation scan) as a function of range from the radar at the time of the tornado/warning for all tornadic vortices (green), only tornadic supercell mesocyclones (black), and only tornadic QLCS mesovortices (blue)100

FIG. 4.14. Highest radar elevation scan with azimuthal shear at or above 0.006 s^{-1} at

time of tornado/false alarm warning for tornadic (green) and non-tornadic (red) vortices within 60 km of the radar for (a) all vortices, (b) only supercell mesocyclones, and (c) only QLCS mesovortices. Median values are indicated by vertical lines. On the left side, “wrong VCP” indicates vortices that occurred when the radar was in a VCP with different elevation scans from the majority of cases, and “weak shear” indicates that the vortex did not have azimuthal shear above 0.006 s^{-1} at the base scan. These two categories were not included in median calculations.....	101
FIG. 4.15. Similar to FIG. 4.5, but for all vortices 60-100 km from the radar.....	102
FIG. 4.16. Similar to FIG. 4.6, but for (a) all vortices 60-100 km from the radar and (b) all vortices more than 100 km from the radar.....	103
FIG. 4.17. Similar to FIG. 4.10, but for vortices 60-100 km from the radar.....	104
FIG. 4.18. Similar to FIG. 4.7, but for only supercell mesocyclones 60-100 km from the radar.....	105
FIG. 4.19. Similar to FIG. 4.8, but for only QLCS mesovortices 60-100 km from the radar.....	106
FIG. 4.20. Similar to FIG. 4.9, but only tornadic vortices whose first HSLC tornado was rated EF1 or greater, and all non-tornadic vortices, 60-100 km from the radar.....	107
FIG. 4.21. Similar to FIG. 4.5., but for all tornadic and non-tornadic vortices more than 100 km from the radar.....	108
FIG. 4.22. Similar to FIG. 4.10, but for (a) tornadic and (b) non-tornadic vortices more than 100 km from the radar.....	109
FIG. 4.23. Similar to FIG. 3.3, but azimuthal shear as a function of range is plotted for all tornadic and non-tornadic vortices.....	110
FIG. 4.24. Similar to FIG. 4.5, but ΔV instead of azimuthal shear, for all vortices within 60 km of the radar.....	111
FIG. 4.25. Similar to FIG. 4.7, but ΔV instead of azimuthal shear, for all tornadic and non-tornadic supercell mesocyclones within 60 km of the radar.....	112
FIG. 4.26. Similar to FIG. 4.8, but ΔV instead of azimuthal shear, for all tornadic and non-tornadic QLCS mesovortices within 60 km of the radar.....	113

FIG. 4.27. Similar to FIG. 4.9, but ΔV instead of azimuthal shear, for only tornadic vortices whose first HSLC tornado was rated EF1 or greater, and all non-tornadic vortices within 60 km of the radar	114
FIG. 4.28. Similar to FIG. 4.15, but ΔV instead of azimuthal shear, for all tornadic and non-tornadic vortices 60-100 km from the radar	115
FIG. 4.29. Similar to FIG. 4.18, but ΔV instead of azimuthal shear, for only tornadic and non-tornadic supercell mesocyclones 60-100 km from the radar	116
FIG. 4.30. Similar to FIG. 4.20, but ΔV instead of azimuthal shear, for only tornadic vortices whose first HSLC tornado was rated EF1 or greater, and all non-tornadic vortices 60-100 km from the radar.....	117
FIG. 4.31. Similar to FIG. 4.21, but ΔV instead of azimuthal shear, for all tornadic and non-tornadic vortices more than 100 km from the radar.....	118
FIG. 4.32. Similar to FIG. 4.30, but for only tornadic vortices whose first HSLC tornado was rated EF1 or greater, and all non-tornadic vortices more than 100 km from the radar.....	119
FIG. 4.33. Similar to FIG. 4.23, but ΔV as a function of range from radar for all tornadic and non-tornadic vortices.....	120
FIG. 4.34. Similar to FIG. 4.5, but peak-to-peak shear (ΔV divided by vortex diameter) is plotted for all tornadic and non-tornadic vortices within 60 km of the radar	121
FIG. 4.35. Similar to FIG. 4.8, but peak-to-peak shear (ΔV divided by vortex diameter) is plotted for only tornadic and non-tornadic QLCS mesovortices within 60 km of the radar	122
FIG. 4.36. Probability of detection (POD, solid green line, percentage of tornadic supercell mesocyclones with given signature identified between 20 min prior to 15 min after tornado touchdown), probability of false detection (POFD, solid red line, percentage of non-tornadic supercell mesocyclones with given signature identified between 20 min prior to 15 min after false alarm warning issuance), false alarm rate (FAR, black dash-dot line, percentage of total number of identified signatures that were associated with non-tornadic supercell mesocyclones), and median lead time for tornadic supercell mesocyclones (dashed blue line, time relative to tornado touchdown when signature was first identified). Signatures include (a) hook echoes, (b) BWERs or WERs, (c) RINs, (d) comma-shaped echoes, and (e) bowing segments	124

FIG. 4.37. Similar to FIG. 4.36, but for reflectivity signatures associated with tornadic and non-tornadic QLCS mesovortices: (a) rear inflow notches, (b) comma-shaped echoes, (c) bowing segments, (d) gust front cusps, (e) forward inflow notches, and (f) hook-like echoes125

FIG. 4.38. (a) Same as FIG. 4.37, but for the broken-S radar signature, and median lead time for the break in the 40 dBZ radar reflectivity contour aloft (at the 0.9, 1.3, or 1.8 degree elevation scans; dashed blue line) and lead time for the time of the break in the 40 dBZ radar reflectivity contour at the 0.5 degree elevation scan (dashed cyan line). (b-e) Histograms of time relative to tornado touchdown for the line break aloft (b,d) and at the base scan (c,e) for broken-S signatures within 60 km of the radar (b-c) and between 60 and 100 km from the radar (d-e).....127

FIG. 4.39. Histogram of time relative to tornado touchdown for cell mergers associated with (a) supercell mesocyclones and (b) QLCS mesovortices128

FIG. 4.40. Box-and-whisker plots of environmental parameters from SPC mesoanalysis data for tornadic and non-tornadic vortices at time of tornado touchdown/false alarm warning, including (a) SBCAPE, (b) SBCIN, (c) mid-level lapse rates, (d) low-level lapse rates, (e) 0-6 km shear vector magnitude, and (f) 0-3 km shear vector magnitude. The box includes the 25th-75th percentiles, with the median indicated in the center of the box. Whiskers extend to 1.5 times the interquartile range, and outliers are indicated by crosses 130

FIG. 4.41. (a-b) Comparison of (a) Significant Tornado Parameter (STP) and (b) Severe Hazards in Environments with Reduced Buoyancy parameter formulation using the 0-3 km shear vector magnitude (SHERBS3) between tornadic and non-tornadic vortices at the time of tornado touchdown/false alarm warning issuance. (c-d) Comparison of SHERBS3 between (c) tornadic vortices producing an EF2+ tornado as their first HSLC tornado and all non-tornadic vortices and (d) tornadic vortices with track lengths ≥ 40 km and all non-tornadic vortices at time of tornado touchdown/false alarm warning issuance. The same plotting conventions are used as in FIG. 4.40.....131

FIG. 4.42. Similar to FIG. 4.5, but a time series of various environmental parameters for vortices with track lengths ≥ 80 km and which were located in an environment with SBCAPE $\geq 500 \text{ J kg}^{-1}$ at some time prior to the tornado, including (a) SBCAPE, (b) low-level lapse rates, (c) mid-level lapse rates, and (d) 0-6 km shear vector magnitude.....132

FIG. 4.43. Similar to FIG. 4.42, but for (a) 0-3 km shear vector magnitude, (b) 0-1 km shear vector magnitude, (c) 0-3 km storm relative helicity (SRH), and

(d) 0-1 km SRH.....133

FIG. 4.44. Similar to FIG. 4.42, but for (a) SHERBS3, (b) STP, (c) azimuthal shear
at the 0.5 degree elevation scan, and (d) range from radar134

Chapter 1

Introduction

Issuing accurate tornado warnings with sufficient lead time, while difficult in all environments, is especially challenging in environments marked by strong vertical wind shear but weak instability, known as high shear, low CAPE (HSLC) environments. HSLC environments are defined in this study as environments with surface-based CAPE (SBCAPE) $< 500 \text{ J kg}^{-1}$ and 0-6 km bulk shear vector magnitudes $> 18 \text{ m s}^{-1}$ (35 kts), a definition that was determined by the consensus of collaborating Mid-Atlantic and Southeast forecasters (see section 3.2). These environments are especially common during severe weather events in the Mid-Atlantic and Southeast (Schneider et al. 2006, Schneider and Dean 2008, Guyer and Dean 2010, Sherburn and Parker 2013). Improved understanding of the typical storm environments and radar observations associated with HSLC tornadoes is necessary for improving forecasts and warnings. A study of mesoscale environmental parameters associated with HSLC tornadoes (and other significant severe events) was recently completed by Sherburn and Parker (2013). The present study focuses on improving the understanding of storm-scale radar observations of HSLC vortices.

Compared to classic supercell structures in Plains high CAPE environments, HSLC radar reflectivity and velocity signatures are often of smaller size and magnitude, with markedly different structures at times (Grant and Prentice 1996, Lane and Moore 2006). Challenges that are especially a problem for HSLC tornadoes include that HSLC vortices may not be sampled well by the radar due to radar beam widening with range, making it difficult to resolve small diameter vortices far from the radar. The increase in the height of the radar beam above the Earth's surface with range means that the radar may potentially overshoot shallow vortices far from the radar. Also, numerous vortices may be present on the radar display, many of which are non-tornadic. This makes it difficult to discriminate between tornadic and non-tornadic vortices in a quickly evolving situation, as a forecaster

must determine which vortices are most deserving of close scrutiny. This study sought methods by which radar reflectivity and velocity signatures associated with tornadic and non-tornadic HSLC vortices could be used by operational forecasters to improve detection and warning skill. The approach was to study many tornadic and non-tornadic vortices from a large number of HSLC cases.

Fundamentally, there are still many aspects of tornadogenesis that are not fully understood, and many storm-scale processes that currently cannot be well-observed operationally. Environmental factors are also important, but not all storms in favorable environments are tornadic. All of these problems contribute to warning uncertainties. Currently, radar observations are still the best tool for tornado warning operations, even though there are some limitations. This includes the radar sampling limitations mentioned in the previous paragraph that are especially troublesome in HSLC environments, as well as a few more general limitations that will now be discussed. Operational Doppler radars rarely can resolve the circulation of the tornado itself, due to the radar beamwidth typically being much larger than the tornado. Therefore, forecasters must consider low-level rotation associated with the parent mesocyclone/mesovortex instead when issuing tornado warnings. This can pose a challenge as many supercells have strong low-level mesocyclones yet are not tornadic (Trapp 1999, Trapp et al. 2005a). Many quasi-linear convective system (QLCS) mesovortices are also likely not tornadic, though the frequency of tornadic QLCS mesovortices is less well-documented. Another limitation of Doppler radars is that they only measure the component of the wind that is parallel to the radar beam, the radial velocity. Therefore, rotation is not directly observed by the radar; rotation is inferred by strong horizontal shear, a strong gradient in radial velocity in the azimuthal direction.

Previous papers have studied azimuthal shear and rotational velocity associated with supercell mesocyclones and QLCS mesovortices typically in one of two ways. Some studies have used a case study approach, manually calculating time series of azimuthal shear or rotational velocity for a handful of tornadic storms (e.g. Funk et al. 1999, Atkins et al. 2004, Atkins et al. 2005, Schumacher and Boustead 2011). Others have focused on azimuthal shear

at one point in time for the purposes of developing tornado and mesocyclone detection algorithms (e.g. Stumpf et al. 1998). These algorithms can be used to develop mesocyclone climatologies (e.g. Wood et al. 1996, Trapp 1999, Jones et al. 2004, Trapp et al. 2005a) in order to determine the percentage of tornadic mesocyclones, for example. In this study, we seek to study *changes in azimuthal shear over time for a composite of a large number of cases*, where supercell mesocyclones and QLCS mesovortices (hereafter collectively referred to as “vortices”) are tracked, not just detected. The unique aspect of this study is the ability to look at temporal changes in vortex strength for a large number of cases in HSLC environments, an approach rarely used even for vortices in higher CAPE environments. Additionally, not only are tornadic vortices studied, but also non-tornadic vortices, in order to determine if there are any discriminating factors that can improve warning skill. Also, the potential lead time for HSLC tornadoes is determined.

In addition to radial velocity information, forecasters also look at radar reflectivity signatures for clues when issuing warnings. These signatures can provide insight into the dynamical processes at work in a storm as well as storm intensity, which complements the information provided by velocity data. For example, a bounded weak echo region (BWER) can indicate an area of strong updraft (Lemon and Doswell 1979), and a rear inflow notch (RIN) can indicate the presence of a rear inflow jet (Przybylinski 1995). Since vortices may not be well-sampled by the radar, forecasters may use reflectivity to help determine where a vortex could be or could develop. For example, in some QLCS mesovortex tornado cases, the radar may not detect rotation until the tornado touches down, but several reflectivity signatures anecdotally appear to provide greater lead time for tornado warnings. It is important to determine how often these signatures actually are associated with tornadoes, how often they are present but a tornado does not occur, and when they occur relative to the tornado.

Chapter 2 provides a review of HSLC tornado climatology and environments, convective modes associated with HSLC tornadoes and their related dynamics, and unique radar signatures associated with HSLC tornadoes. Chapter 3 describes the cases and data

used, as well as the methods used for identifying and tracking HSLC vortices and radar reflectivity signatures. Chapter 4 presents the results for the azimuthal shear and radar reflectivity climatologies, as well as a brief study of environmental characteristics of the vortex tracks. Chapter 5 discusses the results, includes recommendations for improving HSLC tornado warning operations, suggests avenues for future work, and summarizes the primary conclusions of this study.

Chapter 2

Background

2.1 HSLC Tornado Frequency and Annual/Diurnal Trends

HSLC tornadoes have only recently (in comparison to their higher CAPE counterparts) come under close scrutiny by researchers and forecasters. They are much more prevalent than previously thought, especially in the Southeast and during the cool season, challenging conventional wisdom about the typical annual and diurnal trends in tornadoes and traditional methods of forecasting tornadoes (Sherburn 2013, Sherburn and Parker 2013). In a study of tornadoes in low CAPE environments, Guyer and Dean (2010) found that 27.8% of all tornadoes between 2003 and 2009 occurred in environments with mixed-layer CAPE (MLCAPE¹) less than 500 J kg⁻¹. More than half of these (15% of all tornadoes) occurred in environments with very low MLCAPE, less than 250 J kg⁻¹. Despite the presence of low CAPE, HSLC tornadoes are not all weak as might be expected. Schneider and Dean (2008) found that 16.2% of all significant (Enhanced Fujita (EF) scale rating of EF2 or greater) tornadoes between 2003 and 2007 occurred in environments with MLCAPE less than 500 J kg⁻¹. Guyer and Dean (2010) found that tornadoes in low CAPE environments were only slightly less likely to be significant than tornadoes in environments with higher CAPE (7.7 vs. 10.7% of tornadoes, respectively). In addition, they found that three tornadoes in low CAPE environments reached EF4 strength during their six year period of study.

Guyer and Dean (2010) found that tornadoes in low CAPE environments (not necessarily high shear) can occur in numerous types of weather patterns, such as in tropical cyclones, underneath cold core closed upper lows, and along cold fronts associated with extratropical cyclones. Low CAPE tornadoes can occur in locations such as California and the Tennessee and Ohio Valleys (Fig. 2.1). However, low CAPE tornadoes, especially

¹ In the current study, surface-based CAPE (SBCAPE) is used to define a low CAPE environment.

significant ones, are most common in the Southeastern U.S. (Fig 2.2; Schneider et al. 2006, Guyer and Dean 2010, Sherburn and Parker 2013). A number of studies by National Weather Service (NWS) Weather Forecast Offices (WFOs) in this region have noted that HSLC tornadoes make up a significant fraction of all tornadoes that occur in their County Warning Areas (CWAs; Reilly 2004, Konarik and Nelson 2008, Lane 2008, Latimer and Kula 2010). Southeastern HSLC tornadoes tend to occur during the cool and transitional seasons, though they can also occur during late summer and fall in association with landfalling tropical cyclones. During the winter months between 2003 and 2009, 60% of all regional tornadoes occurred in low CAPE environments (Guyer and Dean 2010).

Guyer and Dean (2010) found that the hourly distribution of low CAPE tornadoes still had a diurnal peak during the afternoon, similar to the hourly distribution of tornadoes in environments with higher CAPE. However, the low CAPE tornado peak was earlier in the afternoon and much more subdued, as a substantial number of tornadoes occurred at other times of the day and night. Low CAPE tornadoes were comparatively more likely to occur during the overnight, morning and early afternoon hours than tornadoes in higher CAPE environments. For example, between 40-55% of all tornadoes that occurred during each hour between 0700 and 1700 UTC were in low CAPE environments. Kis and Straka (2010) also found that nocturnal tornadoes tended to have relatively low MLCAPE.

Society is more vulnerable to tornadoes during the night, when many low CAPE tornadoes occur. Affected people may be asleep and not aware of tornado warnings, and it is also more difficult to see tornadoes at night. Ashley et al. (2008) found that 34% of tornado fatalities occurred at night, and that given the occurrence of a tornado, it would be almost twice as likely to cause fatalities during the night as during the day. HSLC tornadoes also tend to occur in seasons where the public may not expect them, and in the Southeast, where there is a greater percentage of mobile home stock than other parts of the nation (Ashley 2007). Ashley et al. (2008) found that this also increases the vulnerability associated with these tornadoes. Finally, it has proved difficult to issue accurate warnings for HSLC tornadoes. Brotzge and Erickson (2010) and Brotzge et al. (2011), respectively, found that

the relative frequencies of unwarned tornadoes and the tornado warning false alarm ratio were greatest at night and during the cool season, when HSLC tornadoes are most likely.

2.2 HSLC Tornado Environments

HSLC tornado environments are distinct from higher CAPE tornado environments in several ways. Tornadoes in low CAPE environments tend to have smaller low-level and mid-level lapse rates compared to environments with higher CAPE (Guyer and Dean 2010). However, Sherburn and Parker (2013) did find that a modest lapse rate threshold (0-3 km lapse rate of 5.2 K km^{-1} and 700-500 hPa lapse rate of 5.6 K km^{-1}) was skillful in discriminating between significant HSLC severe weather and null HSLC events. Guyer and Dean (2010) also found that low CAPE tornadoes are associated with lower temperatures and dew points than higher CAPE tornadoes. The preceding findings are not surprising, since these parameters are all related to the amount of CAPE present. Guyer and Dean (2010) also found that low CAPE tornadoes tend to have somewhat higher 0-6 km bulk shear vector magnitudes than tornadoes in higher CAPE environments, and a more marked increase in 0-3 km and 0-1 km storm relative helicity (SRH). Large amounts of low-level shear (as measured by 0-1 km bulk shear and 0-1 km SRH) are commonly associated with significant tornadoes, as has been consistently found by Thompson et al. (2003), Markowski et al. (2003), Thompson et al. (2012), and others. Lifting condensation levels (LCLs) tend to be lower in low CAPE environments, which Markowski et al. (2002) found to be more favorable for tornadogenesis. This is presumably because low LCLs are associated with rear flank downdraft (RFD) parcels that are less negatively buoyant and therefore more easily lifted by an updraft, resulting in a greater potential for vortex stretching (Markowski et al. 2002). The relative effects of low LCLs and stronger shear versus weaker updraft buoyancy on tornadogenesis in HSLC supercells is still unclear. Guyer and Dean (2010) and Sherburn and Parker (2013) have found that CAPE-shear composite parameters such as the Supercell Composite Parameter (SCP) and the Significant Tornado Parameter (STP; Thompson et al. 2003) tend to be lower for low CAPE tornadoes. This is because these parameters are most

directly influenced by large differences in CAPE, causing them to decrease despite favorable shear values and LCLs.

Adding to the forecast challenge, HSLC environments are present much more often than traditional high CAPE, high shear environments. Schneider and Dean (2008) showed that the number of thunderstorm hours (number of hours with convection in a grid cell summed over all grid cells) in HSLC environments far exceeds the number of high CAPE-high shear thunderstorm hours (Fig. 2.3). While HSLC environments are present for many more hours across the country than high CAPE, high shear environments, the conditional probability of severe weather occurrence given the presence of convection is much lower in HSLC environments than in high CAPE, high shear environments (Fig. 2.4). Therefore, the potential false alarm rate associated with forecasting the development of tornadoes in HSLC environments is larger, as convection is present in these environments for a long time during which few tornadoes will occur. In high CAPE, high shear environments, on the other hand, convection may be present for a shorter period of time but be comparatively more likely to produce a tornado.

2.3 HSLC Convective Modes

The forecasting challenges associated with the somewhat unusual timing and environments of HSLC storms are hopefully by now clear. Because the present study concerns radar detection of threatening HSLC storms, we next review the current knowledge of convective structures and evolution in HSLC settings.

2.3.1 Mini-supercells

Supercells in HSLC environments tend to be smaller in horizontal and vertical size than their higher CAPE counterparts (Figs. 2.5-6), and therefore are referred to as mini-supercells (Davies 1990, Davies 1993). Observations of mini-supercells show that they can be as long-lived and have a similar structure as a normal supercell (e.g. Davies 1990 and 1993, Kennedy et al. 1993, Knupp et al. 1998, Markowski and Straka 2000, Murphy and Knupp 2013). However, their small size causes them to not be as well-sampled by the radar as classic supercells. The small vertical size of a mini-supercell is typically due to a combination of a

weaker updraft and typically lower equilibrium levels. For example, the high CAPE classic supercell in the left panels of Figs. 2.5-6 was in an environment supportive of strong updrafts due to the large buoyancy present (SBCAPE of 3457 J kg^{-1} in a nearby sounding), and the equilibrium level and storm top were both above 12 km (Fig. 2.7). In contrast, the mini-supercells in the right panels of Figs. 2.5-6 were associated with SBCAPE of 450 J kg^{-1} in the Storm Prediction Center's (SPC's) mesoanalysis data (see section 3.2), and an equilibrium level of around 5 km in a nearby sounding (Fig. 2.8). Storm tops were only around 3 km, possibly due to the capping inversion present near 3 km in the nearby sounding.

Mini-supercell's smaller horizontal footprint appears to be due to a combination of weaker updraft mass flux and precipitation not being advected as far downwind due to the shallower storm depth (Wicker and Cantrell 1996). An observational study by Kennedy et al. (1993) also similarly noted that the mini-supercell in their study had a horizontal footprint in radar reflectivity that was half the size of a normal supercell, and its updraft only reached an elevation of 6 km. This mini-supercell contained a mid-level mesocyclone that preceded the low-level mesocyclone and tornado, as in normal supercells. Wicker and Cantrell (1996) found in their simulations that the size of supercell features appeared to scale with storm depth.

In HSLC environments, the large amount of shear can partially compensate for the lack of buoyancy, as dynamic pressure perturbations caused by even a weak updraft tilting large amounts of ambient horizontal shear vorticity into the vertical can lead to a strong updraft through a vertical dynamic pressure gradient acceleration. In simulations of supercells in the environments of landfalling tropical cyclones, McCaul and Weisman (1996) found that updraft speeds in the low levels of a supercell in an environment with around 600 J kg^{-1} of CAPE were comparable to those in the low levels of a typical Plains high CAPE supercell, a result also found by Wicker and Cantrell (1996). This is favorable for stretching of near-ground vertical vorticity, which is one of the necessary components for tornadogenesis. McCaul and Weisman (1996) found that this similarity in low-level updraft speeds was due to the fact that the dynamic vertical pressure gradient forcing dominates in

the low levels of supercell updrafts. The vertical motion in the upper half of the Plains supercell in this study was dominated by buoyancy, however, resulting in stronger vertical motion aloft than what was found in the lower CAPE supercell.

While tornadogenesis in mini-supercells has rarely, if ever, been explicitly studied, the mechanisms are likely similar to those in higher CAPE supercells, since mini-supercells have similar processes as higher CAPE supercells despite having different scales. As reviewed in Markowski and Richardson (2010), rotation in a supercell initially develops in mid-levels (the mid-level mesocyclone), as an updraft tilts horizontal vortex lines from the deep-layer environmental shear into the vertical. The low-level mesocyclone later develops primarily from tilting of horizontal vorticity generated baroclinically by the storm, and also potentially due to tilting of horizontal vorticity associated with low-level environmental shear. Tornadogenesis requires vertical vorticity near the ground, which requires that a downdraft (if there is no pre-existing vertical vorticity) be involved in the tilting process. Once vertical vorticity is present near the ground, it must be stretched for tornadogenesis to occur, with an upward dynamic perturbation pressure gradient force associated with the low-level mesocyclone likely playing a major role.

The small size of mini-supercells makes them difficult to sample with operational radars. In an observational study of mesocyclones in mini-supercells by WSR-88D (Weather Surveillance Radar—1988 Doppler) radars, Burgess et al. (1995) found that mini-supercell mesocyclones had smaller rotational velocities, horizontal diameters, and vertical depths compared to classic supercells. Grant and Prentice (1996) noted that the average mesocyclone diameter for the mini-supercells they studied was a little more than half the diameter assumed in operational mesocyclone nomograms, suggesting that typical radar-based thresholds for issuing tornado warnings need to be modified for mini-supercells. Similar to classic supercells, however, Grant and Prentice (1996) noted a downward trend in mesocyclone base height, and upward trends in low-level rotational velocity and shear leading up to tornado touchdown in the mini-supercell cases that they studied, which were mostly close to the radar. Overall, observational and modeling studies of mini-supercells

have remained limited compared to their classic supercell counterparts, especially mini-supercells not associated with landfalling tropical cyclones, such as the typical HSLC tornado environment in the Mid-Atlantic and Southeast.

2.3.2 QLCSs

Some HSLC tornadoes and damaging wind events in QLCSs are associated with embedded mesovortices. QLCS mesovortices are circulations with diameters on the order of the meso-gamma scale, or about 2-20 km in diameter (Trapp and Weisman 2003). The mesovortices of interest in this study are on the lower end of this scale. They develop along the gust front of a QLCS, quite close to the surface (Fig. 2.9). They are different from supercell mesocyclones, as explained by Weisman and Trapp (2003). QLCS mesovortices initially form at low levels, and may later extend upward into mid-levels, while supercell mesocyclones begin in mid-levels, and may later extend downward into low levels. Supercell mesocyclones are correlated with an updraft in mid-levels. They can strengthen due to a dynamic pressure perturbation induced by the rotating updraft which causes greater vertical motion and an increase in vertical vorticity due to stretching. QLCS mesovortices do not require a long-lived rotating updraft, and so they will only benefit from dynamic pressure perturbations if they are underneath an updraft. Both QLCS mesovortices and supercell mesocyclones can be associated with tornadoes; a QLCS mesovortex would likely need to become collocated with an updraft in order for vortex stretching to produce a tornado from near-surface vertical vorticity. Several theories have been proposed for how QLCS mesovortices are generated (Funk et al. 1999, Trapp and Weisman 2003, Weisman and Trapp 2003, Wakimoto et al. 2006, Wheatley and Trapp 2008, Atkins and St. Laurent 2009a and 2009b), and this is still an area of active research, but not a topic directly addressed by this study. The lack of rotation aloft in QLCS mesovortices compared to supercell mesocyclones can make them more difficult to detect by operational radars. They can potentially develop underneath the height of the lowest scan at longer ranges from the radar, and strong low-level rotation can develop with little lead time.

Most of the mechanisms of QLCS mesovortex genesis that have been studied involve tilting of horizontal vorticity to produce vertical vorticity. In Trapp and Weisman's (2003) simulation, QLCS mesovortices developed by downward tilting of horizontal shear vorticity due to the rear inflow jet (RIJ) or horizontal vorticity baroclinically generated along the gust front. On the other hand, Atkins and St. Laurent (2009b) found that QLCS mesovortices in their simulation developed by *upward* tilting of baroclinically generated vorticity along the gust front. Differing from these mechanisms, Funk et al. (1999) and Wheatley and Trapp (2008) have proposed that shearing instability generates QLCS mesovortices, through a sheet of pre-existing vertical vorticity along the gust front being wrapped up into a vortex. Tornadogenesis associated with QLCS mesovortices has been rarely studied. For all of the genesis mechanisms except shearing instability (where vertical vorticity is always present), what is known is that a downdraft is necessary for vertical vorticity to be present near the ground. There are probably some similarities in the tornadogenesis process between supercell mesocyclones and QLCS mesovortices, with the main differences being the lack of a mid-level mesocyclone correlated with an updraft in QLCS mesovortices, and potentially differences in downdraft structure and the mechanism by which stretching of near-ground vorticity occurs. However, the details of this process remain unresolved.

.Atkins et al. (2004) and (2005) found that tornadic QLCS mesovortices usually had stronger Doppler-observed rotational velocity at low-levels and were longer-lived than non-tornadic mesovortices. However, their shallow nature and small size can make them difficult to detect, especially far from the radar. Also, for the QLCS mesovortices studied by Atkins et al. (2005), tornadogenesis occurred only an average of 12 min after the mesovortex formed, much quicker than the typical time between the development of a mid-level mesocyclone and tornadogenesis in a supercell, on the order of tens of minutes (Brown et al. 1978). Atkins et al. (2005) found that tornadogenesis in QLCS mesovortices usually occurred after the mesovortices quickly strengthened, as indicated by a sudden increase in azimuthal shear (on the order of 0.005 s^{-1}) caused by an increase in rotational velocity and a decrease in vortex diameter. The depth of the tornadic QLCS mesovortices also increased rapidly. Non-tornadic

QLCS mesovortices tended to be much shallower and have weaker azimuthal shear values, without a sudden increase in shear or vortex depth.

QLCS mesovortices, especially tornadic ones, often (but not exclusively) form near or to the north of the apex of a bow echo, if present, such as in Fig. 2.10 (Weisman and Trapp 2003, Trapp and Weisman 2003, Atkins et al. 2005, Atkins and St. Laurent 2009b). However, some QLCS mesovortices may also occur south of the apex when a bowing segment has not yet reached its mature stage (Trapp and Weisman 2003). The association between bow echoes and cool season tornadoes has also been mentioned by Przybylinski (1995) and Burke and Schultz (2004). They noted the importance of short (length <20 km) bow echoes embedded in a squall line for the production of damaging winds and tornadoes in cool season environments with strong synoptic forcing (often HSLC).

RIJs can affect QLCS mesovortices if they descend to near the surface and intersect the gust front. The increased convergence associated with a descending RIJ can increase the lifting along the gust front, resulting in a stronger updraft and more stretching of vertical vorticity in the mesovortex (Atkins et al. 2005), as shown in Fig. 2.11. Also, an elevated RIJ can act as an additional source of horizontal vorticity that can be tilted into the vertical, producing a QLCS mesovortex (Trapp and Weisman 2003). In one of the bow echoes that Atkins et al. (2005) studied, no tornadoes occurred prior to the development of the RIJ. Notably, when the RIJ advects drier air into a QLCS, evaporation of some of the trailing stratiform precipitation can result in indentations in the back edge of the trailing stratiform precipitation, or rear inflow notches (RINs; Smull and Houze 1985 and 1987, Przybylinski 1995, Atkins et al. 2005). RINs can be used by forecasters as a surrogate that indicates the presence of a RIJ (Przybylinski 1995), as often the RIJ is not oriented parallel to the radar beam and therefore is not obvious in radial velocity data.

Tornadoes have also been documented with line-end vortices, a type of QLCS mesovortex also known as a bookend vortex (Weisman and Davis 1998). Such tornadoes typically occur in the southeast portion of the “commahead”, behind the bowing segment (Pfof and Gerard 1997, see Fig. 2.12). Pfof and Gerard (1997) observed that the bookend

vortex diameter, typically rather large compared to a supercell mesocyclone, shrank in size around the time of tornadogenesis. It is unknown what similarities this tornadogenesis scenario shares with cases of tornadogenesis in high-precipitation (HP) supercells that take on comma-shaped echo morphologies as they transition to a bow echo (Moller et al. 1990, Finley et al. 2001) or comma-shape echoes that sometimes develop when a squall line merges with a supercell and subsequent bowing occurs (e.g. Wolf 1998, French and Parker 2012).

Detailed high-resolution observational and modeling studies of QLCS mesovortices in low CAPE environments are scarce, so it is unclear how well the published results for QLCS mesovortices apply to lower CAPE mesovortices. Also, radar sampling limitations, already a problem for higher CAPE mesovortices, become compounded due to the typically decreased horizontal and vertical sizes of HSLC convection.

2.3.3 Climatology of Storm Types

One reason that HSLC tornadoes are challenging for forecasters is their tendency to occur with linear and/or non-discrete convective modes, either in embedded supercells in QLCSs, or in association with QLCS mesovortices. Numerous studies have indirectly shed light on this, indicating the prevalence of linear convective modes in both nocturnal and cool season tornado climatology, times when HSLC tornadoes are most common. Trapp et al. (2005b) and Kis and Straka (2010) found that most nocturnal tornadoes were associated with linear convection, and Grams et al. (2012) found similar numbers of nocturnal significant tornadoes associated with discrete supercells and linear convection.² Trapp et al. (2005b) found that 32% of tornadoes associated with linear convection occurred during the months of January, February, and March. Smith et al. (2012) and Grams et al. (2012) found that tornadoes were almost as likely to occur with linear convective modes as with the typical discrete or cluster right-moving supercell convective modes during the cool season. The prevalence of linear

² Note that Grams et al. (2012), Kis and Straka (2010) and Trapp et al. (2005) did not distinguish embedded supercells from embedded mesovortices in QLCSs. Also, Kis and Straka (2010) did not require contiguous radar reflectivity as a criteria for linear convection. See Smith et al. (2012).

convection in HSLC environments poses a challenge to forecasters, as embedded supercells in QLCSs do not often clearly resemble classic Plains discrete supercells.

Narrowing the focus from all linear convection to only QLCS mesovortex tornadoes (and not tornadoes from embedded supercells), their likely importance in HSLC tornado climatology becomes very clear. Thompson et al. (2012) found that 45% of all QLCS mesovortex tornadoes had MLCAPE less than 500 J kg^{-1} , while only 15% of discrete right-moving supercell tornadoes occurred with MLCAPE below this threshold. They also found that, during the winter, 75% of significant tornadoes from right-moving supercells occurred in environments with MLCAPE greater than 350 J kg^{-1} . Meanwhile, 75% of QLCS mesovortex tornadoes rated EF1 or greater occurred in environments with MLCAPE less than 450 J kg^{-1} (Fig. 2.13). The prevalence of HSLC QLCS mesovortex tornadoes is problematic as the dynamics of QLCS mesovortex tornadoes are much less understood compared to supercell mesocyclone tornadoes (section 2.3.2).

2.4 Unique HSLC Radar Signatures

Several unique radar signatures have been associated with HSLC QLCS mesovortex tornadoes in case studies by forecasters, with the “broken-S” radar signature attracting the most attention. Forecasters have sought useful signatures in radar reflectivity due to the difficulty of detecting HSLC QLCS mesovortices in radial velocity data with adequate lead time (Lane and Moore 2006). The broken-S radar signature was first discussed by McAvoy et al. (2000), in a study of several HSLC tornado cases. It was documented by Grumm and Galzewski (2004) in warm season cases as well. It forms within a small bowing segment developing in a QLCS. The southern portion of this bowing segment begins to move ahead of the northern portion of the bowing segment, giving this portion of the QLCS an “S” shape in radar reflectivity (Figs. 2.14 and 2.15). This eventually results in a break in the convective line. A circulation becomes evident in the area of the line break. A tornado may develop in this region shortly afterward. In some cases, McAvoy et al. (2000) found that tornadoes were only found to occur at the area of the broken-S in the convective line, anecdotally indicating the importance of looking for this signature during warning operations. McAvoy et al. (2000)

speculated that the break in radar reflectivity may be due to evaporation caused by adiabatic warming of subsiding air. The overall structure also somewhat resembles a RIN.

Building on the work of McAvoy et al. (2000), Lane and Moore (2006) found that not all broken-S radar signatures were associated with tornadoes. Some broken-S signatures are not very distinct, and, in one case they studied, the broken-S-like signature that did produce a tornado was not the one that was most similar in appearance to the conceptual model. In broken-S cases, Lane and Moore (2006) state that a tornado may develop concurrently with or soon after rotation becomes evident on radar. Rather than waiting until rotation is apparent in the radial velocity field and a tornado is potentially already on the ground, Lane and Moore (2006) suggest looking for signs of a developing broken-S signature in radar reflectivity and issuing a warning if the environment is favorable in order to achieve warning lead time.

Broken-S signatures were also documented by Clark (2011) in an HSLC environment in the UK, associated with QLCS mesovortices forming along bowing segments in a squall line. While there were signs of a broken-S developing a few minutes prior to a tornado in some instances, the broken-S did not fully develop until after the tornado occurred. Clark (2011) proposed two conceptual models for the broken-S based on this case (Fig. 2.16). In one type of evolution, the southern segment surges eastward and weakens while the northern segment may persist and contain supercell-like characteristics. In the other, cyclic broken-S development occurs, as new QLCS mesovortices to the south of the original broken-S signature successively develop and mature. This results in new bowing segments, and new line breaks.

Similar breaks in reflectivity, while not referred to as broken-S signatures by the authors, can be seen in association with comma-shaped echoes in a bookend vortex tornado case (Fig. 2.12) documented by Pfof and Gerard (1998), and in a squall-line supercell merger case (Fig. 2.17) documented by Wolf (1998). Additionally, Trapp and Weisman (2003) noted in their simulations that the development of some QLCS mesovortices led to undulations and eventually breaks in the leading edge of the QLCS updraft, resulting in a

segmentation of the convective line (Fig. 2.10). This was caused by a downward dynamic pressure gradient force due to the low-level QLCS mesovortex, which weakens the updraft. It is not yet known if this is related to the break in the convective line associated with the broken-S signature; Clark (2011) suggests that it may be. Similar evolutions were also found in observations by Wakimoto et al. (2006). An exact definition of the broken-S signature and its variations remains unresolved, and it has rarely been found in the formal literature, at least under this name. Its kinematics and dynamics remain largely unknown, and to the author's knowledge it has not been explicitly studied in a numerical simulation. Also, the climatological frequency of broken-S signatures remains unknown, as well as how often tornadoes are associated with this signature, a question that will be addressed in the present study through examining tornadic and non-tornadic vortices for broken-S signatures.

2.5 Summary

It has been shown that HSLC tornadoes play an important role in tornado climatology, especially in the Southeast and Mid-Atlantic, and that they pose many challenges to forecasters during warning operations. The frequency of HSLC tornadoes from non-discrete supercells, mini-supercells, and QLCS mesovortices (convective modes that are less well-understood and not as well-sampled by radar as classic Plains supercells), shows the importance of a radar study of large population of HSLC tornadoes. The utility of azimuthal shear for detecting HSLC tornadoes, which appears to show skill in tornado detection in mini-supercells (Grant and Prentice 1996) and QLCS mesovortices (Atkins et al. 2005), needs to be further explored. The usefulness of radar reflectivity signatures, such as the broken-S radar signature and RINs, along with more traditional signatures such as hook echoes and bounded weak echo regions (BWERS) also requires more study. These gaps in the knowledge base serve as the motivation for the present study.

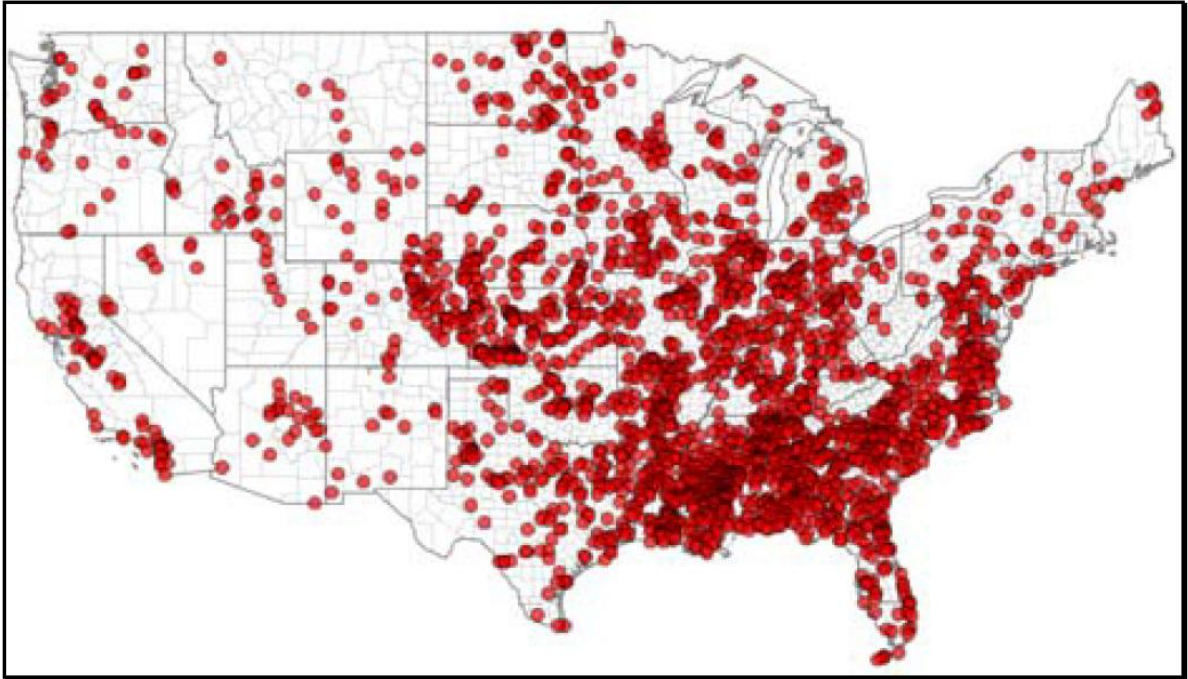


FIG. 2.1. All tornadoes (red circles) with $MLCAPE \leq 500 \text{ J kg}^{-1}$ between 2003 and 2009, from Guyer and Dean (2010).



FIG. 2.2. Same as FIG 2.1, but for (E)F2 and greater tornadoes.

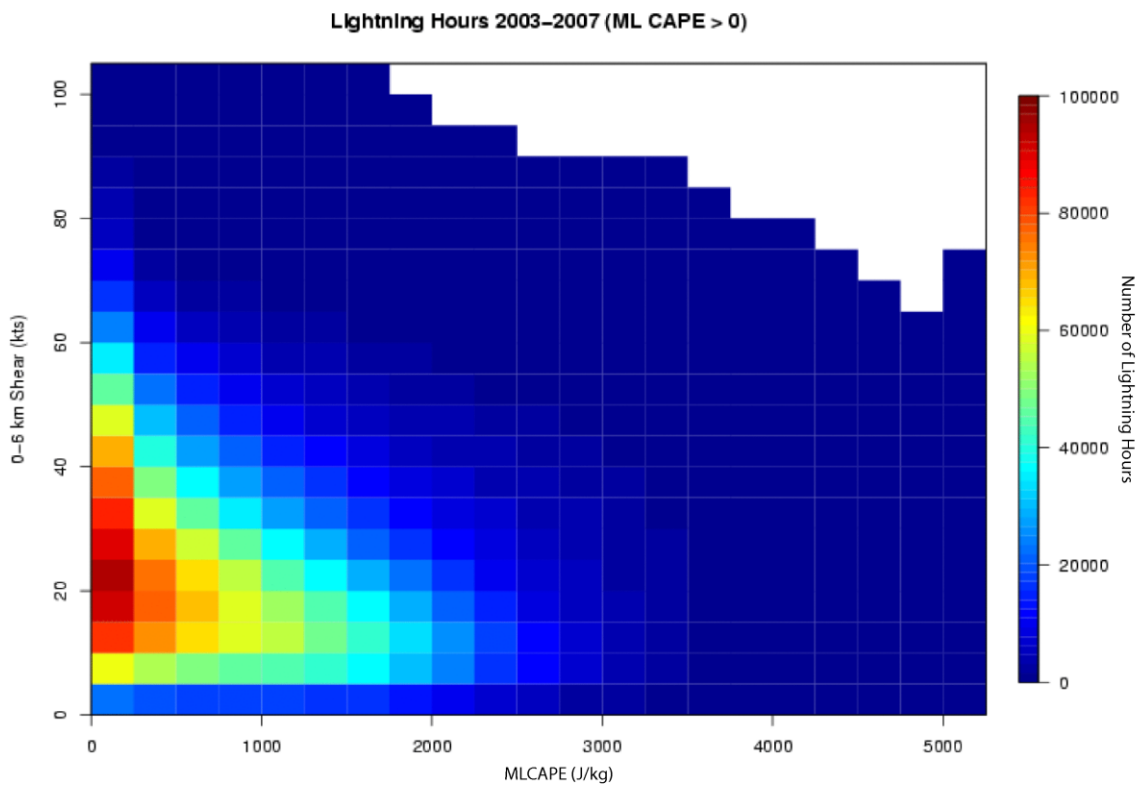


FIG. 2.3. Number of hours between 2003 and 2007 that a SPC mesoanalysis 40 km grid cell had lightning inside of it, binned by MLCAPe and 0-6 km bulk shear vector magnitude, from Schneider and Dean (2008).

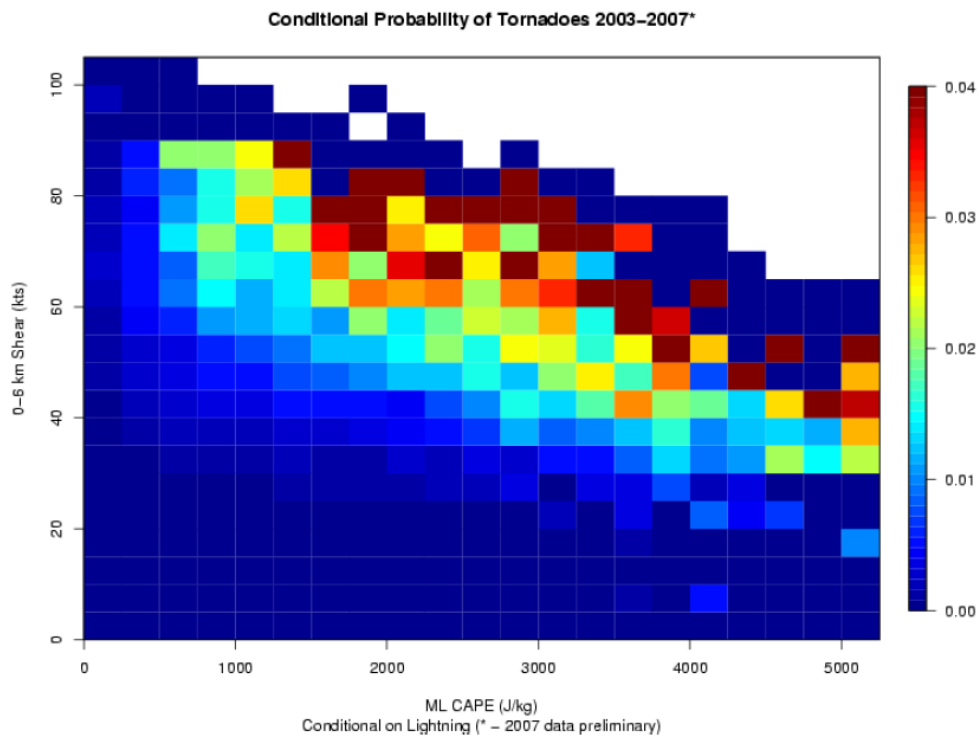


FIG. 2.4. Number of hourly SPC mesoanalysis grid cells that had tornado reports divided by number of grid cells that had lightning, between 2003 and 2007, binned by MLCAPE and 0-6 km bulk shear vector magnitude, from Schneider and Dean (2008). This produces a conditional probability that a tornado will occur given the presence of lightning.

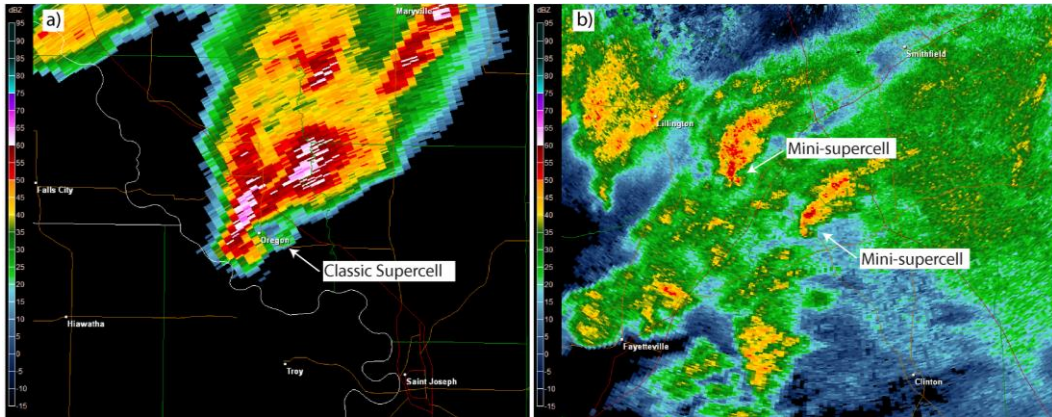


FIG. 2.5. Radar reflectivity (dBZ) using the same spatial scale for (a) a classic Plains supercell (non-tornadic at the time) at 2343 UTC on 7 June 2009 from the Kansas City, MO (KEAX) radar and (b) two mini-supercells (the one on the right was tornadic at this time) at 2238 UTC on 27 March 2009 from the Raleigh, NC (KRAX) radar.

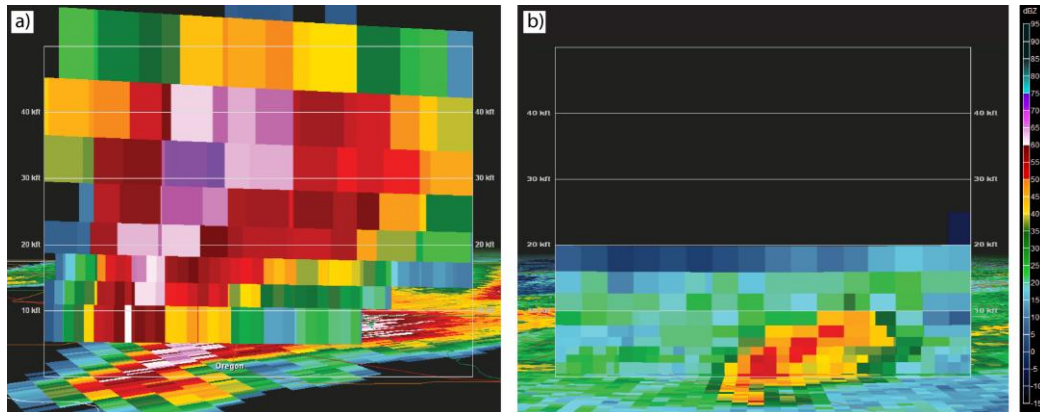
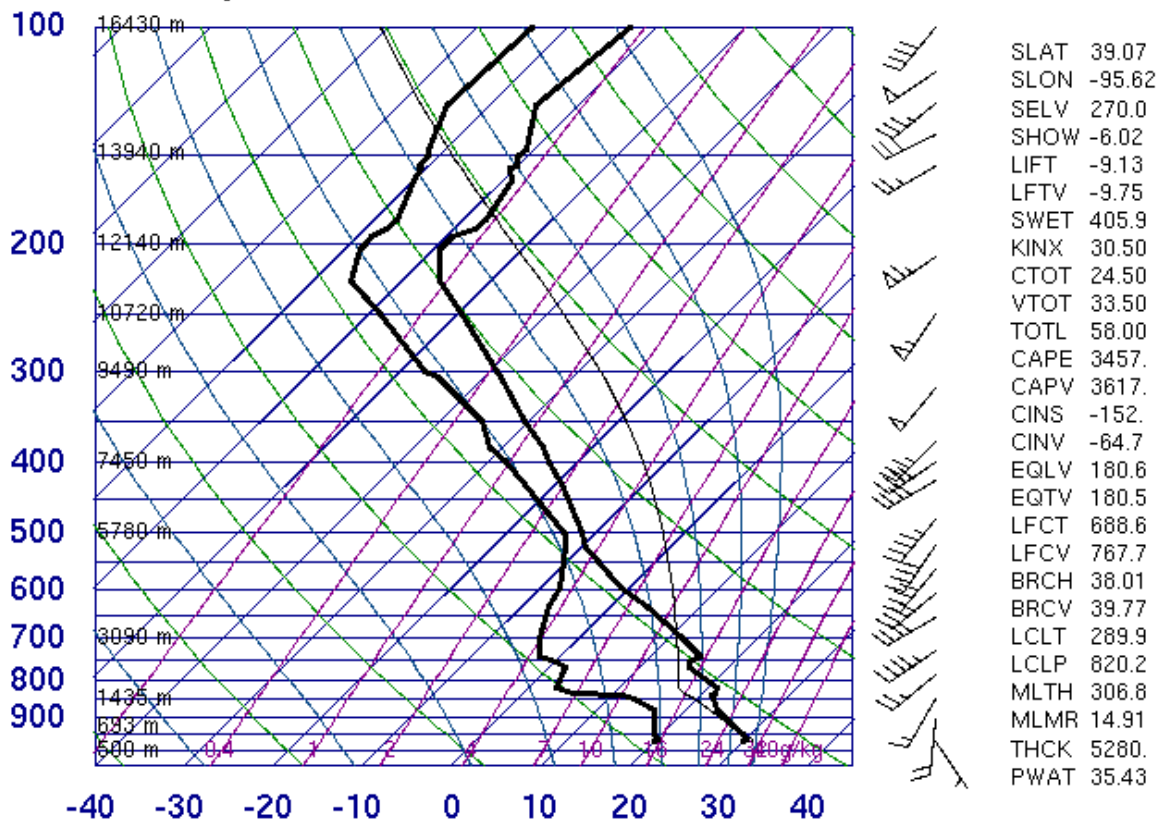


FIG. 2.6. Similar to FIG. 2.5., but a vertical cross-section of radar reflectivity (dBZ). Horizontal lines are drawn for every 10,000 ft (3.05 km) of altitude.

72456 TOP Topeka

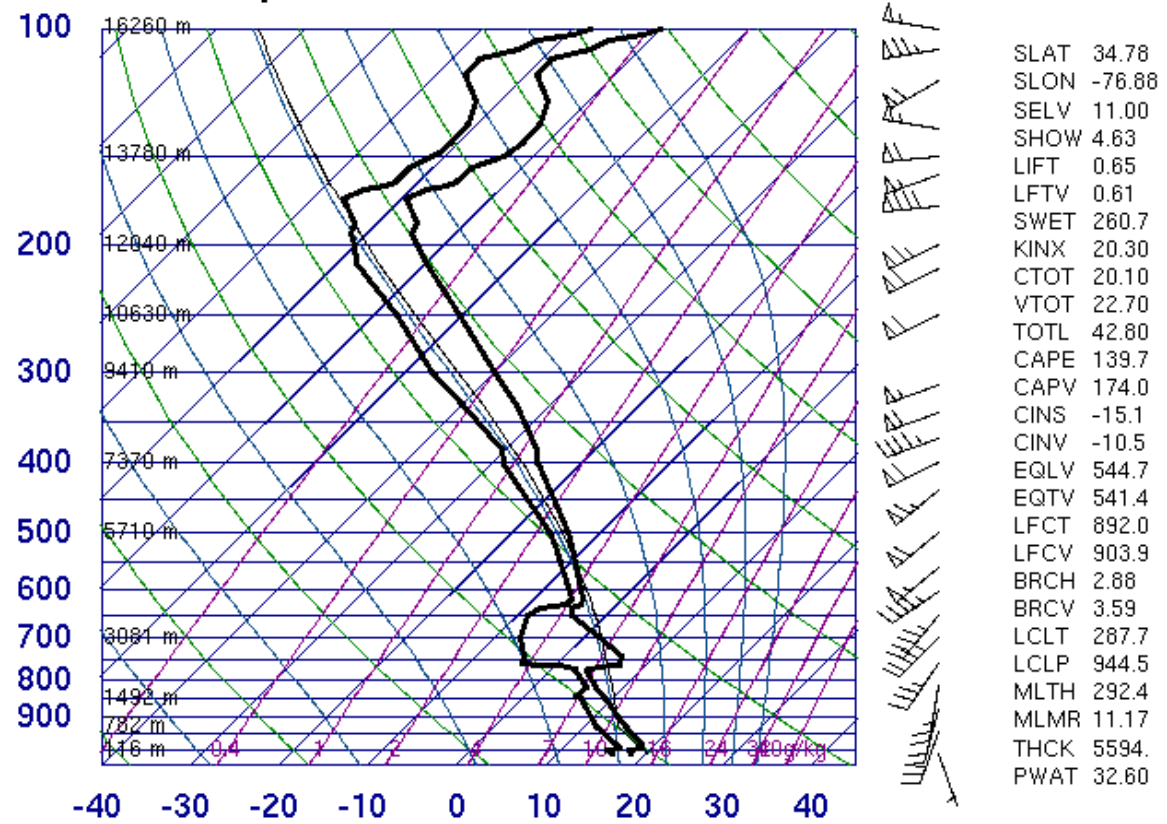


00Z 08 Jun 2009

University of Wyoming

FIG. 2.7. Observed sounding from Topeka, KS (TOP) at 0000 UTC on 8 June 2009, representing the environment of the high CAPE supercell in the left panels of FIGS. 2.5 and 2.6.

72305 MHX Newport



00Z 28 Mar 2009

University of Wyoming

FIG. 2.8. Similar to FIG. 2.7. but from Newport, NC (MHX) at 0000 UTC on 28 March 2009, representing the environment for the mini-supercells in the right panels of FIGS. 2.5 and 2.6.

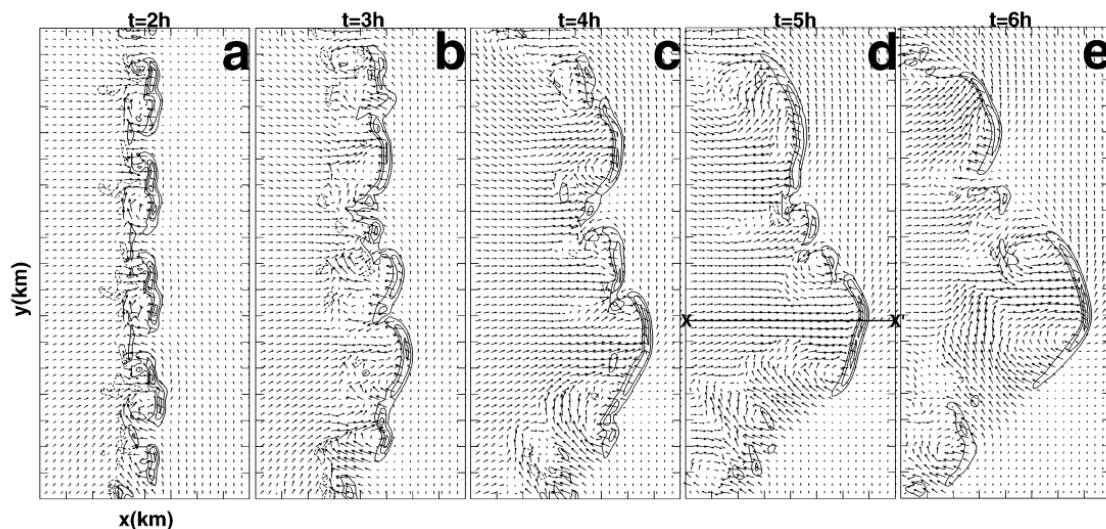


FIG. 2.9. Horizontal cross-section of simulated vertical velocity contours and horizontal wind vectors at $z = 3$ km in QLCS mesovortex simulation by Trapp and Weisman (2003).

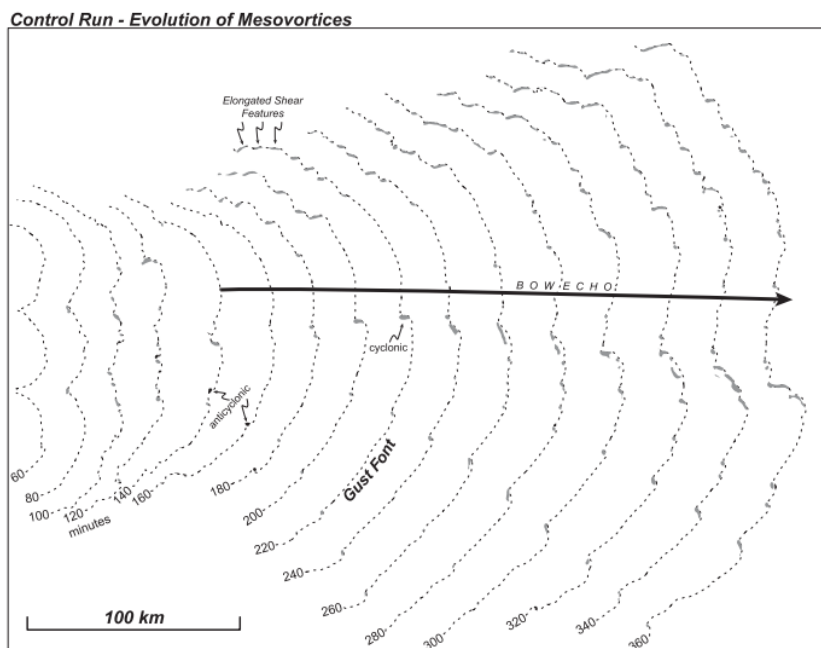


FIG. 2.10. Simulated gust front positions (dashed line) over time (left to right) and mesovortex positions (cyclonic vortices shaded in grey, anticyclonic vortices shaded in black) in mesovortex simulation by Atkins and St. Laurent (2009a).

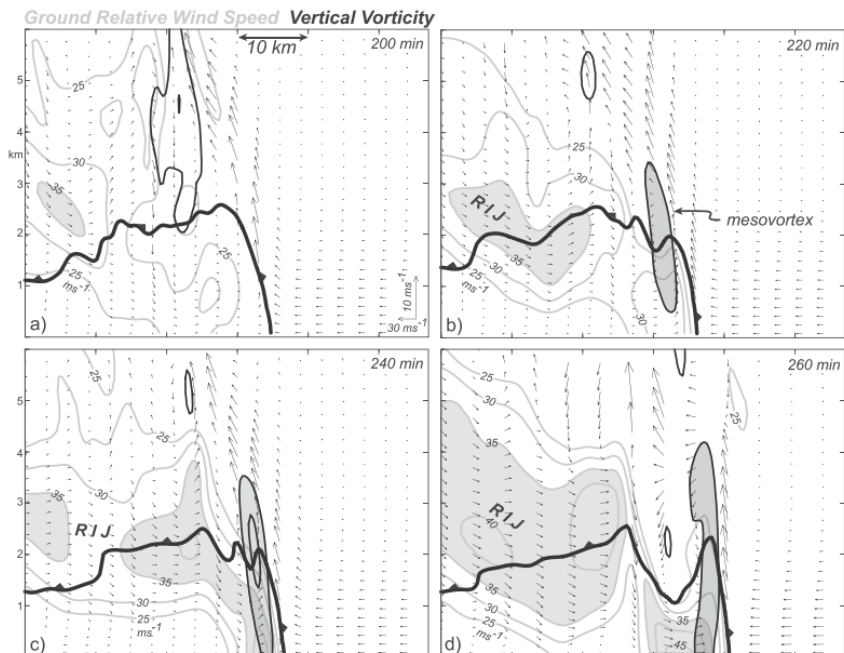


FIG. 2.11. Time evolution of vertical cross-section through bow echo gust front in simulation by Atkins and St. Laurent (2009a). The gust front (299-K θ isotherm) is the solid black line, storm-relative winds are plotted as vectors, grey contours are ground-relative wind speed, and vertical vorticity is contoured in black. The mesovortex is shaded in light grey.

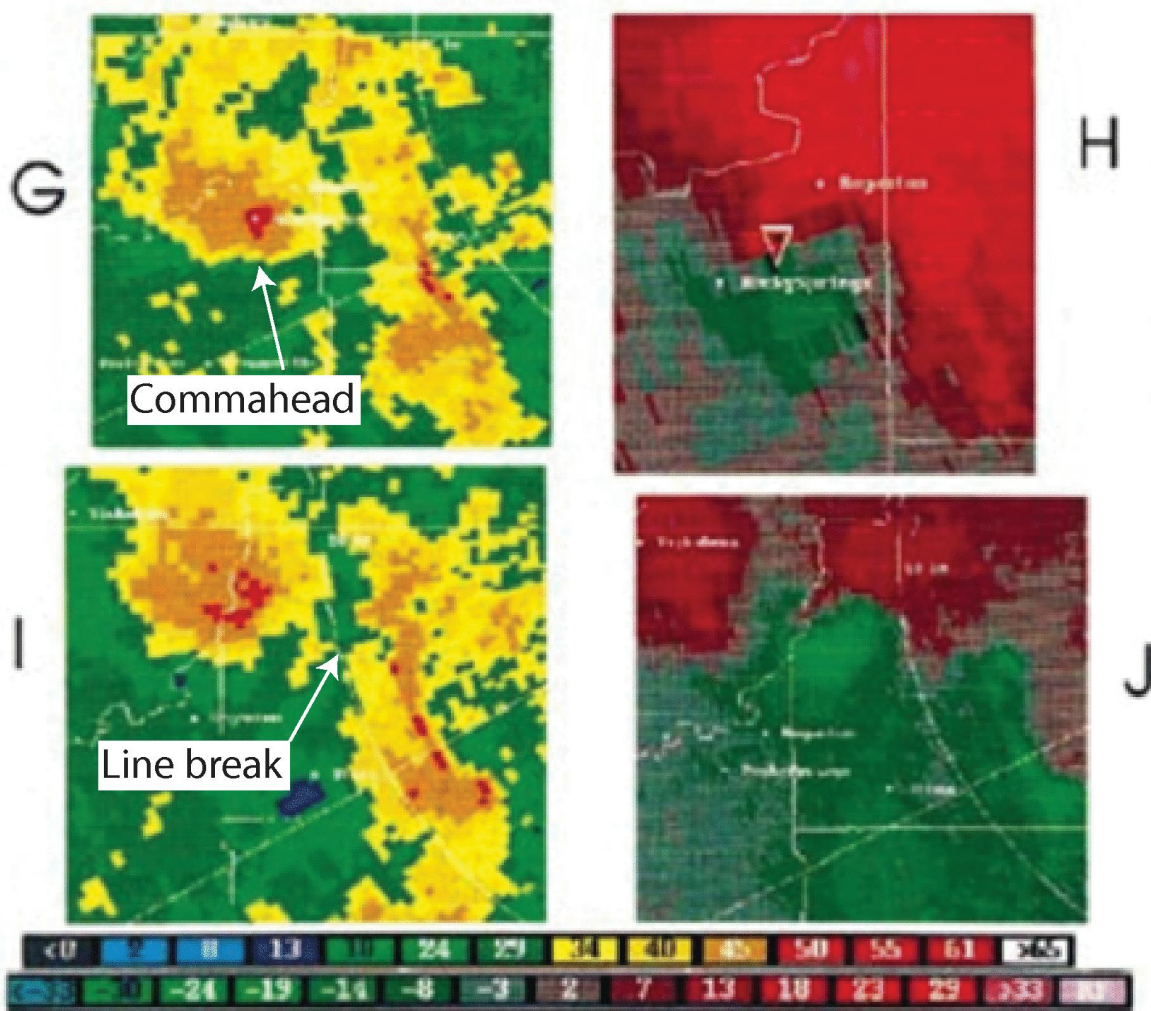


FIG. 2.12. (G) Radar reflectivity at 1952 UTC, (H) storm-relative velocity at 1952 UTC (probable tornado location indicated by red triangle), (I) radar reflectivity at 2007 UTC, and (J) radial velocity at 2007 UTC, all at the 0.5 degree elevation scan on 8 May 1995 from the Jackson, MS WSR-88D, showing a bookend vortex (adapted from Pfost and Gerard 1997 with annotations added).

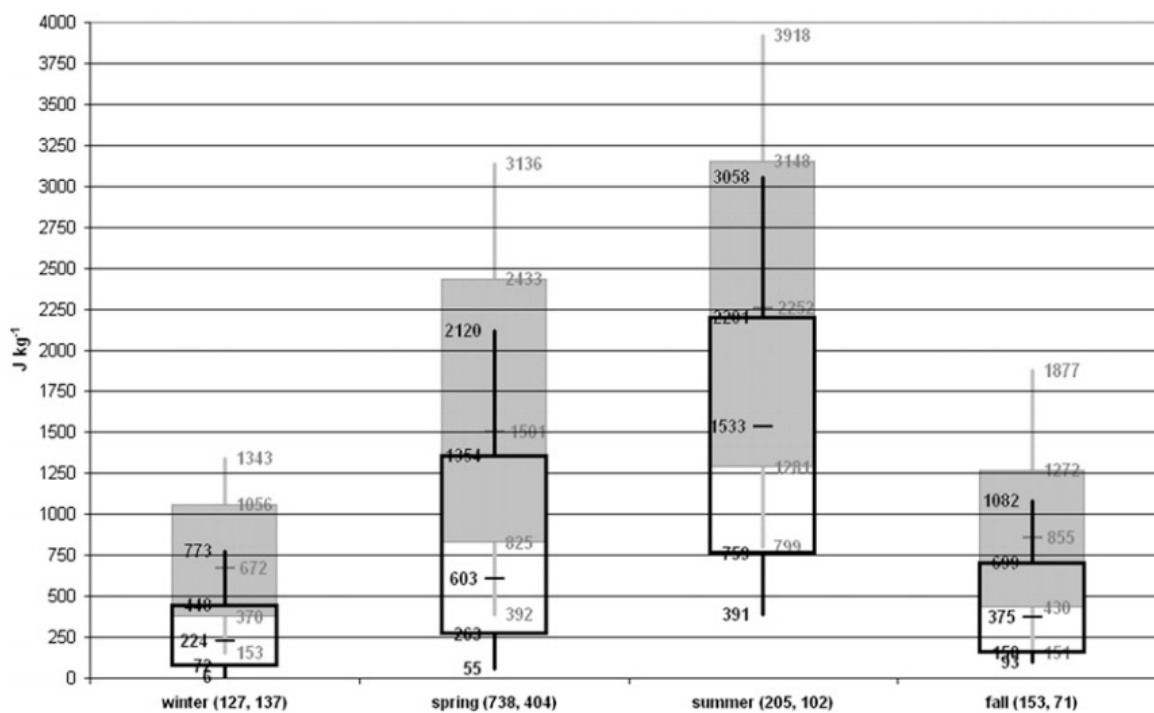


FIG. 2.13. Box-and-whiskers plot of MLCAPE by season for all right-moving supercell mesocyclones that produced EF2 or greater tornadoes (grey shading), and all QLCS mesovortices that produced EF1 or greater tornadoes (black outline), from Thompson et al. (2012). The boxes span the 25th-75th percentiles, and the whiskers extend upward to the 90th and downward to the 10th percentiles, with values for these percentiles also reported. Median values are marked within the boxes, and sample sizes for each season are shown in parentheses.

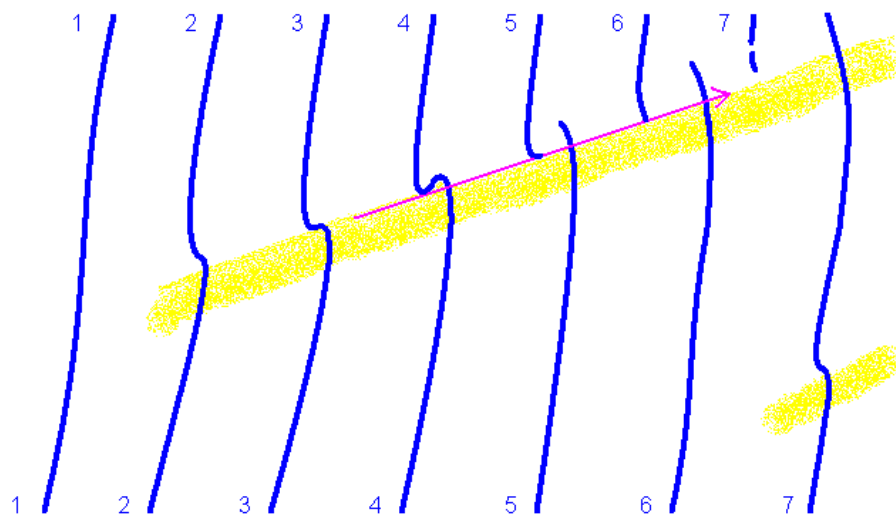


FIG. 2.14. Conceptual model of a broken-S radar signature, courtesy of the NWS Greenville-Spartanburg, SC WFO. The blue line represents radar reflectivity greater than 40 dBZ in a QLCS, plotted every 5 min. The yellow band represents the likely swath of wind damage. The magenta arrow indicates when it is hypothesized that the tornado is likely to occur. At time 7, a second possible location for a broken-S to begin to develop is also shown.

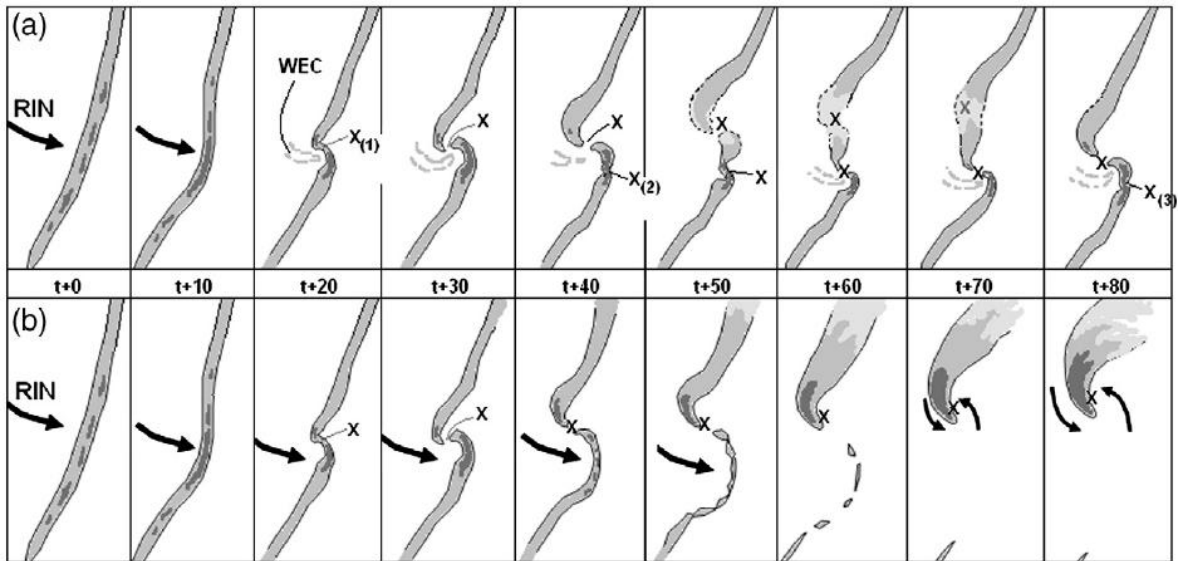


FIG. 2.16. Conceptual model of radar reflectivity associated with different broken-S signature evolutions as discussed in the text, from Clark (2011). ‘X’ denotes the location of vortices. Darker shading represents higher radar reflectivity values. ‘RIN’ and large bold arrows denote the location of the primary rear inflow notch. ‘WEC’ and the dashed grey lines denote the location of smaller weak echo channels associated with individual vortices.

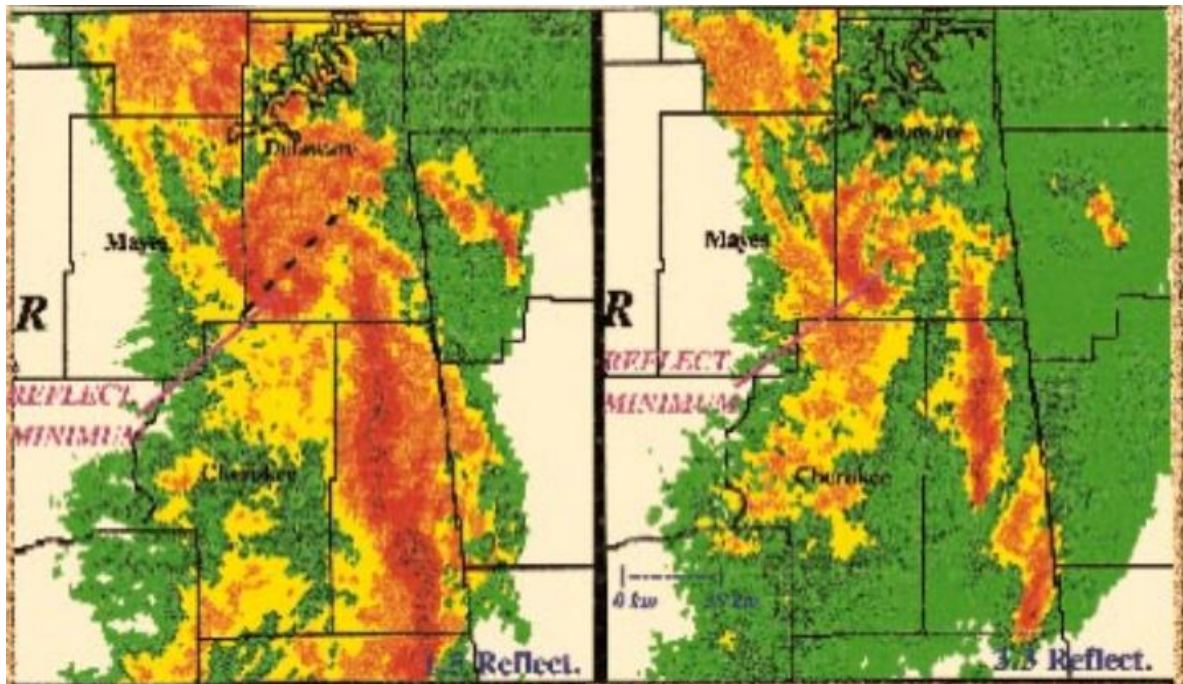


FIG. 2.17. Radar reflectivity at the 1.5 degree (left panel) and 3.3 degree (right panel) elevation scans at 0455 UTC on 17 April 1995 from the Inola, OK WSR-88D for a HP supercell commahead tornado case (from Wolf 1998).

Chapter 3

Data and Methods

3.1 Spatiotemporal Domain

The domain of this study encompasses 11 CWAs in the Southeast and Mid-Atlantic states, including portions of northern Alabama, extreme southern Tennessee, Georgia, the Carolinas, Virginia, extreme southeastern West Virginia, and Maryland. The specific WFOs that are included in this study and their respective CWAs are displayed in Fig. 3.1. These WFOs collaborated throughout this study as a part of the NWS Collaborative Science, Technology, and Applied Research (CSTAR) program. Forecasters at these WFOs identified 107 potential HSLC severe weather cases between January 2006 and April 2011 through comparison of storm reports from *Storm Data*³ with visual inspection of CAPE and shear fields in the national sector view of the Storm Prediction Center's (SPC's) mesoanalysis archive. While HSLC tornadoes can occur with landfalling tropical cyclones, these cases were omitted from the dataset, as tropical cyclone tornadoes have received much more attention in the literature (e.g. McCaul 1991 and 1993, McCaul and Weisman 1996, Schneider and Sharp 2007, Edwards et al. 2012) compared to HSLC tornadoes associated with mid-latitude systems. Table 3.1 lists the cases⁴ used in this study, including 31 tornadic vortex cases and 43 non-tornadic vortex cases (see section 3.2 and 3.3 for details of which vortices were included). Only one case had more than ten vortices, and many days had five vortices or less (see section 3.3 for a description of how these vortices were tracked), suggesting that an individual case should not over-influence the results. 24 of the cases were common to both datasets. Therefore, the null dataset includes some days when both tornadic and non-tornadic vortices were present, suggesting that larger scale conditions were favorable for tornadoes

³ <http://www.ncdc.noaa.gov/stormevents/>

⁴ Vortices were grouped into the same case if no more than 12 h existed between tornadoes/false alarm warnings (so one case can include multiple vortices that happened on the same day).

yet some vortices were non-tornadic, such as 16 April 2011 (Table 3.1). It also includes some days when no tornadic vortices were present, which could suggest that the environment was not favorable for tornadoes, such as 11 December 2008 (Table 3.1).

3.2 Tornado and Environment Data

Tornadoes that occurred on the identified HSLC days were extracted from SPC's severe weather database, which is based on *Storm Data* and was described by Smith et al. (2012) and Thompson et al. (2012). The tornado data are subject to limitations in reporting; weak tornadoes, especially QLCS tornadoes, may go unreported (especially in less populated areas), as discussed by Smith et al. (2012), Trapp et al. (2005b), and many previous studies. Environmental data from the nearest 40 km grid point in the hourly SPC mesoanalysis data were used to determine which tornadoes on these days occurred in an HSLC environment. The SPC mesoanalysis data combines vertical environmental profiles from the Rapid Update Cycle (RUC) model⁵ with an objective analysis of surface observations, as described by Thompson et al. (2012). Tornadoes were included if SBCAPE at the nearest grid point was less than 500 J kg^{-1} and the 0-6 km bulk shear vector magnitude was greater than 18 m s^{-1} , which were our criteria for what constitutes an HSLC environment. 302 tornadoes met these criteria; other tornadoes that occurred on these days but were not in an HSLC environment were removed from the dataset. While storms and tornadoes do not undergo major transformations at these specific thresholds, they represent a convenient way of ensuring internal similarity among our population of HSLC vortices. Although the environmental data are subject to potential errors (especially in regions of strong horizontal gradients) they have been repeatedly used for such climatologies over the last decade (Thompson et al. 2012, Coniglio 2012).

In order to generate a null dataset for comparison, text data for tornado warnings issued on the HSLC days were downloaded from the Iowa Environmental Mesonet archive (<http://mesonet.agron.iastate.edu/archive/>), and CAPE and shear values at the storm location listed in the warning were determined from the SPC mesoanalysis data. The 339 tornado

⁵ The SPC mesoanalysis now uses the Rapid Refresh (RAP) model, but this transition occurred after the timeframe used in this study.

warnings that were in an HSLC environment were retained, and “false alarm” tornado warnings (i.e. those with no proximal tornado report) were determined and used to develop a population of non-tornadic HSLC storms, as will be discussed in section 3.3.

3.3 Azimuthal Shear Climatology

3.3.1 Method of Calculating Azimuthal Shear

WSR-88D Level II radar data were acquired for the HSLC cases that occurred after all of the radars used in this study had been upgraded to “super-resolution” velocity data capabilities (Wood et al. 2001) in the summer of 2008. While the physical beamwidth of the radar did not change, changes in the azimuthal sampling interval resulted in a decrease in the azimuthal spatial resolution of the outputted reflectivity and velocity products. Due to concerns regarding the inconsistency of comparing derivatives (e.g. azimuthal shear) calculated on higher resolution velocity data (azimuthal sampling interval of 0.5 degrees) with calculations performed on the previously available coarser “legacy resolution” velocity data (azimuthal sampling interval of 1.0 degree), only cases with super-resolution velocity data available were used in this study.⁶ Therefore, the time range used in this portion of the study is necessarily shorter than for the original 2006-2011 dataset (section 3.1). This portion of the study includes 151 HSLC tornadoes that occurred between fall 2008 and spring 2011. The radar data were initially processed using the Warning Decision Support System-Integrated Information (WDSS-II; Lakshmanan et al. 2007) application. Automated WDSS-II algorithms were used to attempt to remove non-meteorological echoes from the radar reflectivity data and dealias the radial velocity data.⁷

Azimuthal shear was calculated by WDSS-II using the two-dimensional local, linear least squares derivative (LLSD) technique developed by Smith and Elmore (2004). Traditional azimuthal shear calculations (“peak-to-peak” shear) only use velocity data from

⁶ Archived super-resolution Level II data were not available for two radars that cover our domain during portions of period of study, at Robins Air Force Base (AFB), GA (KJGX) and Columbus AFB, MS (KGWX), and so data from these Department of Defense-operated radars were not included if super-resolution data were not available, and the next closest radar to the storm was used. Additionally, several other WSR-88D radars that cover our domain, also at air force bases, were not used because only Level III archived data were available.

⁷ The dealiasing algorithm used hourly RUC point soundings in order to determine the background wind profile, which aids the algorithm.

two points, taking the difference in radial velocity between the two velocity peaks and dividing by the distance between them, the vortex diameter. In contrast, velocity data from multiple points are used in the LLSD calculation. According to Smith and Elmore (2004) and Newman et al. (2013), this makes the LLSD technique more tolerant of noisy data and less dependent on the azimuthal offset of the vortex relative to the radar beam (but still dependent on range from the radar, as will be discussed in the next paragraph). Conceptually, the LLSD technique fits a two-dimensional surface to the velocity field using the least squares method; the slope of this surface is the azimuthal shear (velocity gradient). The LLSD technique results in some smoothing of the velocity data, so Newman et al. (2013) suggested that LLSD azimuthal shear is most useful for detecting mesocyclone-scale circulations (the purpose of this study) and large tornadoes rather than small tornadoes (which usually cannot be resolved anyway unless they occur very close to the radar).

Due to radar sampling limitations, observed azimuthal shear for two identical vortices will be lower for the vortex that is farther from the radar, if there is no variation in azimuthal shear with height (Newman et al. 2013). This is due to the widening of the radar beam with range, which results in averaging of the returned velocities across a larger area (beam filling), and smoothing of the azimuthal shear field (Fig. 3.2). Fig. 3.3 shows an increase in radar-observed vortex diameter (calculated by a WDSS-II algorithm as the distance between peak inbound and outbound velocities within a 3 km azimuthal radius of the vortex center) with range. There are few vortices with diameters < 3 km observed more than 100 km away from the radar in this plot. This range dependence means that strong rotation far from the radar may have smaller observed azimuthal shear values than weaker rotation close to the radar. An additional factor that can cause range dependence in azimuthal shear is the increase in height of the radar beam with range (Fig 3.2). This means that the lowest radar elevation scan may overshoot rotation occurring at low levels, which could especially be a problem for shallow HSLC vortices. The radar may also detect strong rotation aloft that is not present at low-levels.

Once a polar, gridded azimuthal shear field was generated in WDSS-II, it was interpolated in WDSS-II (using the Cressman scheme) onto a 0.005 degree latitude by 0.005 degree longitude Cartesian grid, which is approximately 0.5 km by 0.5 km. An example of radial velocity and LLSD azimuthal shear for a vortex is shown in Fig. 3.4. The maximum LLSD azimuthal shear for the vortex in this figure is 0.022 s^{-1} , while the maximum traditional peak-to-peak azimuthal shear, calculated as ΔV divided by the vortex diameter, would be 0.046 s^{-1} . While in this case, an unusually strong, well-sampled vortex, the peak-to-peak azimuthal shear is greater than the LLSD azimuthal shear, LLSD azimuthal shear is overall a more robust calculation. Unless otherwise noted, hereafter the use of the term “azimuthal shear” will refer to azimuthal shear calculated using the LLSD method.

3.3.2 Vortex Tracking

Using this azimuthal shear field, both tornadic and non-tornadic supercell mesocyclones and QLCS mesovortices (hereafter collectively referred to as “vortices”) were tracked. Tornadic vortices were initially tracked using the tornado touchdown points as a starting point. Some vortices could potentially produce multiple tornadoes. Only the vortex track associated with the first tornado produced by the vortex was included in further analysis, as operationally it is most useful to know when to first issue a warning on a storm (if a tornado has already occurred a forecaster will typically continue issuing warnings for the storm unless rotation substantially weakens). Non-tornadic vortices were identified by tracking vortices associated with the initial points of tornado warnings; if no tornadoes were reported within a 0.5 degree latitude by 0.5 degree longitude (~50 km by 50 km) box centered on each tracked position of the vortex, within one hour, that vortex was labeled a non-tornadic vortex (associated with an unverified tornado warning). This method does likely eliminate some false alarm warnings in cases where a non-tornadic vortex tracked in close proximity to a tornado from a different vortex. However, it helps to account for small spatiotemporal errors in the tornado database by removing tornado warnings that occurred in proximity to a tornado track. It also removes warnings issued for a vortex that was tornadic at other stages during its lifetime. While it would be operationally useful to know whether or

not a tornado warning should be continued on a previously tornadic storm, we decided that it was most important to discriminate vortices that were tornadic at one time from vortices that were never tornadic at any time.

There are some limitations in using false alarm tornado warnings as a method for developing a null dataset. Warning strategies can vary from WFO to WFO, forecaster to forecaster, and based on how many storms of interest are present. However, it appears that there is no more optimal, realistic way to determine a null dataset⁸, as by definition a null event did not have significant impacts on life or property. Therefore, no comprehensive record of their occurrence is kept. The advantage of using false alarm tornado warnings is that they indicate a storm that appeared to be capable of producing a tornado. It is unlikely that this method would miss strong non-tornadic vortices, and also unlikely that many obviously non-threatening vortices would be included. It also provides operational benefit, with potential to see why some warnings did not verify (without having to include every single possible weak vortex). Finally, these warnings are only used as a *starting point* to know where to search for a vortex, which is then found and tracked using a more objective method.

In rare cases, small (≤ 15 min) manual corrections were made to the time of the tornado if identifiable rotation was not located near the tornado location at the reported time of the tornado, but clearly moved over the tornado location at a different time. One tornado was removed from this study as no areas of rotation or convective storms were present anywhere near the tornado on that day. In the case of tornado warnings, small corrections were made to the initial position of the vortex in a few cases if azimuthal shear could not be found at the time of the warning, but could be found within one or two volume scans in time, and within the area of the warning polygon. If multiple vortices were present at the time of the warning in close proximity to each other, the strongest vortex within the warning polygon

⁸ One could use the Mesocyclone Detection Algorithm (MDA; Stumpf et al. 1998), but this algorithm can be plagued by numerous false detections, and may not detect all vortices of interest. Searching for azimuthal shear maxima above a certain threshold is problematic but large azimuthal shear values can result from gust fronts and noisy velocity data. Manual identification of non-tornadic vortices through study of hours and days of radar loops also does not appear feasible and is still subjective.

at the time of the warning was chosen manually. Clearly one cannot explicitly determine which vortex the forecaster meant to issue the warning for, so this seemed to be the best choice, and in most cases it was clear which vortex the warning was being issued for.

Once identified, vortices were tracked by their local maximum in azimuthal shear for any radar elevation scan in the 0-2 km MSL layer. This layer was used (rather than only using the radar base scan) in order to potentially track vortices before they developed substantial rotation at the lowest elevation scan. The vortex position was initially found by searching for the location of the maximum in azimuthal shear within a 0.1 degree latitude by 0.1 degree longitude square centered on the tornado touchdown point (for tornadic vortices) or the storm location listed in the tornado warning (for non-tornadic vortices). This search was performed on the closest radar's volume scan that immediately preceded the tornado touchdown time/false alarm warning issuance time. If azimuthal shear values of at least 0.006 s^{-1} (a subjectively determined noise threshold that is similar to thresholds used in Newman et al. 2013) could not be found within this box, the vortex was not considered further.

Provided its azimuthal shear was \geq the 0.006 s^{-1} threshold, each vortex was tracked backwards and forwards in time by an objective tracking algorithm that was developed for this study. This process is summarized by the flow chart in Fig. 3.5. The basic philosophy behind this tracking method is to extrapolate the vortex position from an estimated vortex motion, but then search for the actual vortex position within a search radius defined by an estimate of the uncertainty associated with the vortex motion estimate. It incorporates information from the pre-existing operational mesocyclone detection and storm tracking algorithms⁹ to narrow the search radius when possible. However, it also is flexible in order to account for cases that may not trigger these algorithms, or for cases in which using the algorithms alone does not give an accurate track.

Initially, the vortex is tracked backward in time, via an iterative process. A first guess position of the vortex during the previous volume scan is estimated based on the inferred

⁹ Algorithm text data were downloaded from the NCDC Severe Weather Data Inventory at <http://www.ncdc.noaa.gov/swdiws>.

vortex motion. The inferred vortex motion over the first two backward timesteps is initially taken to be the storm motion vector associated with the nearest storm to the vortex, based on output from the WSR-88D Storm Cell Identification and Tracking (SCIT) algorithm (Johnson et al. 1998). Later on in the process, after three vortex positions have been determined, an extrapolation of the three previously found vortex positions is used instead. Using the estimated vortex motion, the position of the vortex is predicted, and then an azimuthal shear maximum is sought within a search radius defined by the typical uncertainty in the vortex motion vector (Fig. 3.6). This motion vector uncertainty was chosen as 18 m s^{-1} over the first three points of the vortex track and 9 m s^{-1} for the remainder of the points, corresponding to four and two standard deviations, respectively, of vortex motion errors calculated for a few test cases. For a typical volume scan time of 5 min, this corresponds to a search radius of 5.4 km over the first three points of the vortex track, and 2.7 km for the rest.

If a mesocyclone detected by the Mesocyclone Detection Algorithm (MDA; Stump et al. 1998) could be found within this search radius¹⁰, the azimuthal shear maximum was searched for within a smaller search radius centered on the MDA-detected mesocyclone's position. Also, if a mesocyclone with the same identification code is found by the MDA within the search radius for at least two consecutive volume scans (since the MDA is sometimes able to track vortices), its position is automatically used rather than searching for an azimuthal shear maximum. Once an azimuthal shear maximum is found, the process repeats itself for the next volume scan back in time. The vortex is tracked backward and forward in time from its initial point in this manner until the azimuthal shear maximum falls below the threshold value of 0.006 s^{-1} . Vortices were only tracked using one radar, the closest radar at the time of the tornado/false alarm warning. Though it is possible that a vortex could move closer to a different radar over the course of the track, data from other radars were not used in order to avoid artificial changes in the azimuthal shear values over time (as the other radar would sample the storm at a different range).

¹⁰ If multiple MDA-detected mesocyclones fell within the initial search radius, the closest one was used.

Once the tracking algorithm was run, all of the vortex tracks were manually checked and corrected. Most of the vortex tracks required manual correction. Azimuthal shear, radial velocity, and radar reflectivity fields at multiple elevation scans were all consulted and looped in order to visually determine what changes, if any, needed to be made to the vortex track. This could include modifying existing positions, adding new ones, or removing erroneous positions in order to ensure that the same vortex was being tracked. It was decided to err on the side of continuing a vortex track rather than prematurely terminating it. It is possible that in some cases one vortex may have dissipated and another reformed between volume scans, but that is the limitation of the temporal resolution (typically 4-5 min) of the operational radar data. For supercells undergoing cyclic mesocyclogenesis (Lemon and Doswell 1979, Adlerman et al. 1999) a vortex track was continued if it was clear that the new mesocyclone was associated with the same supercell updraft (based on consultation of volumetric radar reflectivity data). If the vortex was a QLCS mesovortex, there was less tolerance of discontinuities in the vortex track. In some cases, it could be difficult to determine whether a small discontinuity in the track represented a different nearby vortex or an actual “wobble” in one vortex’s track.

Although the use of azimuthal shear is the basis of the tracking procedure, several situations required more subjective judgment. For example, a gust front often appears as a linear azimuthal shear feature (Fig. 3.7), within which cyclonic rotation associated with embedded vortices appears as a local maximum (Fig. 3.8). If there was a clear localized maximum in azimuthal shear and/or rotation present in radial velocity data (a localized area of enhanced velocities), the vortex track was continued after consulting multiple elevation scans. If not, the vortex track was discontinued (even if the gust front had azimuthal shear \geq the 0.006 s^{-1} azimuthal shear threshold). Also, on occasion, storms moved through the ring of missing (range-folded) velocity data just beyond a radar’s maximum unambiguous range. This missing velocity data contaminates the associated azimuthal shear field. If a vortex could be subjectively tracked before and after the area of range folding, the track was continued even if azimuthal shear fell below threshold in the region of missing velocities.

The range-folded vortex positions were flagged and azimuthal shear values were then set to missing for subsequent analysis.

Once a vortex track was manually corrected, the maximum positive (cyclonic) azimuthal shear value within a 0.04 degree latitude by 0.04 degree longitude (i.e. approximately 4 km by 4 km) search box centered on the vortex position was recorded. For higher radar elevation scans, the vortex position was often downstream from the position found in the 0-2 km MSL layer, due to movement of the storm during the volume scan and possible tilt of the vortex with height. Therefore, the vortex positions (that determine the location of the search box) used for recording azimuthal shear values at the higher tilts were determined using a linear interpolation between the vortex position at the current volume scan and the next volume scan. If no velocity data and/or cyclonic azimuthal shear were present within the search box for a given elevation scan at a given time, the azimuthal shear value was set to missing for that scan. The elevation scans above the base scan were those used in the typical volume coverage pattern (VCP) used by the WSR-88D during severe convective storm situations, VCP 212¹¹. In the relatively rare cases (three tornadic and nine non-tornadic) when the WSR-88D was in a different VCP, only azimuthal shear at the base scan was recorded.

3.4 Convective Mode Identification

As a part of a large national study, SPC forecasters subjectively assigned convective modes to most tornadoes (and significant severe wind and hail reports), as explained by Smith et al. (2012). Tornadoes were filtered such that a convective mode was only assigned to the tornado of strongest magnitude (strongest EF scale rating) within a 40 km SPC mesoanalysis grid box per hour. The Smith et al. (2012) convective mode identification was based on study of radar reflectivity and velocity images from individual radars at the lowest radar tilt, using information from higher elevation scans only when necessary. Storms associated with each tornado were classified as either supercells or non-supercells at the time of the tornado. Supercells were required to contain a mesocyclone (the criteria for which were defined by Smith et al. 2012). Both supercells and non-supercells were further classified by Smith et al.

¹¹ Elevation scans in this VCP are done at 0.5, 0.9, 1.3, 1.8, 2.4, 3.1, 4.0, 5.1, 6.4, 8.0, 10.0, 12.5, 15.6, and 19.5 degrees.

(2012) as being discrete (relatively isolated/embedded in an area of weak reflectivity), in a line, or in a cluster (storms that were neither discrete nor in an identifiable line). Non-supercell storms that were in a line that met their length criteria were identified as QLCSs, with the area of rotation likely being a QLCS mesovortex. Non-supercells *not* classified as QLCSs made up a fairly small fraction of the dataset overall, and will be hereafter be referred to as “other”. To clarify, hereafter all vortices associated with an identifiable supercell will be referred to as supercell mesocyclones, while all non-supercell vortices in a QLCS will be referred to as QLCS mesovortices.

SPC-determined convective modes were not available for the non-tornadic storms in the present study (and for any tornadoes not assigned a mode due to SPC’s filtering criteria), so these had to be manually assigned. To facilitate comparison of the convective mode distributions for the tornadic and non-tornadic vortices, the author also independently assessed convective modes for the tornadic storms. While the independently assigned convective modes followed the spirit of Smith et al. (2012), there were some differences, partly due to using an azimuthal shear-based criterion to identify mesocyclones (rather than rotational velocity as used by Smith et al. 2012). Overall, the reassessed modes agreed with the original Smith et al. (2012) modes 85% of the time, lending confidence that our tornadic and non-tornadic convective mode datasets are consistent with one another.

3.5 Assessment of Radar Signatures

Reflectivity signatures that have been previously determined to be operationally useful (e.g. sections 2.3-2.4) were documented in association with each of the tornadic and non-tornadic vortices. These are listed in Table 3.2 and described below. These signatures were subjectively identified within a window beginning 20 min before the time of the tornado/false alarm warning through 15 min afterward, with a focus on the lowest four elevation scans. While many of these signatures have been commonly observed, uniform definitions typically do not exist. The criteria used in this study were determined by looking at several examples of reflectivity features that appeared to strongly resemble these

signatures and creating criteria that these features would clearly satisfy. The individual criteria are as follows.

For supercell mesocyclones (in this section determined using the author's convective mode classification instead of SPC's), the three main signatures that were documented were the hook echo, the weak echo region (WER), and the bounded weak echo region (BWER), all fundamental features of the supercell conceptual model (Fig. 3.9; e.g. Lemon and Doswell 1979, Markowski 2002). While these features are likely present to some extent in all supercells, they may not be observed by the radar, as these features may not be resolved due to beam filling. A hook echo was defined as a noticeable appendage of 40 dBZ reflectivity on the right-rear flank of the storm, typically associated with the rear of the WER or BWER. A WER was defined as a noticeable notch of reflectivity less than 40 dBZ on the right-rear flank of the storm. Reflectivity greater than 50 dBZ in the same location at a higher elevation scan (echo overhang) was also required. If this area of weak reflectivity was a hole in 40 dBZ reflectivity, rather than a notch, then it was classified as a BWER. These signatures were assessed through the lowest four elevation scans, and it was possible for a storm to have both a WER and a BWER at the same time (e.g. a WER at the base scan and a BWER at the 0.9 and 1.3 degree elevation scans as in Fig. 3.9).

For QLCS mesovortices, several different signatures were documented. The first was a gust front cusp (Fig. 3.10), defined as an inflection point in the gust front as determined via the radial velocity field. Such a feature is typically associated with a distortion in the gust front due to the presence of a mesovortex and/or bowing occurring in one location along the gust front (see figures in Trapp and Weisman 2003). The second QLCS signature was the forward inflow notch (Fig. 3.11), defined as a noticeable indentation in the 40 dBZ contour in the front of the convective line, with vertical continuity. This signature was also likely due to a distortion of the gust front by the mesovortex. Hook-like echoes protruding from the convective line in close proximity to QLCS mesovortices were also documented (Fig. 3.12), using the same definition as supercell hook echoes (40 dBZ appendage). Finally, broken-S signatures (McAvoy et al. 2000, Lane and Moore 2006, Clark 2011) were also documented

(Fig. 3.13). They were defined as a break or near-break in the 40 dBZ convective line with vertical continuity, where the southern segment of the line surges ahead of the northern segment of the convective line.

A few more reflectivity signatures were also documented for both supercell mesocyclone and QLCS mesovortex cases. The first was the rear inflow notch (RIN; Przybylinski 1995), defined as a noticeable indentation in the 40 dBZ contour in the rear of the convective line, with vertical continuity. While RINs may be associated with a notch in the trailing stratiform region of a large bowing MCS, they can also be found in association with smaller scale bowing segments, such as those found in a line-echo wave pattern (LEWP, Nolen 1959). These were the primary types of RINs in this study, since LEWPs are common features in squall lines in cool-season dynamic patterns (Johns 1993). This feature may be associated with a RIJ in a QLCS (Przybylinski 1995; see Fig. 3.14), or the RFD with supercells embedded in QLCSs (Moller et al. 1990, Doswell et al. 1990, Funk et al. 1999, Finley et al. 2001; see Fig. 3.13). Bowing segments, defined as noticeable bow-shaped curvature in the 40 dBZ convective line, with vertical continuity, were also documented (Fig. 3.10a). Finally, comma-shaped echoes were documented (Figs. 3.14-15), which could be associated with bookend vortices (e.g. Przybylinski 1995, Pfof and Gerard 1997, Funk et al. 1999) or bowing HP supercell commahead circulations (Moller et al. 1990, Doswell et al. 1990, Przybylinski et al. 1993, Wolf 1998, Funk et al. 1999). Cell mergers were also recorded, as some correlation between these and tornadoes has been found, though the physical links remain unclear (e.g. Lemon 1976, Goodman and Knupp 1993, Finley et al. 2001, Finley et al. 2002, French and Parker 2012). Mergers were defined as the union of the 45 dBZ contour between two formerly distinct cells.

Table 3.1. List of cases used in this study (using date in UTC time of first vortex from that case), and number of tornadic and non-tornadic vortices for each case. Vortices were included in the same case if no more than 12 h existed between tornadoes/false alarm warnings. Cases highlighted in red indicate common cases between the tornadic and non-tornadic vortices.

Tornadic vortex days	Number of tornadic vortices	Non-tornadic vortex days	Number of non-tornadic vortices
10/8/2008	1	11/14/2008	1
12/10/2008	2	12/10/2008	7
12/24/2008	1	12/11/2008	7
1/6/2009	2	1/6/2009	3
2/18/2009	4	2/11/2009	2
3/27/2009	4	2/18/2009	1
3/28/2009	5	2/28/2009	2
4/10/2009	11	3/27/2009	2
4/13/2009	1	3/28/2009	5
4/19/2009	5	4/10/2009	3
5/3/2009	3	4/13/2009	4
5/6/2009	3	4/19/2009	1
5/7/2009	1	5/3/2009	1
12/2/2009 (afternoon)	2	5/6/2009	9
1/21/2010 (afternoon)	2	5/9/2009	3
3/25/2010	1	6/17/2009	1
3/28/2010 (afternoon)	4	10/30/2009	1
4/8/2010 (afternoon)	1	12/2/2009 (evening)	3
4/24/2010	1	12/2/2009 (afternoon)	3
5/3/2010	2	12/9/2009	4
9/27/2010	1	1/21/10 (evening)	1
10/25/2010	4	1/21/10 (afternoon)	1
10/26/2010 (afternoon)	3	1/25/2010	4
10/27/2010	2	3/12/2010	1
11/17/2010	1	3/28/2010 (evening)	5
11/30/2010 (afternoon)	5	3/28/10 (afternoon)	5
3/6/2011	2	4/8/2010 (evening)	3
3/10/2011	2	4/8/10 (afternoon)	3
4/4/2011	4	4/24/2010	3
4/16/2011	8	5/1/2010	2

Table 3.1 Continued

4/27/2011	7	9/27/2010	1
		10/25/2010	1
		10/26/10 (night)	1
		10/26/10 (afternoon)	3
		10/27/2010	2
		11/17/2010	1
		11/30/2010 (night)	8
		11/30/10 (afternoon)	2
		3/23/11 (evening)	5
		3/23/2011 (afternoon)	1
		4/4/2011	9
		4/16/2011	5
		4/27/2011	5

Table 3.2. List of radar reflectivity signatures documented in association with supercell mesocyclones (left) and QLCS mesovortices (right). Italicized signatures were documented for both. Criteria for the signatures are described in the text.

Supercell Reflectivity Signatures	QLCS Reflectivity Signatures
Hook Echo	Gust Front Cusp
(Bounded) Weak Echo Region-(B)WER	Forward Inflow Notch
<i>Rear Inflow Notch</i>	Hook-like Echo
<i>Comma-shaped Echo</i>	Broken-S
<i>Cell Merger</i>	<i>Rear Inflow Notch</i>
	<i>Comma-shaped Echo</i>
	<i>Cell Merger</i>

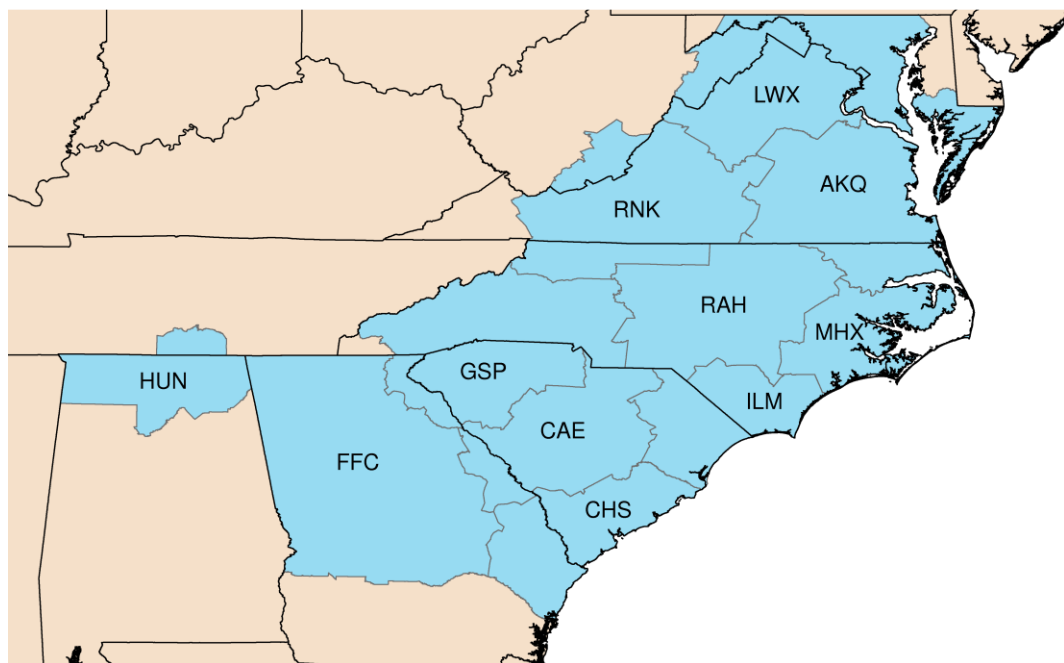


FIG. 3.1. Map of the CWAs that comprised the domain of this study: Huntsville, AL (HUN), Peachtree City, GA (FFC), Charleston, SC (CHS), Columbia, SC (CAE), Greenville-Spartanburg, SC (GSP), Wilmington, NC (ILM), Raleigh, NC (RAH), Newport/Morehead City, NC (MHX), Blacksburg, VA (RNK), Wakefield, VA (AKQ), and Baltimore/Washington (LWX).

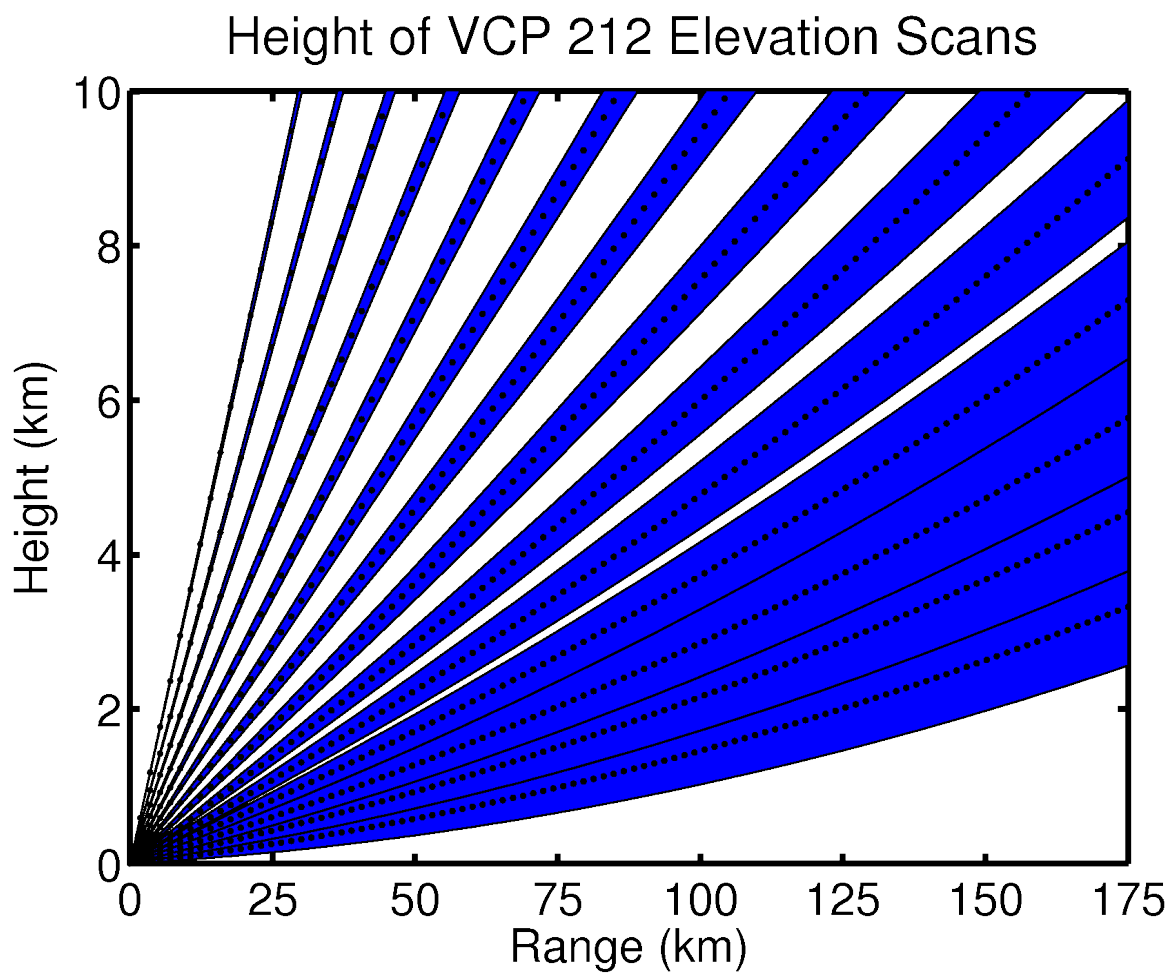


FIG. 3.2. Changes in beam height and beamwidth with range from the radar, for the elevation scans in the WSR-88D's VCP 212. Dashed lines indicate the center of the beam, with the filled region representing the width of the beam.

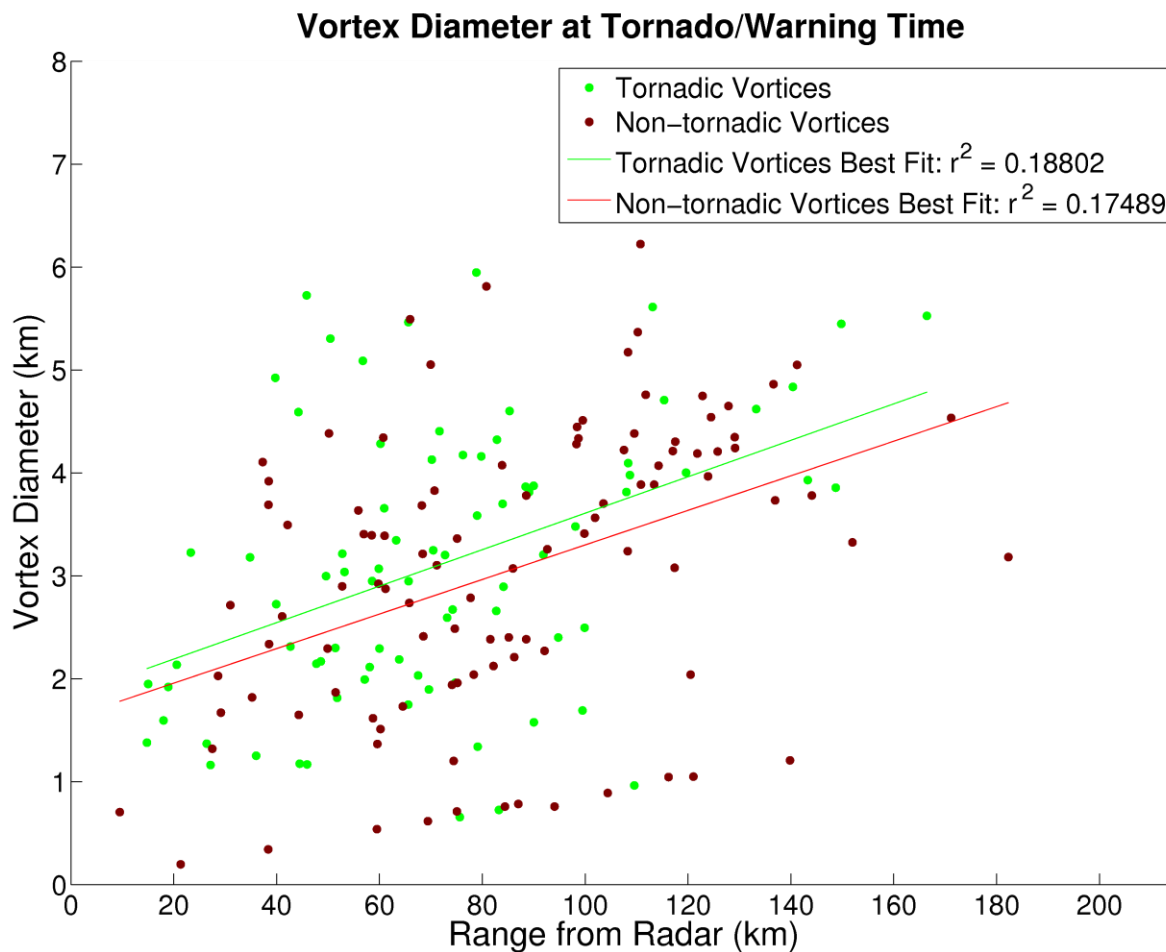


FIG. 3.3. Vortex diameter at the 0.5 degree elevation scan as a function of range from the radar for tornadic vortices (green circles) and non-tornadic vortices (red circles). Best-fit lines are also plotted using the same color convention, with correlation coefficient values reported in the legend.

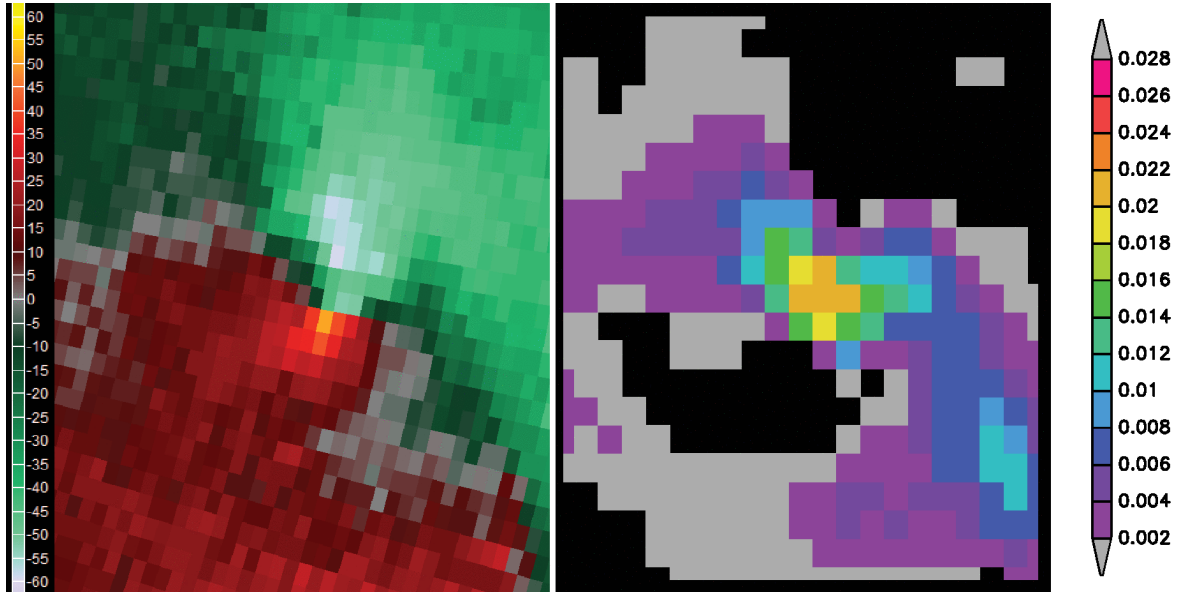


FIG. 3.4. Example plot of radial velocity (kts) and azimuthal shear (s^{-1}) for a vortex, using the same spatial scale for both. The azimuthal shear field is originally calculated on a polar grid of same resolution as the velocity data, but then interpolated to a 0.005 degree latitude by 0.005 degree longitude Cartesian grid. The radar is located west-northwest of these images.

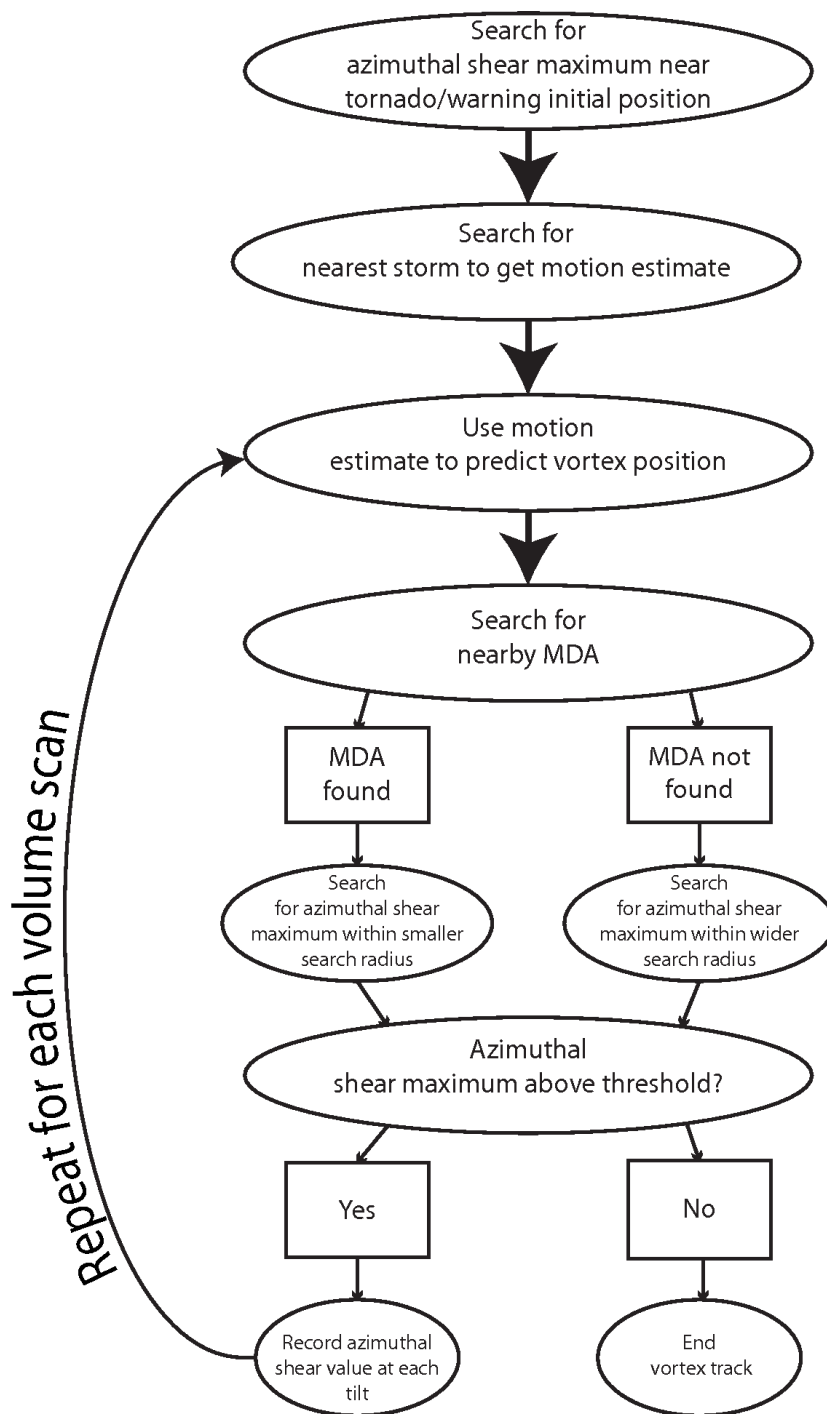


FIG. 3.5. Flow chart for the tracking algorithm that is described in the text.

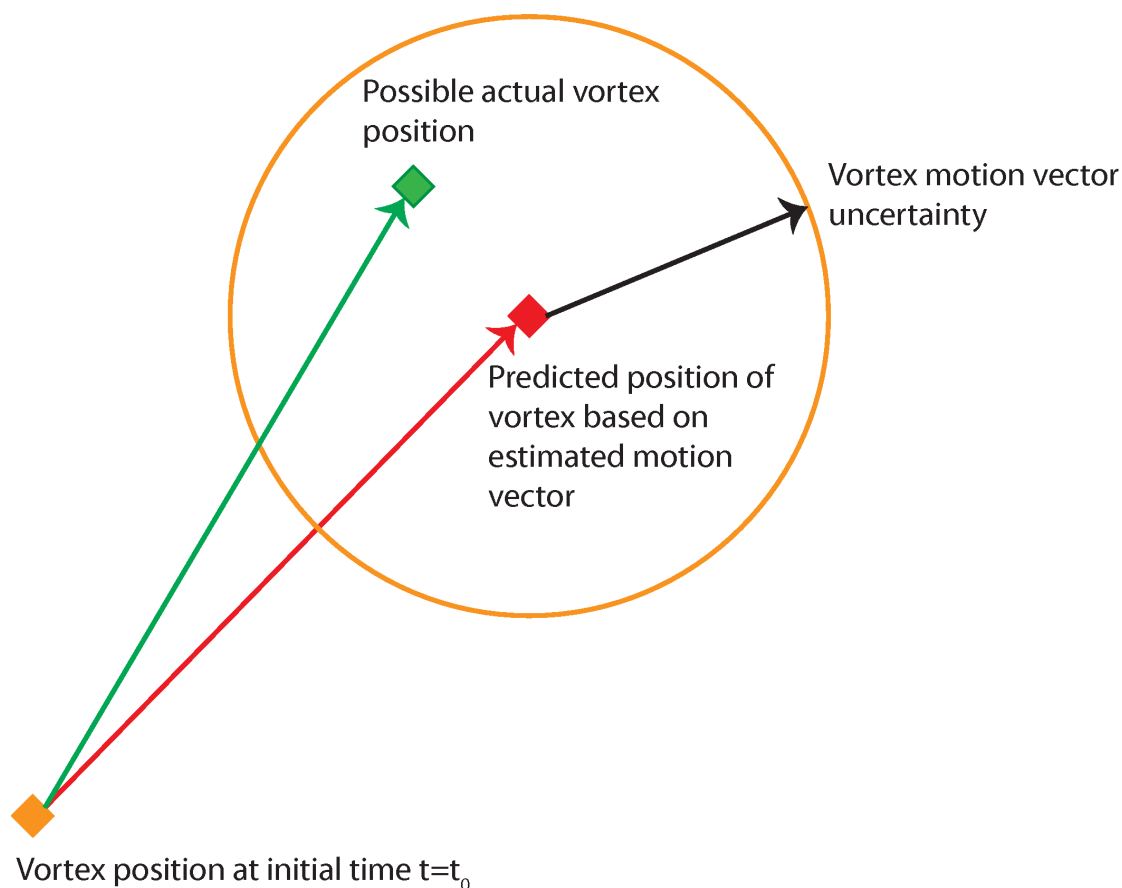


FIG. 3.6. Idealized schematic of tracking algorithm (not to scale). The vortex position, initially found by searching for an azimuthal shear maximum near the tornado touchdown/false alarm warning location, and then found iteratively by repeating the tracking process, is indicated by the orange diamond. A first guess prediction of the vortex is determined based on an estimate of vortex motion (see text for details), which is shown as the red diamond. An estimate of the uncertainty of the vortex motion vector is given by the black arrow (see text for details), which sweeps out the search radius indicated by the orange circle. The tracking algorithm searches for any MDA-detected mesocyclones within this search radius. If one is found, a smaller search radius is used centered on the MDA-detected mesocyclone's position, and if none are found it searches for the azimuthal shear maximum within this search radius (orange circle). The green diamond indicates a possible actual location for vortex.

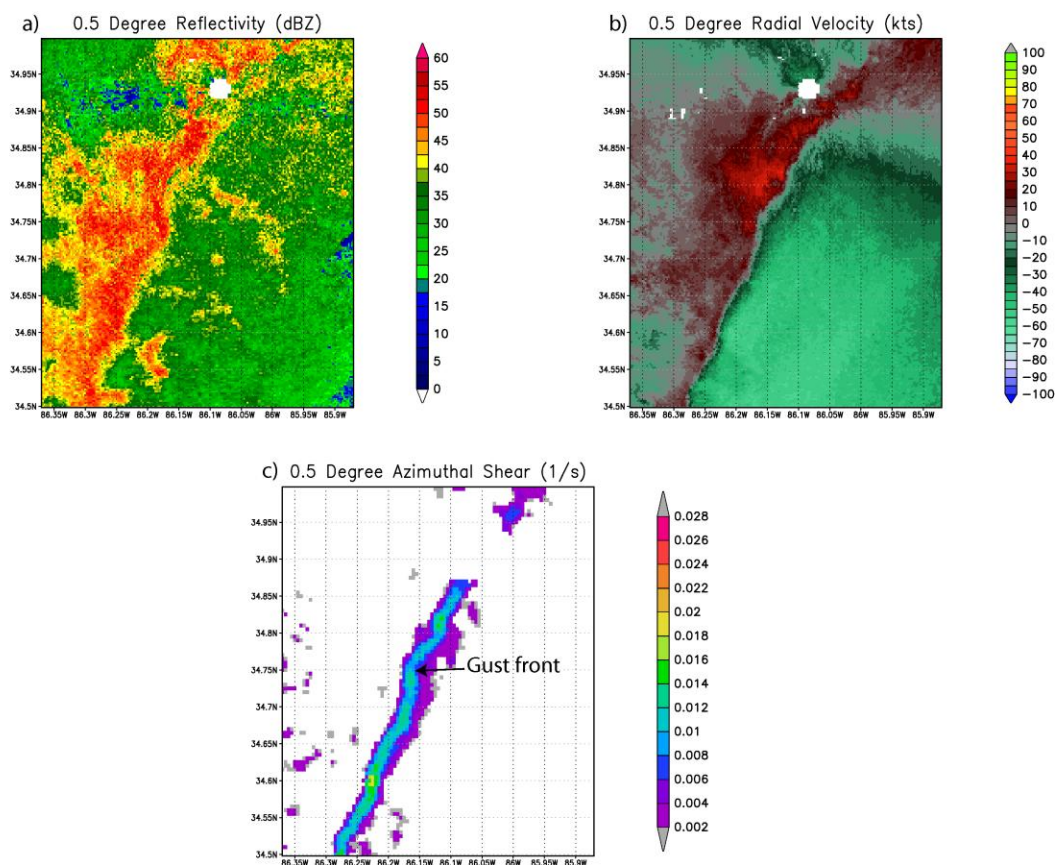


FIG. 3.7. (a) Radar reflectivity, (b) radial velocity, and (c) azimuthal shear at the 0.5 degree elevation scan of the Hytop, AL (KHTX) radar at 0649 UTC on 10 December 2008 for a gust front before the QLCS mesovortex in FIG. 3.8 formed.

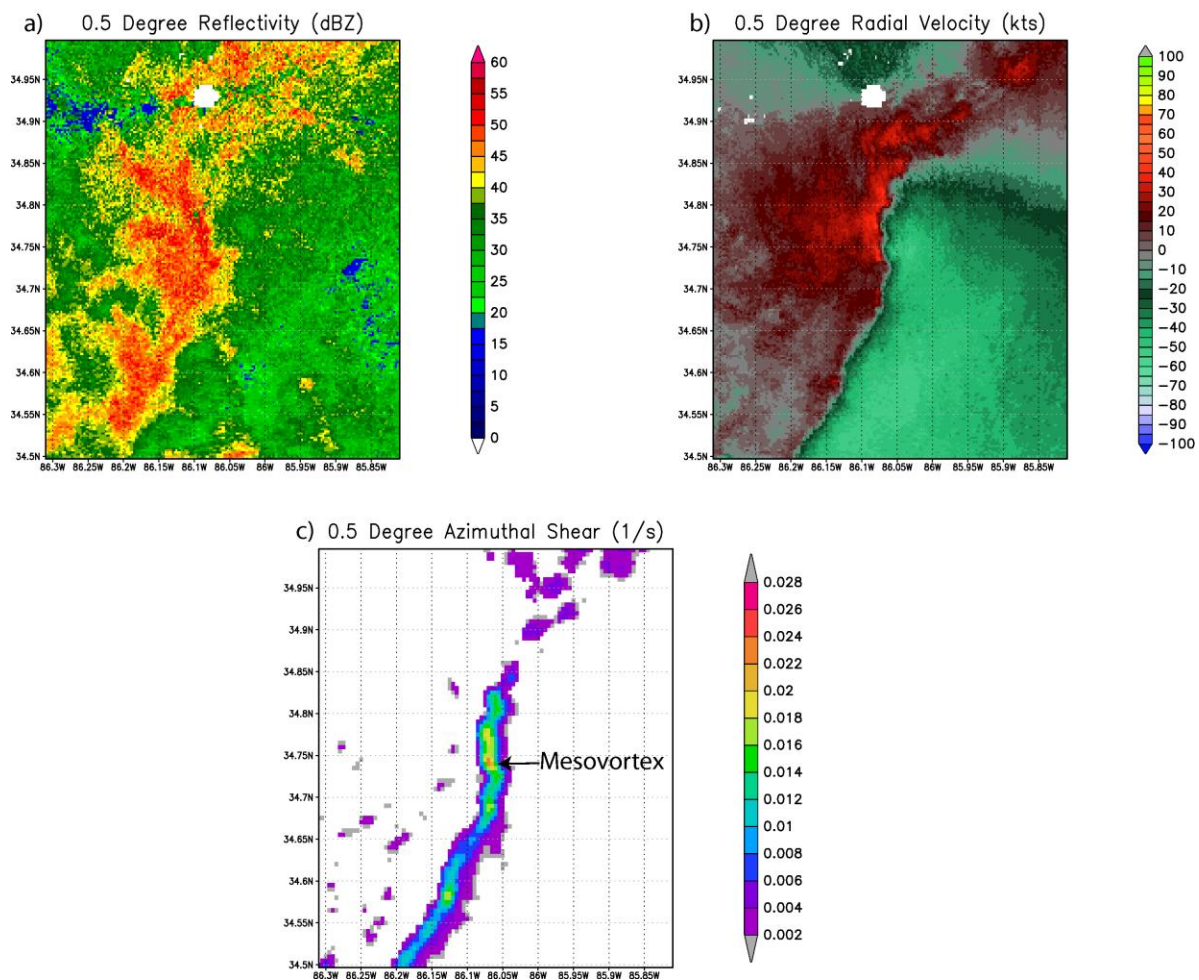


FIG. 3.8. Similar to FIG. 3.7, but at 0659 UTC for an embedded mesovortex along a gust front.

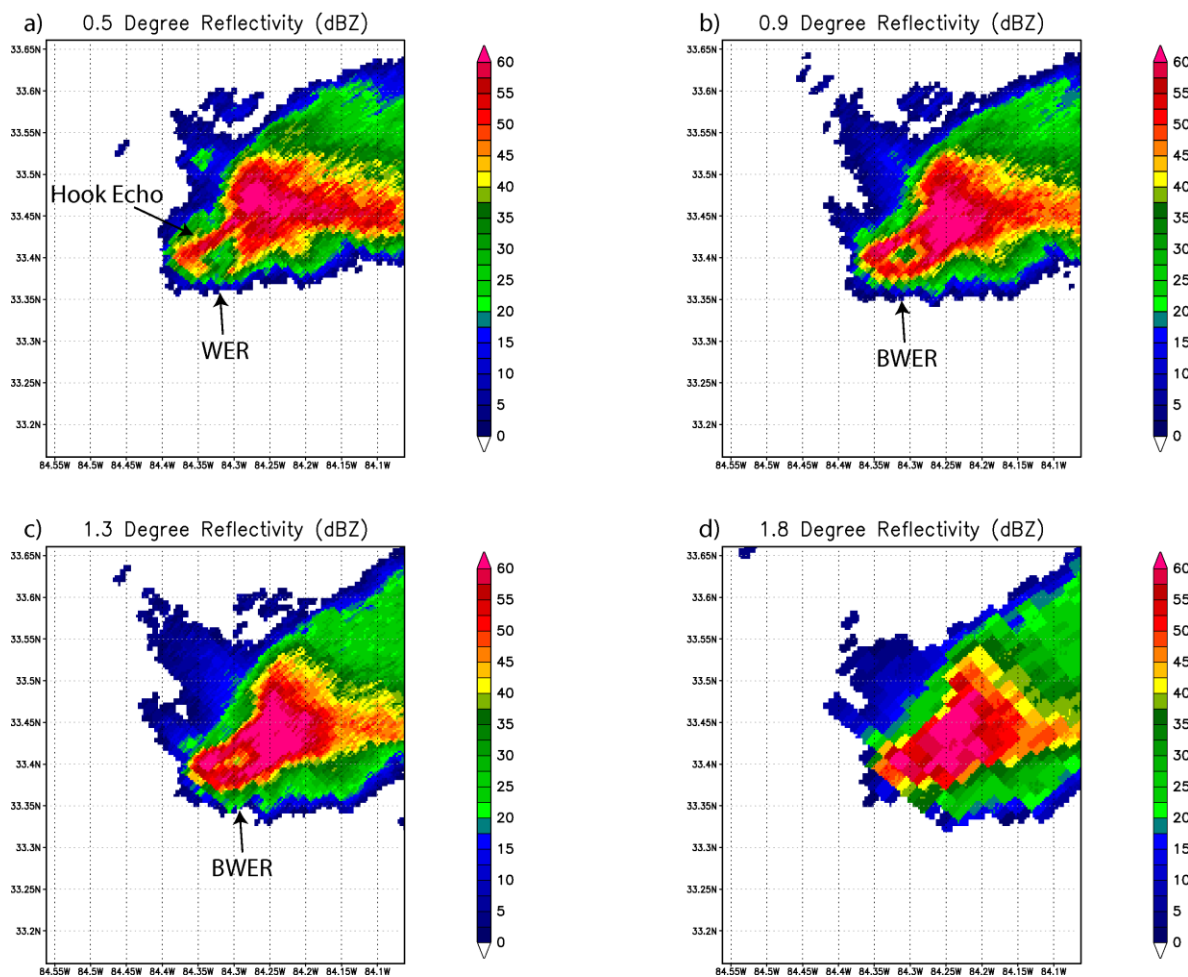


FIG. 3.9. Radar reflectivity at the (a) 0.5 degree, (b) 0.9 degree, (c) 1.3 degree, and (d) 1.8 degree elevation scans from the Robins AFB, GA (KJGX) radar at 2324 UTC on 18 February 2009, showing examples of a hook echo, WER, and BWER.

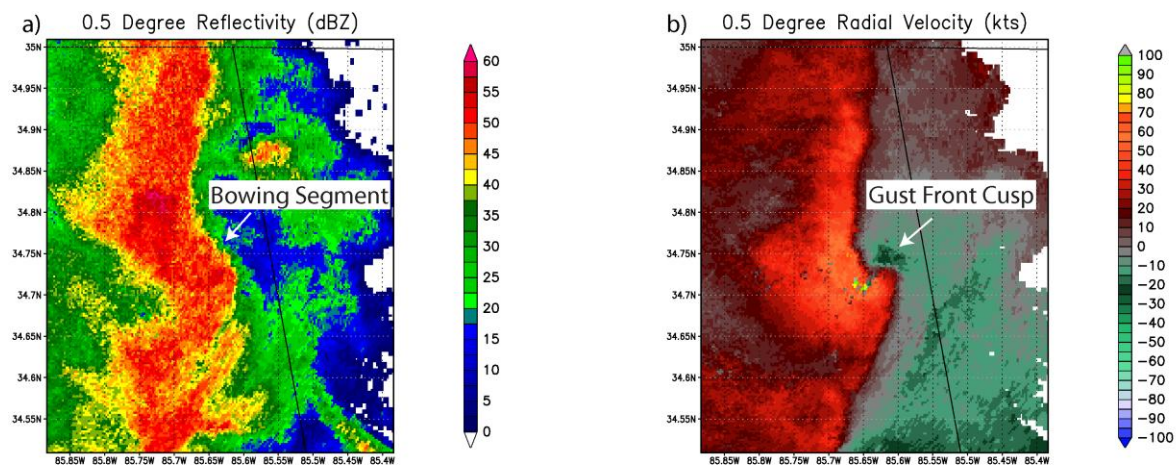


FIG. 3.10. (a) Radar reflectivity and (b) radial velocity at the 0.5 degree elevation scan from the Hytop, AL (KHTX) radar at 0917 UTC on 25 October 2010, showing an example of a bowling segment and a gust front cusp.

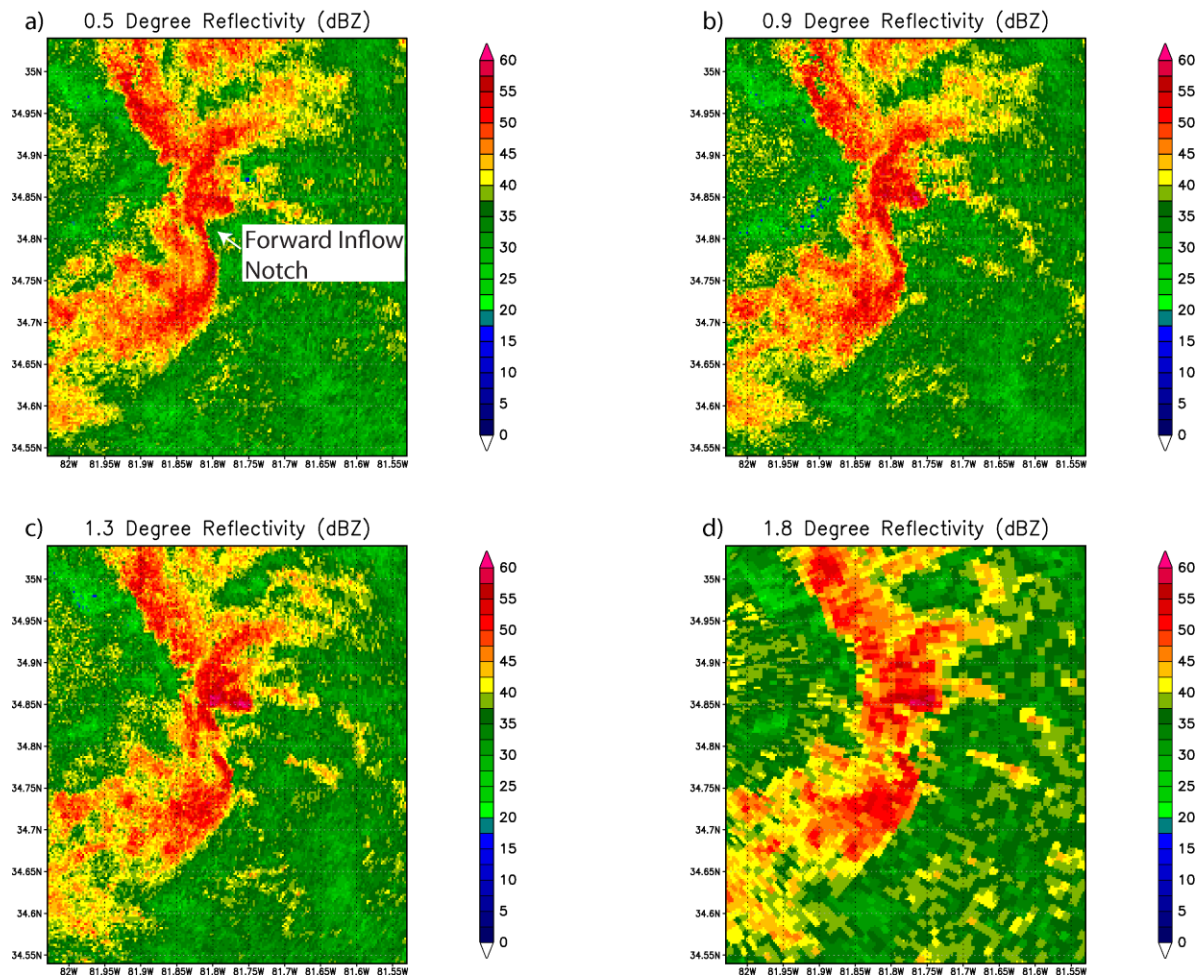


FIG. 3.11. Similar to FIG. 3.9, but from the Greer, SC (KGSP) radar at 0026 UTC on 11 April 2009, showing an example of a forward inflow notch.

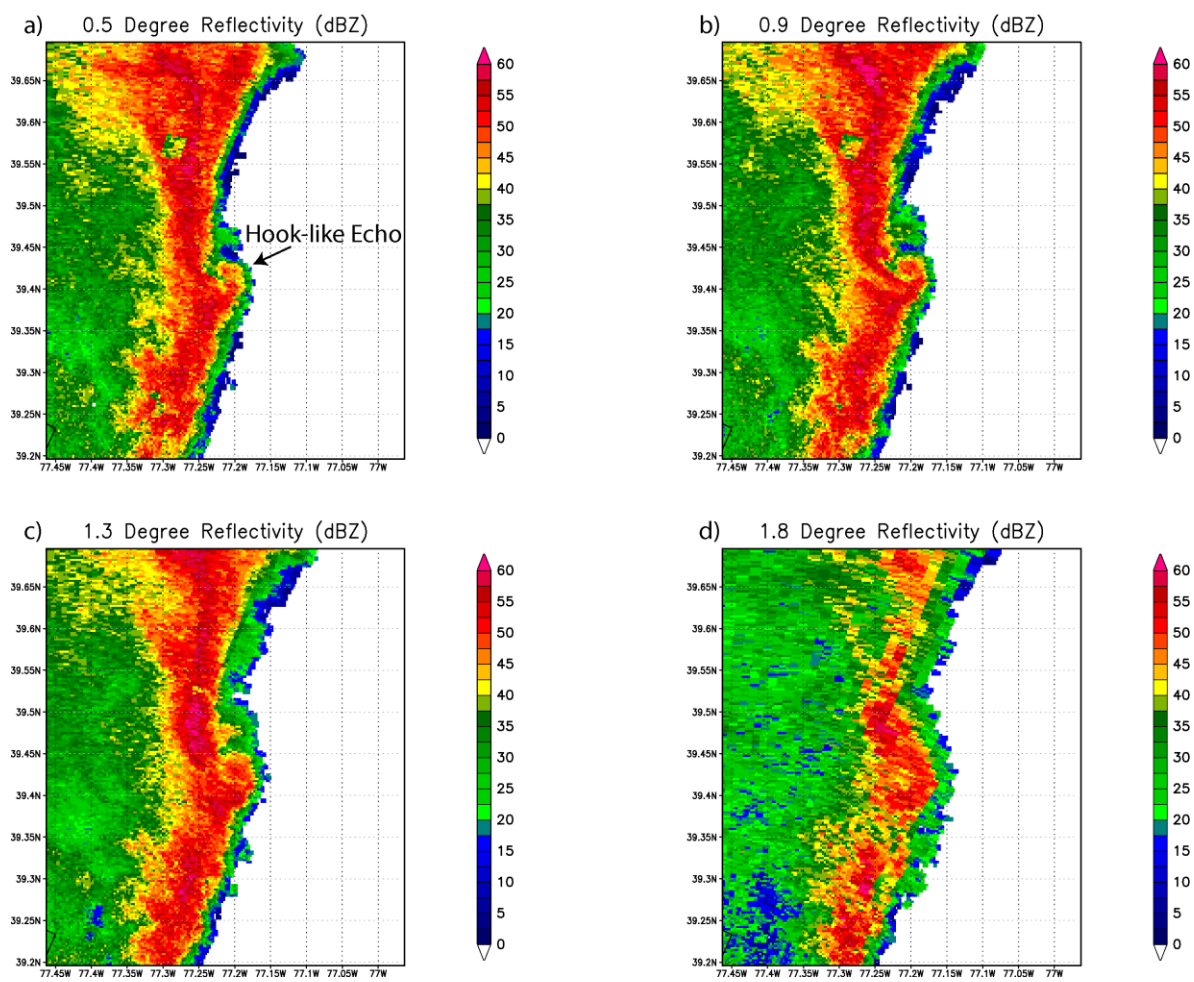


FIG. 3.12. Similar to FIG. 3.9, but from the Sterling, VA (KLWX) radar at 2341 UTC on 16 April 2011, showing an example of a hook-like echo associated with a QLCS mesovortex.

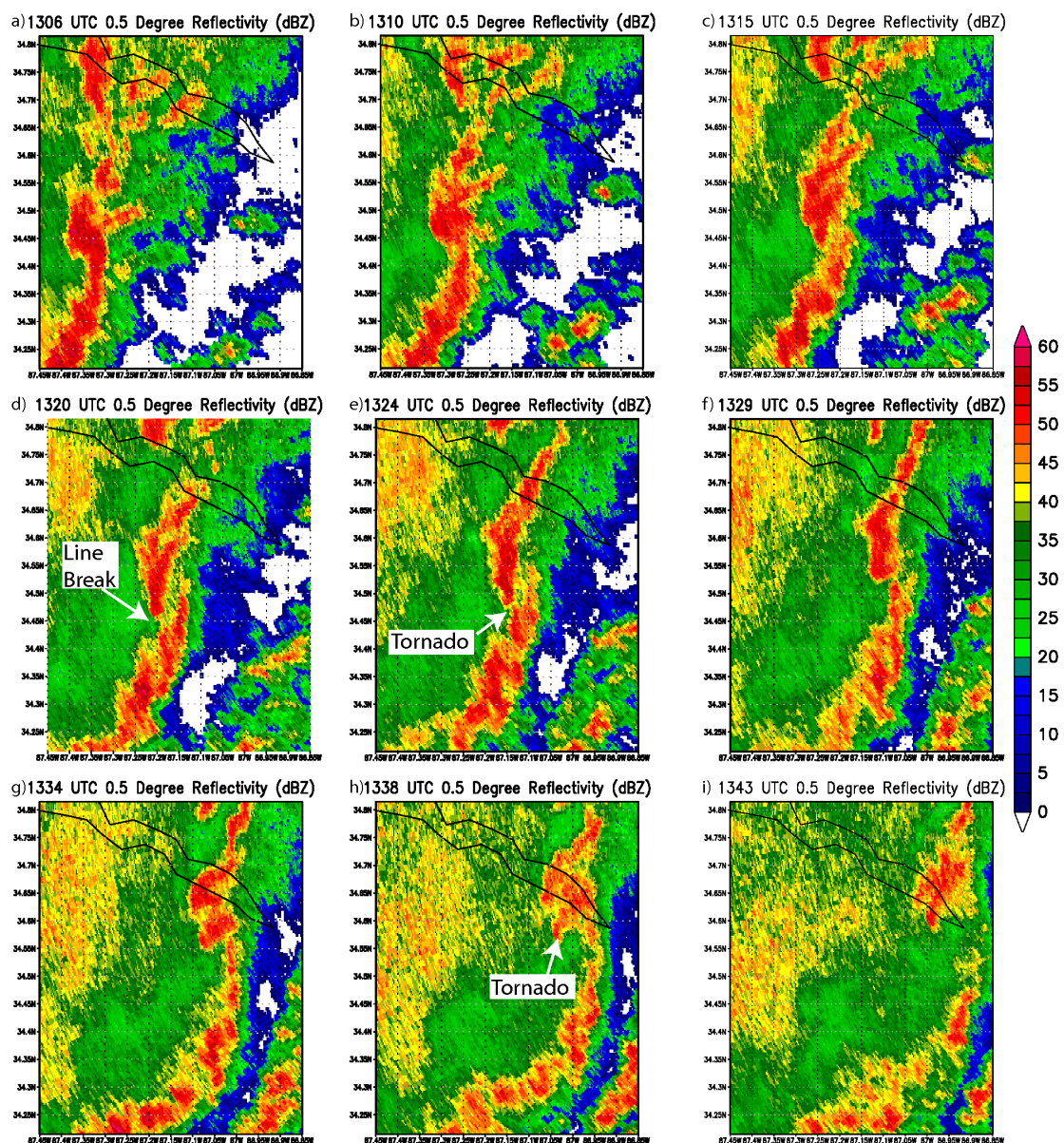


FIG. 3.13. Radar reflectivity at the 0.5 degree elevation scan from the Hytop, AL WSR-88D on 6 May 2009 at (a) 1306, (b) 1310, (c) 1315, (d) 1320, (e) 1324, (f) 1329, (g) 1334, (h) 1338, and (i) 1343 UTC, showing the time evolution of a broken-S signature. The line break at the base scan occurs at 1320 UTC (panel d). Tornadoes occurred at 1325 UTC (after panel e), 1342 UTC (before panel i), and 1359 UTC (not shown). This broken-S signature fell in the 60-100 km range bin.

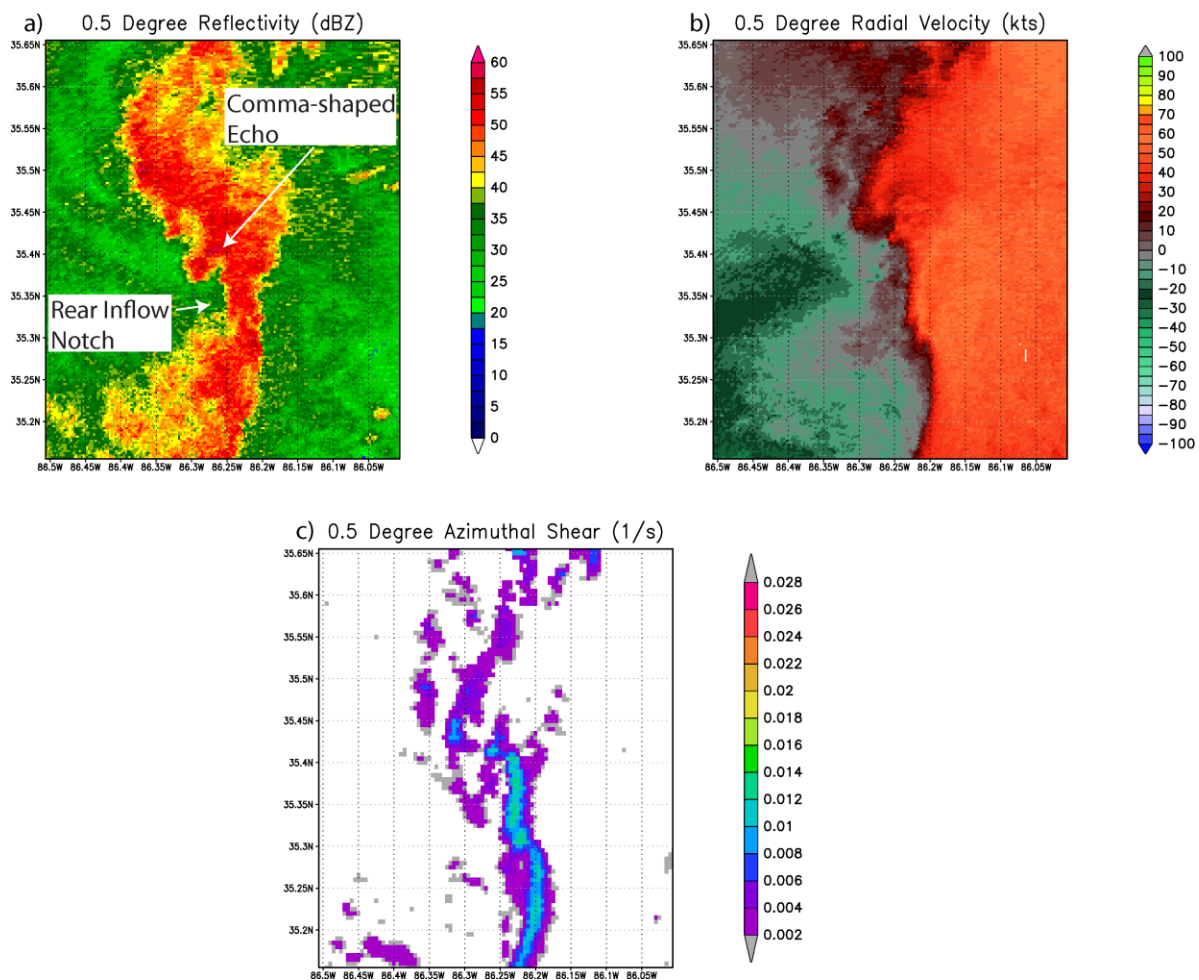


FIG. 3.14. Similar to FIG. 3.7, but from the Hytop, AL (KHTX) radar at 1116 UTC on 27 April 2011 showing an example of a QLCS mesovortex associated with a comma-shaped echo and a RIN.

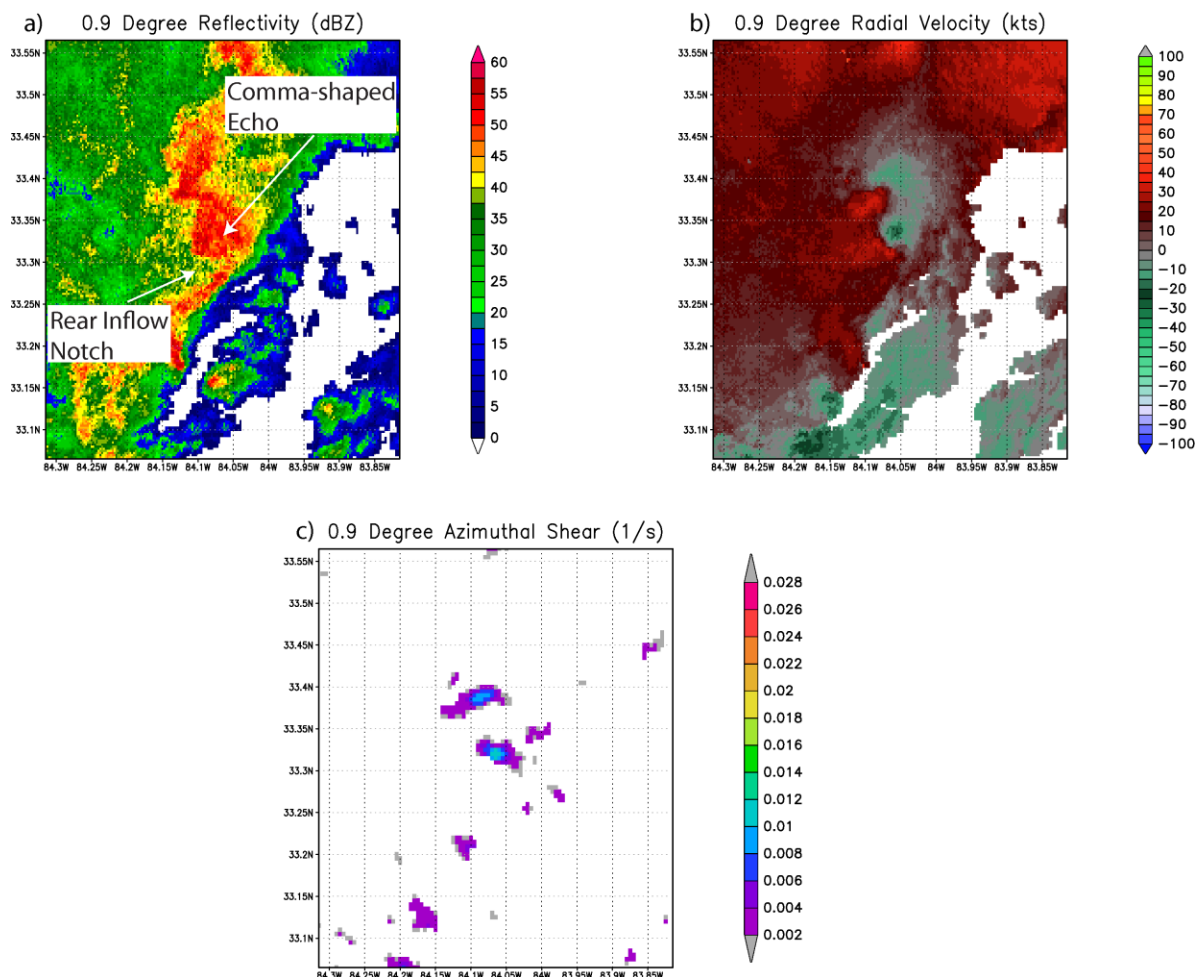


FIG. 3.15. Similar to FIG. 3.7, but at the 0.9 degree elevation scan of the Peachtree City, GA (KFFC) radar at 2116 UTC on 30 November 2010 showing an example of an embedded supercell with a comma-shaped echo and RIN.

Chapter 4

Results

4.1 Convective Modes Climatology

The distribution of convective modes for all 224 HSLC tornadoes with convective mode data in the full dataset, between 2006 and 2011, is shown in Fig. 4.1. Also shown is the convective mode distribution of all (regardless of their associated CAPE and shear values) 10,724 tornadoes classified by Smith et al. (2012) that occurred nationwide between 2003 and 2011. The majority of HSLC tornadoes were associated with supercell mesocyclones, but this percentage was slightly less (by 6%) than for all tornadoes. The percentage of HSLC QLCS mesovortex tornadoes is more than 15% greater than the percentage of QLCS mesovortex tornadoes for all tornadoes. When considering only supercell mesocyclone and QLCS mesovortex tornadoes and not tornadoes in the “other” category, it is especially clear that the relative frequency of QLCS mesovortex tornadoes is greater and the relative frequency of supercell mesocyclone tornadoes is less for HSLC tornadoes compared to all tornadoes. Interestingly, the percentage of supercell mesocyclone tornadoes increases to 79% for SBCAPE between 500 and 1000 J kg⁻¹, and 92% for SBCAPE > 1000 J kg⁻¹ (Fig. 4.2). The climatological importance of QLCS mesovortex tornadoes clearly increases as CAPE decreases.

Fig. 4.1 also shows the distribution of the three supercell sub-classification types for HSLC tornadoes and all tornadoes. Interestingly, 75% of the HSLC supercell mesocyclone tornadoes were from non-discrete supercells (supercells in clusters and supercells in lines) compared to 60% of all supercell tornadoes. The reasons for an enhanced relative frequency of non-discrete supercell tornadoes and QLCS mesovortex tornadoes in HSLC environments are unclear. It is possible that storms in environments with low instability need a greater degree of external forcing in order to survive, resulting in discrete supercells being less

avored. In other words, HSLC environments tend to have more widespread convection than the typical supercell environment in the Plains, possibly due to a stronger synoptic-scale forcing for ascent promoting upscale growth (or a weaker cap). These hypotheses cannot be tested with the data presented here, but they are an area of interest for modeling and observational studies in the future.

Narrowing the focus to only the 95 unique tornadic vortices used in the azimuthal shear climatology (see section 4.2) eliminates double-counting of storms that produce multiple tornadoes (and only uses the time period 2008-2011). When this is done, the importance of QLCS mesovortex tornadoes in HSLC tornado climatology becomes even more clear (Fig. 4.3, top row). Excluding the 11 tornadic vortices for which convective mode data were not available in the SPC database, only 48% of the tornadic vortices were supercell mesocyclones, 44% were QLCS mesovortices, and 8% were unable to be classified as either.¹² Most of the supercells were in clusters, with only a handful each of discrete supercells and supercells embedded in lines.

The convective modes distribution for the 135 non-tornadic vortices (Fig. 4.3, bottom row) is somewhat similar, though the percentage of cases classified as “other” is somewhat greater. These cases were typically storms that looked cellular. However, they were unable to sustain rotation long enough (10-15 min) to be classified as supercells, and/or overall had a disorganized/“messy” appearance. Supercells in clusters made up the majority of the non-tornadic supercells, followed by supercells embedded in squall lines. Only a small fraction were discrete supercells. Overall, however, there were no clear differences in convective modes between the tornadic and non-tornadic vortices, and there were fairly similar numbers of supercell mesocyclones and QLCS mesovortices. This is in contrast to the typical severe weather environment where most tornadoes come from supercell mesocyclones. In the following sections, results for the azimuthal shear and radar reflectivity signature climatologies will be analyzed for both supercell mesocyclones and QLCS mesovortices, as they are almost equally important to understanding HSLC tornado climatology.

¹² When the author performed his own convective mode classification, 53% of the tornadic vortices were supercell mesocyclones, and 42% were QLCS mesovortices.

4.2 Azimuthal Shear Climatology

A map of the 95 tornadic and 135 non-tornadic vortex tracks (identified using the method described in section 3.3) is shown in Fig. 4.4. The greater number of non-tornadic vortices is not surprising given the high false alarm rate (FAR) for NWS tornado warnings, which Brotzge et al. (2011) found nationally to be 75%. Fig. 4.4 shows a wide variety in vortex track lengths, with more tornadic vortices in the southern portion of the domain than the northern portion of the domain.

Due to the range dependence of azimuthal shear, vortices were sorted into three separate range bins (0-60 km, 60-100 km, and > 100 km) based on the distance of each point along the vortex track from the closest radar.¹³ The locations of these bins are shown in Fig. 4.4. Bin sizes were selected in order to have a roughly equal number of tornadic vortices in each bin, and through iterative testing of skill in discriminating between tornadic and non-tornadic vortices, which appeared to decay roughly 50-75 km from the radar (this decay is discussed more later). In the 0-60 km range bin, the number of tornadic vortices slightly outnumbers the number of non-tornadic vortices. In range bins farther away from the radar the number of non-tornadic vortices begins to strongly outnumber the tornadic vortices, suggesting a decrease in warning skill with range. Results will first be presented for vortices within 60 km of the radar, where vortices are fairly well-sampled, followed by a discussion of how these results change for less well-sampled vortices farther from the radar.

4.2.1 Results for Vortices Close to the Radar

Fig. 4.5 shows a composite time series of azimuthal shear at the lowest four elevation scans for vortices within 60 km of the nearest radar in a tornado-relative (for tornadic vortices)/false alarm warning issuance-relative (for non-tornadic vortices) time-coordinate system. Since volume scan times could potentially vary, the azimuthal shear values for each volume scan were placed in 5-min time bins. For example, volume scans 0-5 min prior to tornado touchdown/false alarm warning issuance time are placed in the $t = 0$ -min time bin,

¹³ If one vortex crossed from one range bin to another, azimuthal shear values from each volume scan would be placed in their different respective range bins.

volume scans 5-10 min prior were placed in the $t = -5$ -min time bin, and so on. If two volume scans for the same vortex fell in the same 5-min time bin (e.g. due to the typical 4-5 min volume scan time), azimuthal shear values for the two volume scans were averaged. If no volume scans fell into a time bin (e.g. if the volume scan time was > 5 min), azimuthal shear values for this time bin were set to missing. Since different vortices could be tracked for different amounts of time, the number of samples in each time bin varies, as not every vortex existed or could be tracked forward and backward to every time bin (Fig. 4.6). As would be expected, Fig. 4.6 shows that the number of vortices that could be tracked decreases as one moves farther backward or forward from the tornado/warning time. Median azimuthal shear values are plotted for only the vortices that existed at each time bin, and are only plotted if at least five vortices existed in that time bin. For volume scans farther backward or forward in time, the apparent trends in median azimuthal shear at these times may therefore be due to small sample size.

In Fig. 4.5a, an upward trend in median azimuthal shear at the base scan for the tornadic vortices starts as early as 20-25 min prior to the tornado, suggesting vortex strengthening. Median azimuthal shear values decrease after tornado touchdown, suggesting vortex weakening. Similar increases leading up to false alarm warning issuance time are evident for the non-tornadic vortices, but the overall trend is much flatter and median azimuthal shear values are weaker. Median azimuthal shear values for the tornadic vortices are above the 75th percentile of the non-tornadic vortices' azimuthal shear values starting 5-10 min prior to the tornado/warning time. The difference in median base scan azimuthal shear values between the tornadic and non-tornadic vortices is statistically significant at the 95 percent confidence level according to the Wilcoxon rank sum test, from 5-10 min prior to 1-5 min after the tornado/warning time. Additionally, median azimuthal shear for the non-tornadic vortices is at or below the 25th percentile of azimuthal shear for the tornadic vortices during this time. Forecasters using a warning threshold azimuthal shear value of 0.01 s^{-1} would detect 75 percent of the tornadic vortices while eliminating 50 percent of the false alarms. It should be noted that comparing plots of the tornadic vortices in a tornado-relative

time coordinate system and the non-tornadic vortices in a warning-issuance relative time coordinate system may not be entirely realistic, since ideally a warning would be issued *prior* to the occurrence of a tornado. However, the tornadic vortices still appear to be stronger than the non-tornadic vortices even after the time of warning issuance for the non-tornadic vortices.

Farther aloft, statistically significant differences in azimuthal shear 0-5 min before the tornado/warning could be found at the next two highest volume scans (Fig. 4.5b-c). 5-10 min prior to the tornado/warning, differences aloft were only statistically significant at the 90% confidence level, and only at the 0.9 degree elevation scan. Upward trends in azimuthal shear for the tornadic vortices at these elevation scans did not begin until 5-10 min prior to tornado touchdown, while azimuthal shear at these scans was steady or decreasing over time for the non-tornadic vortices. At the 1.8 degree elevation scan (Fig. 4.5d), statistically significant differences between the tornadic and non-tornadic vortices could only be found after the tornado, and trends were fairly flat. Median azimuthal shear values for the tornadic vortices were lower at the 1.8 degree elevation scan than at the lower elevation scans. On the other hand, for the non-tornadic vortices median azimuthal shear at the 1.8 degree elevation scan was about the same or slightly higher than at the lower scans. The 1.8 degree and higher elevation scans do not have super-resolution velocity data, and therefore vortices will not be sampled as well by these scans due to the coarser legacy resolution velocity data. Overall, these results suggest that when a forecaster looks at velocity and/or azimuthal shear data, they should focus on the base scan.

Fig. 4.7 shows a similar plot for the subset of vortices within 60 km of the radar that are supercell mesocyclones.¹⁴ These make up a little under a third of the tornadic vortices and about half of the non-tornadic vortices within this range bin. At the base scan, median azimuthal shear values for the tornadic supercell mesocyclones are slightly weaker at the tornado/warning time than for the bulk population of vortices at this range (cf. Figs. 4.5a and

¹⁴ Convective modes from the Smith et al. (2012) database were used for the tornadic vortices and convective modes determined by the author for the non-tornadic vortices as discussed in Section 3.4; results using convective modes determined by the author for the tornadic vortices as well were very similar.

4.7a). The non-tornadic supercell mesocyclones have similar median azimuthal shear to the bulk population of non-tornadic vortices. While median azimuthal shear values for the tornadic supercell mesocyclones are still greater than for the non-tornadic supercell mesocyclones, this difference is not statistically significant. Median azimuthal shear for the tornadic supercell mesocyclones is within the interquartile range of azimuthal shear for the non-tornadic supercell mesocyclones. Aloft, at the 1.3 and 1.8 degree elevation scans, median azimuthal shear values are actually slightly greater (but not by a statistically significant margin) for the non-tornadic supercell mesocyclones (Fig. 4.7c-d). These results may be disappointing, but are perhaps not surprising as it is known that many non-tornadic supercells have strong low-level mesocyclones (Trapp 1999, Trapp et al. 2005a).

Somewhat surprisingly, the primary reason for the statistically significant differences between all tornadic and non-tornadic vortices within 60 km of the radar is the statistically significant differences between tornadic and non-tornadic QLCS mesovortices (Fig. 4.8). Statistically significant differences in azimuthal shear at the 95% confidence level can be found from 5-10 min before to 1-5 min after the tornado/warning at the lowest two elevation scans (Fig. 4.8a-b). They can also be found 0-5 min before the tornado/warning at the 1.3 degree elevation scan (Fig 4.8c). These results are consistent with the findings of Atkins et al. (2004) and (2005) that stronger QLCS mesovortices are more likely to produce tornadoes. It is possible that these differences could be an artifact of poor forecaster warning skill for QLCS mesovortices. However, the non-tornadic QLCS mesovortices are not especially weak, and in fact have similar azimuthal shear values as the non-tornadic supercell mesocyclones. The statistically significant differences occurring for only the QLCS mesovortex cases are primarily related to the median azimuthal shear values for the tornadic QLCS mesovortices actually being larger than for the tornadic supercell mesocyclones. The present data suggest the potential for high warning accuracy for QLCS mesovortices close to the radar, which are typically thought to be more challenging than supercell mesocyclones. To assess the volatility of this result, the statistics were rerun with individual prolific tornadic and non-tornadic days excluded. The results were very similar, the only main difference

being that when the prolific HSLC QLCS mesovortex tornado event of 27 April 2011 was removed, statistical significance at the time of the tornado/warning dropped to the 90% confidence level (but remained at the 95% level 5-10 min prior to the tornado).

Doswell et al. (2009) noted that the EF1+ portion of the tornado record is much less prone to error, as many EF0 tornadoes may go unreported, and straight-line winds are occasionally misdiagnosed as EF0 tornadoes (or vice versa). When only tornadic vortices producing EF1 or greater tornadoes (as their *first* HSLC tornado; only the first tornado a vortex produces is included in this study) within 60 km of the radar are included, clear separation in azimuthal shear between these vortices and all the non-tornadic vortices (regardless of convective mode) exists (Fig. 4.9). This may be due to the fact that the majority of EF1+ tornadoes close to the radar were from QLCS mesovortices (12 of 19) and not supercell mesocyclones (5). Low sample sizes of supercell mesocyclones with EF1+ tornadoes close to the radar preclude a determination of whether or not they are stronger than non-tornadic mesocyclones. Strong azimuthal shear values are present at the time of the EF1+ tornadoes, with 75 percent of these vortices having azimuthal shear $\geq 0.013 \text{ s}^{-1}$ at the 0.5 degree elevation scan. This is useful, as EF1+ tornadoes entail a greater risk to life and property than EF0s.

Composite time-height plots of median azimuthal shear were also created (Fig. 4.10). The main differences between the bulk populations of tornadic and non-tornadic vortices within 60 km of the radar (Fig. 4.10a-b) is the strong low-level rotation (azimuthal shear $> 0.012 \text{ s}^{-1}$) that develops in the lowest 1.5 km beginning about 5-10 min prior to the tornado. Above 1.5 km, the tornadic and non-tornadic vortices are not very different from each other, though the 0.01 s^{-1} azimuthal shear contour is about 1 km higher for the tornadic vortices compared to the non-tornadic vortices at the tornado/warning time. While the non-tornadic supercell mesocyclones have azimuthal shear consistently $> 0.012 \text{ s}^{-1}$ above 1 km leading up to the time of the warning, azimuthal shear $> 0.012 \text{ s}^{-1}$ is mainly confined to the lowest 1.5 km for the tornadic supercell mesocyclones (Fig. 4.10c-d). Azimuthal shear $> 0.012 \text{ s}^{-1}$ for the non-tornadic supercell mesocyclones can only be found below 1 km for one datapoint, at

0.5 km at the time of the warning. The tornadic QLCS mesovortices (Fig. 4.10e) also had azimuthal shear $> 0.012 \text{ s}^{-1}$ confined to the lowest 1.5-2 km, with the area of azimuthal shear $> 0.012 \text{ s}^{-1}$ deepening from 1 to 2 km in the 10 min leading up to the tornado. The non-tornadic QLCS mesovortices (Fig. 4.10f) had much weaker azimuthal shear overall, with the azimuthal shear maximum occurring around 1 km over a shallower layer.

Vortex lifetime was calculated by determining the number of consecutive 5-min time bins when the vortex had azimuthal shear at or above a given threshold using a single radar (potentially resulting in an underestimate of lifetime for longer-lived vortices). Fig. 4.11 shows a histogram of vortex lifetime over the whole trackable lifetime (maximum azimuthal shear $\geq 0.006 \text{ s}^{-1}$ at any elevation scan in the lowest 2 km). The median lifetime of the tornadic vortices (including all convective modes) was 40 min, 10 min longer than the median lifetime for the non-tornadic vortices (Fig. 4.11). However, this was not a statistically significant difference. Four of the non-tornadic vortices could not be tracked for more than one volume scan (a lifetime of ≤ 5 min), while all of the tornadic vortices could be tracked for more than one volume scan (Fig. 4.11). Some vortices had very long lifetimes, exceeding 1-2 h, while one tornadic vortex was tracked for almost 4 h. Vortex detection lead time (time preceding the tornado that the vortex existed, *not* the actual warning lead time) was also calculated. The median vortex detection lead time was 15 min (Fig. 4.12), similar to the 14.6 min average NWS tornado warning lead time (Brotzge and Donner 2013). Four cases had no detection lead time, however (Fig. 4.12).

Stratifying the results by convective mode, the supercell mesocyclones had much longer lifetimes than the QLCS mesovortices. The supercell mesocyclone median lifetime was 65 min for tornadic mesocyclones and 50 min for non-tornadic mesocyclones (Fig. 4.13b; not a statistically significant difference). Detection lead time for the tornadic supercell mesocyclones was also greater than for the bulk population of vortices, with a median detection lead time of 25 min (Fig. 4.13d). The median tornadic QLCS mesovortex lifetime, on the other hand, was 30 min, and 20 min for the non-tornadic QLCS mesovortices (Fig. 4.13c). This is again consistent with Atkins et al.'s (2004) and (2005) findings that longer-

lived QLCS mesovortices were more likely to produce tornadoes, though this was not a statistically significant difference. The median detection lead time for tornadic QLCS mesovortices was only 10 min (Fig. 4.13d), and three cases had no lead time (not shown). A couple cases did have lead times greater than 15 min (not shown).

While an azimuthal shear threshold of 0.006 s^{-1} can provide a moderate amount of lead time in many cases, issuing warnings based on this threshold would lead to copious false alarms. Earlier in this section, an azimuthal shear value of 0.01 s^{-1} was found to be a good threshold for retaining 75% of the tornadic vortices and removing 50% of the non-tornadic vortices. For the full population (Fig. 4.13a), tornadic vortices had a median lifetime of 22.5 min at an azimuthal shear threshold of 0.01 s^{-1} , with a median lifetime of 5 min for the non-tornadic vortices (many non-tornadic vortices were below this threshold at the time of the false alarm warning and therefore had a lifetime of 0 min at this threshold). This difference was statistically significant at the 90% confidence level. However, median detection lead time for the tornadic vortices was only 5 min at this threshold (Fig. 4.13d), showing the challenge for forecasters of trying avoid false alarms while still issuing warnings with adequate lead time. Tornadic supercell mesocyclones had a lifetime at this threshold of 25 min, compared to 5 min for the non-tornadic supercell mesocyclones (Fig. 4.13b; not a statistically significant difference), and median detection lead time was 15 min (Fig. 4.13d). Tornadic QLCS mesovortices had a median lifetime of 20 min at this threshold (Fig. 4.13c), and a median detection lead time of 5 min (Figure 4.13). While azimuthal shear could discriminate between tornadic and non-tornadic QLCS mesovortices close to the radar at the time of the tornado/warning, the challenge becomes the short lead time that is possible in these events.

Vortex depth was calculated by determining the highest radar elevation scan where azimuthal shear above threshold could be found. There are limitations in this calculation, as the height of the radar beam varies greatly between ranges of 0 and 60 km. Also, elevation scans above 1.3 degrees do not have super-resolution velocity data available, and so vortices are not as well-sampled. The median highest elevation scan where azimuthal shear above

0.006 s^{-1} could be found (for all vortices within 60 km of a radar) was 4 degrees for the tornadic vortices and between 3.1 and 4 degrees for the non-tornadic vortices (Fig. 4.14a). This corresponds to an approximate beam height under standard refractive conditions of between 0.7 km (at 10 km range) and 4.4 km (at 60 km range). At the median range of tornadic vortices in this range bin, 45 km from the radar, this corresponds to a vortex depth of about 3.3 km. These results show the typically shallow nature of HSLC vortices. For supercell mesocyclones, the median highest elevation scan was 4 degrees for both tornadic and non-tornadic mesocyclones (Fig. 4.14b). However, there was a statistically significant difference in depth between tornadic and non-tornadic QLCS mesovortices, with the median highest elevation scan being 5.1 degrees for tornadic QLCS mesovortices and 1.8 degrees for non-tornadic QLCS mesovortices (Fig. 4.14c). The scan elevations correspond to vortex depths of about 4.1 km and 1.5 km, respectively at the range of 45 km. This is consistent with Atkins et al.'s (2004) and (2005) findings that deeper QLCS mesovortices are more likely to be tornadic.

To summarize, the characteristic (median) tornadic supercell mesocyclone within 60 km of the radar had a base scan azimuthal shear value of 0.013 s^{-1} , had a lifetime of 65 min, existed 25 min prior to the tornado, had a depth of 3.5 km, and had a base scan diameter of 2 km. The characteristic non-tornadic supercell mesocyclone was very similar, having an azimuthal shear value of 0.011 s^{-1} , a lifetime of 50 min, a depth of 3.5 km, and a base scan diameter of 1.8 km. The characteristic tornadic QLCS mesovortex had a base scan azimuthal shear value of almost 0.016 s^{-1} , a lifetime of 30 min, existed 10 min prior to the tornado, was 4.1 km tall, and had a base scan diameter of 2.1 km. The characteristic non-tornadic QLCS mesovortex had a base scan azimuthal shear value of 0.011 s^{-1} , had a lifetime of 20 min, was about 1.5 km tall, and had a base scan diameter of 3.1 km. Statistically significant differences in azimuthal shear between tornadic and non-tornadic QLCS mesovortices were found beginning 5-10 min prior to the tornado/warning, as well as vortex depth. No statistically significant differences were found between tornadic and non-tornadic supercell mesocyclones.

4.2.2 Results for Vortices Farther from the Radar

Moving farther away from the radar, radar sampling limitations become apparent, and lead to a loss of skill in using azimuthal shear to discriminate between tornadic and non-tornadic vortices. Fig. 4.15 shows a time series of azimuthal shear for all vortices located 60-100 km from the nearest radar, which are based on the sample sizes shown in Fig. 4.16. Median azimuthal shear values remain flat for both the tornadic and non-tornadic vortices at the base scan (Fig. 4.15a), with slight downward trends at the 0.9 and 1.3 degree elevation scans (Fig. 4.15b-c). At the base scan, there is no difference in azimuthal shear between the tornadic and non-tornadic vortices (Fig. 4.15a). Median azimuthal shear for the tornadic vortices at this range is slightly weaker than for the tornadic vortices 0-60 km from the radar, but the non-tornadic vortices are actually *stronger* at this range. This seems surprising because it would be expected that azimuthal shear would weaken with range, due to the wider beam being unable to properly resolve the vortices. It is possible that this increase in azimuthal shear with range may be due to the fact that the beam is higher. Perhaps these non-tornadic vortices have strong rotation aloft (e.g. a strong mid-level mesocyclone at radar beam height) but not in low-levels. Time-height cross-sections of median azimuthal shear (Fig. 4.17) similarly indicate no significant trends in azimuthal shear over time, and similar profiles for the tornadic and non-tornadic vortices. No data are available below 1 km due to the height of the beam. Close to the radar, it was found that the primary azimuthal shear differences between the tornadic and non-tornadic vortices were in the lowest 1.5 km (Fig. 4.10). Therefore, it does appear that not being able to detect near-ground rotation is the primary reason for why the tornadic and non-tornadic vortices cannot be distinguished at this range. This will be further discussed in chapter 5.

Further aloft, interestingly, there are some statistically significant differences in azimuthal shear between tornadic and non-tornadic vortices at the 90% confidence level (Fig. 4.15b-c). This may mean that the tornadic storms have a deeper area of rotation, but it is difficult to determine if this difference is real as the median azimuthal shear for the tornadic vortices is within the interquartile range for the non-tornadic vortices, and the non-tornadic

vortices' azimuthal shear values match or exceed the tornadic vortices' values by the time of the tornado/warning. Also, some of the statistically significant differences aloft at this range disappear when certain prolific tornado cases are removed, such as 10 April 2009. At the 1.8 degree elevation scan (Fig. 4.15d), the strong range dependence of azimuthal shear calculated from legacy resolution velocity data is clear, as azimuthal shear values are less than half of what they are at the base scan. When only including supercell mesocyclones 60-100 km from the radar, median azimuthal shear values are relatively similar to the population of all vortices at this range (cf. Fig. 4.15, 4.18). Interestingly, a time-height plot of azimuthal shear for the tornadic supercell mesocyclones (Fig. 4.17c-d) does show strong azimuthal shear values $> 0.014 \text{ s}^{-1}$ 5-10 min prior to the tornado between 1 and 1.5 km, greater than the median at the 0.5 degree elevation scan in the time series plots (where values were not interpolated to constant height levels). Sample size is fairly low at this height, as many of the supercell mesocyclones in this range bin occurred at greater ranges where the radar did not sample the mesocyclone at this height. However, this does suggest the importance of observing vortices in the lowest 1.5 km.

For QLCS mesovortices 60-100 km from the closest radar (Fig. 4.19), azimuthal shear values are overall weaker than for the supercell mesocyclones, and azimuthal shear is very similar for the tornadic and non-tornadic QLCS mesovortices. Time-height plots for the QLCS mesovortices (Fig. 4.19e-f) indicate overall weaker azimuthal shear values. This again shows the importance of observing vortices in the lowest 1.5 km which is not possible at farther ranges from the radar. The time series plot for only EF1+ tornadoes 60-100 km from the radar, regardless of convective mode (Fig. 4.20), looks fairly similar to the plot with EF0 tornadoes included (Fig. 4.15), though somewhat stronger rotation exists aloft for the tornadic vortices.

For the range bin farthest from the radar, $> 100 \text{ km}$ (Fig. 4.21), azimuthal shear values are overall somewhat weaker, probably because the vortices are less well-sampled at this range. However, 5-15 min prior to the tornado they are still fairly strong, with a median azimuthal shear value for tornadic vortices of 0.012 s^{-1} at the base scan. Unexpectedly,

median azimuthal shear values for both the tornadic and non-tornadic vortices *decrease* leading up to the time of tornado touchdown/false alarm warning issuance, to below 0.01 s^{-1} (Fig. 4.21a). This is important to note for forecasters, as a weakening in azimuthal shear at this range apparently does not correspond to a decreasing threat for a tornado. It is possible that this weakening is due to the vortex contracting to a diameter that is not well-resolved by the radar at this range. There are a few statistically significant differences aloft, especially at the 1.8 degree elevation scan (Fig. 4.21d). This may again suggest that storms with stronger mid-level rotation are more likely to produce a tornado, as well as deeper storms. The radar beam is 3-4 km above the radar at this elevation scan and range, overshooting the median vortex depth found in the preceding sub-section. However, some of these differences again disappear when a prolific tornado day is removed, so they may not be real. Also, the overall low ($< 0.006 \text{ s}^{-1}$) azimuthal shear values at this elevation scan may simply be associated with noise, and also could be an artifact of this elevation scan not having super-resolution velocity data. Time-height plots of azimuthal shear also indicate little difference between the tornadic and non-tornadic vortices (Fig. 4.22), as the vortices are not sampled below 2 km which was where the main differences were found close to the radar.

Overall, a scatterplot of azimuthal shear versus range for the whole population of vortices (Fig. 4.23) shows a slight downward trend in azimuthal shear with range, but the correlation coefficient is extremely weak. More than 100 km from the radar, few strong vortices are observed. It appears that azimuthal shear varies with range partly due to the increasing effective beamwidth (which would tend to diminish shear values), and partly due to the increasing beam height (which could either increase or decrease shear values). This will be further discussed in chapter 5.

Vortex lifetimes and detection lead times also varied with range. The median lifetime for both tornadic and non-tornadic supercell mesocyclones producing their first tornado/false alarm warning 60-100 km from the radar was actually greater than for supercell mesocyclones producing their first tornado/false alarm warning within 60 km of the radar

(Figure 4.13b).¹⁵ This is possibly an artifact of only using a single radar to track vortices. Non-tornadic supercell mesocyclones actually had slightly longer lifetimes than the tornadic supercell mesocyclones at this range. Greater than 100 km from the radar, there was a more pronounced lifetime difference between tornadic and non-tornadic supercell mesocyclones at the 0.006 s^{-1} threshold (Fig. 4.13b). This suggests that forecasters should focus on longer-lived vortices far from the radar. Median detection lead time remained high for tornadic supercell mesocyclones using the 0.006 s^{-1} threshold at this range (Fig. 4.13d). Tornadic and non-tornadic QLCS mesovortex lifetimes and lead times were similar between the 0-60 km and 60-100 km range bins. Lifetimes decreased in the $> 100 \text{ km}$ range bin, with median detection lead time falling to 0 min (Figure 4.13c-d). Lifetimes and lead times at the 0.01 s^{-1} azimuthal shear threshold fell to zero $> 100 \text{ km}$ from the radar for both supercell mesocyclones and QLCS mesovortices. Overall, lifetimes and detection lead times for supercell mesocyclones and QLCS mesovortices remained fairly constant within 100 km of the radar. They then decreased in most cases more than 100 km from the radar, where the vortices were barely resolvable. Supercell mesocyclones and QLCS mesovortices could rarely maintain azimuthal shear above 0.01 s^{-1} for a meaningful length of time more than 100 km from the radar since they were not well-sampled.

An attempt was made to calculate vortex depth for vortices more than 60 km from the radar. However, the highest elevation scan with azimuthal shear $\geq 0.006 \text{ s}^{-1}$ was almost always 1.3 degrees, the highest super-resolution elevation scan. This suggests that the strong range dependence of the higher, legacy resolution elevation scans was the strongest signal in the data. Therefore, no meaningful conclusions about vortex depth could be made for vortices more than 60 km from the radar. Presuming that the calculated depths for the 0-60 km bin are robust (section 4.2.2), one would expect the highest scan with azimuthal shear $\geq 0.006 \text{ s}^{-1}$ to be the 2.4 degree scan which reaches a height of 3.7 km at 80 km range.

¹⁵ Unlike in the time series plots, for the vortex lifetime calculations the results were binned only by the range from radar of the vortex at the time of the tornado/warning, not the range from radar of the vortex at each individual volume scan. For example, a vortex that produces its first tornado/warning in the 0-60 km range bin but moves into the 60-100 km range bin before or after this time will have its lifetime include the time it spent in the 60-100 km range bin even though it is placed in the 0-60 km range bin.

4.2.3 Evaluation of Other Rotational Metrics

Noting that vortex diameter increases with range (Fig. 3.3) but that azimuthal shear falls off only weakly with range (Fig. 4.23), it is possible that other rotational metrics are useful. Some such metrics are currently used by the NWS in warning operations. The difference between the peak inbound and outbound velocities associated with the vortex at a constant range (ΔV , equivalent to twice the rotational velocity), is commonly used by forecasters. Unlike azimuthal shear it is easy to calculate on-the-fly (azimuthal shear is not currently available operationally). However, also unlike azimuthal shear it does not discriminate between broad and tight circulations. For the present study, ΔV was calculated by a WDSS-II algorithm, which searched for the peak velocities within 3 km in each azimuthal direction of a given point. The maximum in the ΔV field generated by WDSS-II was recorded within the same 0.04 degree latitude by 0.04 degree longitude box in which the maximum in azimuthal shear was recorded. For vortices within 60 km of the radar, time series of ΔV (Fig. 4.24-27) look similar to the time series for azimuthal shear (Fig. 4.5,7-9). There are statistically significant differences in ΔV between the tornadic and non-tornadic vortices at the base scan beginning 5-10 min prior to the tornado/warning (Fig. 4.24a). However, the separation in ΔV between the tornadic and non-tornadic vortices is not as pronounced as the separation in azimuthal shear (Fig. 4.5). Also, some of the statistically significant differences in azimuthal shear between tornadic and non-tornadic vortices at higher elevation scans are lost when ΔV is used. A base scan ΔV threshold of about 25 m s^{-1} would retain 75 percent of the tornadic vortices while removing 50 percent of the non-tornadic vortices.

For vortices 60-100 km from the radar, median ΔV is slightly greater for the tornadic vortices (Fig. 4.28a), but this difference is only statistically significant 10-15 min prior to the tornado/warning at the 90% confidence level. At the 1.3 degree and 1.8 degree elevations scans (Figure 4.28c-d), ΔV also shows some statistically significant differences between tornadic and non-tornadic vortices with a possible slight improvement over azimuthal shear. A ΔV plot for only supercell mesocyclones shows that there are signs of stronger ΔV for the tornadic supercell mesocyclones at the 1.3 and 1.8 degree elevation scans (Fig. 4.29c-d).

Also, when only tornadic vortices with EF1 and greater tornadoes are included (Fig. 4.30), there are statistically significant differences in ΔV that were not present in the plots of azimuthal shear (Fig. 4.18c). Overall, however, both azimuthal shear and ΔV are poor discriminators between tornadic and non-tornadic vortices at this range.

Greater than 100 km from the radar, the ΔV and azimuthal shear plots look fairly similar, though there is not a downward trend in ΔV at the base scan (cf. Fig. 4.21a, 4.31a). When ΔV for only EF1 and greater tornadoes are plotted, there is a sudden increase in median ΔV 5-10 min prior to the tornado at the base scan. However, this is not a statistically significant difference between the tornadic and non-tornadic vortices (Fig. 4.32a). A plot of ΔV at the base scan as a function of range indicates no range dependence of ΔV (Fig. 4.33). This was true even at the legacy resolution 1.8 degree elevation scan (not shown). Even though the radar is not sampling the vortices very well at long ranges, it apparently is still detecting strong peak velocities, or at least strong differences in peak velocities, associated with the vortices.¹⁶ It may be that the smoothing in the LLSD azimuthal shear calculation has a greater effect when fewer radials cross the vortex. While LLSD azimuthal shear appears to be slightly superior to ΔV close to the radar, 60-100 km from the radar they perform about the same. ΔV may perform slightly better > 100 km from the radar, due to less range dependence.

The traditional “peak-to-peak” azimuthal shear variable was also analyzed, defined as ΔV divided by the vortex diameter. This is a variable typically calculated on-the-fly by forecasters as the calculation is far less complicated than for LLSD azimuthal shear (see section 3.3.1). The maximum ΔV at each point along the vortex track (analyzed in the previous paragraph) was divided by the WDSS-II calculated vortex diameter (distance between velocity peaks) at that point. Time series plots indicate that this variable is much noisier than LLSD azimuthal shear (cf. Fig. 4.34-35; 4.5, 7-8), as it only uses velocity data from two pixels. Meanwhile, LLSD azimuthal shear uses velocity data from multiple pixels and smoothes the velocity data. While the median peak-to-peak shear for the tornadic

¹⁶ Note that ΔV was not calculated in regions of weak azimuthal shear.

vortices is still greater than for the non-tornadic vortices close to the radar, this difference is not statistically significant due to large spread (Fig. 4.34). The interquartile range of peak-to-peak shear for the non-tornadic vortices is very wide, spanning an order of magnitude. There is a statistically significant difference in peak-to-peak shear for the QLCS mesovortices 5-10 min prior to the tornado/warning at the base scan close to the radar (Fig. 4.35a). Overall, however, it is clear that LLSD azimuthal shear performs much better than the peak-to-peak shear calculation close to the radar. Greater than 60 km from the radar, however, neither variable is skillful at discriminating between tornadic and non-tornadic vortices.

4.2.4 Operational Ramifications

The primary result of the azimuthal shear study is that statistically significant differences in LLSD azimuthal shear and ΔV could be found between tornadic and non-tornadic vortices within 60 km of the radar. This was primarily due to statistically significant differences between tornadic and non-tornadic QLCS mesovortices, not between tornadic and non-tornadic supercell mesocyclones. Azimuthal shear calculated using the traditional “peak-to-peak” method was plagued by inherent noisiness, and is not recommended. More than 60 km from the radar, no variable could discriminate between tornadic and non-tornadic vortices, though there were some signals that the tornadic vortices may have had stronger rotation aloft. Unfortunately, radar sampling limitations made it difficult to clearly determine if there are meaningful differences in depth between tornadic and non-tornadic vortices and the extent to which resolution and beam height offset one another at longer ranges. The results suggest that there is potential for warning lead time in many cases (although at the cost of false alarms at lower shear thresholds or longer ranges). There is greater potential lead time for the supercell mesocyclones than the QLCS mesovortices, but for both the potential lead time becomes poorer farther from the radar. Using a shear threshold of 0.01 s^{-1} (at least for this population of vortices) provides a POD of 88% and a FAR of 40%, as well as a median detection lead time of 5 min for vortices within 60 km of the radar. For reference, the national tornado warning POD is currently 75%, and the FAR is 74% (Brotzge and Donner 2013). Since not every false alarm warning is included in the dataset, the FARs in the present

results do not completely translate to warning FARs (the overall FAR for the present dataset is lower). The overall FARs for mesocyclones in the dataset (calculated as the percentage of supercell mesocyclones in the dataset that were non-tornadic) ranged from 50% within 60 km of the radar to 61% more than 100 km of the radar. Similarly, the overall FARs for QLCS mesovortices (percentage of QLCS mesovortices in the dataset that were non-tornadic) ranged from 43% within 60 km of the radar to 77% more than 100 km from the radar.

4.3 Radar Reflectivity Signatures Climatology

The somewhat limited utility of radial velocity signatures at long range motivated a corresponding investigation of whether reflectivity signatures could add skill to tornado warnings. The particular signatures, along with the motivation for choosing them and example images were reviewed in section 3.5. Overall, while some radar reflectivity signatures had a high probability of detection (POD, the percentage of tornadic vortices that were associated with the given signature), many also had a high false alarm rate (FAR, the percentage of signatures that were associated with a non-tornadic vortex). Also, range from radar again had an effect on whether or not the various signatures could be detected.

For tornadic supercell mesocyclones 0-60 and 60-100 km of the radar, as expected, hook echoes and BWERs/WERs (Fig. 4.36a-b) were present in a large majority of cases. These signatures typically appeared well before the tornado, with median lead times of 15-20 min. However, these signatures were also present with a large majority of the non-tornadic supercells close to the radar as well (a high probability of false detection, or POFD). This resulted in FARs of around 50% for both signatures, the same as the overall false alarm rate for supercells within 100 km of the radar (section 4.2.4). This is not surprising given that these are fundamental parts of supercell structure, and most supercells are non-tornadic.

For supercells greater than 100 km from the radar, the effects of radar sampling limitations become very apparent. Only 36% of tornadic supercells had hook echoes and BWERs/WERs (Fig. 4.36a-b), likely due to the effects of beam filling and the increase in height of the radar beam. These would both have pronounced consequences for mini-supercells. When hook echoes did occur, however, they had a median lead time of 19 min.

The POFD for hook echoes and BWERs/WERs also decreased. RINs, comma-shaped echoes, and bowing segments (Fig. 4.36c-e) were only found in a handful of supercell cases in each range bin, but were found with greater frequency in the non-tornadic supercells. This resulted in FARs above 60%. Therefore, these signatures do not appear useful in determining whether or not a supercell is tornadic, and they did not provide very much lead time, either.

Reflectivity signatures for QLCS mesovortices (Fig. 4.37), especially those close to the radar, appeared to show somewhat more skill than for supercells due to lower FARs for some signatures. However, as with azimuthal shear lead time was again the primary problem. Within 60 km of the radar, a large majority of QLCS mesovortex tornadoes were associated with RINs, bowing segments, gust front cusps, and forward inflow notches (Fig. 4.37a-d). However, a large majority of non-tornadic QLCSs were also associated with RINs and forward inflow notches. In contrast, only half of non-tornadic QLCSs had bowing segments and gust front cusps, resulting in FARs for these two signatures of around 35%. Median lead time for the RINs was almost 10 min, while for the bowing segments, gust front cusps, and forward inflow notches the median lead time was only 5 min. Also, a little under half of the forward inflow notches developed after the time of the tornado. These results overall appear to support the correlation between QLCS tornadoes and rear inflow jets (found by Przybylinski 1995 to be associated with RINs) as well as bow echoes found by Przybylinski (1995), Atkins et al. (2005), Atkins and St. Laurent (2009a), and others. Comma-shaped echoes (Fig. 4.37e) were only present in a few tornadic cases, and very few non-tornadic QLCSs. This resulted in the lowest FAR and highest median lead time of all the signatures, but low POD. Hook-like echoes were rare for both tornadic and non-tornadic QLCSs, with little lead time (Fig. 4.37f). These two signatures were uncommon farther from the radar as well. Overall frequencies of most of the QLCS reflectivity signatures decreased for the 60-100 km range bin, and FARs also typically increased (Fig. 4.37). More than 100 km from the radar, there were few tornadic QLCSs, and a larger number of non-tornadic QLCSs. Sample sizes for the signatures were low, but what signatures did occur had some lead time.

The broken-S signature (Figure 4.38a), of special interest to this study (see section 2.4 and Fig. 3.11), was associated with 35% of tornadic QLCS mesovortices and 27% of non-tornadic QLCS mesovortices within 60 km of the radar, with a FAR of 36%. However, there likely are an unknown number of non-tornadic broken-S signatures not associated with a tornado warning, and therefore the null broken-S dataset is incomplete. Lead time for the time of the broken-S line break varied. The median lead time for when the line break occurred aloft (at the 0.9, 1.3, or 1.8 degree elevation scans) was -1 min (Fig. 4.38b), with the line break occurring before the tornado in only two cases and more than 5 min after the tornado in three cases. Similarly, at the base scan the median lead time for the line break was -4 min, occurring prior to the tornado in two cases and more than 5 min after the tornado in two cases. This suggests that the broken-S signature has limited utility for issuing tornado warnings prior to tornado touchdown at this range.

Interestingly, 64% (9) of the tornadic QLCS mesovortices 60-100 km from the radar were associated with broken-S signatures (Fig. 4.38a), while none of the non-tornadic QLCS mesovortices had broken-S signatures. The median lead time for the line break aloft was 16 min. However, a bimodal lead time distribution was present, with five cases having lead times of 15 min or more, and four cases having a line break after the tornado. The median lead time for the line break at the base scan was -6 min, occurring after the time of tornado touchdown, with three cases having a line break at the base scan before tornado touchdown.¹⁷ The exact reasons for this apparent increase in broken-S skill between the 0-60 km range bin and 60-100 km range bin remain unknown, however, as well as the true number of non-tornadic broken-S signatures at this range. Increasing beam height may play a role, especially in the apparent improved lead time farther from the radar, given the typical “top-down” line break evolution in broken-S cases. An attempt was made to test this hypothesis by looking for broken-S signatures at higher tilts (2.4 degrees and above), but the lack of super-res reflectivity data at higher tilts (including the 1.8 degree elevation scan) makes it difficult to

¹⁷ In a couple cases, azimuthal shear for broken-S signatures fell below threshold between tornadoes, resulting in these tornadoes being treated as separate tornadic vortices. Therefore, the broken-S signature was counted twice, with a greater amount of lead time.

discern features. Therefore, this question remains unresolved. More than 100 km from the radar, POD became low and FAR became high again. When broken-S signatures did occur there were lead times of several minutes, with greater lead times aloft (Fig. 4.38a), but POD was low and FAR was high for this signature.

Finally, cell mergers (see section 3.5) were found to occur just as frequently in association with tornadic and non-tornadic vortices. They were more common with supercell mesocyclones (29% of supercells; either supercells merging with other cells or merging with a squall line) than with QLCS mesovortices (15% of QLCSs; QLCSs merging with cells). Overall FARs were above 50%. The median merger lead time for the supercells was 9 min, but there was a fairly wide distribution of lead times varying from over 20 min prior to 20 min after the tornado (Fig. 4.39a). The median merger lead time for QLCS mesovortices was 6 min, with most mergers occurring prior to the tornado and two cases occurring after the tornado (Fig. 4.39b). This is consistent with the findings of previous studies (e.g. Lemon 1976, Goodman and Knupp 1993, Finley et al. 2001, Finley et al. 2002, French and Parker 2012) that cell mergers may be relevant to tornadogenesis. However, cell mergers and tornadogenesis can occur independently of one another, and there is no clear favored time for tornadogenesis relative to the merger.

There does seem to be some value in looking at many of these reflectivity signatures, as some signatures had very high PODs. However, using these radar reflectivity signatures comes at a cost of high FARs, as many of these same signatures are associated with many non-tornadic vortices as well. Ideally it would be advantageous to use these signatures at ranges from the radar where the vortices are not well-sampled. However, radar sampling limitations degrade the appearance of or limit the detection of these signatures as well, typically at ranges beyond 100 km from the radar. Also, detection lead times for most of these signatures are similar to the detection lead times for the vortices themselves. The broken-S signature does show some potential usefulness in the 60-100 km range bin, but further study is needed.

4.4 Tornadic and Non-tornadic Vortex Environments

To this point, discrimination between tornadic and non-tornadic vortices has been presented as a purely radar-driven operation. Of course, another important aspect of the warning process is knowing whether the prevailing convective environment is favorable for tornadoes. Sherburn and Parker (2013) found that a product of mid-level lapse rates, low-level lapse rates, and shear magnitudes such as the 0-3 km shear vector magnitude was skillful in discriminating between significant tornadoes/significant wind reports and nulls. The formulation of this parameter that uses the 0-3 km shear vector magnitude, the Severe Hazards in Environments with Reduced Buoyancy (SHERBS3) parameter, proved most skillful in the part of their dataset that overlapped with this study. However, their requirements for a null event required the issuance of a warning with no severe reports in a given CWA. Meanwhile, the requirements for a null event in this study were based on no tornado reports within a radius of a vortex track associated with an unverified tornado warning. It is of interest to know how well their composite parameter does on the scale of individual vortices (for days where tornadic and non-tornadic vortices may co-exist). It would be useful to know whether SHERBS3 or any other environmental parameters differ significantly between the tornadic and non-tornadic vortex populations.

Overall, using the SPC mesoanalysis data at the time of the tornado/warning, the tornadic and non-tornadic vortices were associated with similar CAPE, shear, lapse rates, and helicity values, while the tornadic vortices had a slightly lower magnitude of CIN (Fig. 4.40). Values of the Significant Tornado Parameter (STP; Thompson et al. 2003) were also similar, with most vortices occurring in an environment with STP less than the operational threshold of 1 (Fig. 4.41a). The SHERBS3 was also similar for tornadic and non-tornadic vortices, with a median value above the optimal threshold of 1. However, when only the 12 significant tornadoes (using the magnitude of the first HSLC tornado produced by the vortex) in the dataset are compared to the non-tornadic vortices, SHERBS3 is a good discriminator (Fig. 4.38c). This is not surprising since it was developed using significant severe events, not all severe events. Additionally, SHERBS3 showed discrimination between tornadic vortices (of

all magnitudes) with track lengths of at least 40 km (the top 50% of tornadic vortex track lengths) and nulls (Fig. 4.41d). It is probably unsurprising that most of these differences are subtle, given the 40 km grid spacing of the mesoanalysis data and the common occurrence of tornadic and non-tornadic vortices in rather close proximity to one another on outbreak days.

Taking a different angle, it was also possible to determine how many of the tornadic vortices *originated* in a higher CAPE environment (at least as could be determined using a single radar to track them). Supercells originating in a higher CAPE environment could potentially be stronger. They could take advantage of more substantial instability early in their lifetime and then maintain themselves through vertical accelerations caused by their own pressure perturbations after they move into an environment with lower instability. Only 21% of the tornadic vortices could be tracked backwards into an environment with SBCAPE $> 500 \text{ J kg}^{-1}$. 14% could be tracked back to an environment with SBCAPE $> 750 \text{ J kg}^{-1}$, and 10.5% to an environment with SBCAPE $> 1000 \text{ J kg}^{-1}$. When only EF1 and greater tornadoes were included, 27% of these tornadic vortices originated in a higher CAPE environment, and 25% of significantly tornadic (EF2+) vortices originated in a higher CAPE environment (using the magnitude of the first HSLC tornado produced by the vortex). On the other hand, only 5% of the non-tornadic vortices could be tracked backwards into an environment with SBCAPE $> 500 \text{ J kg}^{-1}$, 3% to SBCAPE $> 750 \text{ J kg}^{-1}$, and 1% to SBCAPE $> 1000 \text{ J kg}^{-1}$. This may be partially related to the typically shorter lifetimes of the non-tornadic vortices, but suggests the importance for forecasters of focusing on storms moving into an HSLC environment from a higher CAPE environment.

Thirteen of the tornadic supercell mesocyclones originating in higher CAPE had track lengths of at least 80 km (twice the grid spacing in the SPC mesoanalysis data). For these long track vortices, SBCAPE decreased leading up to the time of the first HSLC tornado, with median values of SBCAPE dropping to 500 J kg^{-1} 20 min prior to the tornado (Fig. 4.42a). SBCIN increased slightly (not shown), while mid-level lapse rates remained constant and 0-3 km lapse rates decreased slightly (Fig. 4.42b-c). While instability was decreasing, shear parameters remained favorable, as 0-6 km, 0-3 km, and 0-1 km bulk shear vector

magnitudes remained constant (Fig. 4.42d, Fig. 4.43a-b). 0-3 km SRH and 0-1 km SRH both increased slightly (Fig. 4.43c-d). While STP decreased sharply as CAPE decreased (Fig. 4.44a), with 50% of these vortices having a value of STP below its operational threshold of 1, SHERBS3 remained steady or only slightly decreased, with values well above its optimal threshold of 1 (Fig. 4.44b). This shows the utility of the SHERBS3 parameter for storms moving into lower CAPE environments. It correctly indicated that the threat for tornadoes continued despite the decrease in CAPE (which reduces the effectiveness of other composite parameters like STP). During this period of decreasing CAPE, a time series showed an increase of median azimuthal shear during this time of transition (Fig. 4.44c), while median range from radar remained constant (Fig. 4.44d). Radar reflectivity for most of these cases revealed supercell that had large horizontal footprints and did not resemble mini-supercells (e.g. Fig. 3.7). This more classic supercellular appearance may be a hallmark of storms originating in higher CAPE environments.

To summarize, there were no significant differences in mesoscale environmental parameters between the tornadic and non-tornadic vortices at the time of the tornado/warning. This suggests that storm-scale processes or environmental differences not depicted in the SPC mesoanalysis data may have been the primary reasons why some vortices were non-tornadic. However, environmental factors potentially modulated the magnitude of the tornado and vortex longevity. While the majority of tornadic vortices appeared to originate in an HSLC environment, a fraction large enough to deserve closer scrutiny originated in a higher CAPE environment, and these vortices appeared more likely to be tornadic. These vortices also provided an opportunity to highlight how a new composite parameter, the SHERBS3, depicts the continued threat for severe weather in HSLC environments better than pre-existing composite parameters (e.g. STP). The presence of classic-looking supercells that originated in higher CAPE environments suggests that storms may have some “memory” of their initial setting, which could help to maintain them later in an environment with less buoyancy.

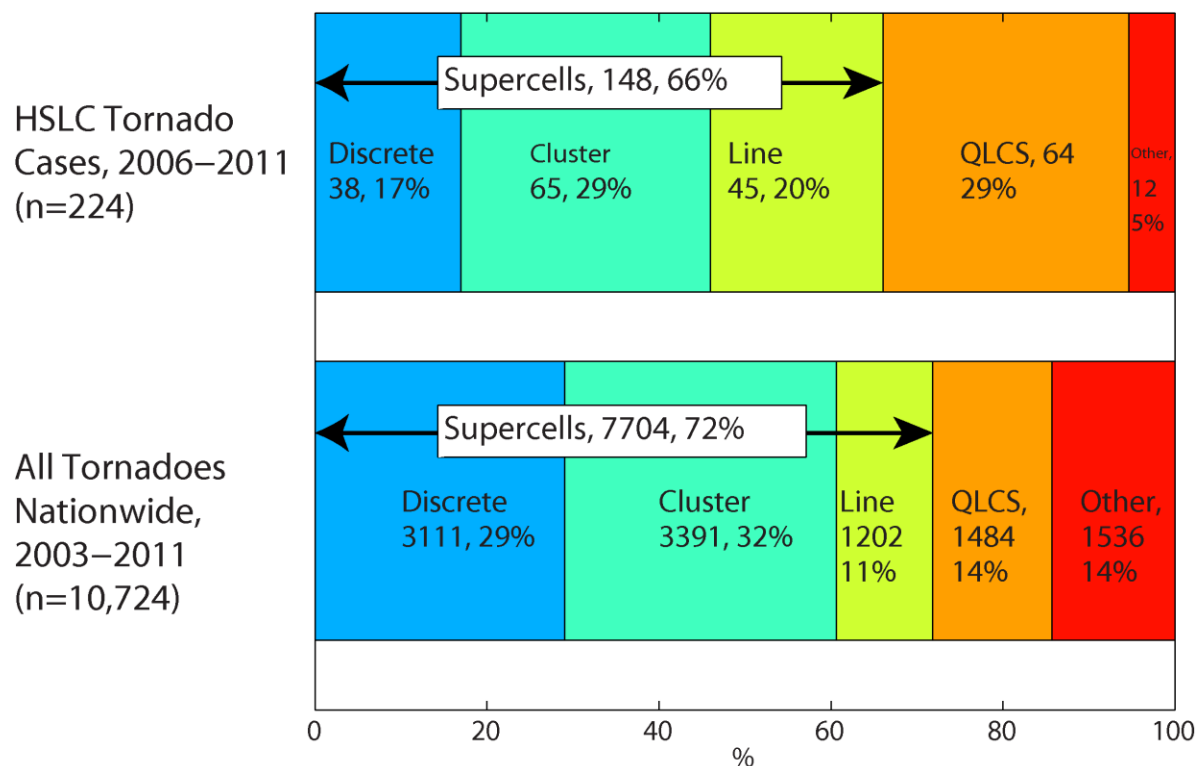


FIG. 4.1. Convective mode distributions for the HSLC tornadoes included in the full 2006–2011 HSLC dataset (top), and for all tornadoes nationwide (2003–2011) that were included in the Smith et al. (2012) convective mode database (bottom). Convective mode classifications are described in section 3.4 and in Smith et al. (2012). Percentages are out of 224 for the HSLC tornadoes and out of 10,724 for all tornadoes.

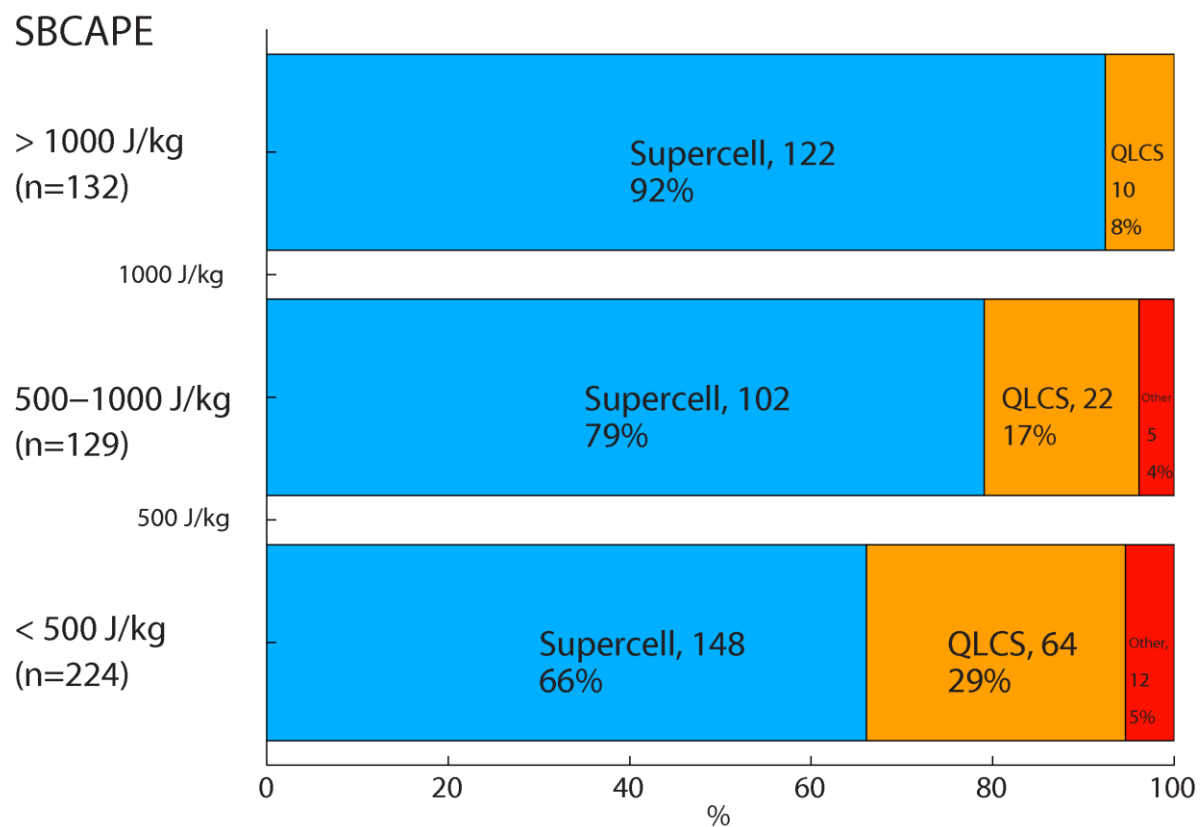


FIG. 4.2. Convective mode distributions for all tornadoes occurring in the domain during HSLC cases, including non-HSLC tornadoes, stratified by SBCAPE, using convective mode data from Smith et al. (2012).

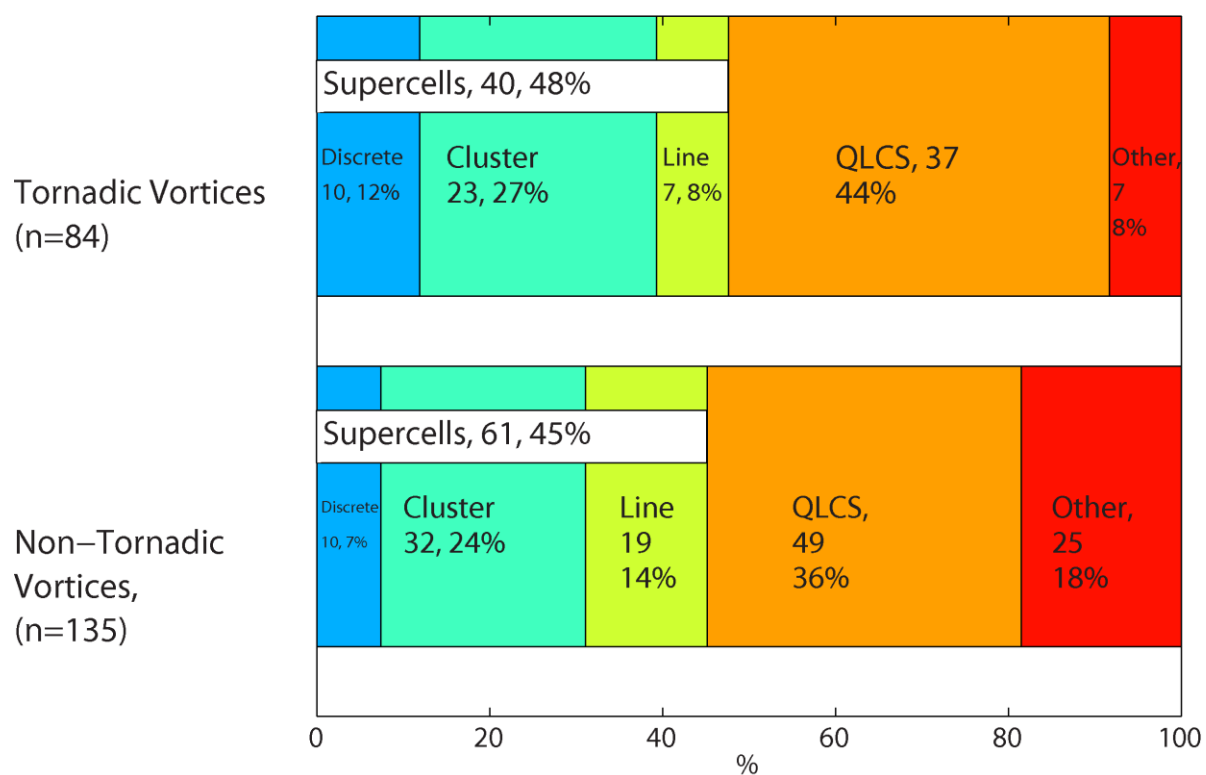


FIG. 4.3. Similar to FIG. 4.1, but comparing convective modes for the tornadic vortices used in the azimuthal shear climatology for which convective mode data was available from the Smith et al. (2012) database, and the non-tornadic vortices, whose convective modes were classified by the author.

Vortex Tracks and Distance from Radar

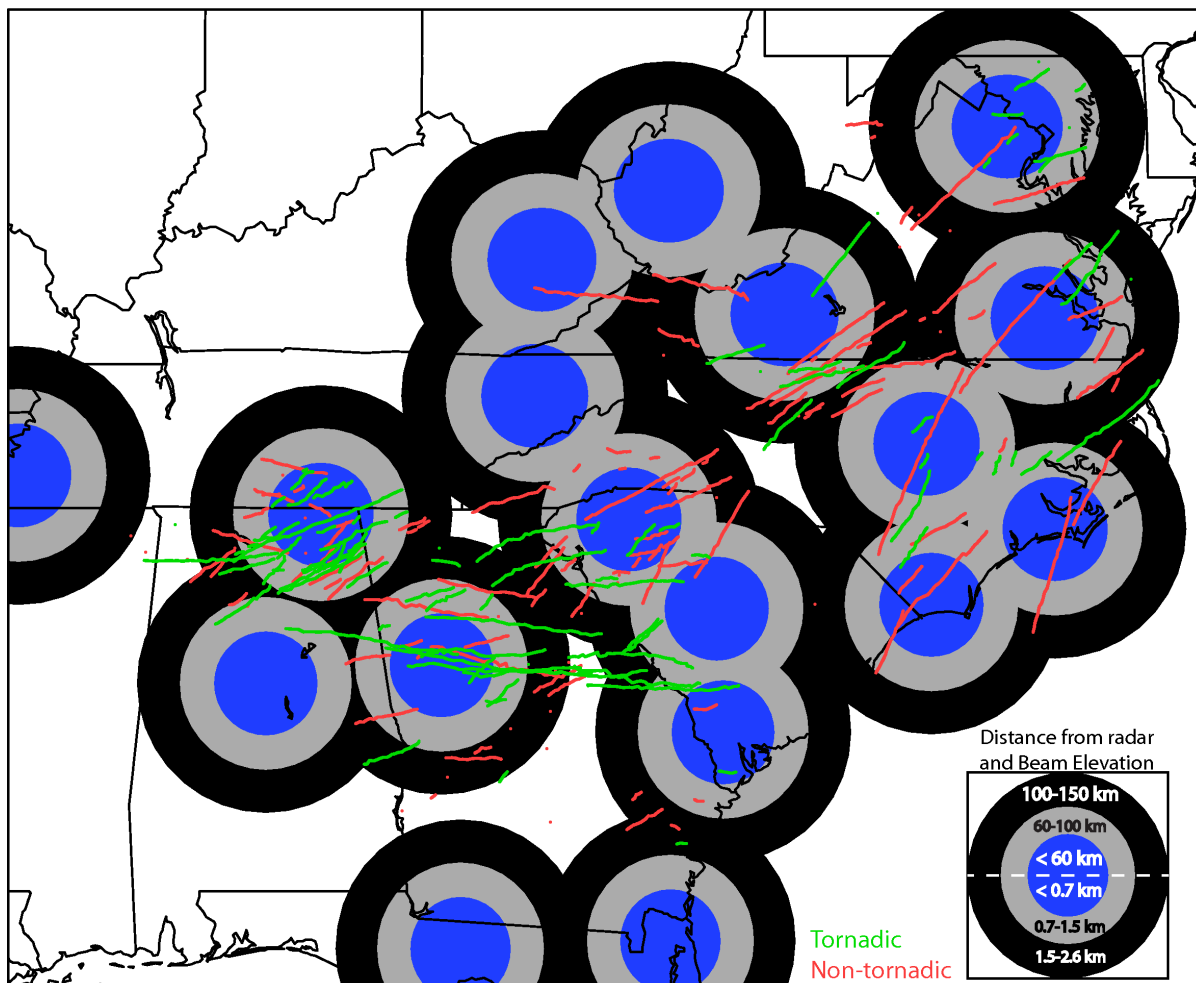


FIG. 4.4. Tracks of the 95 tornadic vortices (green lines) and 135 non-tornadic vortices (red lines) in this study (see section 3.3.2 for tracking methods). Concentric circles indicate range bins for the radars used in this study (vortices more than 150 km from the nearest radar are placed in the > 100 km range bin). Ranges included in each bin are shown in the top of the legend, and approximate elevations of the 0.5 degree elevation scan for these ranges are shown in the bottom of the legend. The Robins AFB radar (KJGX) was only used in a couple cases when archived super-resolution velocity data was available, and is not included in this figure.

Azimuthal Shear for All Vortices within 60 km of a Radar

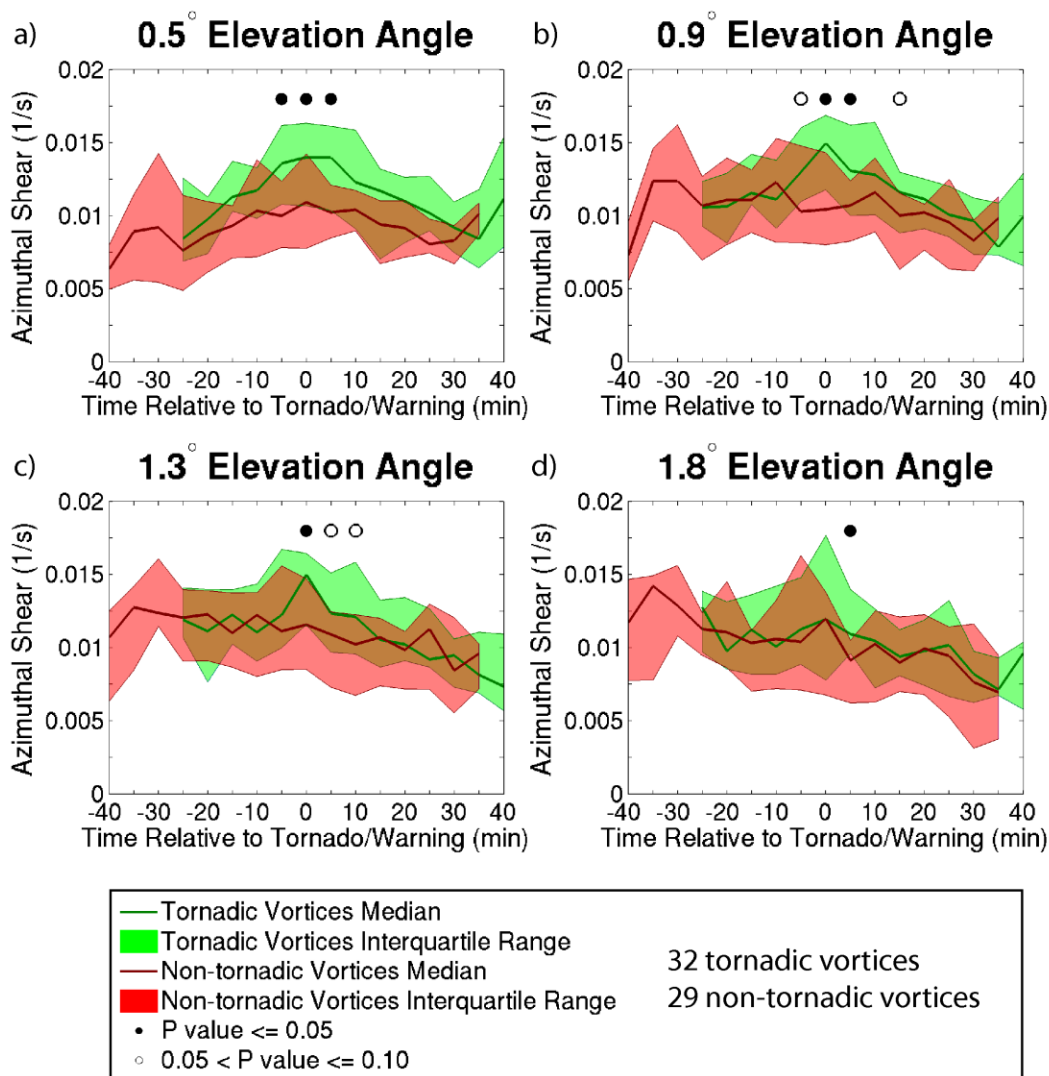


FIG. 4.5. Azimuthal shear time series, plotted relative to the time of first HSLC tornado touchdown for the tornadic vortices (green) and first HSLC tornado warning issuance for the non-tornadic vortices (red), for all vortices ≤ 60 km from nearest radar, at the (a) 0.5 degree, (b) 0.9 degree, (c) 1.3 degree, and (d) 1.8 degree elevation scans. Solid lines indicate median values while filled regions indicate the interquartile range. Solid circles above the time series indicate statistically significant positive differences at the 95% confidence level (p value ≤ 0.05) in median azimuthal shear between the tornadic and non-tornadic vortices at that time using the Wilcoxon rank-sum difference of medians test, and open circles indicate statistically significant differences at the 90% confidence level (p value between 0.05 and 0.1).

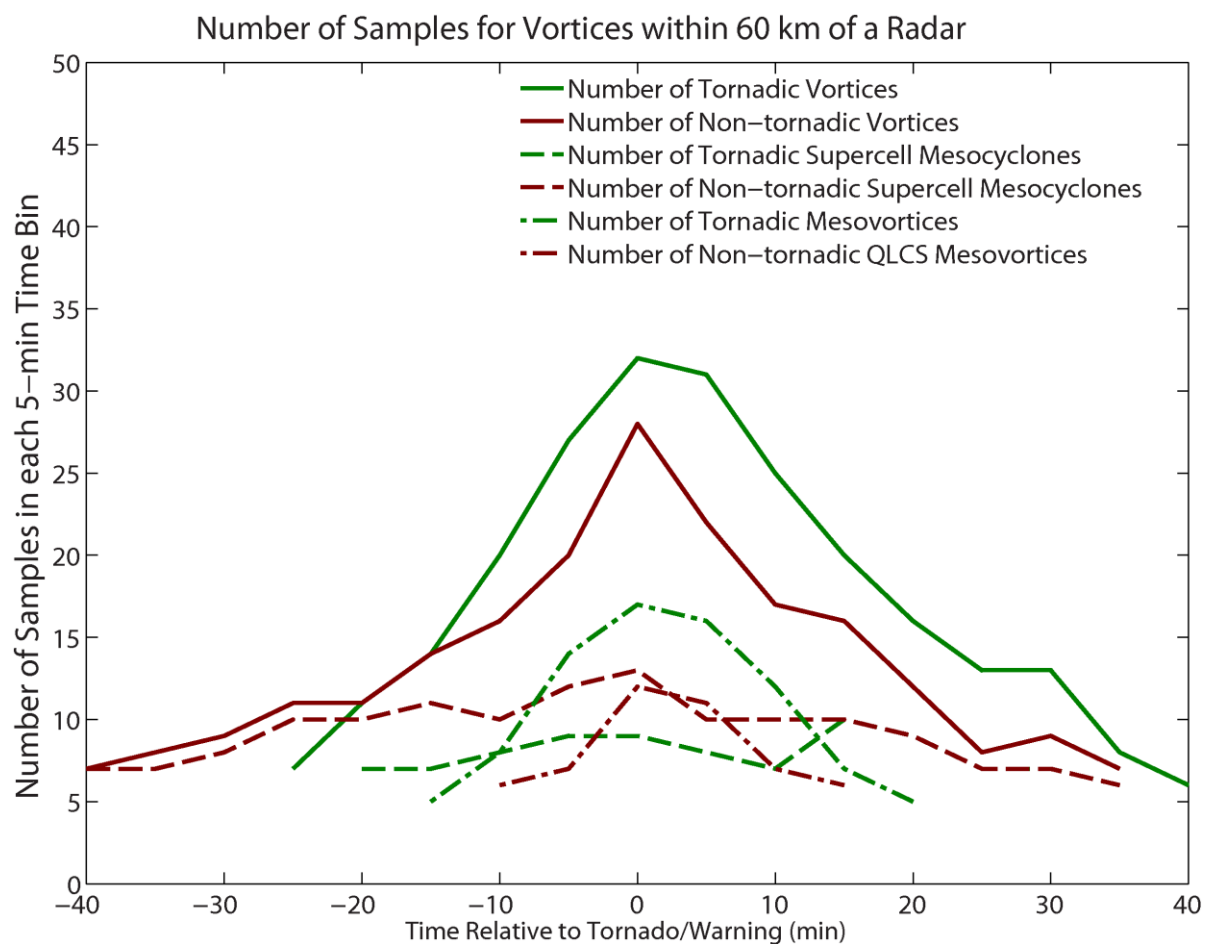


FIG. 4.6. Number of samples (volume scans where vortices existed) in each 5-min time bin, for all tornadic (green) and non-tornadic (red) vortices within 60 km of a radar (solid lines), only tornadic and non-tornadic supercell mesocyclones within 60 km of a radar (dashed lines), and only tornadic and non-tornadic QLCS mesovortices within 60 km of a radar (dash-dotted lines).

Azimuthal Shear for Supercell Mesocyclones within 60 km of a Radar

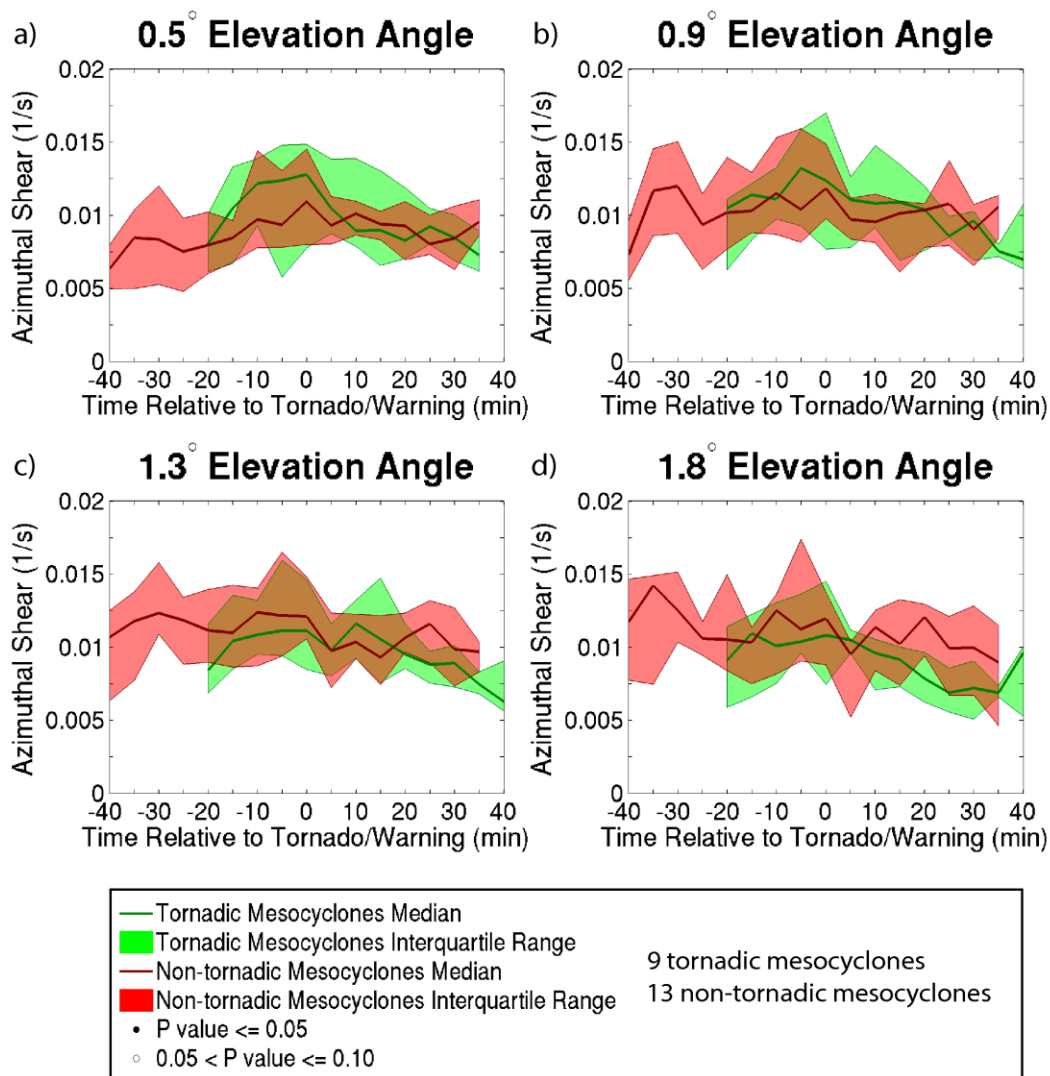


FIG. 4.7. Similar to FIG. 4.5, but for only tornadic and non-tornadic supercell mesocyclones within 60 km of the radar, using convective modes from the SPC database for the tornadic vortices, and convective modes assigned by the author for the non-tornadic vortices.

Azimuthal Shear for QLCS Mesovortices within 60 km of a Radar

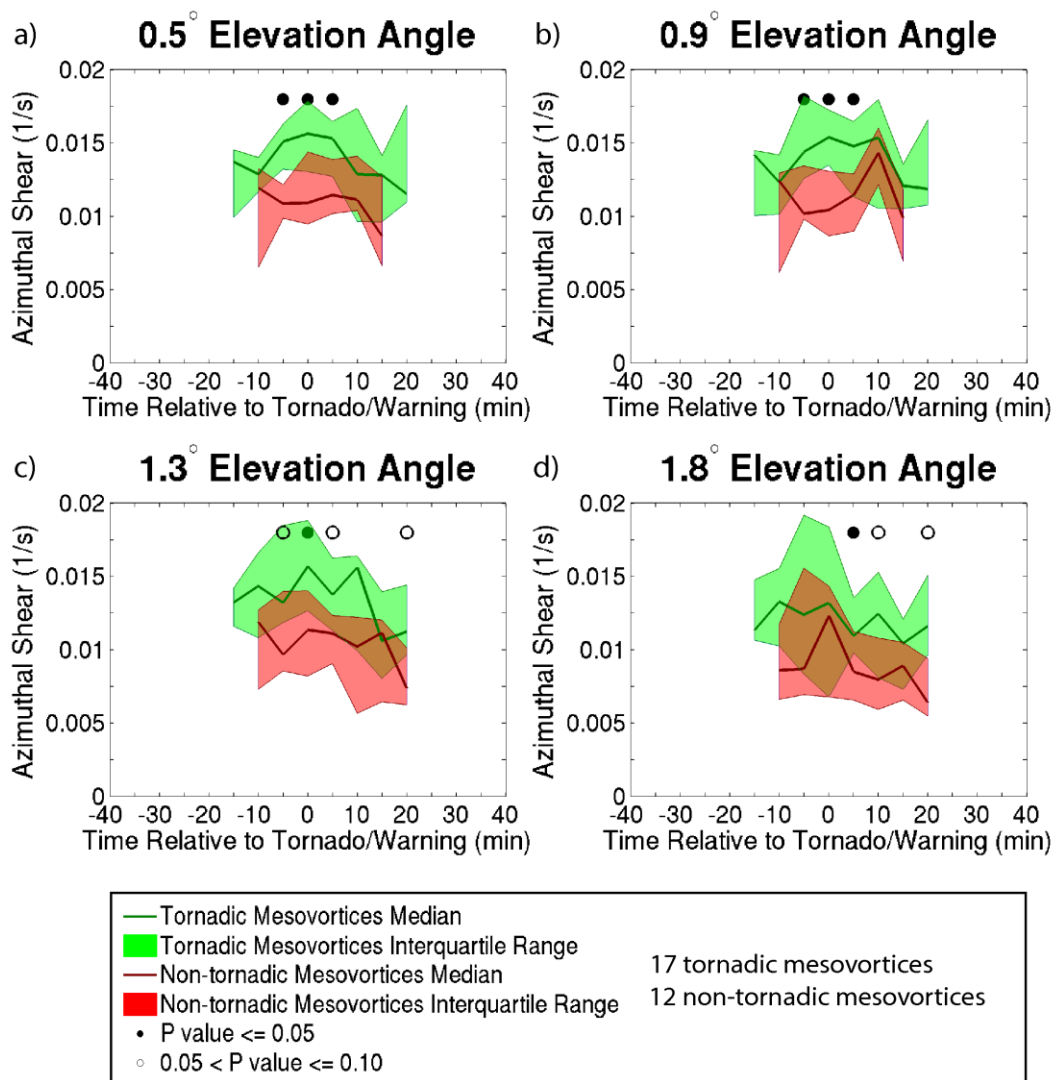


FIG. 4.8. Similar to FIG. 4.7, but only tornadic and non-tornadic QLCS mesovortices within 60 km of the radar.

Azimuthal Shear for EF1+ Tornadoes within 60 km of a Radar

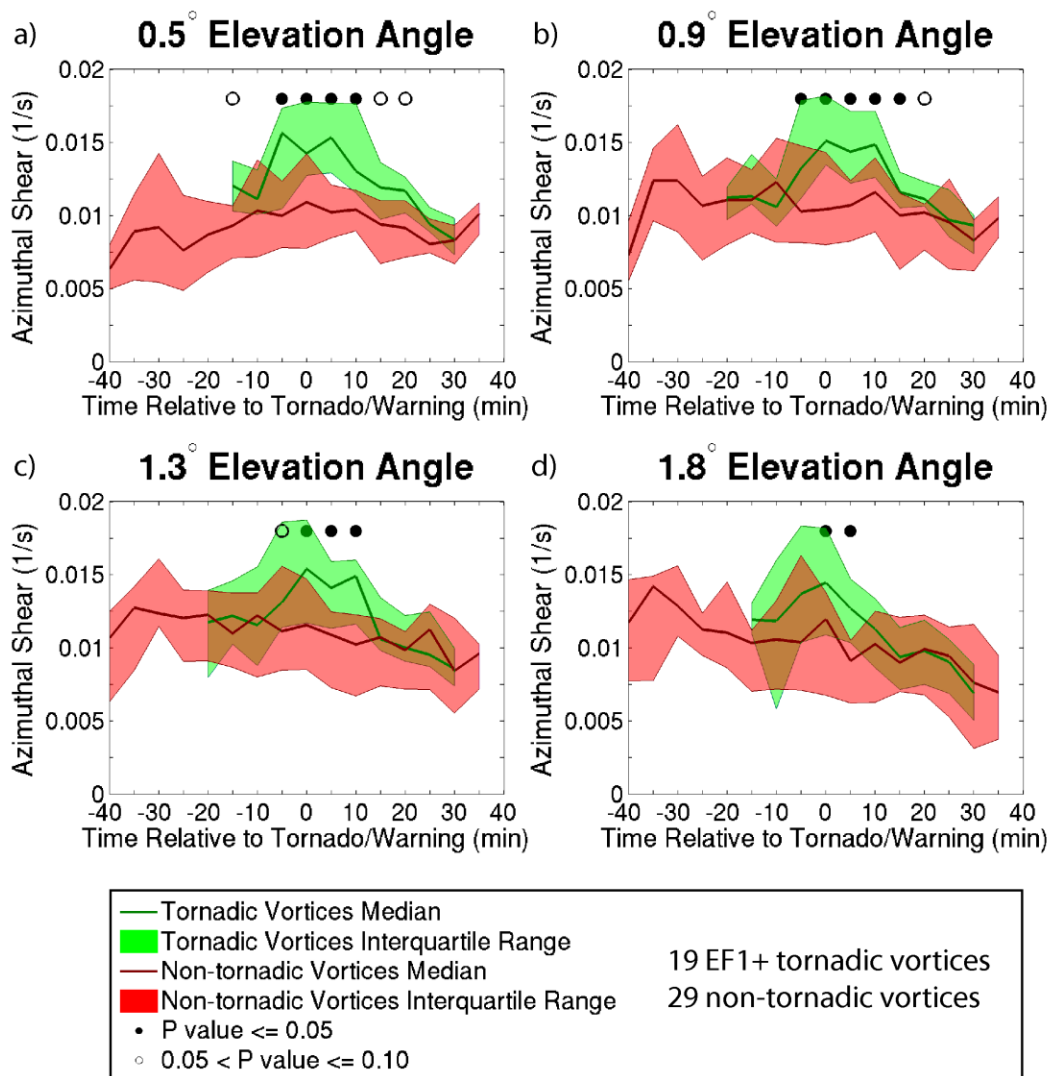
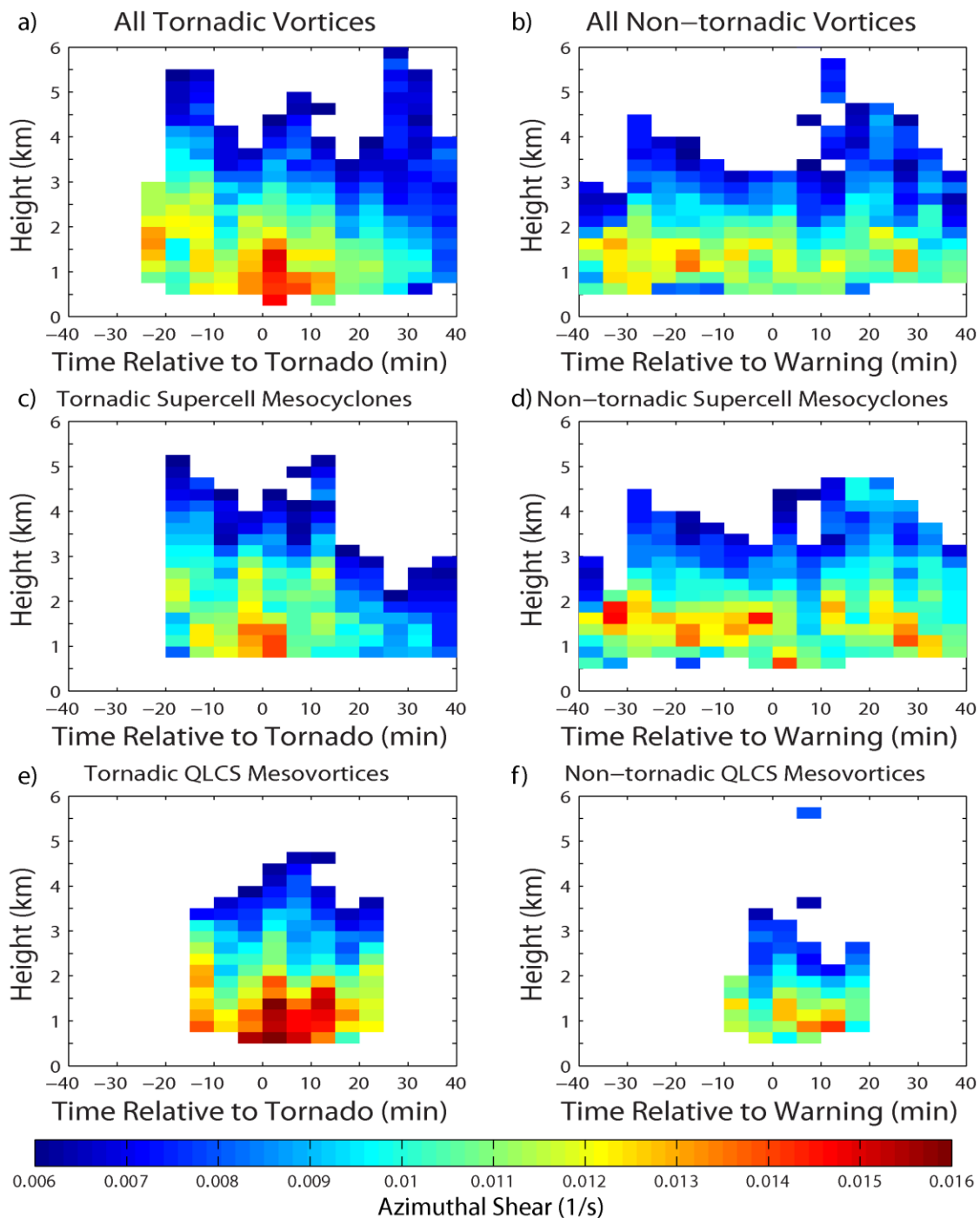


FIG. 4.9. Same as FIG. 4.5, but only tornadic vortices whose first HSLC tornado was rated EF1 or greater, and all non-tornadic vortices, within 60 km of a radar.

FIG. 4.10. Time-height cross-sections of median azimuthal shear for vortices within 60 km of the radar, including (a) all tornadic vortices, (b) all non-tornadic vortices, (c) only tornadic supercell mesocyclones, (d) only non-tornadic supercell mesocyclones, (e) only tornadic QLCS mesovortices, and (f) only non-tornadic QLCS mesovortices. Values are plotted relative to the time of the first HSLC tornado touchdown (for tornadic vortices) or the first HSLC false alarm warning (for non-tornadic vortices). Azimuthal shear for each vortex at each time bin was linearly interpolated to a 250 m vertical grid, and then the median azimuthal shear value at each time-height gridpoint was calculated. Beam heights were calculated assuming standard atmospheric refraction, and are affected by spreading of the beam in the vertical. Values were only plotted if at least five vortices were present at each time-height gridpoint.

Azimuthal Shear for All Vortices within 60 km of a Radar



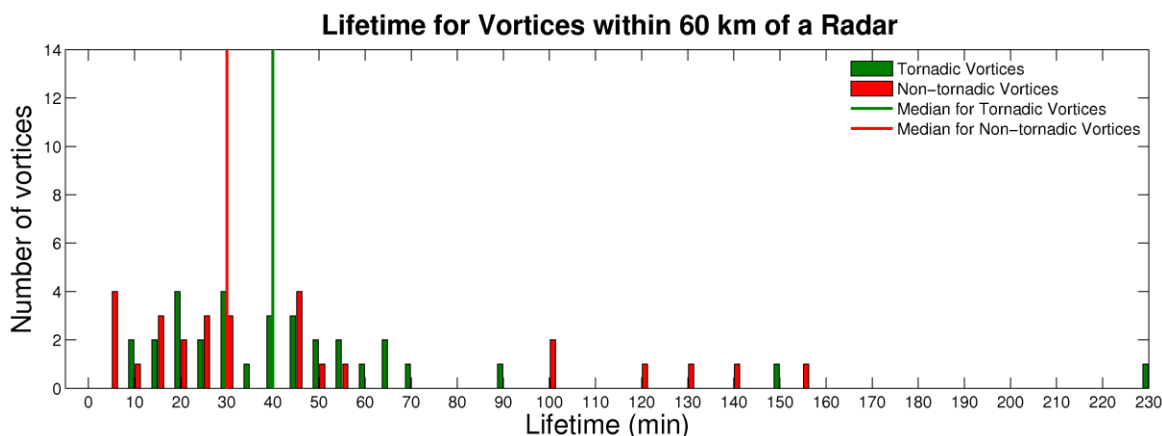


FIG. 4.11. Histogram of vortex lifetime (trackable time with azimuthal shear $\geq 0.006 \text{ s}^{-1}$ at any elevation scan in the lowest 2 km, using a single radar) for all tornadic (green) and non-tornadic (red) vortices within 60 km of a radar at the time of the tornado/warning. Median lifetimes are indicated by vertical lines.

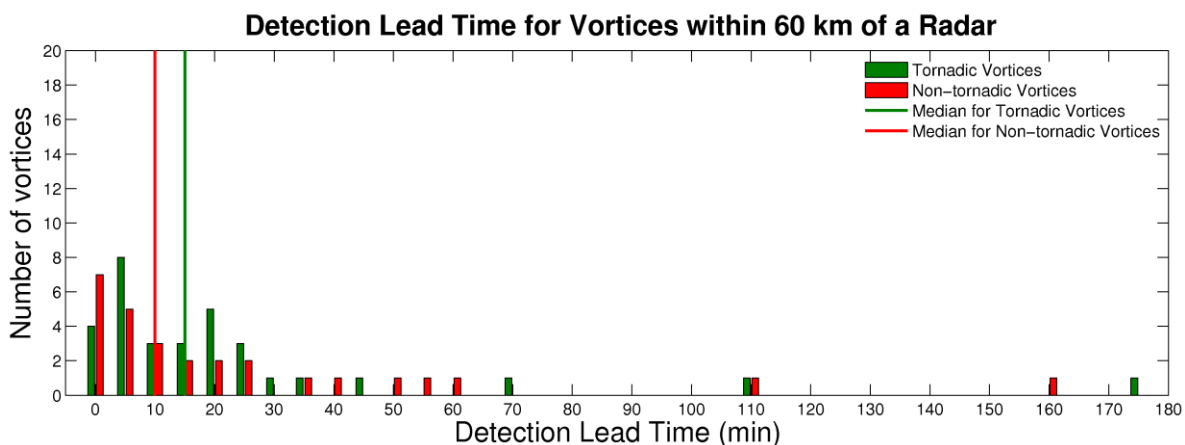


FIG. 4.12. Similar to FIG. 4.11 but for vortex detection lead time, the length of time the vortex could be tracked with azimuthal shear $\geq 0.006 \text{ s}^{-1}$ prior to first HSLC tornado touchdown (for tornadic vortices) or first HSLC false alarm warning issuance (for non-tornadic vortices), for vortices within 60 km of the radar at the time of the tornado/warning.

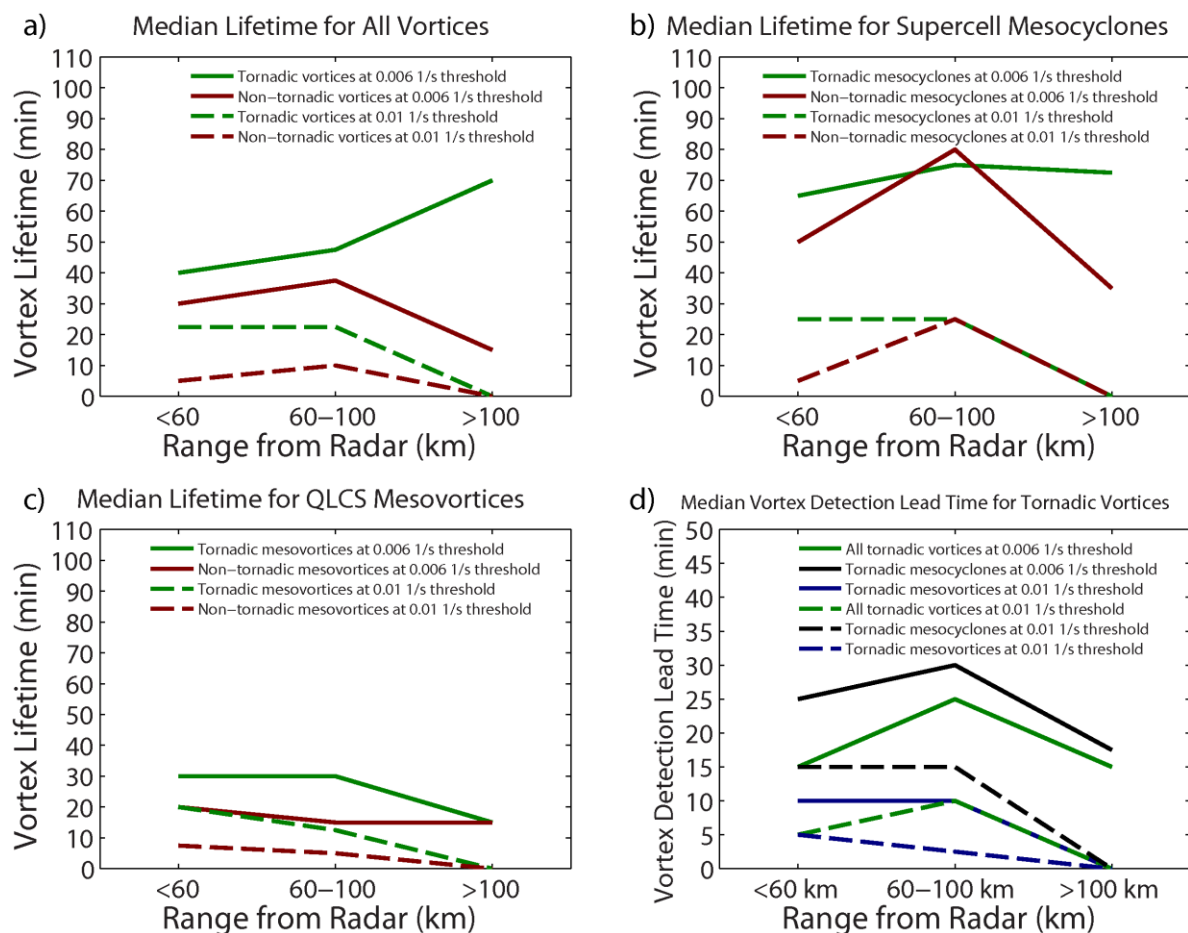


FIG. 4.13. (a–c) Median vortex lifetime with azimuthal shear above 0.006 s^{-1} (solid lines; calculated using same method as in FIG. 4.11 caption) and 0.01 s^{-1} (dashed lines; consecutive time including the time of the tornado/warning that the vortex maintained azimuthal shear at or above this threshold, only using the 0.5 degree elevation scan) as a function of range from the radar at time of the tornado/warning, for (a) all vortices, (b) only supercell mesocyclones, and (c) only QLCS mesovortices. (d) Median tornadoic vortex detection lead time at the 0.006 s^{-1} azimuthal shear threshold (solid lines; using same method as in FIG. 4.12 caption) and 0.01 s^{-1} azimuthal shear threshold (dashed lines; consecutive time prior to the tornado that the vortex maintained azimuthal shear above this threshold including the 5-min time bin prior to the tornado, only using the 0.5 degree elevation scan) as a function of range from the radar at the time of the tornado/warning for all tornadoic vortices (green), only tornadoic supercell mesocyclones (black), and only tornadoic QLCS mesovortices (blue).

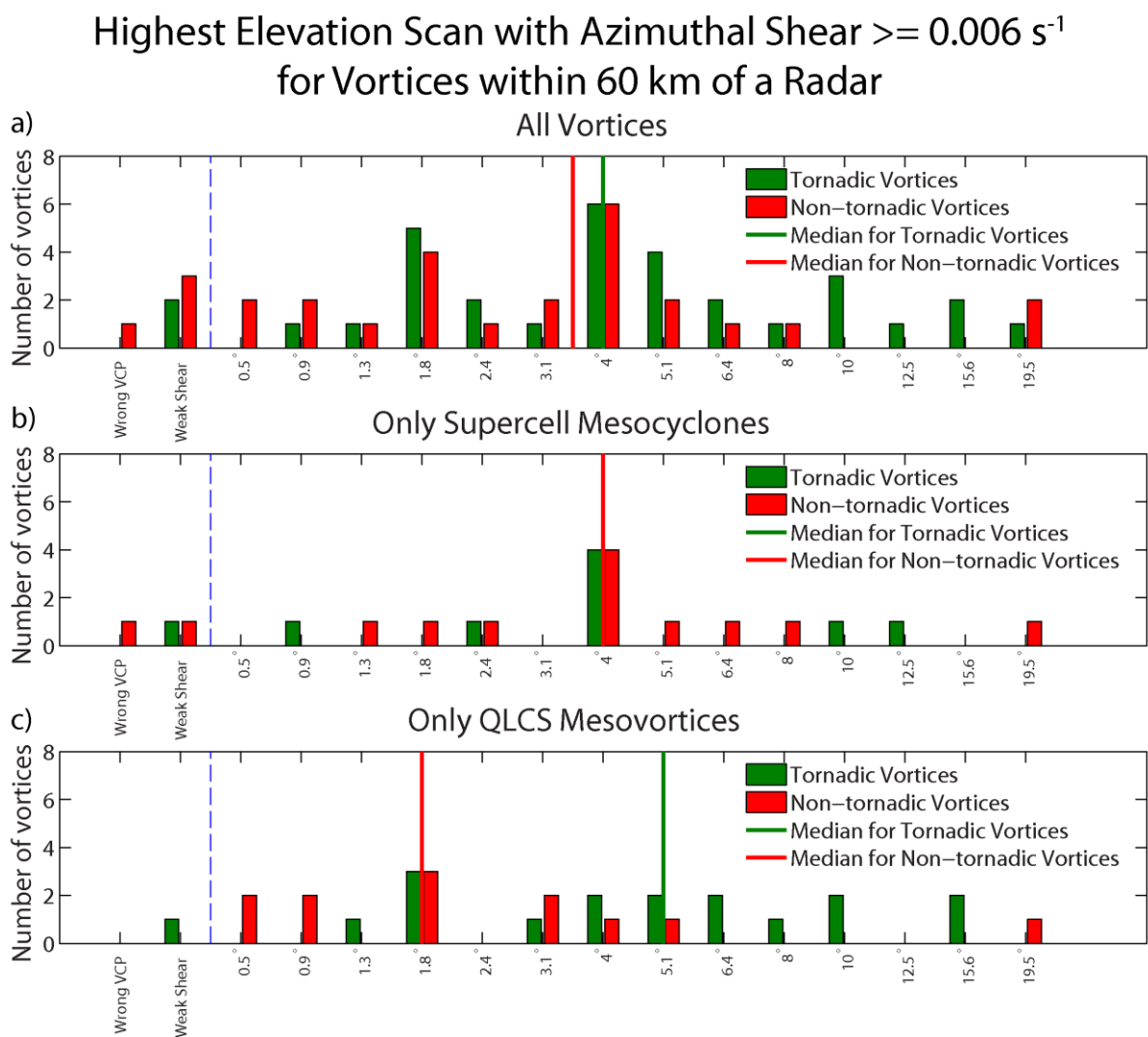


FIG. 4.14. Highest radar elevation scan with azimuthal shear at or above 0.006 s^{-1} at time of tornado/false alarm warning for tornadic (green) and non-tornadic (red) vortices within 60 km of the radar for (a) all vortices, (b) only supercell mesocyclones, and (c) only QLCS mesovortices. Median values are indicated by vertical lines. On the left side, “wrong VCP” indicates vortices that occurred when the radar was in a VCP with different elevation scans from the majority of cases, and “weak shear” indicates that the vortex did not have azimuthal shear above 0.006 s^{-1} at the base scan. These two categories were not included in median calculations.

Azimuthal Shear for All Vortices 60-100 km from a Radar

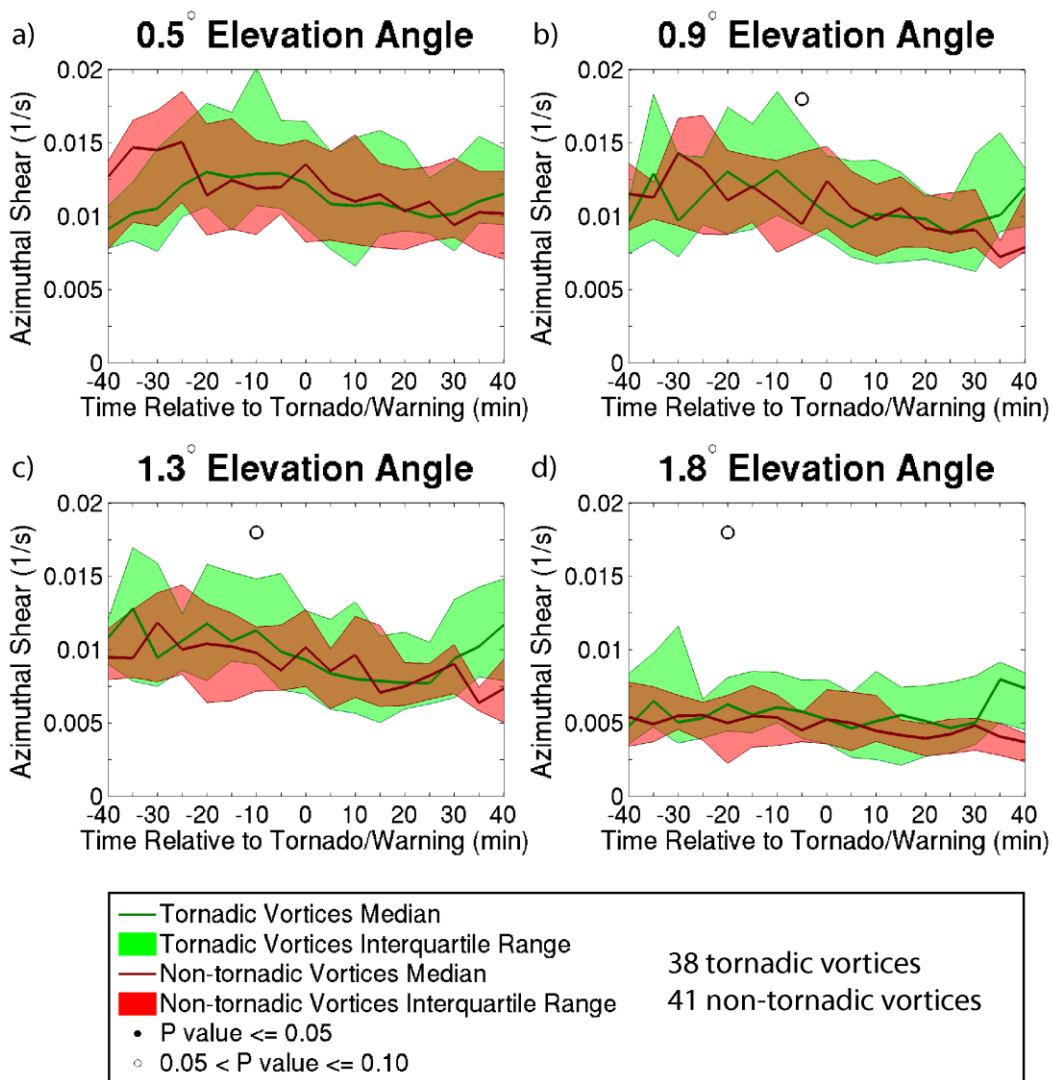


FIG. 4.15. Similar to FIG. 4.5, but for all vortices 60-100 km from the radar.

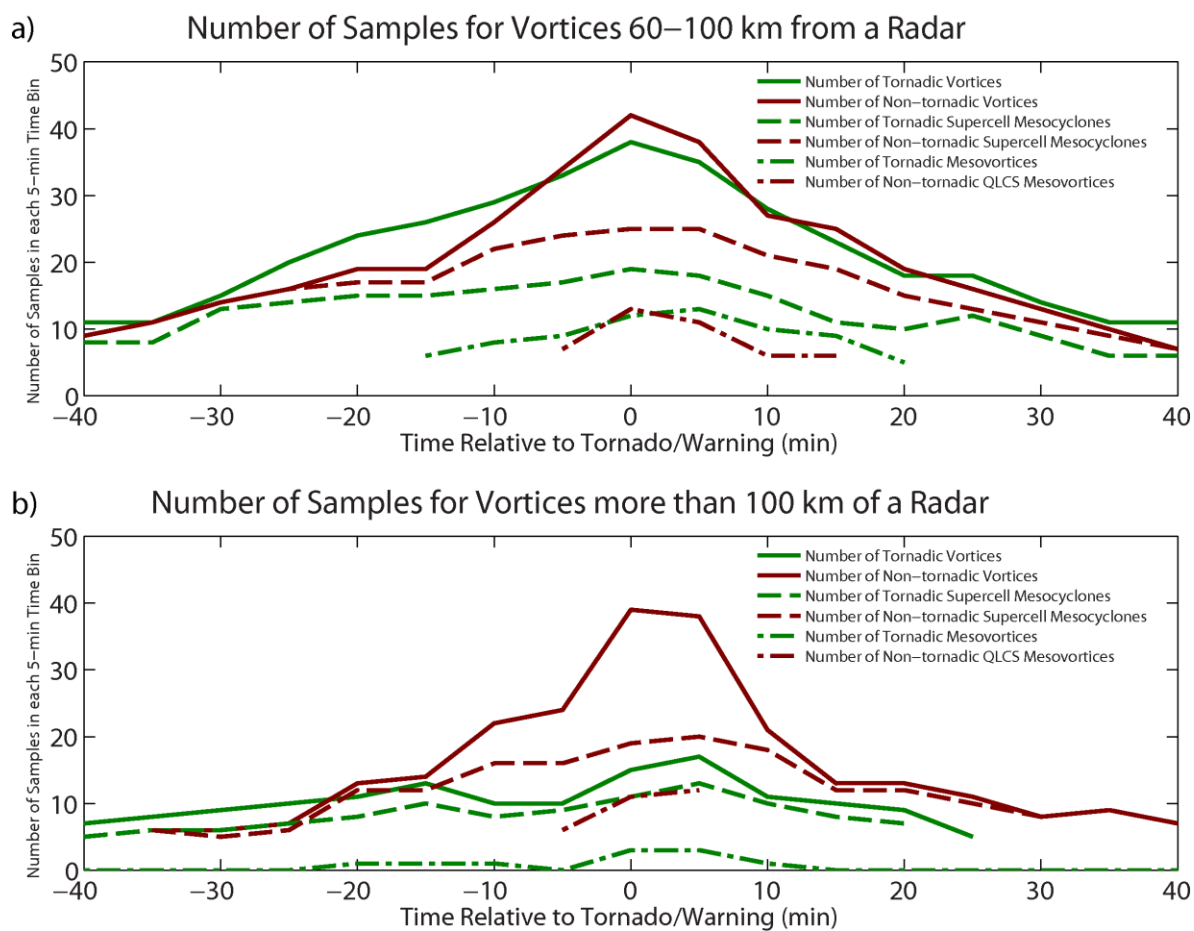


FIG. 4.16. Similar to FIG. 4.6, but for (a) all vortices 60-100 km from the radar and (b) all vortices more than 100 km from the radar.

Azimuthal Shear for All Vortices 60-100 km from a Radar

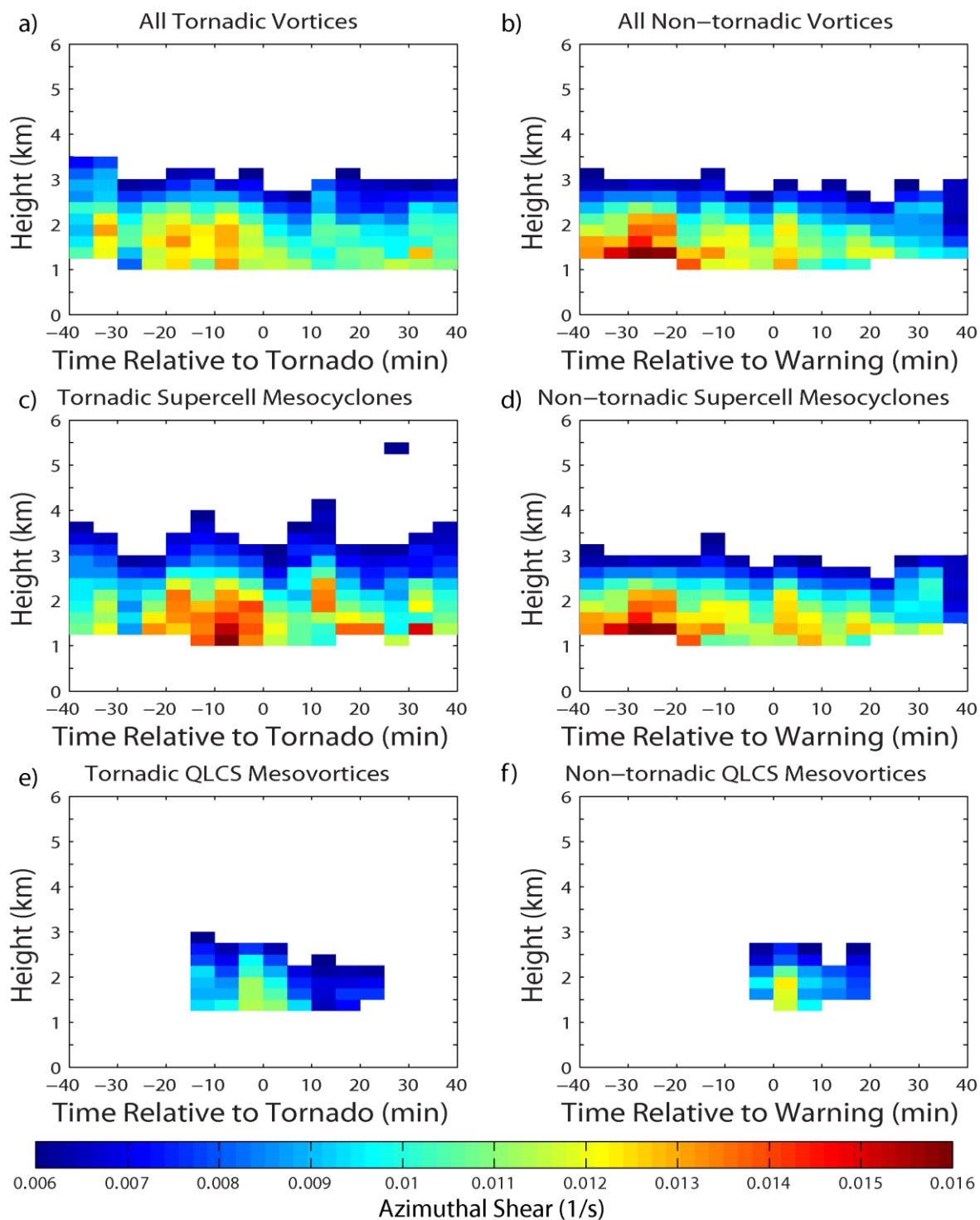


FIG. 4.17. Similar to FIG. 4.10, but for vortices 60-100 km from the radar.

Azimuthal Shear for Supercell Mesocyclones 60-100 km from a Radar

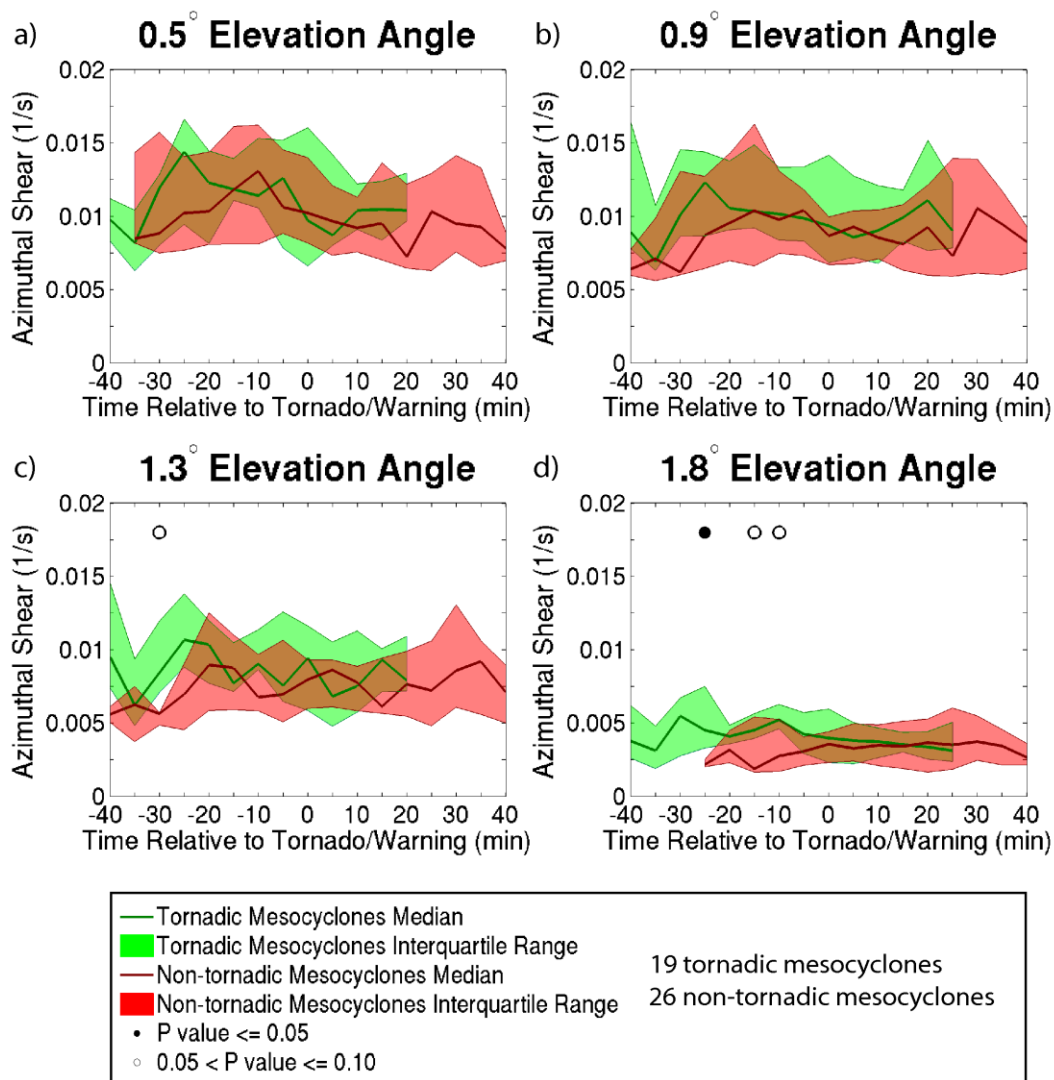


FIG. 4.18. Similar to FIG. 4.7, but for only supercell mesocyclones 60-100 km from the radar.

Azimuthal Shear for QLCS Mesovortices 60-100 km from a Radar

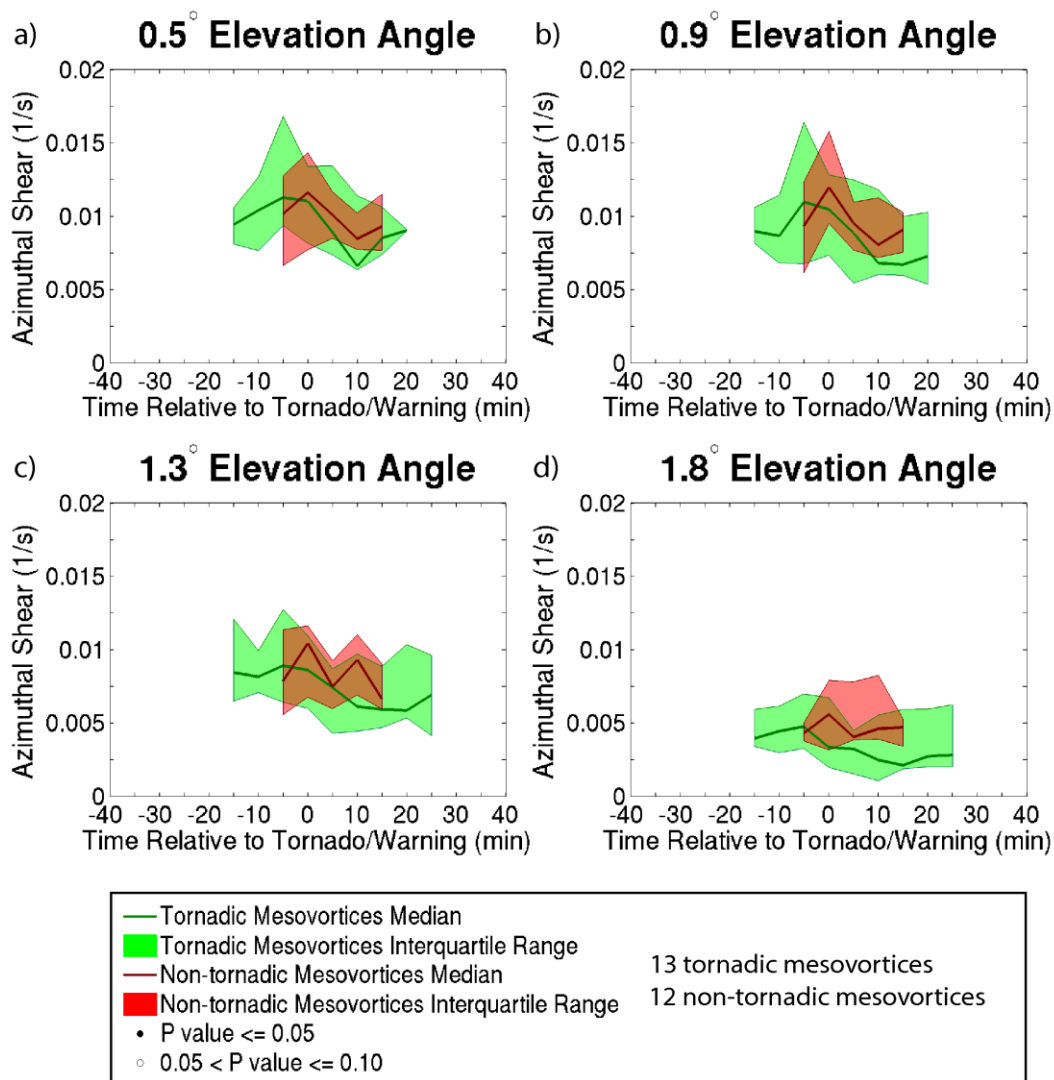


FIG. 4.19. Similar to FIG. 4.8, but for only QLCS mesovortices 60-100 km from the radar.

Azimuthal Shear for EF1+ Tornadoes 60-100 km from a Radar

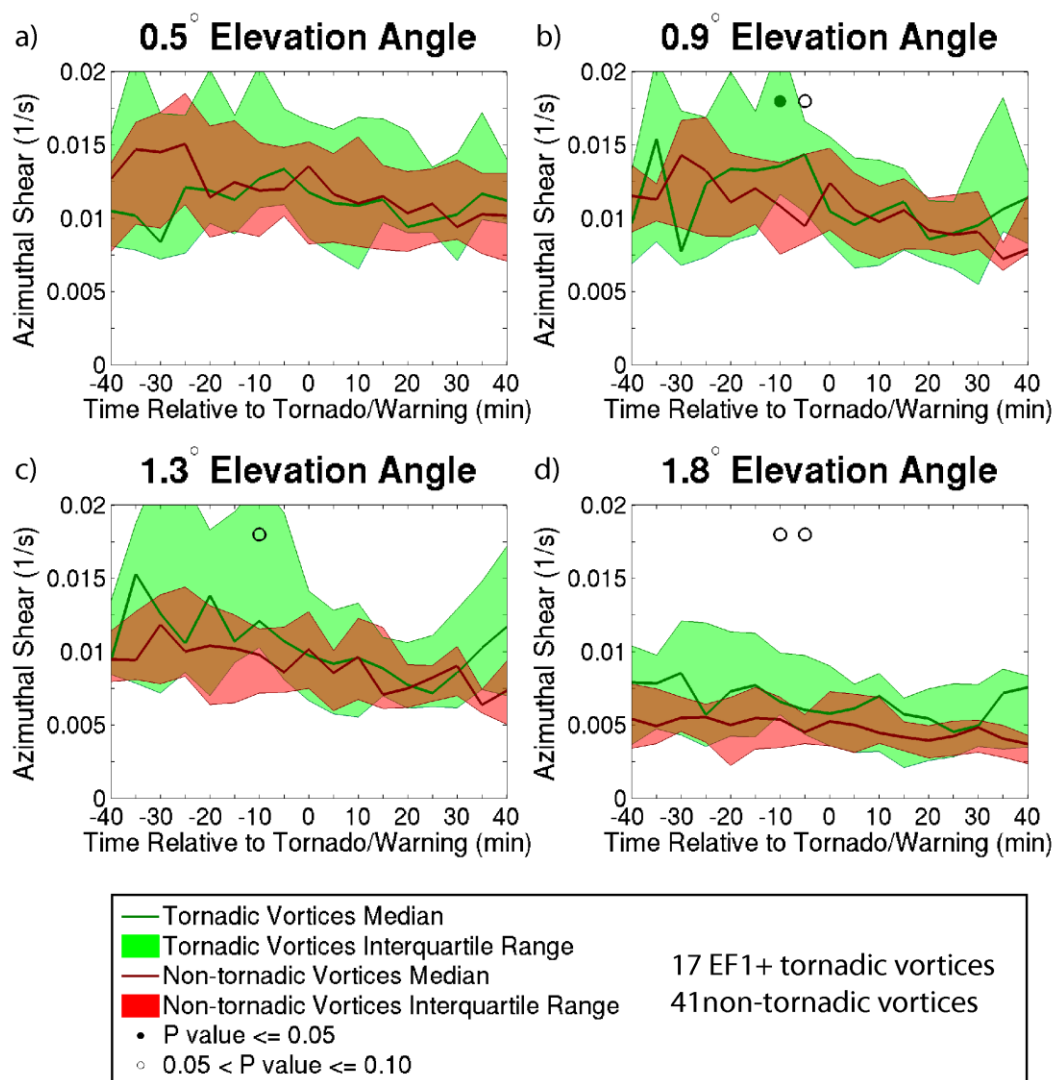


FIG. 4.20. Similar to FIG. 4.9, but only tornadic vortices whose first HSLC tornado was rated EF1 or greater, and all non-tornadic vortices, 60-100 km from the radar.

Azimuthal Shear for All Vortices more than 100 km from a Radar

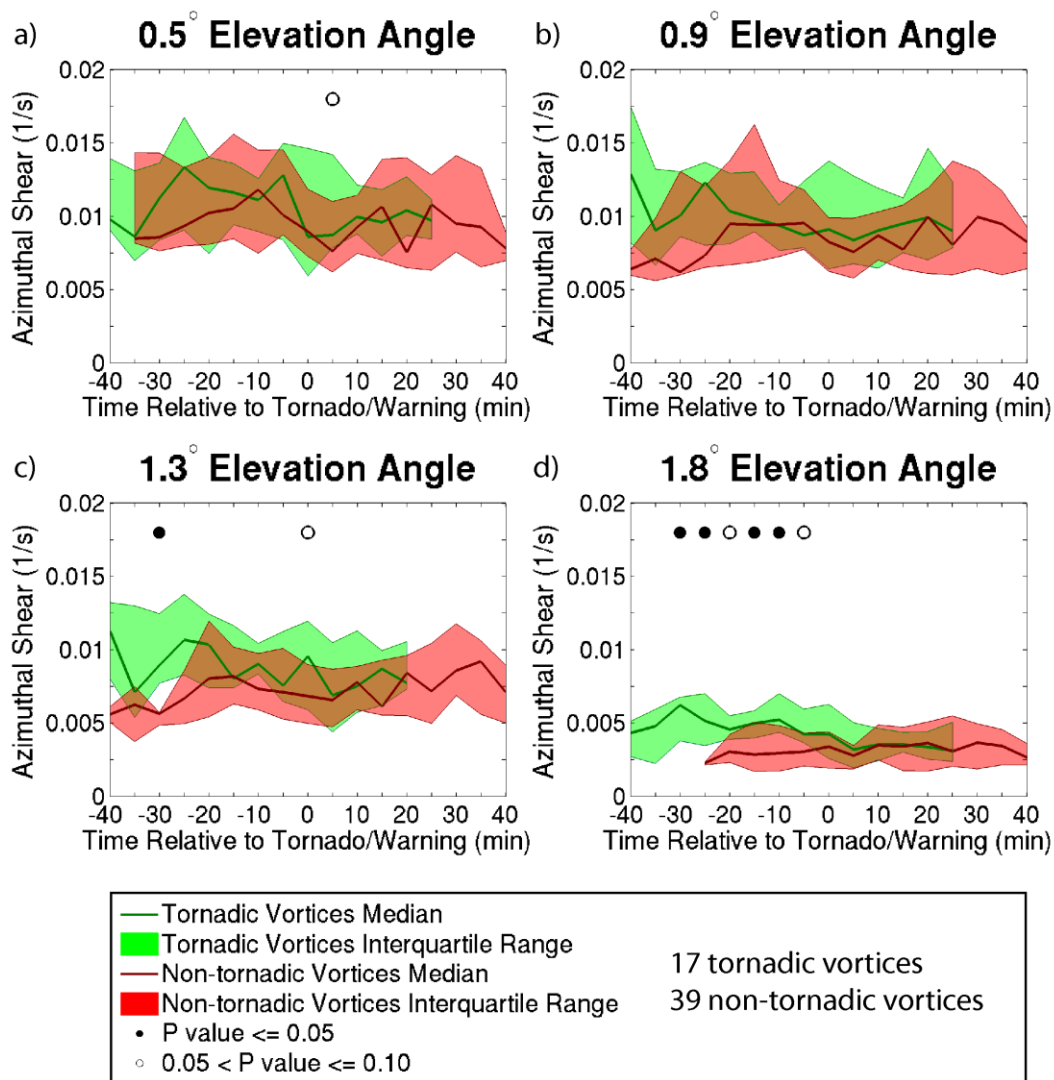


FIG. 4.21. Similar to FIG. 4.5, but for all tornadic and non-tornadic vortices more than 100 km from the radar.

Azimuthal Shear for All Vortices more than 100 km from a Radar

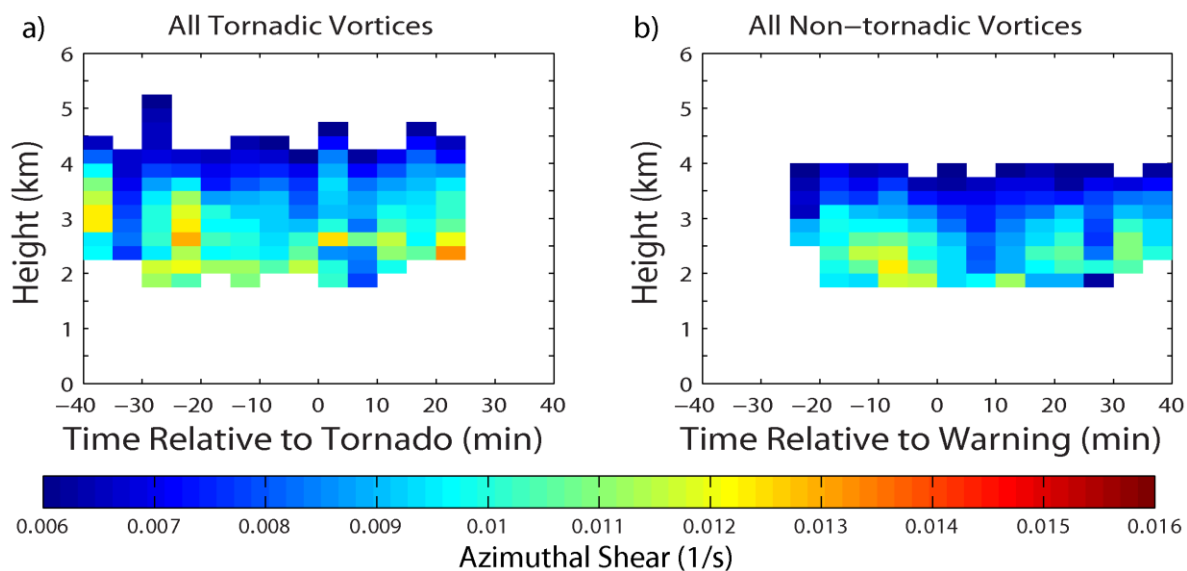


FIG. 4.22. Similar to FIG. 4.10, but for (a) tornadic and (b) non-tornadic vortices more than 100 km from the radar.

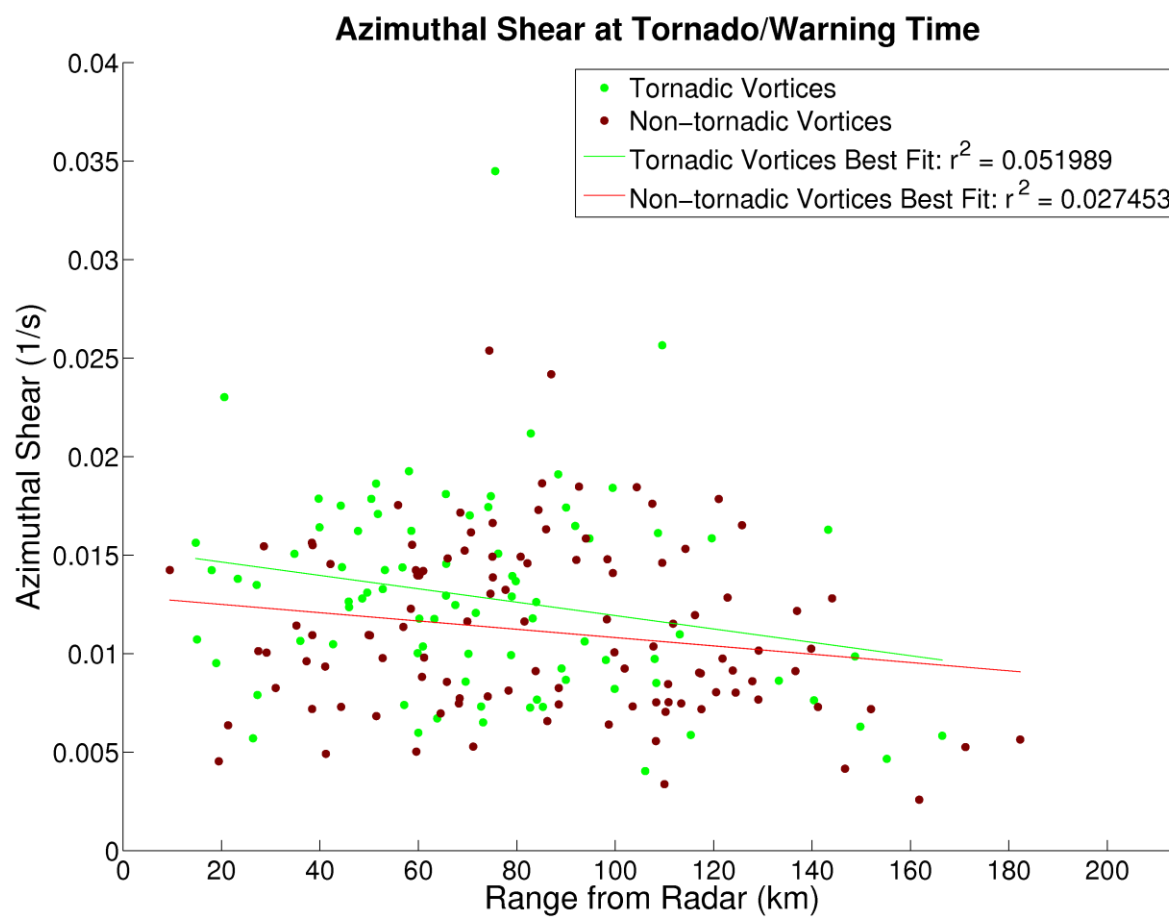


FIG. 4.23. Similar to FIG. 3.3, but azimuthal shear as a function of range is plotted for all tornadoic and non-tornadoic vortices.

ΔV for All Vortices within 60 km of a Radar

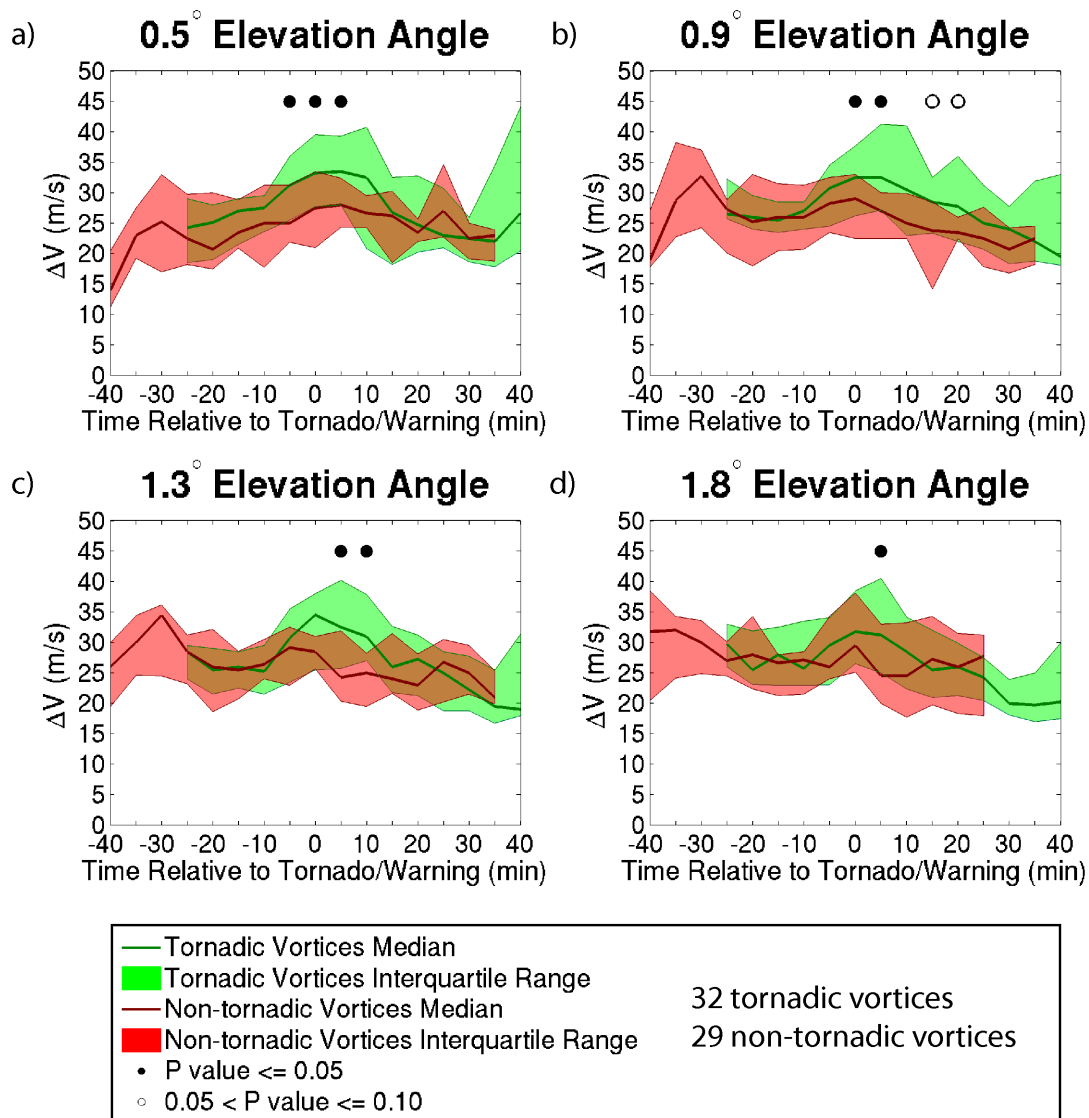


FIG. 4.24. Similar to FIG. 4.5, but ΔV instead of azimuthal shear, for all vortices within 60 km of the radar.

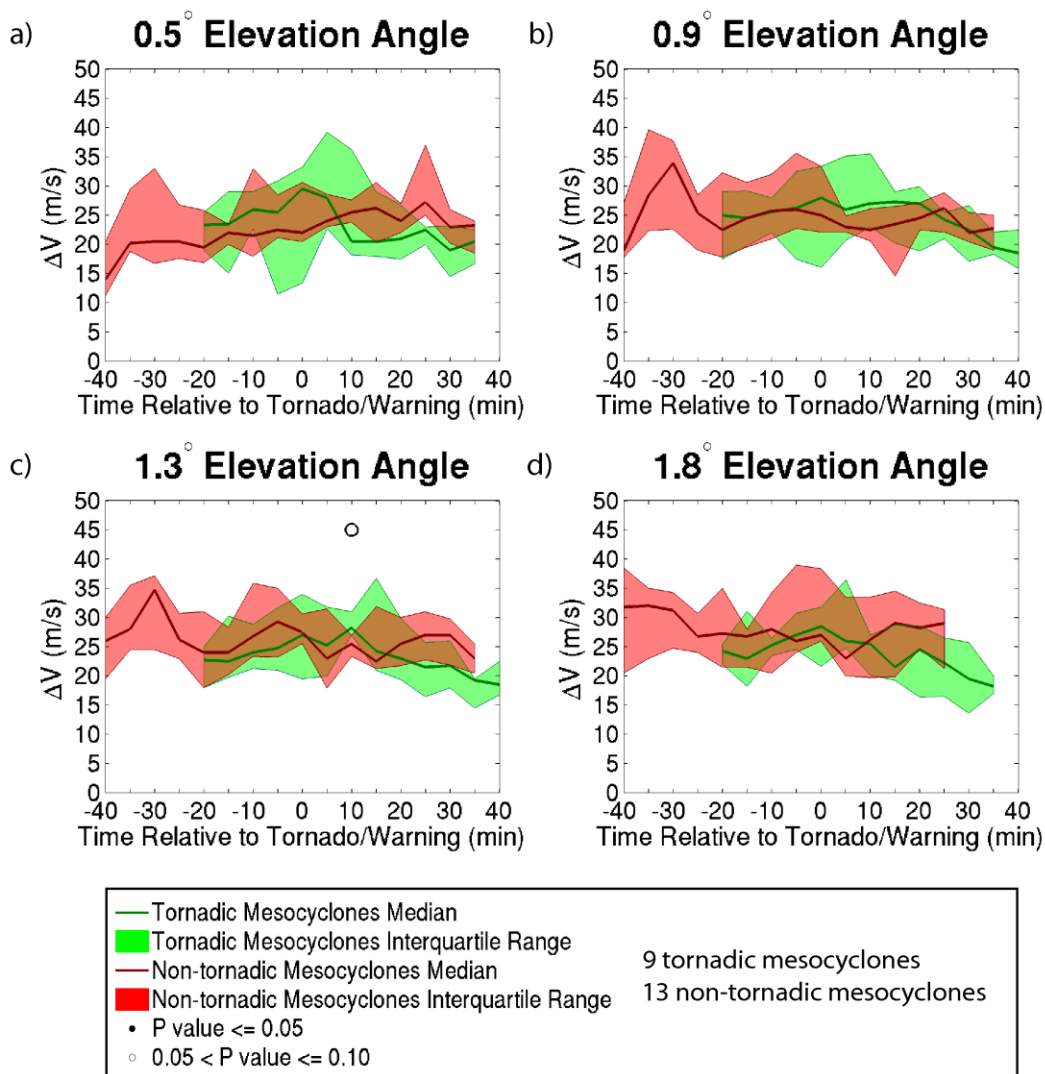
ΔV for Supercell Mesocyclones within 60 km of a Radar


FIG. 4.25. Similar to FIG. 4.7, but ΔV instead of azimuthal shear, for all tornadic and non-tornadic supercell mesocyclones within 60 km of the radar.

ΔV for QLCS Mesovortices within 60 km of a Radar

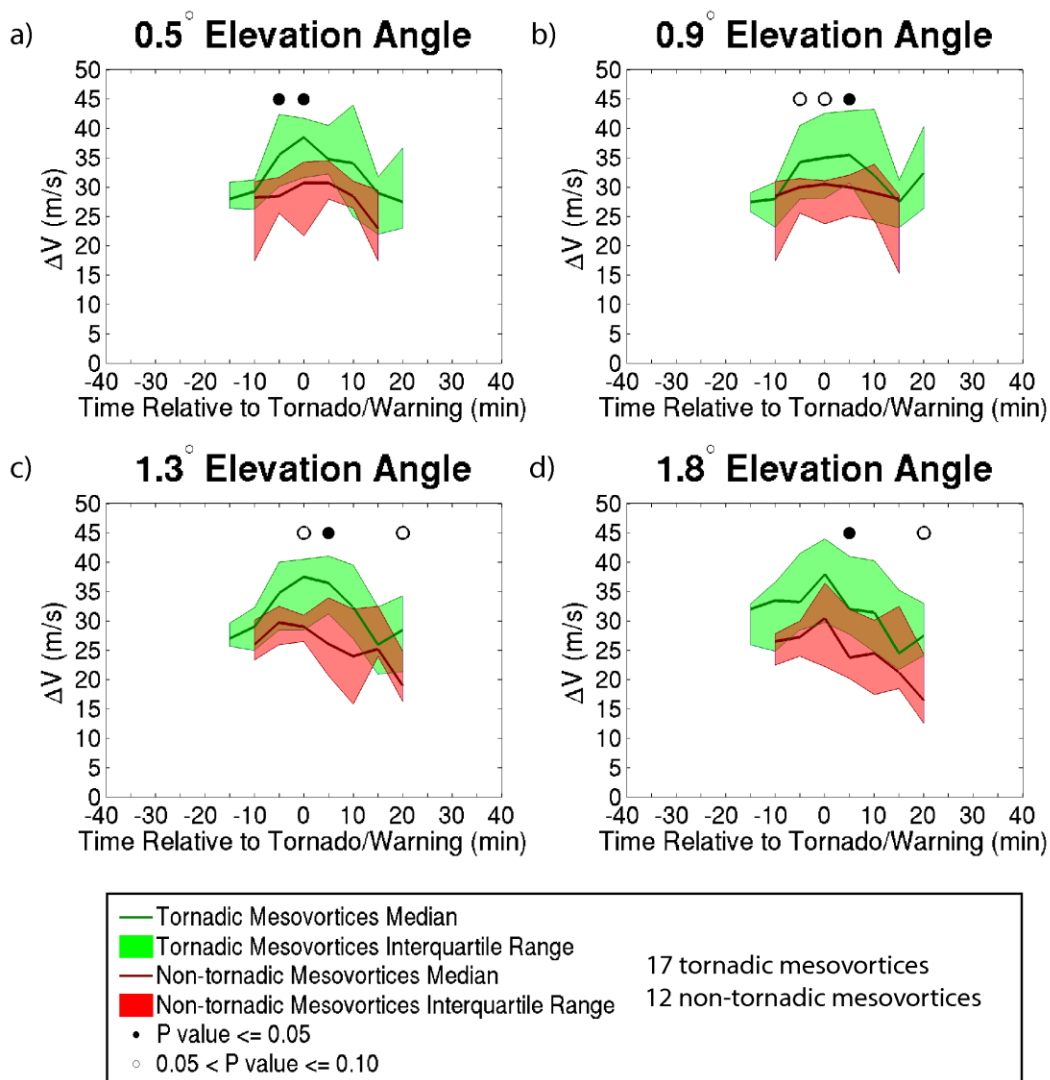


FIG. 4.26. Similar to FIG. 4.8, but ΔV instead of azimuthal shear, for all tornadic and non-tornadic QLCS mesovortices within 60 km of the radar.

ΔV for EF1+ Tornadoes within 60 km of a Radar

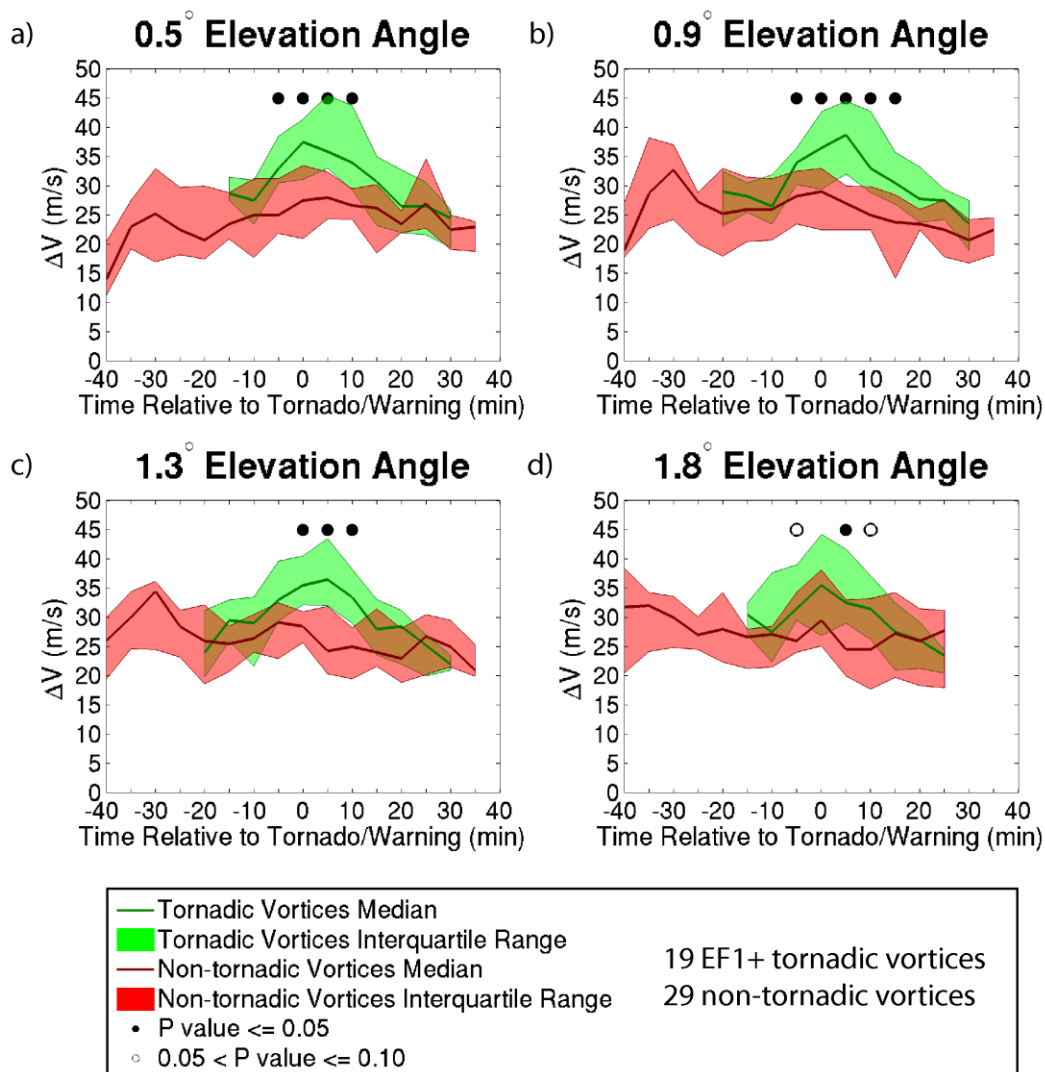


FIG. 4.27. Similar to FIG. 4.9, but ΔV instead of azimuthal shear, for only tornadoic vortices whose first HSLC tornado was rated EF1 or greater, and all non-tornadoic vortices within 60 km of the radar.

ΔV for All Vortices 60-100 km from a Radar

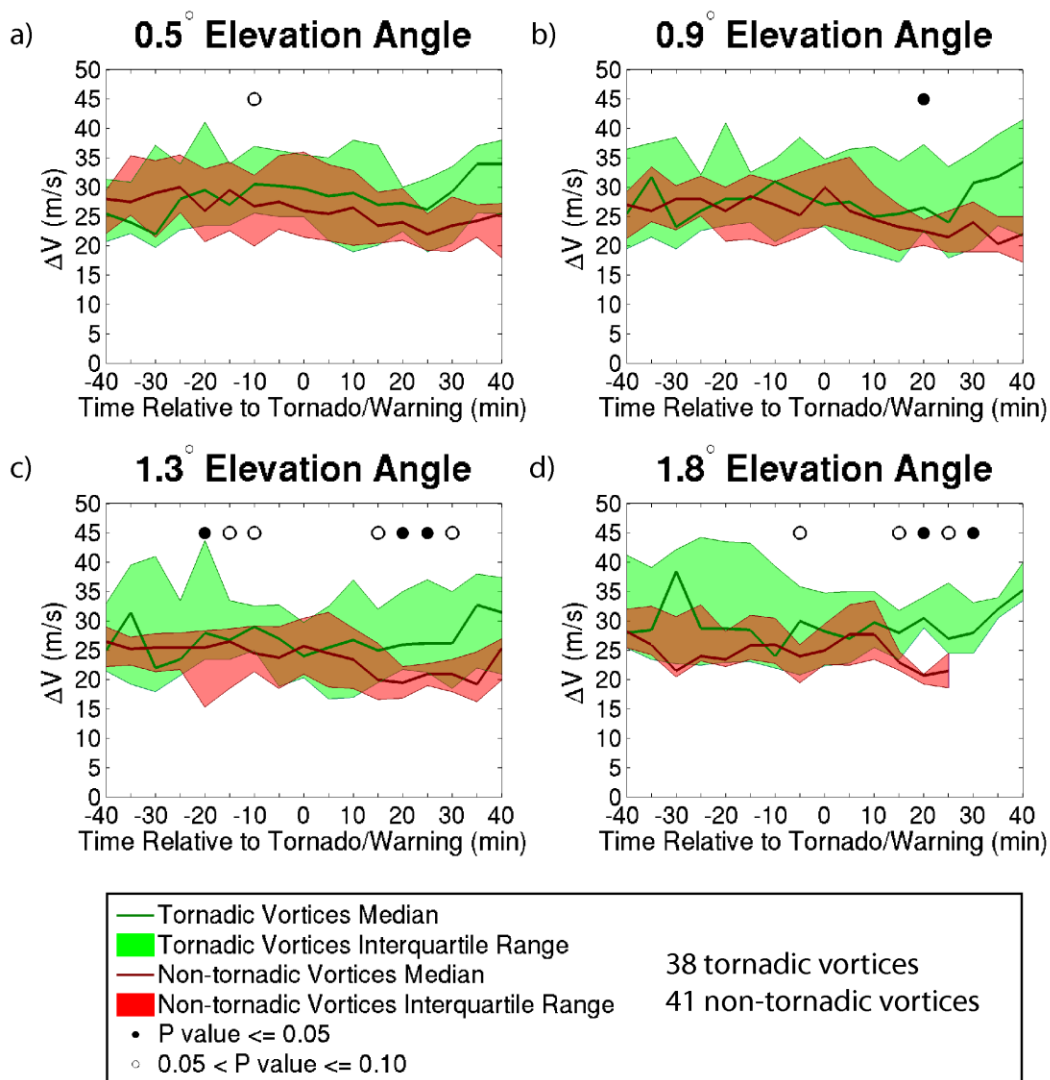


FIG. 4.28. Similar to FIG. 4.15, but ΔV instead of azimuthal shear, for all tornadic and non-tornadic vortices 60-100 km from the radar.

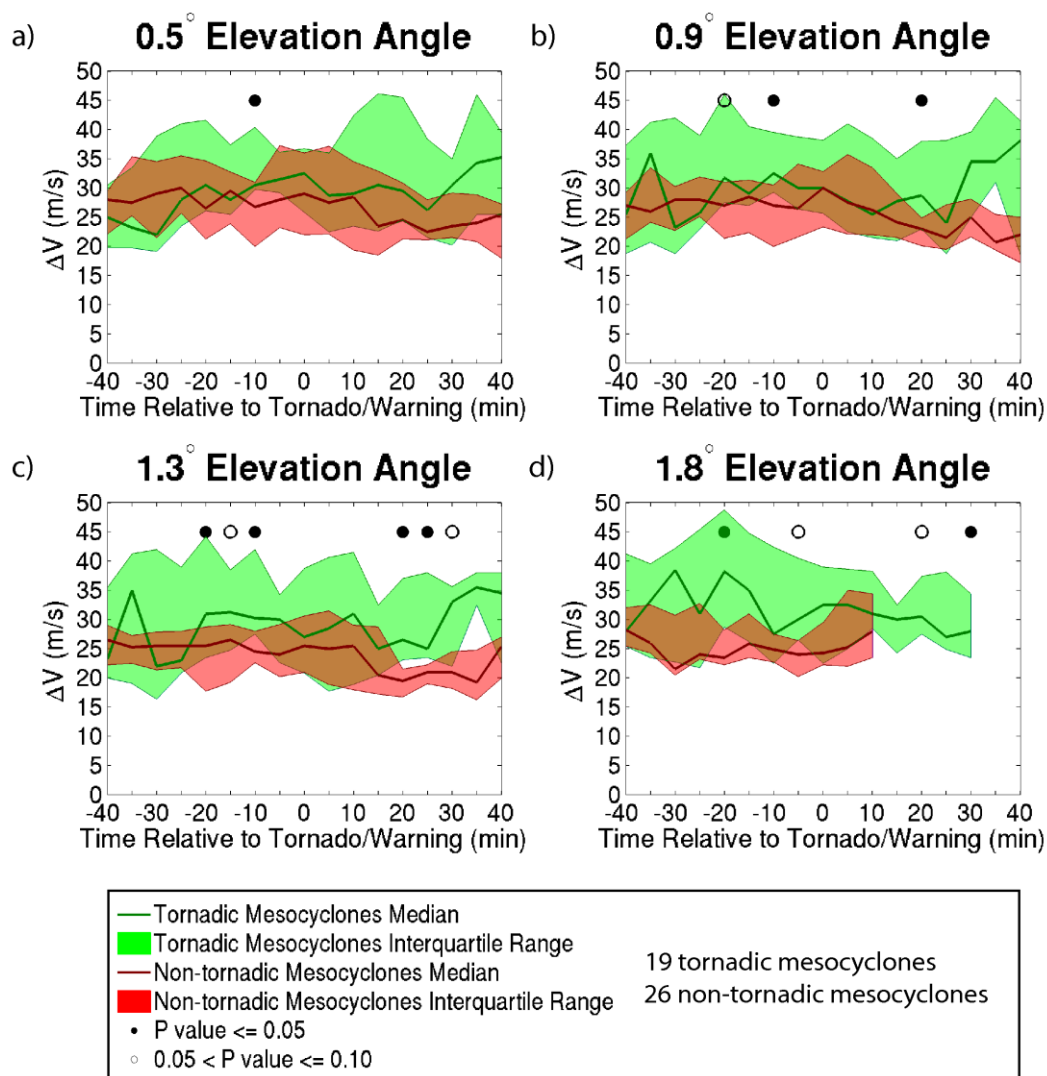
ΔV for Supercell Mesocyclones 60-100 km from a Radar


FIG. 4.29. Similar to FIG. 4.18, but ΔV instead of azimuthal shear, for only tornadic and non-tornadic supercell mesocyclones 60-100 km from the radar.

ΔV for EF1+ Tornadoes 60-100 km from a Radar

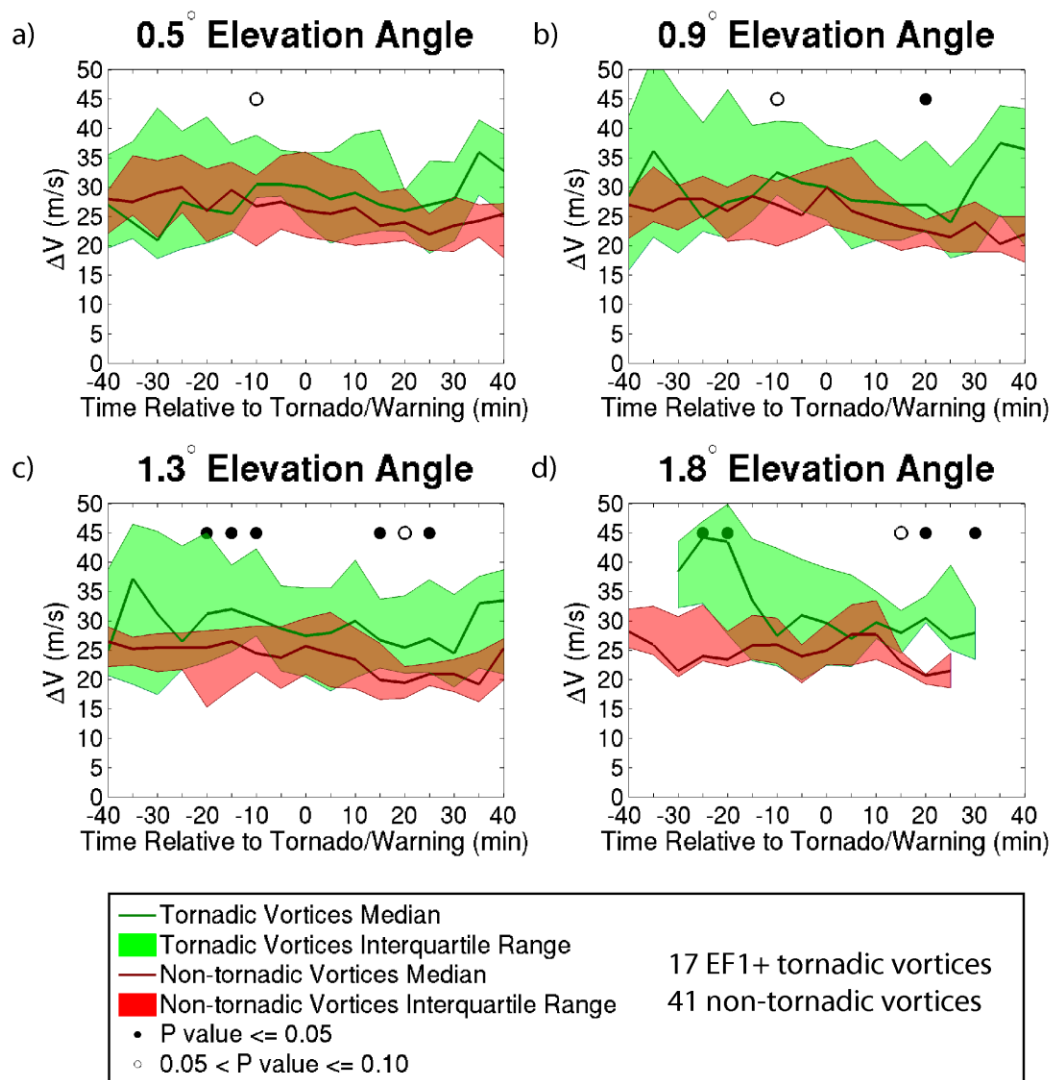


FIG. 4.30. Similar to FIG. 4.20, but ΔV instead of azimuthal shear, for only tornadic vortices whose first HSLC tornado was rated EF1 or greater, and all non-tornadic vortices 60-100 km from the radar.

ΔV for All Vortices more than 100 km from a Radar

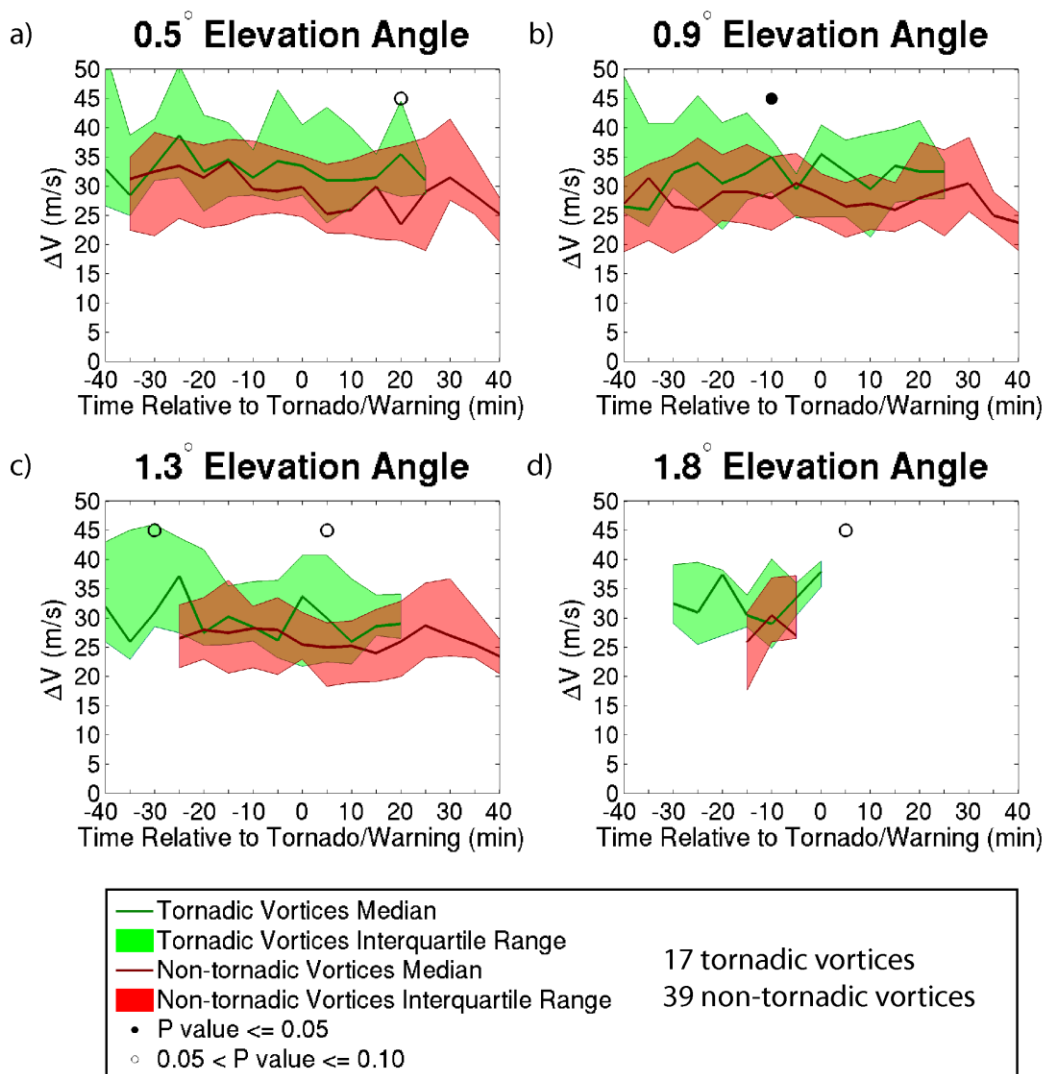


FIG. 4.31. Similar to FIG. 4.21, but ΔV instead of azimuthal shear, for all tornadic and non-tornadic vortices more than 100 km from the radar.

ΔV for EF1+ Tornadoes more than 100 km from a Radar

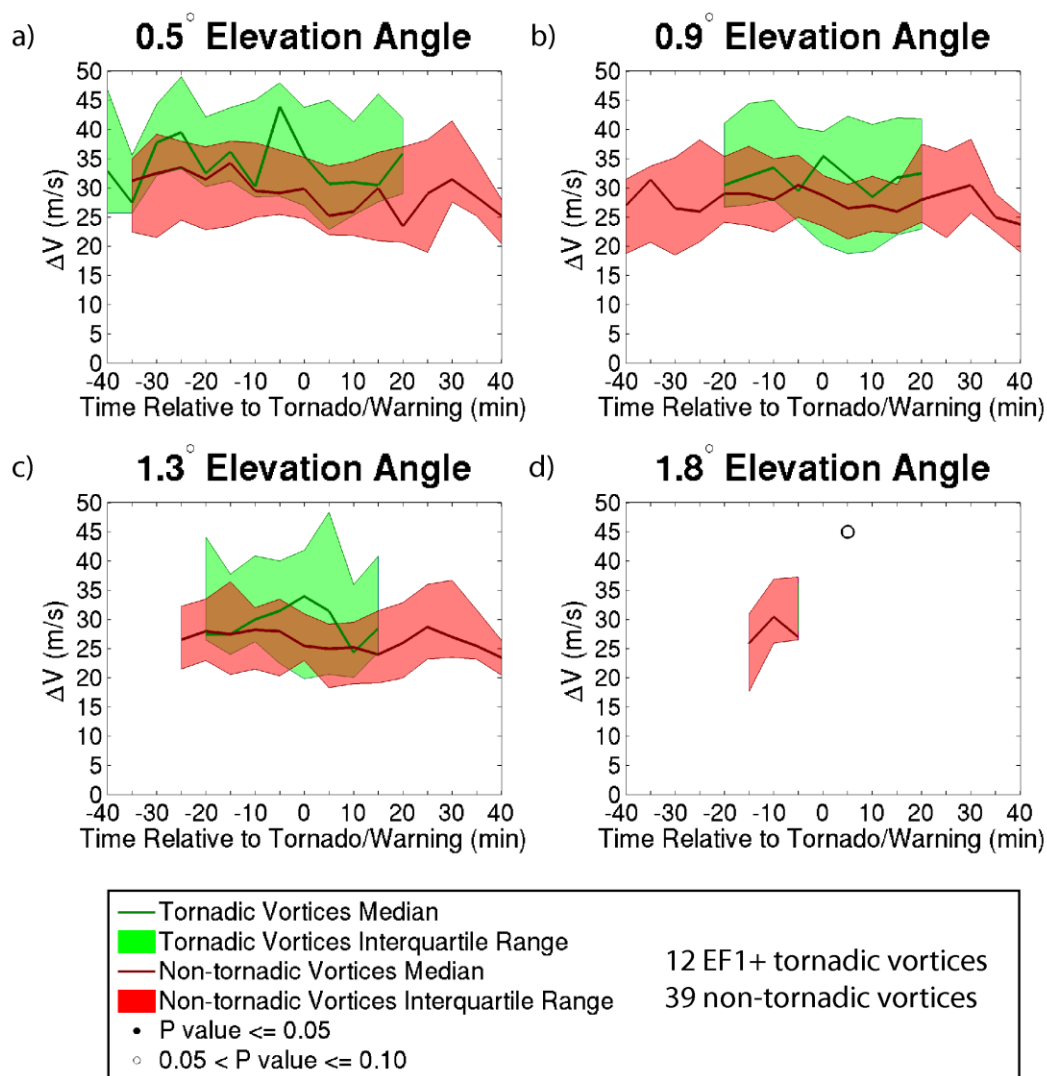


FIG. 4.32. Similar to FIG. 4.30, but for only tornadoic vortices whose first HSLC tornado was rated EF1 or greater, and all non-tornadoic vortices more than 100 km from the radar.

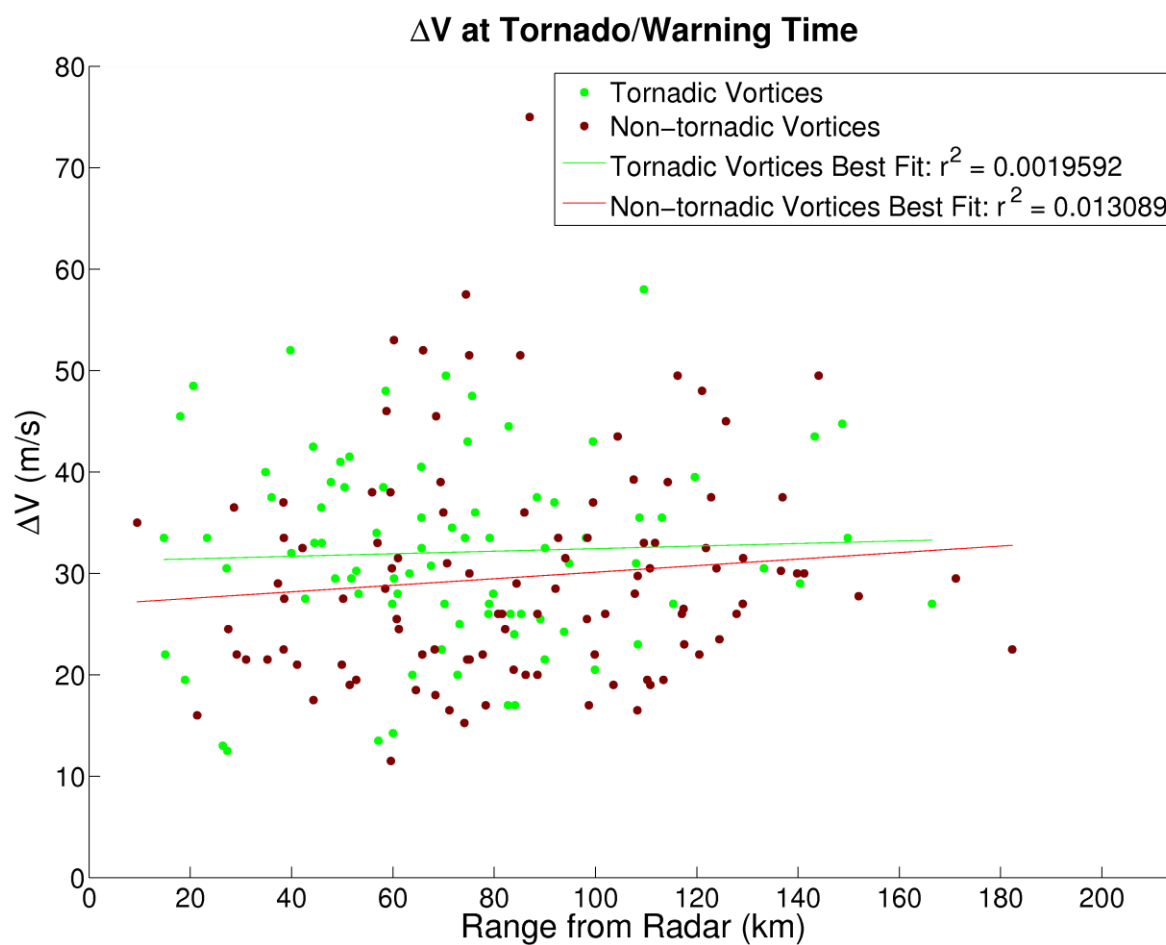


FIG. 4.33. Similar to FIG. 4.23, but ΔV as a function of range from radar for all tornadic and non-tornadic vortices.

Peak-to-peak Shear for All Vortices within 60 km of a Radar

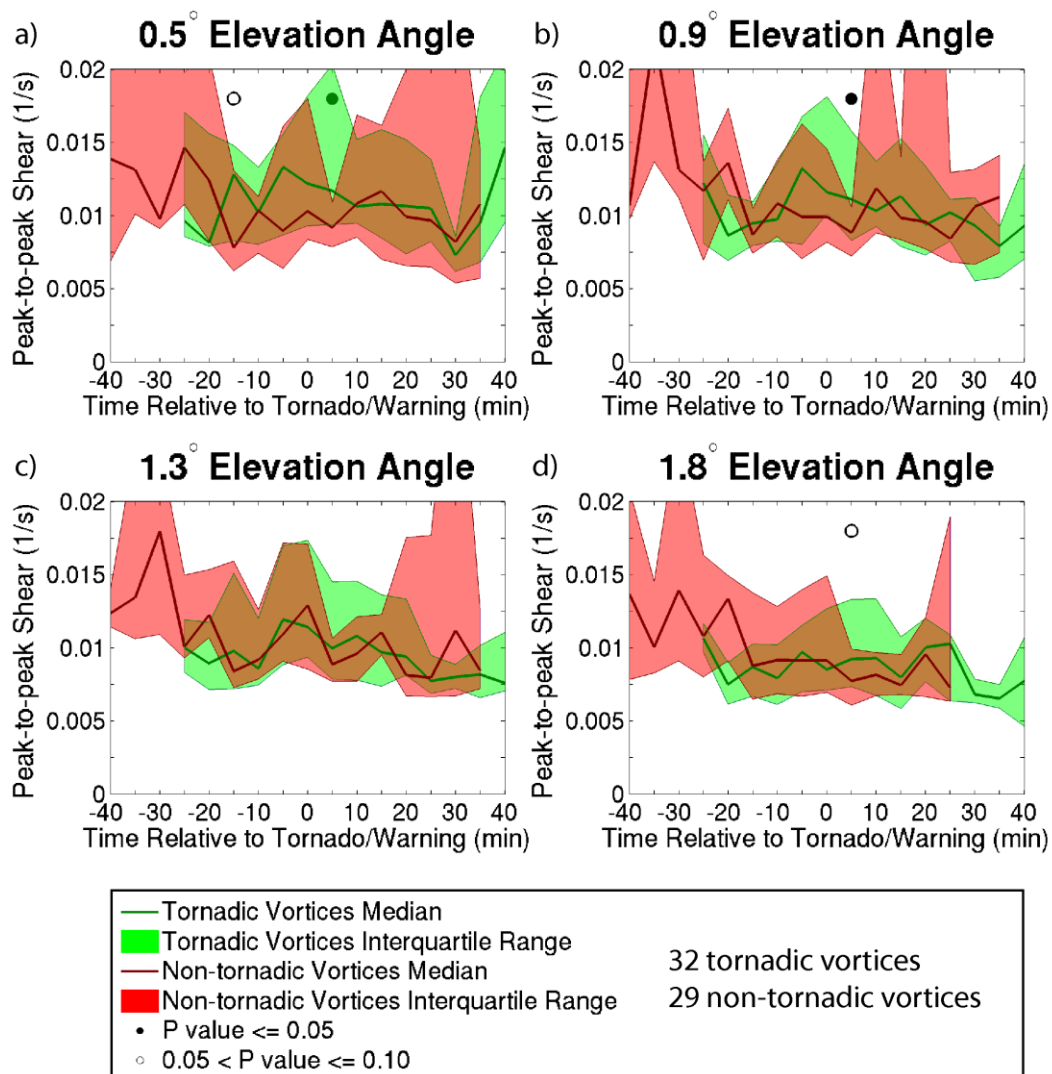


FIG. 4.34. Similar to FIG. 4.5, but peak-to-peak shear (ΔV divided by vortex diameter) is plotted for all tornadic and non-tornadic vortices within 60 km of the radar.

Peak-to-peak Shear for QLCS Mesovortices within 60 km of a Radar

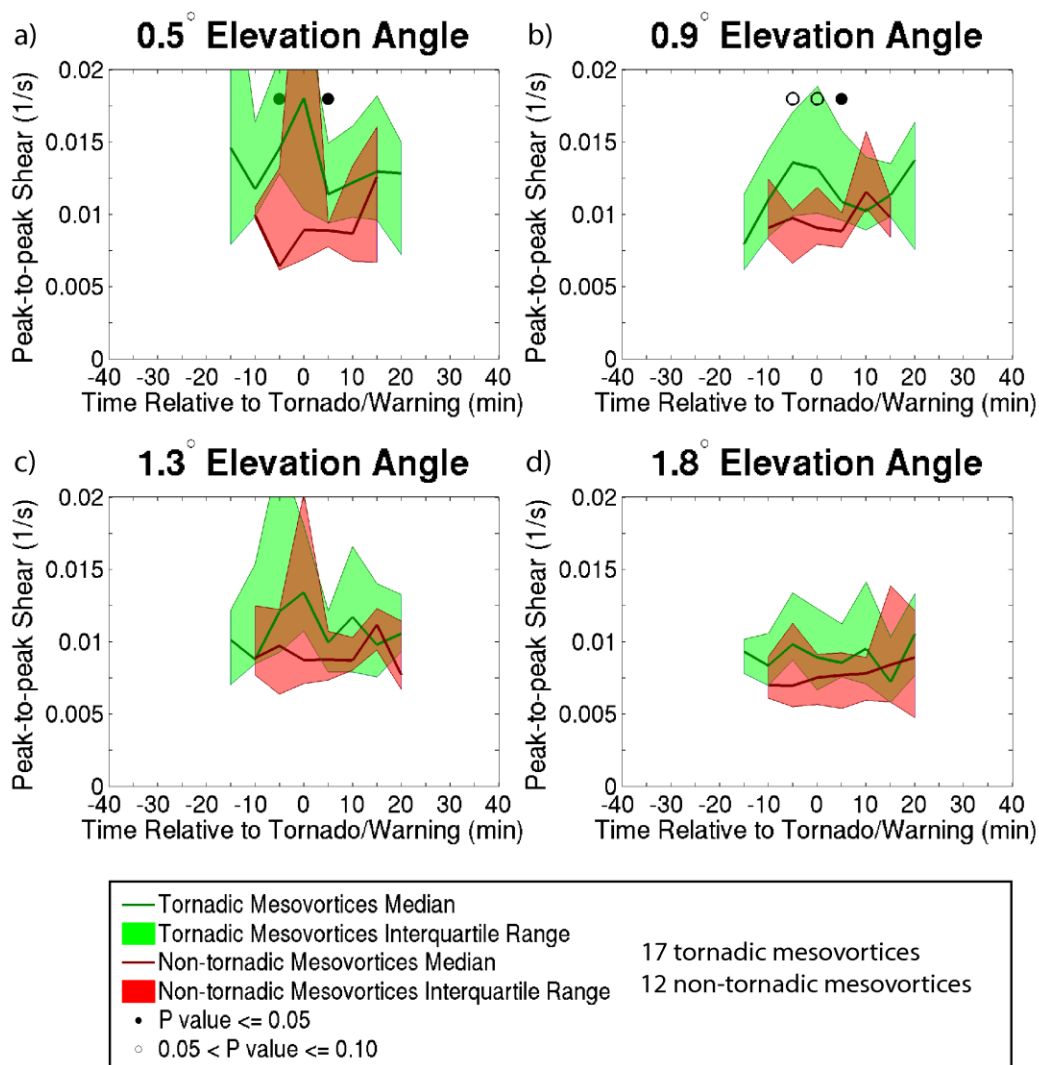
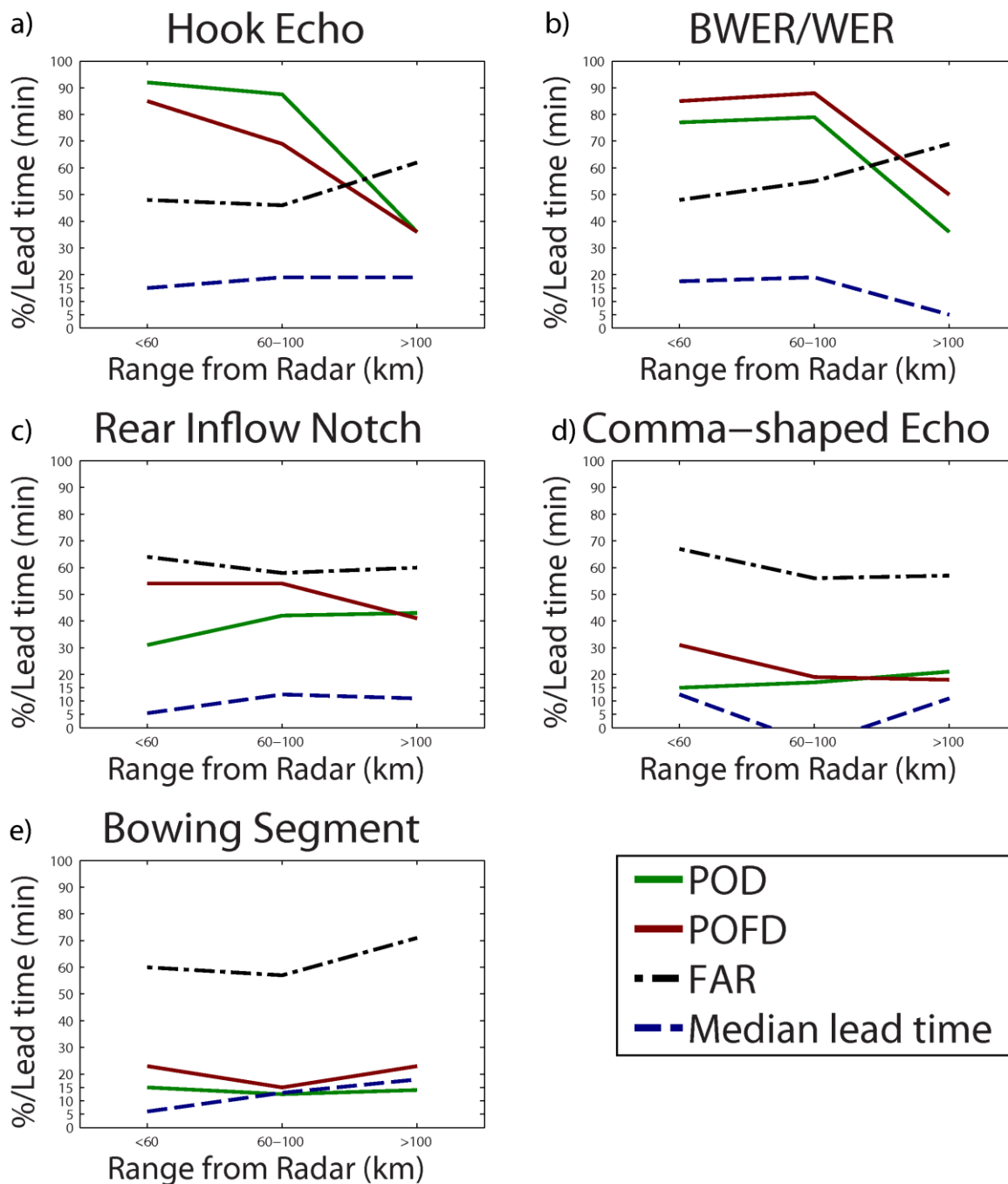


FIG. 4.35. Similar to FIG. 4.8, but peak-to-peak shear (ΔV divided by vortex diameter) is plotted for only tornadic and non-tornadic QLCS mesovortices within 60 km of the radar.

FIG. 4.36. Probability of detection (POD, solid green line, percentage of tornadic supercell mesocyclones with given signature identified between 20 min prior to 15 min after tornado touchdown), probability of false detection (POFD, solid red line, percentage of non-tornadic supercell mesocyclones with given signature identified between 20 min prior to 15 min after false alarm warning issuance), false alarm rate (FAR, black dash-dot line, percentage of total number of identified signatures that were associated with non-tornadic supercell mesocyclones), and median lead time for tornadic supercell mesocyclones (dashed blue line, time relative to tornado touchdown when signature was first identified). Signatures include (a) hook echoes, (b) BWERs or WERs, (c) RINs, (d) comma-shaped echoes, and (e) bowing segments.

Supercell Mesocyclones



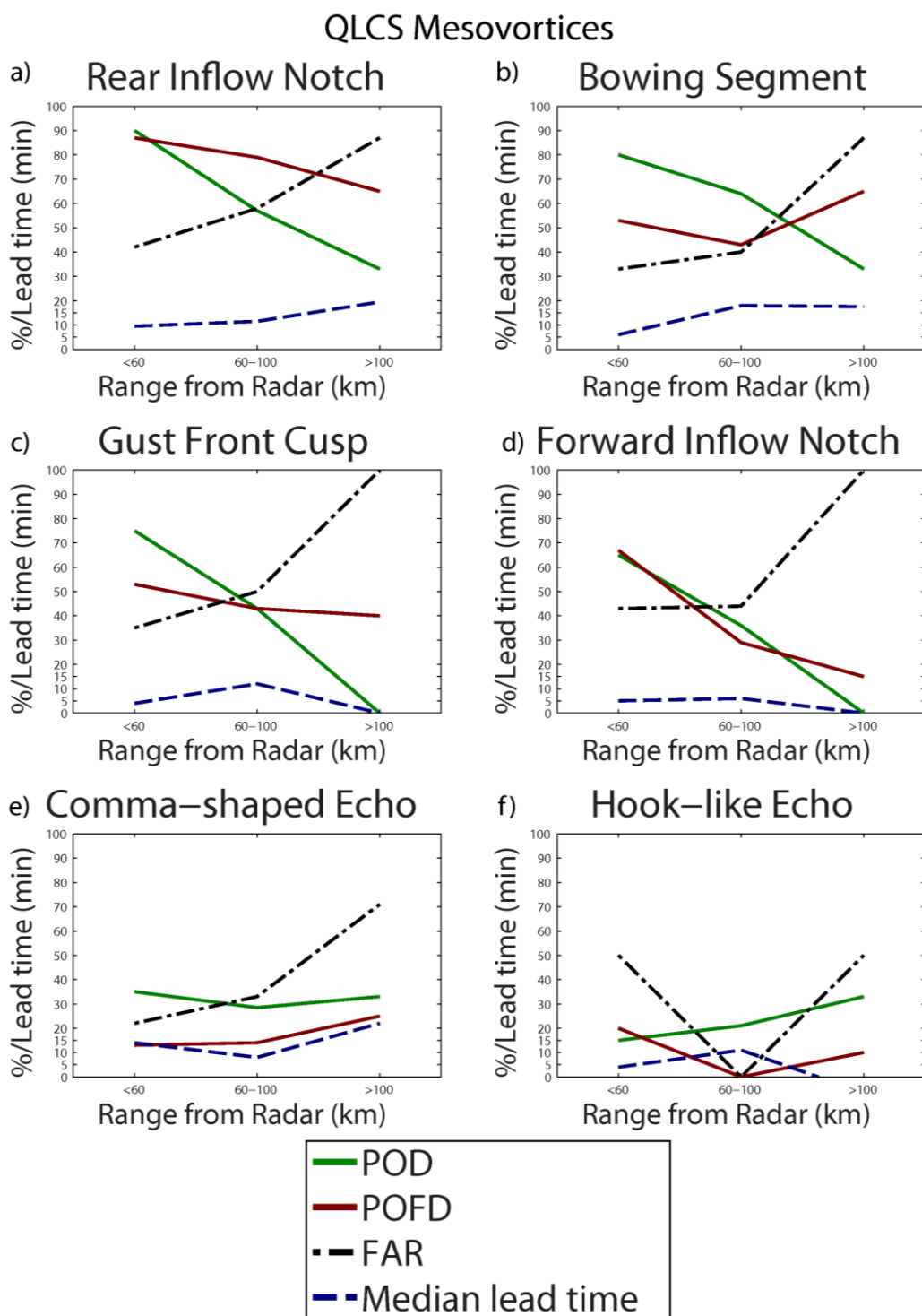
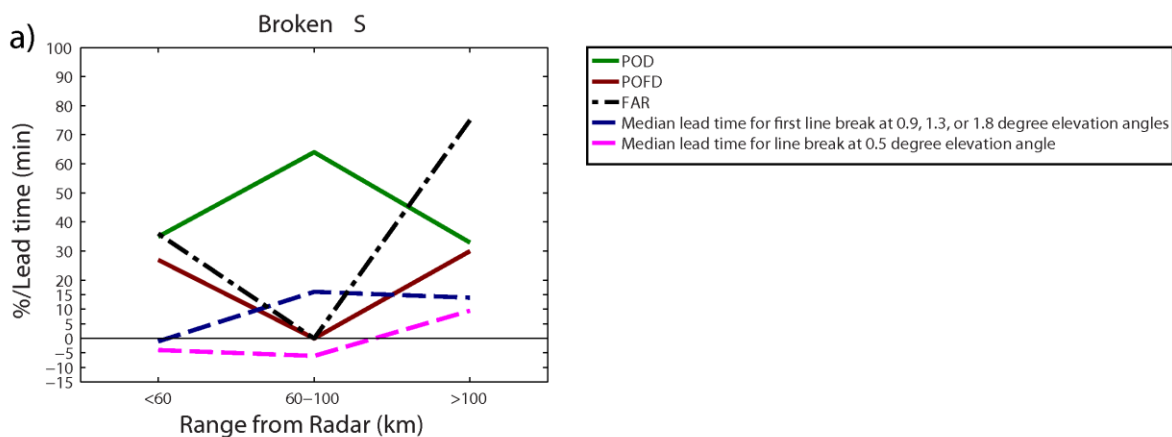
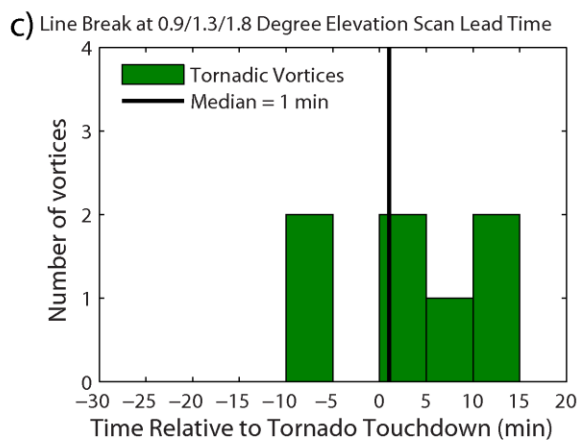
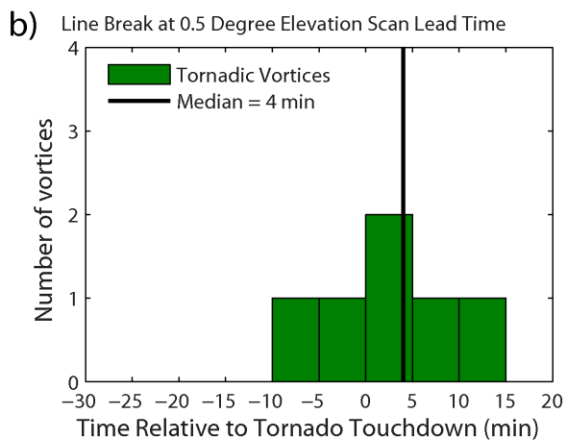


FIG. 4.37. Similar to FIG. 4.36, but for reflectivity signatures associated with tornadic and non-tornadic QLCS mesovortices: (a) rear inflow notches, (b) comma-shaped echoes, (c) bowing segments, (d) gust front cusps, (e) forward inflow notches, and (f) hook-like echoes.

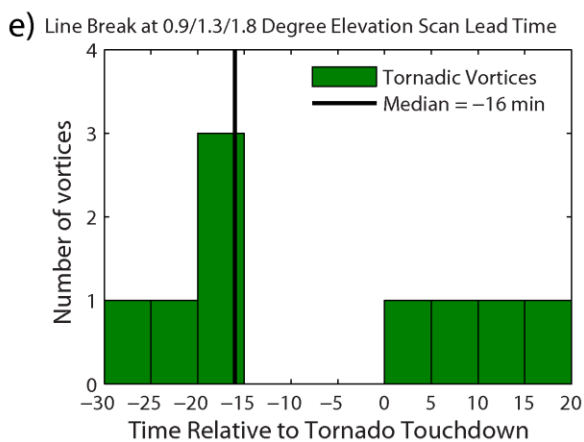
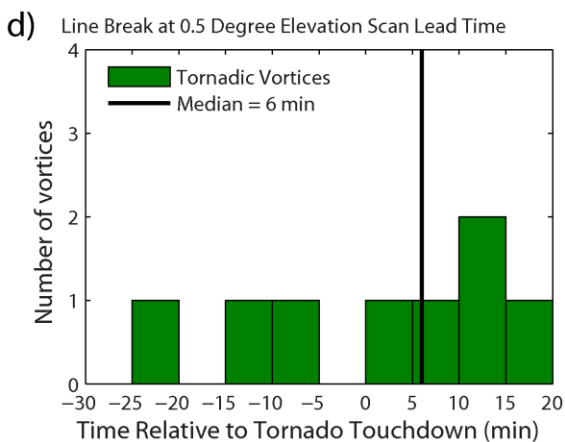
FIG. 4.38. (a) Same as FIG. 4.37., but for the broken-S radar signature, and median lead time for the break in the 40 dBZ radar reflectivity contour aloft (at the 0.9, 1.3, or 1.8 degree elevation scans; dashed blue line) and lead time for the time of the break in the 40 dBZ radar reflectivity contour at the 0.5 degree elevation scan (dashed cyan line). (b-e) Histograms of time relative to tornado touchdown for the line break aloft (b,d) and at the base scan (c,e) for broken-S signatures within 60 km of the radar (b-c) and between 60 and 100 km from the radar (d-e).



Within 60 km of a Radar



60-100 km from a Radar



Cell Merger Lead Time

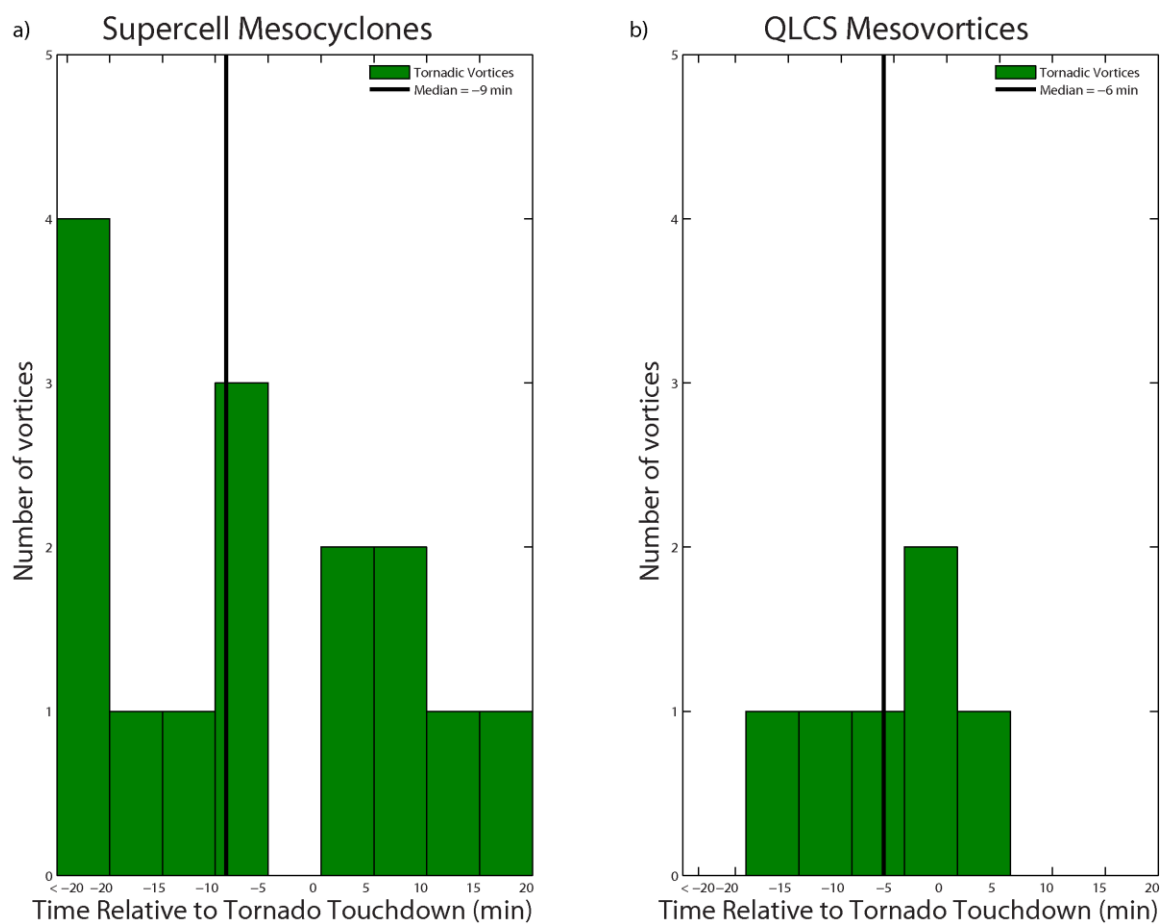
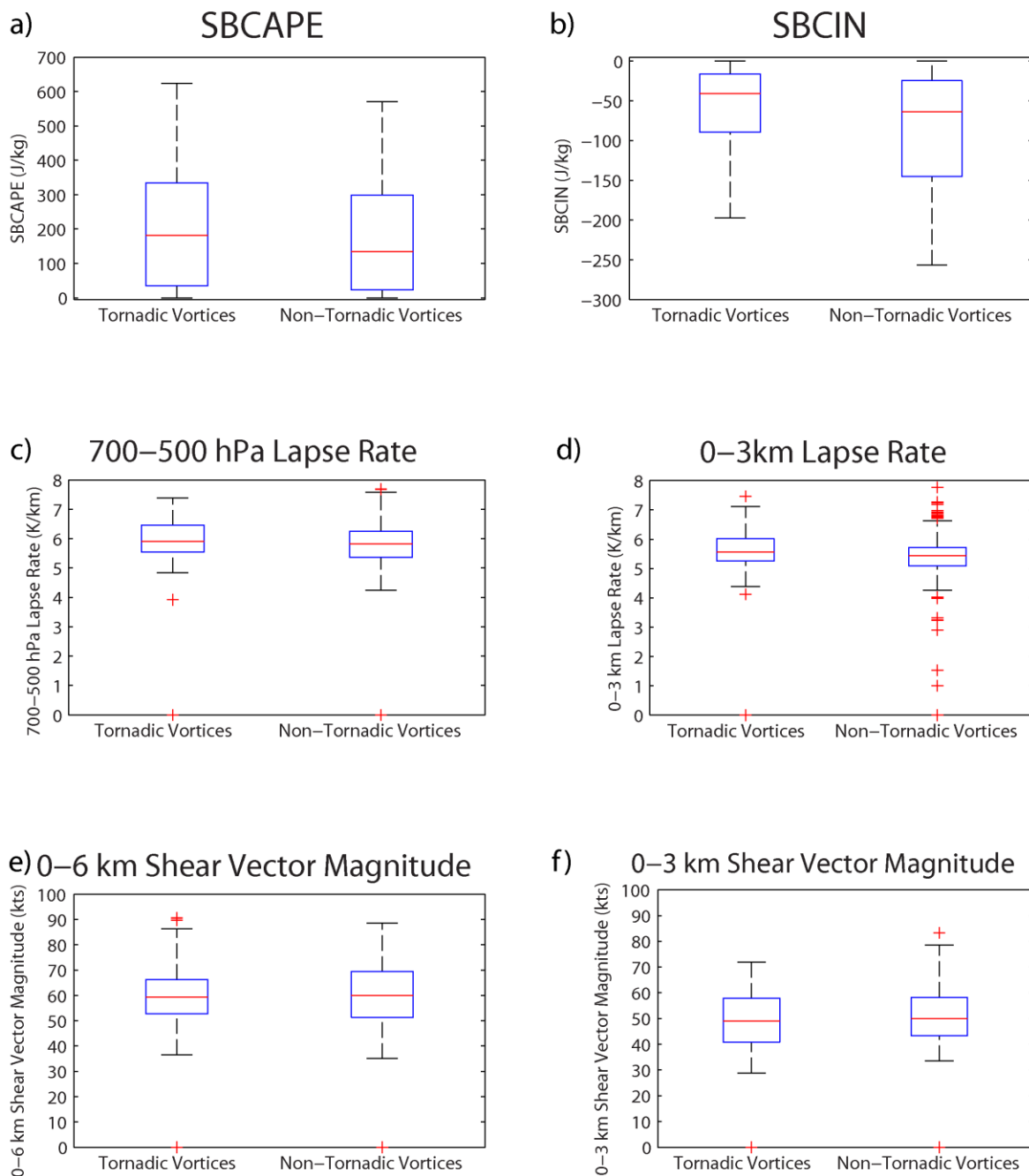


FIG. 4.39. Histogram of time relative to tornado touchdown for cell mergers associated with (a) supercell mesocyclones and (b) QLCS mesovortices.

FIG. 4.40. Box-and-whisker plots of environmental parameters from SPC mesoanalysis data for tornadic and non-tornadic vortices at time of tornado touchdown/false alarm warning, including (a) SBCAPE, (b) SBCIN, (c) mid-level lapse rates, (d) low-level lapse rates, (e) 0-6 km shear vector magnitude, and (f) 0-3 km shear vector magnitude. The box includes the 25th-75th percentiles, with the median indicated in the center of the box. Whiskers extend to 1.5 times the interquartile range, and outliers are indicated by crosses

Parameters at Time of Tornado/False Alarm Warning



Parameters at Time of Tornado/False Alarm Warning

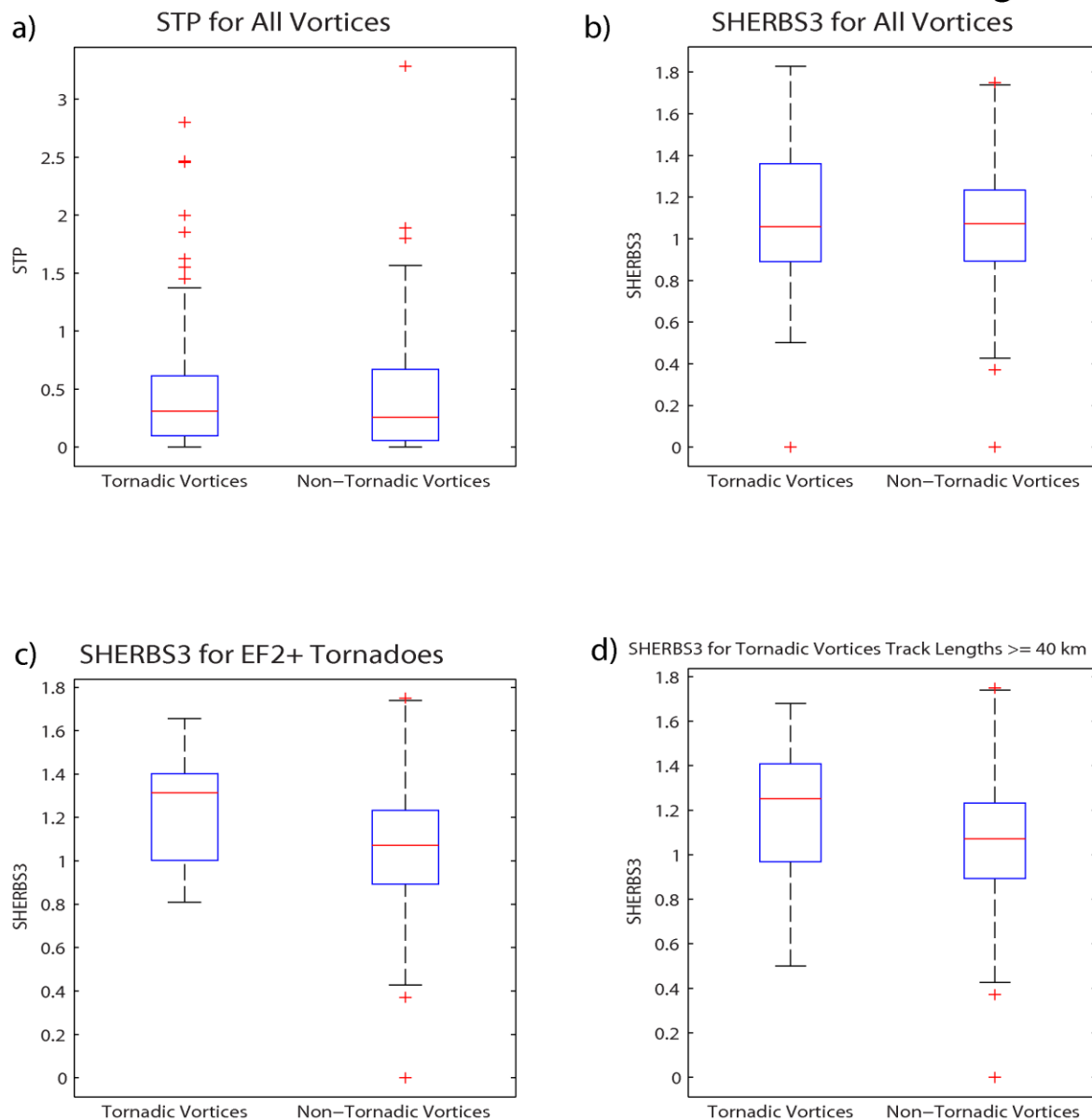


FIG. 4.41. (a-b) Comparison of (a) Significant Tornado Parameter (STP) and (b) Severe Hazards in Environments with Reduced Buoyancy parameter formulation using the 0-3 km shear vector magnitude (SHERBS3) between tornadic and non-tornadic vortices at the time of tornado touchdown/false alarm warning issuance. (c-d) Comparison of SHERBS3 between (c) tornadic vortices producing an EF2 tornado as their first HSLC tornado and all non-tornadic vortices and (d) tornadic vortices with track lengths ≥ 40 km and all non-tornadic vortices at time of tornado touchdown/false alarm warning issuance. The same plotting conventions are used as in FIG. 4.40.

Tornadic Vortices Originating in a Higher CAPE Environment

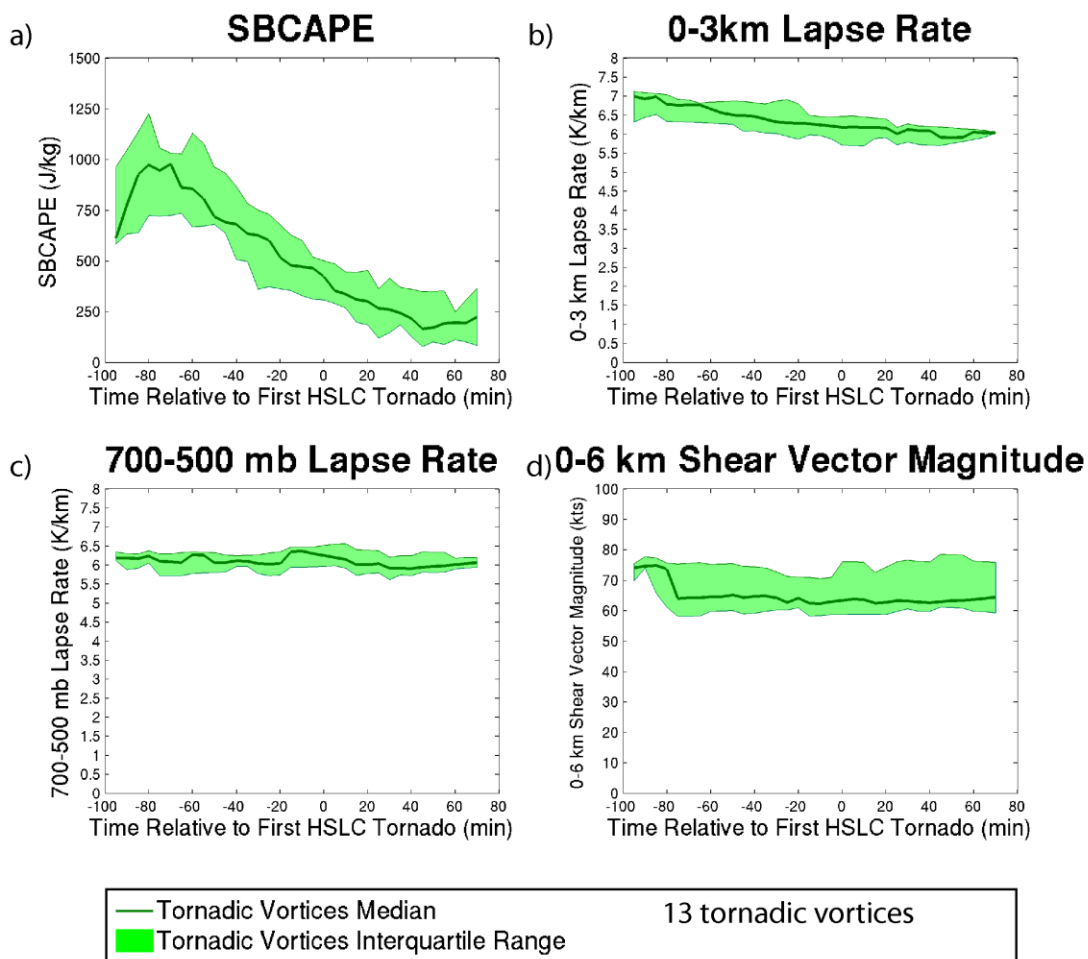


FIG. 4.42. Similar to FIG. 4.5, but a time series of various environmental parameters for vortices with track lengths ≥ 80 km and which were located in an environment with SBCAPE $\geq 500 \text{ J kg}^{-1}$ at some time prior to the tornado, including (a) SBCAPE, (b) low-level lapse rates, (c) mid-level lapse rates, and (d) 0-6 km shear vector magnitude.

Tornadic Vortices Originating in a Higher CAPE Environment

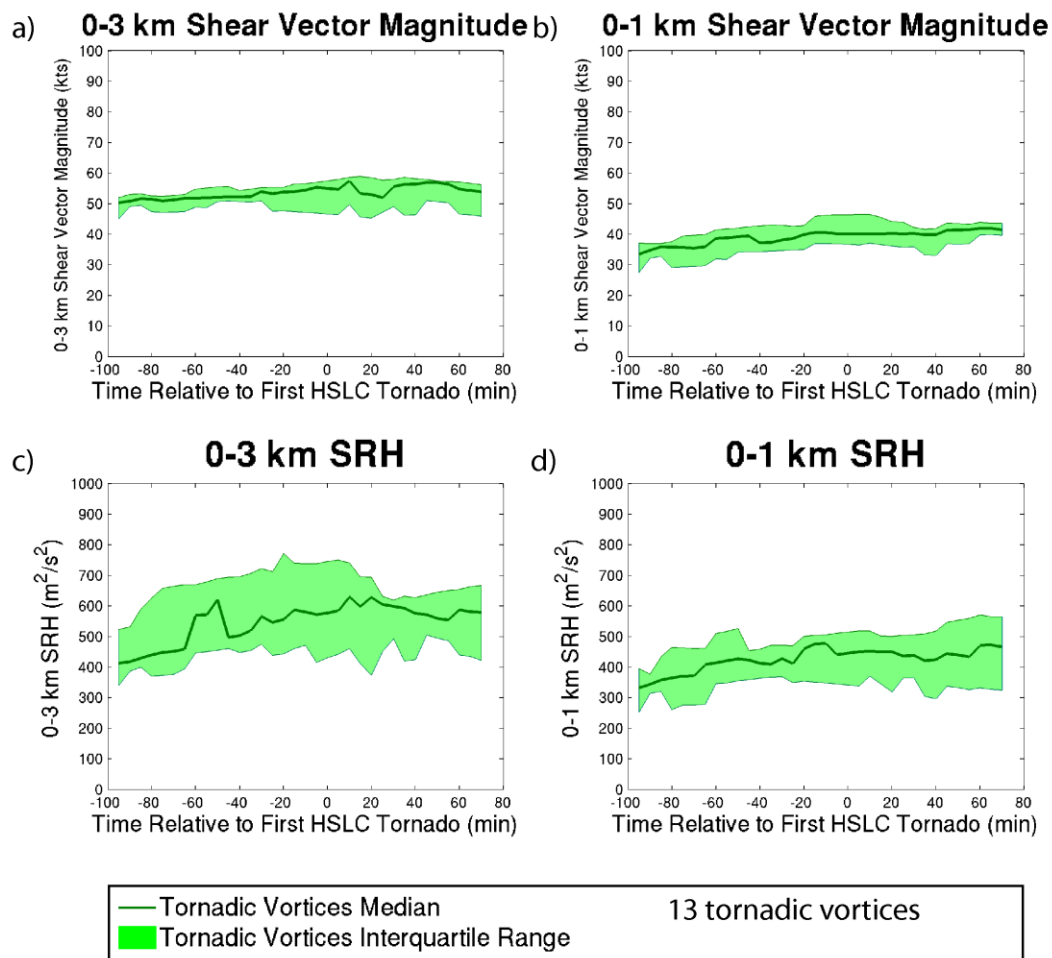


FIG. 4.43. Similar to FIG. 4.42, but for (a) 0-3 km shear vector magnitude, (b) 0-1 km shear vector magnitude, (c) 0-3 km storm relative helicity (SRH), and (d) 0-1 km SRH.

Tornadic Vortices Originating in a Higher CAPE Environment

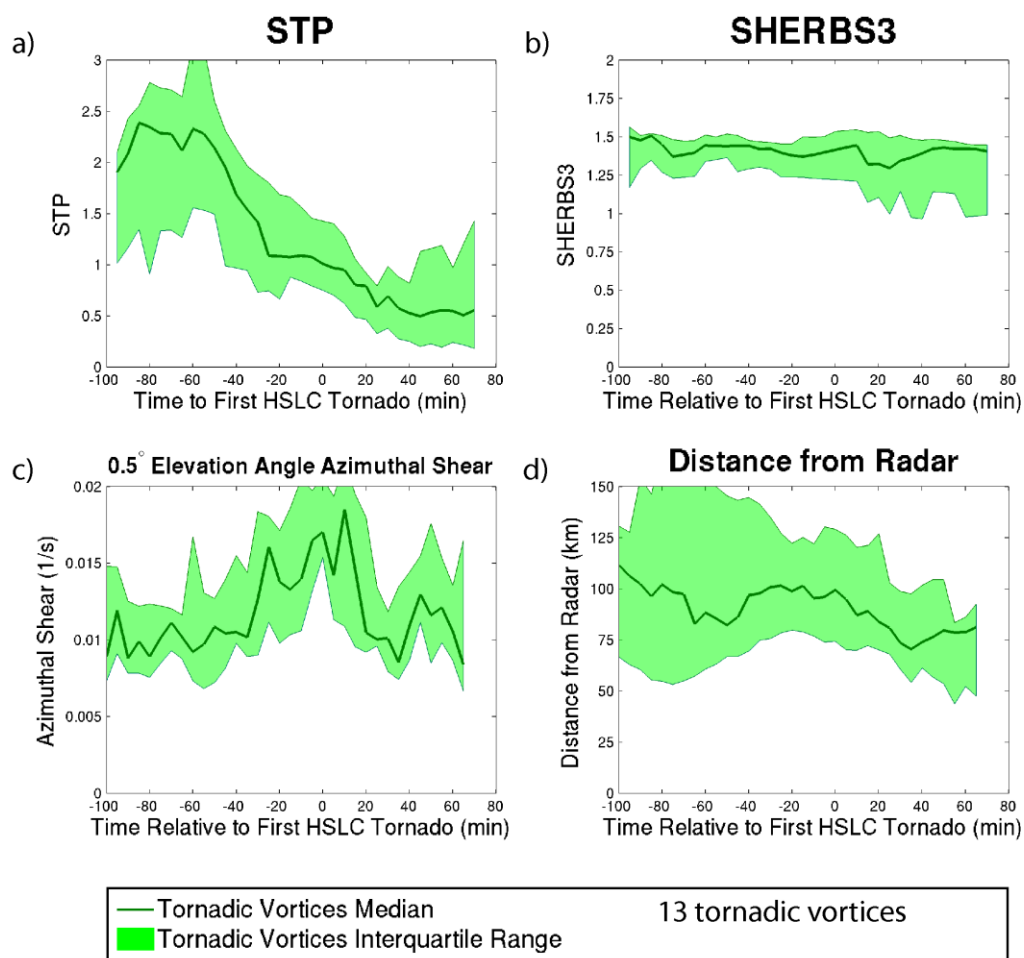


FIG. 4.44. Similar to FIG. 4.42, but for (a) SHERBS3, (b) STP, (c) azimuthal shear at the 0.5 degree elevation scan, and (d) range from radar.

Chapter 5

Discussion and Conclusions

5.1 Interpretation of Principal Results

Within 60 km of the radar, statistically significant differences in azimuthal shear between tornadic and non-tornadic vortices were found at the 0.5 degree elevation scan. This was where vortices were well-resolved by the radar and the radar beam was close to the ground. These differences became more pronounced when only the QLCS mesovortex subset was isolated. No statistically significant differences were found between tornadic and non-tornadic supercell mesocyclones, though azimuthal shear did appear to be slightly stronger for the tornadic supercell mesocyclones. This result may be surprising, but it is consistent with Atkins et al. (2004), who found that tornadic QLCS mesovortices tended to be stronger, deeper, and longer-lived than non-tornadic QLCS mesovortices. Atkins et al. (2004) suggested that this means that it may be possible to discriminate between tornadic and non-tornadic QLCS mesovortices, even though it is currently not possible to discriminate between tornadic and non-tornadic supercell mesocyclones (Trapp 1999 and Trapp et al. 2005a). It is still not known why some supercells with near-ground rotation produce tornadoes and some do not, even in the widely studied Plains high CAPE environments. Therefore, these questions still remain unanswered in both high and low CAPE environments. The dynamics of QLCS mesovortices also remain poorly-understood, but if differences between tornadic and non-tornadic QLCS mesovortices continue to be found this should lead to greater warning accuracy in these events.

The loss of any skill in discriminating between tornadic and non-tornadic vortices more than 60 km from the radar is due to two factors. First, the increase in effective beamwidth degrades resolution, and second, the increase in beam height means that different parts of storms are sampled at different ranges (Fig. 3.2). It is hard to quantify the exact

contributions of these two factors. Newman et al.'s (2013) criteria for the minimum resolvable diameter of a vortex suggests that vortices 60-100 km from the radar should still be resolvable, as the typical vortex diameter of 2-2.2 km (based on observed vortices close to the radar) should be resolvable out to about 100 km. The increase in beam height may be a leading order factor 60-100 km from the radar, considering that within 60 km of the radar statistically significant differences in azimuthal shear were only found through the 1.3 degree elevation scan. This elevation scan reaches a height of about 1.1 km, at 45 km range (the median range of vortices in this bin). Statistically significant differences were absent at the 1.8 degree elevation scan (within 60 km range) which corresponds to a height of 1.5 km, at 45 km range. In the 60-100 km range bin, the height of the 0.5 degree scan increases from 0.7 km to 1.5 km, which is around the height where statistical significance vanishes in the 0-60 km range bin. This interpretation is further supported by the fact that the non-tornadic vortices were stronger at the base scan 60-100 km from the radar than within 60 km of the radar. Also, composite time-height cross-section plots of azimuthal shear also showed that the primary differences between the tornadic and non-tornadic vortices were in the lowest 1.5 km. The overall implication is that a different fundamental layer of the storm was being sampled. In mini-supercells, this is likely a mid-level mesocyclone, which would be present at a relatively low altitude given the observed mesocyclone depth of 3.5-4 km. These results are also consistent with Atkins et al. (2004)'s finding that the primary difference in strength between tornadic and non-tornadic QLCS mesovortices was in the lowest 2 km.

If this explanation is correct, being able to observe *low-level* rotation in supercell mesocyclones and especially shallow QLCS mesovortices appears to be of primary concern in determining the likelihood of a tornado. In the future, this would be best tested in a model simulation using a simulated radar. For now, these results suggest that a high POD is still possible 60-100 km from the radar, but a high FAR will also have to be tolerated. Beyond 100 km, small HSLC vortices are not resolvable according to Newman et al.'s (2013) criteria. This explains the decrease in azimuthal shear values at this range and continued lack of skill in using azimuthal shear to discriminate between tornadic and non-tornadic vortices.

It is also consistent with Brotzge and Erickson's (2010) finding that tornadoes more than 100 km from a radar were less likely to be warned than tornadoes within 100 km of a radar, by a statistically significant margin.

Most HSLC vortices were not transient and could be tracked for a meaningful period of time. Supercell mesocyclones had longer lifetimes than the QLCS mesovortices as expected, often being trackable for an hour or more. This is consistent with Kennedy et al. (1993) and others' findings that mini-supercells can be just as long-lived as classic supercells. The median lifetime for the tornadic supercell mesocyclones was 20 min shorter than the mean lifetime of the supercell mesocyclones in Wood et al.'s (1996) Plains mesocyclone climatology (although lifetimes here were assessed using only a single radar). In the present study, tornadic and non-tornadic supercell mesocyclones had similar lifetimes, which is different from Wood et al.'s (1996) finding that tornadic supercell mesocyclones were longer-lived than non-tornadic supercell mesocyclones. Tornadic QLCS mesovortices were shorter-lived than supercell mesocyclones, but still trackable for a meaningful amount of time, on the order of 30 min. This was 25 min shorter than the mean tornadic QLCS mesovortex lifetime found in a high CAPE QLCS case studied by Atkins et al. (2005), although their case was a particularly prolific event. The present tornadic QLCS mesovortices were longer-lived than the non-tornadic QLCS mesovortices, consistent with the results of Atkins et al. (2004) and (2005), though this difference was only 10 min and not statistically significant.

While it is important to know the lifetime of the vortices, what forecasters care most about is the potential lead time possible for tornadoes, which is here referred to as the "vortex detection lead time". Vortex detection lead times were again greater for the supercell mesocyclones than for the QLCS mesovortices. The median detection lead time at the 0.006 s^{-1} threshold was 25-30 min for the tornadic supercell mesocyclones, and only 10 min for the tornadic QLCS mesovortices. It is well-known that the development of the mesocyclone in supercells, especially the mid-level mesocyclone, precedes the tornado by a meaningful amount of time. The shorter detection lead time for QLCS mesovortices is consistent with the

mean 12 min value found for the high CAPE case studied by Atkins et al. (2005). However, using a higher threshold of 0.01 s^{-1} in order to minimize false alarms drops the median lead time for QLCS mesovortices to only 5 min within 60 km of the radar, with little to no lead time farther from the radar. Faster volume scan times could improve lead times by only a couple minutes, and still would require quick warning decisions. These results suggest that “one-size-fits-all” warning lead time goals (typically stated as on the order of 10-15 min) may not be the suitable across all environments and storm types. While azimuthal shear could discriminate between tornadic and non-tornadic QLCS mesovortices close to the radar, lead times greater than a few minutes are not possible in these cases. For supercell mesocyclones greater lead times are possible, but more false alarms are likely.

Radar reflectivity signatures can help forecasters know which storms to focus on, though detection of these signatures also degrades with range. Several signatures had high PODs and potential lead times, but typically also high FARs. Hook echoes and BWERs/WERs, common features in supercells, were found in almost all tornadic and non-tornadic supercells, with median lead times of 15-20 min. They were much less frequently observed more than 100 km from the radar. RINs, bowing segments, gust front cusps and forward inflow notches were frequently observed with tornadic QLCS mesovortices. RINs and forward inflow notches were also observed with many non-tornadic QLCS mesovortices as well, with somewhat lower FARs for bowing segments and gust front cusps. The presence of RINs and bowing segments do offer some clues as to the possible dynamics at work in HSLC QLCS mesovortex tornado cases. Like with azimuthal shear, median lead times were around 5 min for the best-performing QLCS signatures. Detection of these signatures likewise decreased with range.

The broken-S signature (widely discussed and used in the Southeast) had mixed results. Within 60 km of the radar and more than 100 km from the radar it was detected in about a third of tornadic and non-tornadic QLCS mesovortices. In the 60-100 km range bin it was detected with almost two-thirds of tornadic QLCS mesovortices and no non-tornadic QLCS mesovortices, although we have no additional evidence to explain this peak in skill at

intermediate range. In most cases, the time of the line break provided little to no lead time, but at medium ranges from the radar the time of the line break aloft sometimes provided modest lead time. As this was the first study to take a systematic look at the broken-S signature, these results serve as motivation for future study of the frequency and dynamics of this signature, using both observational data and model simulations. Overall, use of radar reflectivity signatures may have some utility for aiding warning decisions, such as improving situational awareness. However, they cannot compensate for the range dependence and short lead times associated with azimuthal shear as well as forecasters may have hoped (Lane and Moore 2006), unless very high FARs are accepted.

5.2 Recommendations

These results indicate that a denser network of radars could potentially improve tornado warning performance in this region, especially for QLCS mesovortex tornadoes, given the climatological importance of HSLC tornadoes in this region. Fig. 4.4 shows that only a small fraction (21.7%) of this domain is within 60 km of a WSR-88D, and many areas are more than 100 km away. While adding multiple WSR-88Ds would be very costly, a network of smaller radars similar to the Collaborative and Adaptive Sensing of the Atmosphere (CASA; Proud et al. 2009) project would be helpful. Forecasters have also found Terminal Doppler Weather Radars (TDWRs) to be beneficial, even though their primary function is to detect microbursts near airports. For example, Lane and Moore (2006) found that the Charlotte, NC TDWR (TCLT) was especially useful, given its location near a gap in radar coverage. The increase in the azimuthal sampling interval by the WSR-88Ds, allowing the retrieval of super-resolution velocity data, has also been beneficial in this region given the prevalence of small HSLC vortices. Wood et al. (2001) found that the range at which a given mesocyclone can be detected increased by at least 50% by using this technique.

Another recommendation is for LLSD azimuthal shear to be available operationally to forecasters. This variable performed best out of all parameters tested. Although ΔV was also shown to have utility as well, it is hampered by its inability to discriminate between broad and tight circulations. The more traditional peak-to-peak shear calculation was very

noisy and not as useful. Having an azimuthal shear product available to forecasters would save them time (from having to calculate ΔV or peak-to-peak shear) and would allow them to focus on the most threatening vortices and their trends in rotation strength. This derived product is not a substitute for the base reflectivity and velocity products however, as forecasters should still use reflectivity and velocity data to determine whether maxima in azimuthal shear are associated with a vortex or a gust front (or noise). Looking at LLSD azimuthal shear in tandem with the base reflectivity and velocity products is recommended as the best approach for warning operations. A threshold azimuthal shear value of 0.01 s^{-1} would retain 75 percent of tornadic vortices within 60 km of the radar and remove 50% of the non-tornadic vortices. For QLCS mesovortices close to the radar this threshold could be increased to 0.0125 s^{-1} and still retain 75 percent of tornadic vortices while removing almost 75 percent of the non-tornadic vortices. 60-100 km from the radar, 75 percent of tornadic vortices would be detected using this threshold, but also about 75 percent of the non-tornadic vortices. More than 100 km from the radar, this threshold would have to be lowered to around 0.007 s^{-1} in order to detect most tornadic vortices. A comparable ΔV threshold of about 25 m s^{-1} could also be used with some skill. In either case, at increasing ranges from the radar false alarms must be tolerated if a reasonable POD is to be achieved.

5.3 Future Work

Because this study uses a new method, future work should expand the azimuthal shear climatology to include vortices in higher CAPE environments as well. It is possible that there may be some skill extending to greater ranges from the radar in higher CAPE environments, as larger diameter vortices may be better-sampled. Beam height would still be a problem, however, and it is not yet known how well correlated vortex strength at various heights is to tornado potential. If this climatology were extended to a larger population, more sophisticated tracking methods would be helpful, in order to minimize manual intervention, as well as pattern recognition algorithms to detect reflectivity signatures. As more HSLC cases with super-res data accumulate over time, the increase in sample size could also allow study of more specific subsets of the data. For example, one could combine the results from

the azimuthal shear and radar reflectivity climatologies to determine if the presence of a certain reflectivity signature along with azimuthal shear above a given threshold would have more skill than either feature in isolation. Also, it would be useful to determine if there are any subclasses of QLCS mesovortices with unique characteristics and/or unique genesis mechanisms.

Idealized sensitivity tests and real-data modeling simulations should be done to improve the understanding of the dynamics of HSLC mini-supercells and QLCS mesovortices. It would also then be beneficial to place a simulated radar into such simulations and change its location relative to the simulated storm. This could more definitively determine how radar sampling limitations affect the radar depiction of a HSLC storm, and also what particular kinematic and dynamic processes are associated with commonly observed radar “fingerprints”. Given that 21% of HSLC tornadic vortices originated in higher CAPE environments, modeling and observational studies of supercells moving from high to low CAPE environments would be of additional interest. Also, case studies by area WFOs have indicated that mesoscale boundaries (such those associated with cold air damming and outflow boundaries) may be important in HSLC events, and the role of fronts especially in QLCSs needs to be examined. Further observational and modeling studies of storm interactions with synoptic and mesoscale boundaries should be done.

Because it is widely discussed by regional forecasters, study of the dynamics of the broken-S signature seems warranted. It did not appear to be particularly useful in this study, with the exception of a somewhat mysterious peak in skill 60-100 km from the radar. There may be multiple types of broken-S evolution (as theorized by Clark 2011) but very low sample sizes precluded any meaningful conclusions about them. Research-quality observational datasets, such as mobile radar data, high-density surface observations, and dual Doppler analyses, would be useful. These observations would help improve understanding of the dynamics of HSLC supercell mesocyclones and QLCS mesovortices in comparison to their more plentiful high CAPE Plains counterparts. However, the road network, terrain and dense tree cover in the Southeast, plus the intermittency of HSLC severe weather, make this

kind of data collection a challenge. Notably, the WSR-88Ds were recently upgraded to provide dual-polarization data, and once cases begin to accumulate there may be polarimetric signatures of interest. For example, Tornadic Debris Signatures (TDSs) have already been observed with HSLC tornadoes from the Peachtree City, GA (KFFC) radar (though the TDS does not provide any lead time).

5.4 Conclusions

This study examined an unprecedented number of cases HSLC vortices (225). This allowed analysis of results for various subsets of the data, including tornadic and non-tornadic vortices, vortices at varying ranges from the radar, and both supercell mesocyclones and QLCS mesovortices. Information about the typical scales of HSLC vortices was learned. A common theme of results for both the azimuthal shear and radar reflectivity portions of the climatology was the importance of radar sampling limitations, as the increase in beam height and effective beamwidth with range was a primary signal in the results. It was difficult to find differences that clearly discriminate between tornadic and non-tornadic vortices. Clear differences in azimuthal shear were only present for vortices within 60 km of the radar, and then primarily for QLCS mesovortices rather than supercell mesocyclones. While azimuthal shear and radar reflectivity signatures have the potential to provide high probability of detection within about 100 km of the radar, the results suggest that false alarms will still be a major problem. Lead time also remains a problem, as even when there are differences in azimuthal shear between the tornadic and non-tornadic vortices these differences only manifest themselves a few minutes prior to tornado touchdown. These results suggest that a forecaster needs to utilize all tools available to them during tornado warning operations, including radar reflectivity and velocity data, knowledge of the storm environment, forecasting experience, and ground truth reports from spotters. Unfortunately, there is no single “silver bullet”.

The primary conclusions of this study are as follows:

- Statistically significant differences in azimuthal shear were found between tornadic and non-tornadic vortices within 60 km of the radar from 5-10 min before to 1-5 min

after tornado touchdown/false alarm warning issuance time. This was primarily due to statistically significant differences between tornadic and non-tornadic QLCS mesovortices, not between tornadic and non-tornadic supercell mesocyclones. A threshold azimuthal shear value of 0.01 s^{-1} would retain 75 percent of tornadic vortices and remove 50 percent of non-tornadic vortices.

- Vortices within 60 km of the radar had a median diameter of 2 km and a median depth of 3.5-4 km.
- No statistically significant differences were found beyond 60 km from the radar, primarily due to the increasing beam height 60-100 km from the radar causing low-level rotation to be obscured. Beyond 100 km vortices were very poorly resolved (in combination with the aforementioned beam height issue).
- Within 60 km of the radar, tornadic supercell mesocyclones maintained azimuthal shear above a threshold of 0.01 s^{-1} for a median of 25 min prior to the tornado, while this detection lead time fell to 5 min for QLCS mesovortices.
- Most tornadic and non-tornadic supercell mesocyclones were associated with hook echoes and BWER/WERs, 15 min prior to tornado touchdown, but these were detected much less often more than 100 km from the radar.
- Rear inflow notches, bowing segments, gust front cusps, and forward inflow notches were found with most tornadic and non-tornadic QLCS mesovortices close to the radar, typically developing only a few minutes prior to the tornado and not being detected very well far from the radar.

Although there are optimistic signs for warning operations in these results, it appears that major gains in skill will require the routine availability of azimuthal shear to forecasters, and preferably (though quite expensive) the installation of a denser Doppler radar network.

REFERENCES

- Adlerman, E.J., and K.K. Droegemeier, 2005: The dependence of numerically simulated cyclic mesocyclogenesis upon environmental vertical wind shear. *Mon. Wea. Rev.*, **133**, 3595–3623.
- Ashley, W.S., 2007: Spatial and temporal analysis of tornado fatalities in the United States: 1880–2005. *Wea. Forecasting*, **22**, 1214–1228.
- , A. J. Krmenc, and R. Schwantes, 2008: Vulnerability due to nocturnal tornadoes. *Wea. Forecasting*, **23**, 795–807.
- Atkins, N.T., J.M. Arnott, R.W. Przybylinski, R.A. Wolf, and B.D. Ketcham, 2004: Vortex structure and evolution within bow echoes. Part I: Single-Doppler and damage analysis of the 29 June 1998 derecho. *Mon. Wea. Rev.*, **132**, 2224–2242.
- , C.S. Bouchard, R.W. Przybylinski, R.J. Trapp, and G. Schmocker, 2005: Damaging surface wind mechanisms within the 10 June 2003 Saint Louis bow echo during BAMEX. *Mon. Wea. Rev.*, **133**, 2275–2296.
- , and M. St. Laurent, 2009: Bow echo mesovortices. Part I: Processes that influence their damaging potential. *Mon. Wea. Rev.*, **137**, 1497–1513.
- , and -----, 2009: Bow echo mesovortices. Part II: Their genesis. *Mon. Wea. Rev.*, **137**, 1514–1532.
- Brotzge, J., S. Erickson, and H. Brooks, 2011: A 5-yr climatology of tornado false alarms. *Wea. Forecasting*, **26**, 534–544.
- , and -----, 2010: Tornadoes without NWS warning. *Wea. Forecasting*, **25**, 159–172.
- , and W. Donner, 2013: The tornado warning process: A review of current research, challenges, and opportunities. *Bull. Amer. Meteor. Soc.*, in press.
- Brown, R.A., L.R. Lemon, and D.W. Burgess, 1978: Tornado detection by pulsed Doppler radar. *Mon. Wea. Rev.*, **106**, 29–38.
- Burgess, R., L. Lee, S. S. Parker, S. J. Keighton, and D. L. Floyd, 1995: A study of mini supercells observed by WSR-88D radars. Preprints, *27th Conf. on Radar Meteorology*, Vail, CO, Amer. Meteor. Soc., 1.2.
- Burke, P.C., and D.M. Schultz, 2004: A 4-yr climatology of cold-season bow echoes over the

- continental United States. *Wea. Forecasting*, **19**, 1061–1074.
- Clark, M.R., 2011: Doppler radar observations of mesovortices within a cool-season tornadic squall line over the UK. *Atmos. Res.*, **100**, 749–764.
- Coniglio, M.C., 2012: Verification of RUC 0–1-h forecasts and SPC mesoscale analyses using VORTEX2 soundings. *Wea. Forecasting*, **27**, 667–683.
- Davies, J. M., 1990: Midget supercell spawns tornadoes. *Weatherwise*, **43** (10), 260–261.
- Davies, J. M., 1993: Small tornadic supercells in the central plains. Preprints, *17th Conf. Severe Local Storms*, St. Louis, MO, Amer. Meteor. Soc., 305–309.
- Doswell, C.A. III, Moller, A. R., and R. Przybylinski, 1990: A unified set of conceptual models for variations on a supercell theme. Preprints, *16th Conf. on Severe Local Storms*, Kananaskis Park, AB, Canada, Amer. Meteor. Soc., 40–45.
- , H.E. Brooks, and N. Dotzek, 2009: On the implementation of the enhanced Fujita scale in the USA. *Atmos. Res.*, **93**, 554–563.
- Edwards, R., A.R. Dean, R.L. Thompson, and B.T. Smith, 2012: Convective modes for significant severe thunderstorms in the contiguous United States. Part III: Tropical cyclone tornadoes. *Wea. Forecasting*, **27**, 1507–1519.
- Finley, C.A., W. R. Cotton, and R. A. Pielke, 2001: Numerical simulation of tornadogenesis in a high-precipitation supercell. Part I: Storm evolution and transition into a bow Echo. *J. Atmos. Sci.*, **58**, 1597–1629.
- , -----, and -----, 2002: Tornadogenesis in a simulated HP supercell. Preprints, *21st Conf. on Severe Local Storms*, San Antonio, TX, Amer. Meteor. Soc., P10.1.
- French, A.J., and M.D. Parker, 2012: Observations of mergers between squall lines and isolated supercell thunderstorms. *Wea. Forecasting*, **27**, 255–278.
- Funk, T.W., K.E. Darmofal, J.D. Kirkpatrick, V.L. DeWald, R.W. Przybylinski, G.K. Schmocker, and Y.J. Lin, 1999: Storm reflectivity and mesocyclone evolution associated with the 15 April 1994 squall line over Kentucky and southern Indiana. *Wea. Forecasting*, **14**, 976–993.
- Goodman, S. J., and K. R. Knupp, 1993: Tornadogenesis via squall line and supercell interaction: The November 15, 1989, Huntsville, Alabama tornado. *The Tornado: Its Structure, Dynamics, Prediction, and Hazards*, C.R. Church et al., Eds., Amer.

- Geophys. Union, 183–199.
- Grams, J.S., R.L. Thompson, D.V. Snively, J.A. Prentice, G.M. Hodges, and L.J. Reames, 2012: A climatology and comparison of parameters for significant tornado events in the United States. *Wea. Forecasting*, **27**, 106–123.
- Grant, B. N., and R. Prentice, 1996: Mesocyclone characteristics of mini supercell thunderstorms. Preprints, *15th Conf. on Weather Analysis and Forecasting*, Norfolk, VA , Amer. Meteor. Soc., 362-365.
- Grumm, R. H., and M. Glazewski, 2004: Thunderstorm types associated with the “broken-S” radar signature. Preprints, *22nd Conf. on Severe Local Storms*, Hyannis, MA, Amer. Meteor. Soc., P7.1. [Available online at <http://ams.confex.com/ams/pdfpapers/81537.pdf>]
- Guyer, J. L., and A. R. Dean, 2010: Tornadoes within weak CAPE environments across the continental United States. Preprints, *25th AMS Conf. on Severe Local Storms*, Amer. Meteor. Soc., Denver, CO, 1.5. [Available online at <http://ams.confex.com/ams/pdfpapers/175725.pdf>]
- Johns, R.H., 1993: Meteorological conditions associated with bow echo development in convective storms. *Wea. Forecasting*, **8**, 294–299.
- Johnson, J. T., P.L. MacKeen, A. Witt, E.D. Mitchell, G.J. Stumpf, M.D. Eilts, and K.W. Thomas, 1998: The storm cell identification and tracking algorithm: An enhanced WSR-88D algorithm. *Wea. Forecasting*, **13**, 263–276.
- Jones, T.A., K.M. McGrath, and J.T. Snow, 2004: Association between NSSL Mesocyclone Detection Algorithm-detected vortices and tornadoes. *Wea. Forecasting*, **19**, 872–890.
- Kennedy, P. C., N. E. Westcott, and R. W. Scott, 1993: Single-Doppler radar observations of a minisupercell tornadic thunderstorm. *Mon. Wea. Rev.*, **121**, 1860–1870.
- Kis, A.K., and J.M. Straka, 2010: Nocturnal tornado climatology. *Wea. Forecasting*, **25**, 545–561.
- Knupp, K. J., J. Stalker, and E. W. McCaul Jr., 1998: An observational and numerical study of a mini-supercell storm. *Atmos. Res.*, **49**, 35–63.
- Konarik, S. B., and S. E. Nelson, 2008: Cool season tornadoes in the southeast U.S. Preprints, *24th Conf. on Severe Local Storms*, Savannah, GA, Amer.

- Meteor. Soc., P8.2. [Available online at <http://ams.confex.com/ams/pdfpapers/141591.pdf>]
- Lakshmanan, V., T. Smith, G. Stumpf, and K. Hondl, 2007: The Warning Decision Support System–Integrated Information. *Wea. Forecasting*, **22**, 596–612.
- Lane J.D., and P.D. Moore, 2006: Observations of a non-supercell tornadic thunderstorm from terminal Doppler weather radar. Preprints, *23rd Conf. Severe Local Storms*, St. Louis, MO, Amer. Meteor. Soc., P4.5. [Available online at <http://ams.confex.com/ams/pdfpapers/115102.pdf>]
- , 2008: A sounding-derived climatology of significant tornado events in the Greenville-Spartanburg, South Carolina county warning area (1948-2006). Preprints, *24th Conf. on Severe Local Storms*, Savannah, GA, Amer. Meteor. Soc., P12.14. [Available online at <http://ams.confex.com/ams/pdfpapers/142046.pdf>]
- Latimer, S., and A. Kula, 2010: A comparison of warm and cool season tornadic quasi-linear convective systems in north Alabama. Preprints, *26th Conf. on Int. Interactive Info. and Processing Sys. (IIPS) for Meteor., Ocean., and Hydro.*, Atlanta, GA, Amer. Meteor. Soc., 11B.6. [Available online at <http://ams.confex.com/ams/pdfpapers/158140.pdf>]
- Lemon, L.R., 1976: The flanking line, a severe thunderstorm intensification source. *J. Atmos. Sci.*, **33**, 686–694.
- , and C.A. Doswell III, 1979: Severe thunderstorm evolution and mesocyclone structure as related to tornadogenesis. *Mon. Wea. Rev.*, **107**, 1184–1197.
- Markowski, P.M., and J.M. Straka, 2000: Some observations of rotating updrafts in a low-buoyancy, highly sheared environment. *Mon. Wea. Rev.*, **128**, 449–461.
- , 2002: Hook echoes and rear-flank downdrafts: A review. *Mon. Wea. Rev.*, **130**, 852–876.
- , J.M. Straka, and E.N. Rasmussen, 2002: Direct surface thermodynamic observations within the rear-flank downdrafts of nontornadic and tornadic supercells. *Mon. Wea. Rev.*, **130**, 1692–1721.
- , C. Hannon, J. Frame, E. Lancaster, A. Pietrycha, R. Edwards, and R.L. Thompson, 2003: Characteristics of vertical wind profiles near supercells obtained from the rapid update cycle. *Wea. Forecasting*, **18**, 1262–1272.

- , and Y.P. Richardson, 2010: *Mesoscale Meteorology in Midlatitudes*. Wiley-Blackwell, 407 pp.
- McAvoy, B. P., W. A. Jones, and P. D. Moore, 2000: Investigation of an unusual storm structure associated with weak to occasionally strong tornadoes over the eastern United States. Preprints, *20th Conf. on Severe Local Storms*, Orlando, FL, Amer. Meteor. Soc., 182-185. [Available online at <http://www.erh.noaa.gov/gsp/localdat/ConfPapers/Broken-S.pdf>]
- McCaul, E.W., 1991: Buoyancy and shear characteristics of hurricane-tornado environments. *Mon. Wea. Rev.*, **119**, 1954–1978.
- , 1993: Observations and simulations of hurricane-spawned tornadic storms. *The Tornado: Its Structure, Dynamics, Prediction, and Hazards*, C.R. Church et al., Eds., Amer. Geophys. Union, 119–142.
- , and M. L. Weisman, 1996: Simulation of shallow supercell storms in landfalling hurricane environments. *Mon. Wea. Rev.*, **124**, 408–429.
- Moller, A.R., C.A. Doswell, and R. Przybylinski, 1990: High-precipitation supercells: A conceptual model and documentation. Preprints, *16th Conf. on Severe Local Storms*, Kananaskis Park, Alberta, Amer. Meteor. Soc., 52-57.
- Murphy, T.A., and K.R. Knupp, 2013: An analysis of cold season supercell storms using the synthetic dual-Doppler technique. *Mon. Wea. Rev.*, **141**, 602–624.
- Newman, J.F., V. Lakshmanan, P.L. Heinselman, M.B. Richman, and T.M. Smith, 2013: Range-correcting azimuthal shear in Doppler radar data. *Wea. Forecasting*, **28**, 194–211.
- Nolen, R.H., 1959: A radar pattern associated with tornadoes. *Bull. Amer. Meteor. Soc.*, **40**, 277-279.
- Pfost, R.L., and A.E. Gerard, 1997: “Bookend vortex” induced tornadoes along the Natchez Trace. *Wea. Forecasting*, **12**, 572–580.
- Proud, J.L., K.K. Droegemeier, V.T. Wood, and R.A. Brown, 2009: Sampling strategies for tornado and mesocyclone detection using dynamically adaptive Doppler radars: A simulation study. *J. Atmos. Oceanic Technol.*, **26**, 492–507.
- Przybylinski, R.W., Snow, J. T., E. M. Agee, and J. T. Curran, 1993: The use of volumetric

- radar data to identify supercells: A case study of June 2, 1990. *The Tornado: Its Structure, Dynamics, Prediction, and Hazards*, C.R. Church et al., Eds., Amer. Geophys. Union, 241–250.
- , 1995: The bow echo: Observations, numerical simulations, and severe weather detection methods. *Wea. Forecasting*, **10**, 203–218.
- Reilly, D. H., 2004: Environmental conditions associated with weak tornadoes across southern Virginia and northeast North Carolina in 2003 and 2004. Preprints, *22nd Conf. on Severe Local Storms*, Hyannis, MA, Amer. Meteor. Soc., 2.6. [Available online at <http://ams.confex.com/ams/pdfpapers/80958.pdf>]
- Schneider, D., and S. Sharp, 2007: Radar signatures of tropical cyclone tornadoes in central North Carolina. *Wea. Forecasting*, **22**, 278–286.
- Schneider, R.S., A.R. Dean, S.J. Weiss, and P.D. Bothwell, 2006: Analysis of estimated environments for 2004 and 2005 severe convective storm reports. Preprints, *23rd Conf. Severe Local Storms*, St. Louis MO, Amer. Meteor. Soc., 3.5. [Available online at <http://ams.confex.com/ams/pdfpapers/115246.pdf>]
- , and A.R. Dean, 2008: A comprehensive 5-year severe storm environment climatology for the continental United States. Preprints, *24th Conf. Severe Local Storms*, Savannah GA, Amer. Meteor. Soc., 16A.4. [Available online at <http://ams.confex.com/ams/pdfpapers/141748.pdf>]
- Schumacher, P.N., and J.M. Boustead, 2011: Mesocyclone evolution associated with varying shear profiles during the 24 June 2003 tornado outbreak. *Wea. Forecasting*, **26**, 808–827.
- Sherburn, K.D., 2013: Improving the understanding and forecasting of severe high shear, low CAPE environments. Thesis, Dept. of Marine, Earth, and Atmospheric Sciences, North Carolina State University, 124 pp. [Available online at <http://www.lib.ncsu.edu/resolver/1840.16/8666>]
- , and M.D. Parker, 2013: Climatology and ingredients of significant severe convection in high shear, low CAPE environments. *Wea. Forecasting*, submitted.
- Smith, T., and K. L. Elmore, 2004: The use of radial velocity derivatives to diagnose rotation and divergence. Preprints, *11th Conf. on Aviation, Range, and Aerospace*, Hyannis, MA, Amer. Meteor. Soc., P5.6. [Available online at <http://ams.confex.com/ams/pdfpapers/81827.pdf>]

- Smith, B.T., R.L. Thompson, J.S. Grams, C. Broyles, and H.E. Brooks, 2012: Convective modes for significant severe thunderstorms in the contiguous United States. Part I: Storm classification and climatology. *Wea. Forecasting*, **27**, 1114–1135.
- Smull, B. F., and R. A. Houze Jr., 1985: A midlatitude squall line with a trailing region of stratiform rain: Radar and satellite observations. *Mon. Wea. Rev.*, **113**, 117–133.
- , and -----, 1987: Rear-inflow in squall lines with trailing stratiform precipitation. *Mon. Wea. Rev.*, **115**, 2869–2889.
- Stumpf, G.J., A. Witt, E. D. Mitchell, P.L. Spencer, J. T. Johnson, M.D. Eilts, K.W. Thomas, and D.W. Burgess, 1998: The National Severe Storms Laboratory Mesocyclone Detection Algorithm for the WSR-88D. *Wea. Forecasting*, **13**, 304–326.
- Thompson, R. L., R. Edwards, J. A. Hart, K. L. Elmore, and P. Markowski, 2003: Close proximity soundings with supercell environments obtained from the Rapid Update Cycle. *Wea. Forecasting*, **18**, 1243–1261.
- Thompson, R.L., B.T. Smith, J.S. Grams, A.R. Dean, and C. Broyles, 2012: Convective modes for significant severe thunderstorms in the contiguous United States. Part II: Supercell and QLCS tornado environments. *Wea. Forecasting*, **27**, 1136–1154.
- Trapp, R. J., 1999: Observations of nontornadic low-level mesocyclones and attendant tornadogenesis Failure during VORTEX. *Mon. Wea. Rev.*, **127**, 1693–1705.
- , and M.L. Weisman, 2003: Low-level mesovortices within squall lines and bow echoes. Part II: Their genesis and implications. *Mon. Wea. Rev.*, **131**, 2804–2823.
- , G.J. Stumpf, and K.L. Manross, 2005: A reassessment of the percentage of tornadic mesocyclones. *Wea. Forecasting*, **20**, 680–687.
- , S.A. Tessendorf, E.S. Godfrey, and H.E. Brooks, 2005: Tornadoes from squall lines and bow echoes. Part I: Climatological distribution. *Wea. Forecasting*, **20**, 23–34.
- Wakimoto, R.M., H.V. Murphey, C.A. Davis, and N.T. Atkins, 2006: High winds generated by bow echoes. Part II: The relationship between the mesovortices and damaging straight-line winds. *Mon. Wea. Rev.*, **134**, 2813–2829
- Weisman, M.L., and C.A. Davis, 1998: Mechanisms for the generation of mesoscale vortices within quasi-linear convective systems. *J. Atmos. Sci.*, **55**, 2603–2622.

- , and R.J. Trapp, 2003: Low-level mesovortices within squall lines and bow echoes. Part I: Overview and dependence on environmental shear. *Mon. Wea. Rev.*, **131**, 2779–2803.
- Wheatley, D.M., and R. J. Trapp, 2008: The effect of mesoscale heterogeneity on the genesis and structure of mesovortices within quasi-linear convective systems. *Mon. Wea. Rev.*, **136**, 4220–4241.
- Wicker, L. J., and L. Cantrell, 1996: The role of vertical buoyancy distributions in miniature supercells. Preprints, *18th Conf. on Severe Local Storms*, San Francisco, CA, Amer. Meteor. Soc., 225–229.
- Wolf, P.L., 1998: WSR-88D radar depiction of supercell–now echo interaction: unexpected evolution of a large, tornadic, “comma-shaped” supercell over eastern Oklahoma. *Wea. Forecasting*, **13**, 492–504.
- Wood, V.T., R.A. Brown, and D.W. Burgess, 1996: Duration and movement of mesocyclones associated with southern Great Plains thunderstorms. *Mon. Wea. Rev.*, **124**, 97–101.
- , -----, and D. Sirmans, 2001: Technique for improving detection of WSR-88D mesocyclone signatures by increasing angular sampling. *Wea. Forecasting*, **16**, 177–184.